



UNIVERSITY OF LEEDS

Modelling and Optimization of Coal-Fired Power Plant Generation Systems with CO₂ Capture

Elvis Osamudiamen AGBONGHAE

Primary Supervisor: Professor Mohamed Pourkashanian

Co-supervised by: Professor Derek B. Ingham

Dr Lin Ma

Dr Kevin J. Hughes

Submitted in accordance with the requirements for the degree of
Doctor of Philosophy (PhD)

The University of Leeds
School of Chemical and Process Engineering

January, 2015

The candidate confirms that the work submitted is his own, except where work which has formed part of jointly-authored publications has been included. The contribution of the candidate and the other authors to this work has been explicitly indicated below. The candidate confirms that appropriate credit has been given within the thesis where reference has been made to the work of others.

The work in **Chapter 5** of the thesis has appeared in publication as follows:

E.O. Agbonghae, K.J. Hughes, D.B. Ingham, L. Ma, M. Pourkashanian, A Semi-Empirical Model for Estimating the Heat Capacity of Aqueous Solutions of Alkanolamines for CO₂ Capture, Ind. Eng. Chem. Res., 53 (19) (2014) p. 8291–8301.

The other authors were my supervisors who acted in an advisory role and gave suggestions regarding the research direction and analysis methods.

The work in **Chapter 6** of the thesis has appeared in publication as follows:

E.O. Agbonghae, T. Best, K.N. Finney, C. Font Palma, K.J. Hughes, M. Pourkashanian, Experimental and Process Modelling Study of Integration of a Micro-turbine with an Amine Plant, Energy Procedia, 63 (2014) p. 1064-1073.

The contributions from **T. Best**, **K. N. Finney** and **C. Font Palma** in the publication are not included in this thesis. The other authors were my supervisors who acted in an advisory role and gave suggestions regarding the research direction and analysis methods.

The work in **Chapter 7** of the thesis has appeared in publication as follows:

E.O. Agbonghae, K.J. Hughes, D.B. Ingham, L. Ma, M. Pourkashanian, Optimal Process Design of Commercial-scale Amine-based CO₂ Capture Plants, Ind. Eng. Chem. Res., 53 (38) (2014) p. 14815-14829.

The other authors were my supervisors who acted in an advisory role and gave suggestions regarding the research direction and analysis methods.

This copy has been supplied on the understanding that it is copyright material and that no quotation from the thesis may be published without proper acknowledgement.

The right of Elvis Osamudiamen AGBONGHAE to be identified as Author of this work has been asserted by him in accordance with the Copyright, Designs and Patents Act 1988.

© 2015 The University of Leeds and Elvis Osamudiamen AGBONGHAE

Acknowledgements

*First and foremost, I would like to express my sincere gratitude to my supervisors, **Prof M. Pourkashanian, Prof D. B. Ingham, Dr L. Ma and Dr K. J. Hughes**, for their excellent supervision and for their guidance over the past three years. Their ideas, suggestions, and timely contributions, which led to the realization of the aims and objectives of this thesis, are most appreciated. I would also like to use this medium to express my appreciation to the other members of staff in the Energy Technology and Innovation Initiative (ETII) group at the University of Leeds. All I can say is thank you all for the job well done. However, my special thanks go to **Mrs Lisa Flaherty and Miss Charlotte Kelsall** for being there all the time and for their willingness to assist promptly whenever their assistance was needed.*

*My sincere appreciation goes to members of my family for their love and support. I must not fail to mention the spiritual buffer from my dad, **Mr. Augustine Agbonghae**. I want to say thank you dad for your love, prayer and faith in me. I would also love to express my appreciation to my mum, **Mrs. Roseline Agbonghae**, for her love as well as my siblings: **Ikponmwoza, Orobosa, Osahon, Joy and Wisdom** for their faith in me. I love you all!*

*It will be an act of ingratitude on my part if I fail to appreciate my sponsor, the **Commonwealth Scholarship Commission in the UK**, for the commonwealth scholarship awarded to me to undertake the study in this thesis. This particular study would not have been possible if not for the scholarship award. Also, I must not fail to appreciate my employer in Nigeria, the **University of Benin**, for granting me study leave to undertake the research work in this thesis.*

*Lastly, and above all, my utmost and sincere gratitude and appreciation go to **Almighty God**, the father and creator of the universe and without whom I am naught.*

Publications and Conferences

Journal Papers

[1] **E.O. Agbonghae**, K.J. Hughes, D.B. Ingham, L. Ma, M. Pourkashanian, A Semi-Empirical Model for Estimating the Heat Capacity of Aqueous Solutions of Alkanolamines for CO₂ Capture, *Ind. Eng. Chem. Res.*, 53 (19) (2014) pp 8291–8301.

[2] **E.O. Agbonghae**, K.J. Hughes, D.B. Ingham, L. Ma, M. Pourkashanian, Optimal Process Design of Commercial-scale Amine-based CO₂ Capture Plants, *Ind. Eng. Chem. Res.*, 53 (38) (2014) pp 14815-14829.

[3a] **E.O. Agbonghae**, T. Best, K.N. Finney, C. Font Palma, K.J. Hughes, M. Pourkashanian, Experimental and Process Modelling Study of Integration of a Micro-turbine with an Amine Plant, *Energy Procedia*, 63 (2014) pp 1064-1073.

[4a] **E.O. Agbonghae**, C. Font Palma, K.J. Hughes, D.B. Ingham, L. Ma, M. Pourkashanian, Optimal Integration of a Coal-fired Power Plant to a CO₂ Capture Plant Based on Parametric Studies, *Fuel*, (2014) Submitted for Publication.

[5a] **E.O. Agbonghae**, C. Font Palma, K.J. Hughes, D.B. Ingham, L. Ma, M. Pourkashanian, Modelling and Simulation of a Coal-fired Supercritical Power Plant Integrated to a CO₂ Capture Plant, *Fuel*, (2014) Submitted for Publication.

Conferences (Oral Presentations)

[3b] **Agbonghae, E. O.**; Best, T.; Finney, K. N.; Font Palma, C.; Hughes, K. J.; Pourkashanian, M. Experimental and Process Modelling Study of Integration of a Micro-turbine with an Amine Plant. In *12th International Conference on Greenhouse Gas Control Technologies (GHGT-12)*: Austin, Texas, 5th - 9th October, 2014.

[4b] **Agbonghae, E. O.**; Font Palma, C.; Hughes, K. J.; Ingham, D. B.; Ma, L.; Pourkashanian, M. Optimal Integration of a Coal-fired Power Plant to a CO₂ Capture Plant Based on Parametric Studies. In *10th European Conference on Coal Research and its Applications (10th ECCRIA)*: University of Hull, UK, 15th - 17th September, 2014.

[5b] **Agbonghae, E. O.**; Font Palma, C.; Hughes, K. J.; Ingham, D. B.; Ma, L.; Pourkashanian, M. Modelling and Simulation of a Coal-fired Supercritical Power Plant Integrated to a CO₂ Capture Plant. In *10th European Conference on Coal Research and its Applications (10th ECCRIA)*: University of Hull, UK, 15th - 17th September, 2014.

Abstract

This thesis investigates the capture of CO₂ from the flue gas of coal-fired power plants using an aqueous solution of MEA, and the main aim of this thesis is the development of an optimized amine-based post-combustion CO₂ capture (PCC) process that can be integrated optimally with a pulverized coal-fired power plant.

The relevance of this thesis cannot be overemphasised because the reduction of solvent regeneration energy is the focus of most of the solvent-based post-combustion CO₂ capture (PCC) research currently being performed globally. From the view point of current research and development (R&D) activities worldwide, three main areas are being investigated in order to reduce the regeneration energy requirement of an amine-based PCC process, namely: (i) development of new solvents with better overall performance than 30 wt% monoethanolamine (MEA) aqueous solution, (ii) PCC plant optimization, and (iii) optimal integration of the PCC Plant, including the associated CO₂ compression system, to the upstream power plant.

In this thesis, PCC plant optimization and the optimal integration of an optimized PCC Plant, including the associated CO₂ compression system, with an upstream coal-fired power plant has been investigated. Thus, an integrated process comprising ~550 MWe (net power after CO₂ capture and compression) pulverized coal-fired (PC-fired) supercritical power plant, an MEA-based post-combustion capture (PCC) plant and a CO₂ compression system has been modelled, simulated and optimized. The scale-up design of the PCC plant was performed using a novel method based on a rate-based calculation and thus the unnecessary over-design of the PCC plant columns was avoided.

Furthermore, because of the importance of the operating pressure of the stripper in a PCC plant integrated to a PC-fired power plant, the impact of the operating pressure of the stripper on the net plant efficiency of the integrated system has been quantified. Also, the impacts of coal type on the overall performance of the integrated process have been quantified.

Table of Contents

Acknowledgements	iv
Publications and Conferences	v
Abstract	vi
Table of Contents	vii
List of Tables	xiii
List of Figures	xvi
Nomenclature	xxii
Chapter 1 Introduction	1
1.1 Research Background.....	1
1.1.1 CO ₂ Emissions	1
1.1.2 CO ₂ Emissions and Climate Change.....	3
1.1.3 Resolving the Problem of Climate Change.....	3
1.1.3.1 CO ₂ Capture and Storage (CCS)	4
1.2 Motivation of the Thesis	9
1.3 Scope.....	10
1.4 Aim and Objectives	10
1.5 Relevance	11
1.6 Thesis Outline	12
Chapter 2 An Introduction to Gas Purification Processes	13
2.1 An Overview of Gas Purification Processes.....	13
2.1.1 Absorption	13
2.1.2 Adsorption	14
2.1.3 Membrane Separation.....	14
2.1.4 Chemical conversion	15
2.1.5 Condensation	15
2.2 A Review of Alkanolamines used in Gas Purification	15
2.2.1 Primary Alkanolamines	17
2.2.1.1 Monoethanolamine (MEA)	17
2.2.1.2 2-(2-Aminoethoxy) Ethanol (DGA)	18
2.2.2 Secondary Alkanolamines.....	18
2.2.2.1 Diethanolamine (DEA)	18

2.2.2.2	Diisopropanolamine (DIPA).....	19
2.2.3	Tertiary Alkanolamines.....	19
2.2.3.1	Triethanolamine (TEA).....	19
2.2.3.2	Methyldiethanolamine (MDEA)	19
2.2.4	Sterically Hindered Amines	20
2.2.5	Mixed Amines.....	21
Chapter 3	Chemistry and Kinetics of CO₂ Reaction with Aqueous Solution of Alkanolamines	22
3.1	Chemistry of CO ₂ Reaction with Aqueous Alkanolamines.....	22
3.1.1	Mechanism of CO ₂ Reaction with Aqueous Alkanolamines.....	23
3.1.1.1	Zwitterion Mechanism	23
3.1.1.2	Termolecular Mechanism.....	24
3.1.1.3	Base-catalysed Hydration Mechanism.....	25
3.1.2	Kinetics of the CO ₂ Reaction with Aqueous Alkanolamines.....	25
3.1.2.1	CO ₂ Reaction with Primary and Secondary Alkanolamines.....	26
3.1.2.2	CO ₂ Reaction with Tertiary Alkanolamines	29
3.1.2.3	CO ₂ Reaction with Mixed Amines	29
Chapter 4	Thermodynamics of CO₂-Alkanolamines-H₂O Systems	32
4.1	Gas-Liquid Phase Equilibria	33
4.1.1	Fugacity and Fugacity Coefficient	34
4.1.2	Activity and Activity Coefficient.....	37
4.2	Standard States and Normalization Conventions.....	38
4.2.1	Normalization Convention I	39
4.2.2	Normalization Convention II	39
4.2.3	Normalization Convention III	40
4.3	Liquid Phase Chemical-Reaction Equilibria.....	41
4.4	Rigorous Vapour-Liquid-Equilibrium (VLE) Models for CO ₂ -Alkanolamines-H ₂ O Systems	43
4.4.1	Models for the Fugacity Coefficient	46
4.4.2	Models for the Activity Coefficient	47
4.4.2.1	Electrolyte-NRTL Model.....	48
4.5	Other Thermodynamic Properties	55
4.5.1	Gibbs Energy	56

4.5.2	Enthalpy	57
4.5.3	Entropy.....	58
4.5.4	Vapour pressure.....	59
4.5.5	Enthalpy of Vapourization	60
4.5.6	Heat Capacity.....	62
4.6	Heat of Solution (Heat of Absorption).....	64
Chapter 5	A Semi-Empirical Model for Estimating the Heat Capacity of Aqueous Solutions of Alkanolamines for CO₂ Capture	68
5.1	Introduction	68
5.2	Modelling.....	69
5.3	Data Regression and Parameters Estimation	72
5.4	Results and Discussion.....	74
5.4.1	Pure Components	74
5.4.2	Binary Systems	83
5.4.2.1	MEA-H ₂ O System	86
5.4.2.2	DEA-H ₂ O System.....	86
5.4.2.3	MDEA-H ₂ O System.....	87
5.4.2.4	AMP-H ₂ O System	87
5.4.2.5	PZ-H ₂ O System	88
5.4.2.6	Non-aqueous Binary Systems.....	88
5.4.3	Ternary Systems (without CO ₂ Loading)	89
5.4.4	CO ₂ -Loaded Systems.....	93
5.4.4.1	CO ₂ -MEA-H ₂ O System	93
5.4.4.2	CO ₂ -DEA-H ₂ O System.....	97
5.4.4.3	CO ₂ -MDEA-H ₂ O System.....	98
5.4.4.4	CO ₂ -PZ-H ₂ O System.....	99
5.4.4.5	CO ₂ -MEA-MDEA-H ₂ O System	100
5.4.4.6	CO ₂ -DEA-MDEA-H ₂ O System	101
5.4.4.7	CO ₂ -PZ-MEA-H ₂ O System.....	101
5.5	Conclusions.....	104
Chapter 6	Modelling and Simulation of MEA-based CO₂ Capture Process at Pilot-scale.....	105
6.1	Introduction	105
6.2	Pilot Plants and Process Description	105
6.2.1	The UKCCSRC/PACT Pilot Plant.....	105

6.2.2	The University of Kaiserslautern Pilot Plant	107
6.3	Modelling Framework.....	111
6.3.1	Thermodynamic Model.....	111
6.3.2	Reaction Kinetics Model.....	111
6.3.3	Transport Property Models.....	112
6.3.4	Implementation of the Pilot Plant Models in Aspen Plus®	113
6.4	Model Validation.....	117
6.4.1	Validation of the UKCCSRC/PACT Pilot Plant Model	117
6.4.2	Validation of the University of Kaiserslautern Pilot Plant Model	118
6.5	Conclusions.....	130
Chapter 7	Optimal Process Design of Commercial-scale Amine-based CO₂ Capture Plants.....	131
7.1	Introduction	131
7.2	Process Description	134
7.3	Process Design of Absorption and Stripping Columns.....	138
7.3.1	Column Diameter Sizing.....	138
7.3.2	Packed Height based on HETP.....	139
7.4	Model Validation at Pilot-scale and Design Philosophy.....	140
7.4.1	Aspen Plus Rate-based Model Validation at Pilot-scale.....	140
7.4.2	Design Philosophy Implementation in Aspen Plus®	143
7.4.3	Design Philosophy Validation at Pilot-Scale.....	144
7.5	Scale-up Applications.....	145
7.5.1	Commercial-scale MEA-based CO ₂ Capture plants for Natural Gas Combined Cycle (NGCC) Power Plants.....	151
7.5.2	Commercial-scale MEA-based CO ₂ Capture plants for Pulverized Coal (PC) Power Plants.....	155
7.6	Conclusions.....	159
Chapter 8	Optimal Integration of Amine-based CO₂ Capture Plant to a Coal-Fired Power Plant.....	161
8.1	Introduction	161
8.2	Process Description and Modelling Framework	163
8.2.1	Process Description	163
8.2.2	Modelling Framework.....	166
8.3	Optimal Process Design of the PCC Plant in the Integrated System	169

8.4	Integration of the PC-fired Power Plant to the PCC Plant and the CCU	173
8.4.1	Steam tapping from the IP-LP cross-over pipe at 5.07 bar	175
8.4.2	Steam tapping from the LP turbine at 4 bar.....	177
8.4.3	Steam tapping from the LP Turbine at 3 bar	180
8.4.4	The Effect of Stripper Pressure on the Lean/Rich Heat Exchanger	182
8.4.5	Steam Cycle Condensate Pre-heating	183
8.5	Conclusions.....	184
Chapter 9	Modelling and Simulation of a Coal-Fired Power Plant Integrated to an Amine-based CO₂ Capture Plant	186
9.1	Introduction	186
9.2	Process Description and Modelling Framework	187
9.2.1	Process Description	187
9.2.2	Modelling Framework.....	191
9.3	Results and Discussions	191
9.3.1	Optimum Lean CO ₂ Loading and Liquid/Gas Ratio	195
9.3.2	Effect of the Temperature of the Flue Gas (Absorber Inlet).....	203
9.3.3	Effect of the Temperature of the Lean Amine Solution (Absorber Inlet)	205
9.3.4	Effect of CO ₂ Capture Level.....	206
9.3.5	Effect of Amine Concentration.....	207
9.4	Conclusions.....	210
Chapter 10	Conclusions and Recommendations	212
10.1	Heat Capacity of Aqueous Solutions of Alkanolamines (Chapter 5).....	213
10.1.1	Conclusions	213
10.1.2	Recommendations for Future Research Work	213
10.2	Modelling and Simulation of Pilot-scale CO ₂ Capture Plant (Chapter 6).....	214
10.2.1	Conclusions	214
10.2.2	Recommendations for Future Research Work	215
10.3	Process Design of Commercial Scale Amine-based CO ₂ Capture Plant (Chapter 7)	216
10.3.1	Conclusions	216
10.3.2	Recommendations for Future Research Work	217

10.4 Optimal Integration of a PPC Plant with a PC Power Plant (Chapter 8)	218
10.4.1 Conclusions	218
10.4.2 Recommendations for Future Research Work	219
10.5 Simulation of a PC Power Plant Integrated with a PCC Plant and a CCU (Chapter 9)	219
10.5.1 Conclusions	219
10.5.2 Recommendations for Future Research Work	221
Appendix A: Derivation of Eq. (5.2.13)	222
Appendix B: Standard Errors and Confidence Levels, as well as the Correlation Matrices, of the Model Parameters in Chapter 5.	223
Appendix C: Derivation of Eq. (7.5.1)	242
Appendix D: Optimum design data for the MEA-based CO₂ capture plants designed in Chapter 7.	245
List of References	248

List of Tables

Table 1.1. Relationship between climate change and CO ₂ emissions. ⁸	3
Table 1.2. Carbon dioxide capture technology toolbox. ¹³	10
Table 1.3. Status of CO ₂ capture technologies as at 2011. ²⁰	12
Table 4.1. Assignment of Parameters for the RK, SRK and PR Equations of State. ¹⁰²	47
Table 4.2. Aspen Plus [®] Default Parameters for the Extended Antoine Equation.	59
Table 4.3. Aspen Plus [®] Default Parameters for the Watson Enthalpy of Vapourization Model.....	61
Table 4.4. Aspen Plus [®] Default Parameters for the DIPPR Enthalpy of Vapourization Model.....	62
Table 5.1. Heat Capacity Data used in the Regression of the Parameters for Pure Alkanolamines and Pure Water.	75
Table 5.2. Heat Capacity Data used in the Regression of the Parameters for the Excess Heat Capacity contribution due to Binary Interactions.....	76
Table 5.3. Heat Capacity Data used in the Regression of the Parameters for the Excess Heat Capacity contribution due to Ternary Interactions.....	77
Table 5.4. Heat Capacity Data used in the Regression of the Parameters for the Excess Heat Capacity contribution due to CO ₂ Loading Effect.	78
Table 5.5. Parameters for the Heat Capacity of Pure Water and Pure Alkanolamines based on Eq. (5.2.6).	81
Table 5.6. Parameters for the Excess Heat Capacity contribution due to Binary Interactions based on Eqs. (5.2.7) and (5.2.8).....	83
Table 5.7. Statistics of the Heat Capacity Model Predictions for the Binary Systems against the Experimental Data used in the Fitting.	84
Table 5.8. Parameters for the Excess Heat Capacity contribution due to Ternary Interactions based on Eqs. (5.2.9) and (5.2.10).....	91
Table 5.9. Statistics of the Heat Capacity Model Predictions for the Ternary Systems against the Experimental Data used in the Fitting.	92
Table 5.10. Parameters for the Excess Heat Capacity contribution due to CO ₂ Loading Effect based on Eqs. (5.2.11) and (5.2.12).....	94

Table 5.11. Statistics of the Heat Capacity Model Predictions for the CO₂ loaded Systems against the Experimental Data used in the Fitting.....	95
Table 6.1. Key data for the columns in the UKCCSRC/PACT Pilot Plant.¹⁴⁷	106
Table 6.2. Survey data for the University of Kaiserslautern Pilot Plant.¹⁴⁸	109
Table 6.3. Kinetic expressions for MEA carbamate and bicarbonate reactions in the absorber and stripper.¹⁵⁰	112
Table 6.4. Summary of the models in Aspen Plus® that were used for transport properties calculations.⁸⁷	113
Table 6.5. The key parameters and sub-models used in setting up the pilot plants models.	113
Table 6.6. Comparison of experimental and simulation results for the UKCCSRC/PACT CO₂ capture pilot plant.¹⁴⁷	117
Table 6.7. Comparison of the key pilot plant and simulation results for the University of Kaiserslautern CO₂ capture pilot plant.	122
Table 7.1. Summary of the design data for the standard configuration of an MEA-based CO₂ capture process, including the key assumptions made, as reported by different authors in the open literature.....	135
Table 7.2. Flue gas conditions and compositions adopted for the design cases.....	147
Table 7.3. Design and Economic Analysis Assumptions used for the design cases in this Chapter.	148
Table 7.4. Summary of the key design results for the absorber and stripper columns.	149
Table 8.1. A comparison of the stripper pressure adopted for a MEA-based CO₂ capture plant by various authors.	162
Table 8.2. The properties of Illinois No. 6 bituminous coal.²⁰⁴	166
Table 8.3. Inter-stage pressure of the CO₂ Compressor.¹⁹²	168
Table 8.4. Optimal design data for the absorber and stripper columns in the PCC plant.....	169
Table 8.5. The optimum performance data for the PCC plant, including the compression and intercooling duties of the CCU.	172
Table 9.1. The proximate analysis, the ultimate analysis and the heating value of the three different types of coal investigated.²⁰⁴	189
Table 9.2. The key performance data of the PC power plant when fired with the three different types of coal investigated.	192

Table 9.3. The conditions and composition of the flue gas from the combustion of the different types of coal investigated at various locations.....	194
Table 9.4. Optimal design data for the absorber and stripper columns in the CO₂ capture plant based on Illinois No. 6 bituminous coal.....	195
Table 9.5. The optimum performance data for the CO₂ capture plant with a 30 wt% MEA solution, including the compression and intercooling duties of the CO₂ compression system, for the three different types of coal investigated.....	196
Table 9.6. A comparison of the optimum energy performance of the integrated system for the three different types of coal.^b	198
Table 9.7. Overall performance of the integrated PC power plant-PCC-CCU system for the three different types of coal investigated, and for different MEA concentrations.	199
Table B.1. Standard Errors and Confidence Levels of the Parameters for Pure Water and Pure Alkanolamines based on Eq.(5.2.6).	223
Table B.2. Standard Errors and Confidence Levels of the Parameters for the Excess Heat Capacity contribution due to Binary Interactions based on Eqs. (5.2.7) and (5.2.8).	225
Table B.3. Standard Errors and Confidence Levels of the Parameters for the Excess Heat Capacity contribution due to Ternary Interactions based on Eqs. (5.2.9) and (5.2.10).	228
Table B.4. Standard Errors and Confidence Levels of the Parameters for the Excess Heat Capacity contribution due to CO₂ Loading Effect based on Eqs. (5.2.11) and (5.2.12).	230
Table B.5. Correlation Matrices for the Pure Component Parameters.	233
Table B.6. Correlation Matrices for the Binary Interaction Parameters.	234
Table B.7. Correlation Matrices for the Ternary Interaction Parameters.	238
Table B.8. Correlation Matrices for the CO₂ Loading Effect Parameters.	239

List of Figures

Figure 1.1. Global atmospheric CO ₂ concentration and temperature as a function of the year. ¹	1
Figure 1.2 Global CO ₂ emissions by sector in 2011. ²	2
Figure 1.3. Projected contributions of different technology options to global CO ₂ emissions reduction. ⁷	4
Figure 1.4. Schematic diagram of possible CCS systems. ¹⁰	5
Figure 1.5. Technical options for CO ₂ capture from coal-fired power plants. ¹	6
Figure 1.6: Technologies for CO ₂ separation and capture. ¹⁹	7
Figure 2.1. Structural formulas of alkanolamines commonly used in gas treating. ¹⁷	16
Figure 2.2. Structural formulas of some sterically hindered amines. ⁶²	20
Figure 3.1. Schematic of the termolecular mechanism. ⁸¹	24
Figure 3.2. Schematic of the base-catalysed mechanism. ⁷⁹	25
Figure 4.1. A Schematic of the coupling of the chemical and phase equilibria in CO ₂ -MEA-H ₂ O system. ⁸⁸	32
Figure 5.1. Molar heat capacity of pure MEA.	74
Figure 5.2. Molar heat capacity of pure MDEA	79
Figure 5.3. Molar heat capacity of pure DEA	79
Figure 5.4. Molar heat capacity of pure AMP	80
Figure 5.5. Molar heat capacity of Pure PZ	80
Figure 5.6. Percentage uncertainties of the model predictions of the heat capacity of pure H ₂ O against the pure H ₂ O heat capacity data from the International Association for the Properties of Water and Steam (IAPWS) ¹⁴⁵ and the National Institute of Standards and Technology (NIST) database. ¹⁴⁶	82
Figure 5.7. The variations of the heat capacity of aqueous solutions of MEA, $c_p/(\text{kJ}\cdot\text{kg}^{-1}\cdot\text{K}^{-1})$, with CO ₂ loading, $\alpha/(\text{mol}\cdot\text{mol}^{-1})$, at a fixed temperature of 298.15 K.....	96
Figure 5.8. The variations of the heat capacity of 3.5 mol·kg ⁻¹ aqueous solutions of MEA, $c_p/(\text{kJ}\cdot\text{kg}^{-1}\cdot\text{K}^{-1})$, with temperature, T/K, for zero CO ₂ loading and for three different CO ₂ loadings	96
Figure 5.9. The variations of the heat capacity of 7.0 mol·kg ⁻¹ aqueous solutions of MEA, $c_p/(\text{kJ}\cdot\text{kg}^{-1}\cdot\text{K}^{-1})$, with temperature, T/K, for zero CO ₂ loading and for three different CO ₂ loadings	97

Figure 5.10. The variations of the heat capacity of aqueous solutions of DEA, $c_p/(\text{kJ}\cdot\text{kg}^{-1}\cdot\text{K}^{-1})$, with CO_2 loading, $\alpha/(\text{mol}\cdot\text{mol}^{-1})$, at a fixed temperature of 298.15 K.....	98
Figure 5.11. The variations of the heat capacity of aqueous solutions of MDEA, $c_p/(\text{kJ}\cdot\text{kg}^{-1}\cdot\text{K}^{-1})$, with CO_2 loading, $\alpha/(\text{mol}\cdot\text{mol}^{-1})$, at a fixed temperature of 298.15 K.....	99
Figure 5.12. The variations of the heat capacity of 2.0 mol·kg ⁻¹ aqueous solutions of PZ, $c_p/(\text{kJ}\cdot\text{kg}^{-1}\cdot\text{K}^{-1})$, with temperature, T/K, for zero CO_2 loading and for three different CO_2 loadings ..	100
Figure 5.13. The variations of the heat capacity of 3.6 mol·kg ⁻¹ aqueous solutions of PZ, $c_p/(\text{kJ}\cdot\text{kg}^{-1}\cdot\text{K}^{-1})$, with temperature, T/K, for zero CO_2 loading and for two different CO_2 loadings.....	101
Figure 5.14. The variations of the heat capacity of aqueous solutions of MEA/MDEA blends, $c_p/(\text{kJ}\cdot\text{kg}^{-1}\cdot\text{K}^{-1})$, with CO_2 loading, $\alpha/(\text{mol}\cdot\text{mol}^{-1})$, at a fixed temperature of 298.15 K.....	102
Figure 5.15. The variations of the heat capacity of aqueous solutions of DEA/MDEA blends, $c_p/(\text{kJ}\cdot\text{kg}^{-1}\cdot\text{K}^{-1})$, with CO_2 loading, $\alpha/(\text{mol}\cdot\text{mol}^{-1})$, at a fixed temperature of 298.15 K.....	103
Figure 5.16. The variations of the heat capacity of aqueous solutions made up of 2.0 mol·kg ⁻¹ of PZ and 3.5 mol·kg ⁻¹ of MEA, $c_p/(\text{kJ}\cdot\text{kg}^{-1}\cdot\text{K}^{-1})$, with temperature, T/K, for zero CO_2 loading and for three different CO_2 loadings.....	103
Figure 5.17. The variations of the heat capacity of aqueous solutions made up of 2.0 mol·kg ⁻¹ of PZ and 7.0 mol·kg ⁻¹ of MEA, $c_p/(\text{kJ}\cdot\text{kg}^{-1}\cdot\text{K}^{-1})$, with temperature, T/K, for zero CO_2 loading and for three different CO_2 loadings.....	104
Figure 6.1. A Schematic of the UKCCSRC/PACT CO_2 Capture Pilot Plant. ¹⁴⁷	106
Figure 6.2. Process and Instrumentation Diagram (P&ID) of the Pilot Plant at the University of Kaiserslautern. ¹⁴⁸	108
Figure 6.3. Process flow diagram of the model of the UKCCSRC/PACT pilot plant as implemented in Aspen Plus®. ¹⁴⁷	115
Figure 6.4. Process flow diagram of the model of the University of Kaiserslautern pilot plant as implemented in Aspen Plus®.....	116
Figure 6.5. Variation of the solvent flowrate at constant flue gas rate of approximately 71.2 kg/h, constant CO_2 partial pressure of approximately 54.7 mbar in the flue gas, and constant CO_2 capture rate of approximately 76%. (a) Temperature profile in the absorber. (b) Temperature profile in the stripper.	124

Figure 6.6. Variation of the solvent flowrate at constant flue gas rate of approximately 70.8 kg/h, constant CO ₂ partial pressure of approximately 53.7 mbar in the flue gas, and constant CO ₂ capture rate of approximately 88%. (a) Temperature profile in the absorber. (b) Temperature profile in the stripper.	124
Figure 6.7. Variation of the solvent flowrate at constant flue gas rate of approximately 99.6 kg/h, constant CO ₂ partial pressure of approximately 57.1 mbar in the flue gas, and constant CO ₂ capture rate of approximately 75%. (a) Temperature profile in the absorber. (b) Temperature profile in the stripper.	125
Figure 6.8. Variation of the solvent flowrate at constant flue gas rate of approximately 75.5 kg/h, constant CO ₂ partial pressure of approximately 107.5 mbar in the flue gas, and constant CO ₂ capture rate of approximately 54%. (a) Temperature profile in the absorber. (b) Temperature profile in the stripper.	125
Figure 6.9. Variation of the desorber pressure. (a) Temperature profile in the absorber. (b) Temperature profile in the stripper.....	126
Figure 6.10. Variation of MEA mass fraction at a constant CO ₂ partial pressure of approximately 55.5 mbar in the flue gas. (a) Temperature profile in the absorber. (b) Temperature profile in the stripper.	126
Figure 6.11. Variation of MEA mass fraction at a constant CO ₂ partial pressure of approximately 109.5 mbar in the flue gas. (a) Temperature profile in the absorber. (b) Temperature profile in the stripper.	127
Figure 6.12. Variation of the lean solvent temperature. (a) Temperature profile in the absorber. (b) Temperature profile in the stripper.	127
Figure 6.13. Variation of the CO ₂ partial pressure in the flue gas. (a) Temperature profile in the absorber. (b) Temperature profile in the stripper.	128
Figure 6.14. Variation of the fluid dynamic load (F-factor) in the absorber at a constant liquid/gas ratio of 2.8. (a) Temperature profile in the absorber. (b) Temperature profile in the stripper.....	128
Figure 6.15. Variation of the CO ₂ removal rate at a CO ₂ partial pressure of approximately 54.6 mbar. (a) Temperature profile in the absorber. (b) Temperature profile in the stripper.	129
Figure 6.16. Variation of the CO ₂ removal rate at a CO ₂ partial pressure of approximately 109.6 mbar. (a) Temperature profile in the absorber. (b) Temperature profile in the stripper.....	129

Figure 6.17. Variation of the flue gas temperature. (a) Temperature profile in the absorber. (b) Temperature profile in the stripper.....	130
Figure 7.1. The basic flowsheet for an amine-based CO ₂ capture process.	134
Figure 7.2. Comparison of key simulation results with the pilot plant results reported by Notz et al. ¹⁴⁸	141
Figure 7.3. Comparison of absorber and stripper profile results at constant liquid/gas ratio (L/G = 2.8) with the pilot plant results reported by Notz et al. ¹⁴⁸	142
Figure 7.4. Design philosophy validation at pilot scale.	145
Figure 7.5. Design results for an MEA-based CO ₂ capture plant that can service a 400 MWe (gross) NGCC power plant at 90% CO ₂ capture rate.....	152
Figure 7.6. Design results for an MEA-based CO ₂ capture plant that can service a 450 MWe (gross) NGCC power plant at 90% CO ₂ capture rate.....	152
Figure 7.7. Economic results for an MEA-based CO ₂ capture plant that can service a 400 MWe (gross) NGCC power plant at 90% CO ₂ capture rate.....	153
Figure 7.8. Economics results for an MEA-based CO ₂ capture plant that can service a 450 MWe (gross) NGCC power plant at 90% CO ₂ capture rate.....	154
Figure 7.9. Design results for an MEA-based CO ₂ capture plant that can service a 673 MWe (gross) subcritical PC power plant at 90% CO ₂ capture rate.....	156
Figure 7.10. Design results for an MEA-based CO ₂ capture plant that can service an 827 MWe (gross) ultra-supercritical PC power plant at 90% CO ₂ capture rate.	157
Figure 7.11. Design results for an MEA-based CO ₂ capture plant that can service a 673 MWe (gross) subcritical PC power plant at 90% CO ₂ capture rate.....	157
Figure 7.12. Design results for an MEA-based CO ₂ capture plant that can service an 827 MWe (gross) ultra-supercritical PC power plant at 90% CO ₂ capture rate.	158
Figure 8.1. The process flow diagram (PFD) of the integrated power plant-PCC-CCU system with a PC-fired boiler firing Illinois No. 6 (bituminous coal), a once-through supercritical single-reheat steam cycle, and with throttled steam tapped from the IP-LP cross-over pipe.....	165
Figure 8.2. Design results for an MEA-based CO ₂ capture plant that can service a 663 MWe (gross) supercritical PC power plant at 90% CO ₂ capture rate.....	170

Figure 8.3. Design results for an MEA-based CO ₂ capture plant that can service a 663 MWe (gross) supercritical PC power plant at 90% CO ₂ capture rate.....	171
Figure 8.4. The reboiler conditions, tapped steam condition requirement and the maximum stripper temperature at different stripper pressure.	174
Figure 8.5. The variations of specific reboiler duty, specific condenser duty and the tapped steam mass flowrate with stripper pressure.....	175
Figure 8.6. The performance of the integrated power plant-PCC plant-CCU system if steam is tapped from the IP-LP cross-over pipe in the steam cycle.	176
Figure 8.7. The performance of the integrated power plant-PCC plant-CCU system if a low pressure (LP) steam at 4 bar is tapped from the low pressure turbine in the steam cycle.	179
Figure 8.8. The performance of the integrated power plant-PCC plant-CCU system if a low pressure (LP) steam at 3 bar is tapped from the low pressure turbine in the steam cycle.	181
Figure 8.9. The variations of the heat duty and the heat transfer area of the lean/rich heat exchanger.....	182
Figure 9.1. The process flow diagram (PFD) of the integrated power plant-PCC-CCU system with a PC-fired boiler and a once-through supercritical single-reheat steam cycle.	188
Figure 9.2. (a) The variations of the specific reboiler duty and liquid/gas with lean CO ₂ loading for 90% CO ₂ capture with 30 wt% MEA solution. Lines: Solid lines, specific reboiler duty; dashed lines, liquid/gas ratio. (b) The variations of the net plant efficiency with lean CO ₂ loading. Lines: Solid lines, net plant efficiency with CO ₂ capture only; dashed lines, net plant efficiency with CO ₂ capture and compression.....	202
Figure 9.3. (a) The variations of the lean and rich pumps duty with lean CO ₂ loading for 90% CO ₂ capture with 30 wt% MEA solution. Lines: Solid lines, lean pump; dashed lines, rich pump. (b) The variations of the heat duty and the heat transfer area of the lean/rich heat exchanger. Lines: Solid lines, heat exchanger duty; dashed lines, heat exchanger area.....	202
Figure 9.4. (a) The variations of the specific reboiler duty and reboiler duty with flue gas temperature at the absorber inlet, and for 0.18 mol/mol optimum CO ₂ loading. Lines: Solid lines, specific reboiler duty; dashed lines, reboiler duty. (b) The variations of the CO ₂ capture efficiency with flue gas temperature at the absorber inlet.	204

Figure 9.5. (a) The variations of the specific reboiler duty with lean amine solution temperature at the absorber inlet, and for 0.18 mol/mol optimum CO₂ loading. (b) The variations of the CO₂ capture efficiency with lean amine solution temperature at the absorber inlet.....	205
Figure 9.6. (a) The variations of the specific reboiler duty and the net plant efficiency with CO₂ capture level, and for 0.18 mol/mol optimum CO₂ loading. Lines: Solid lines, specific reboiler duty; dashed lines, net plant efficiency. (b) The variations of liquid/gas ratio at 0.18 lean CO₂ loading with CO₂ capture level. S	206
Figure 9.7. (a) The variations of the specific reboiler duty and liquid/gas with lean CO₂ loading for 90% CO₂ capture with 35 wt% MEA solution. Lines: Solid lines, specific reboiler duty; dashed lines, liquid/gas ratio. (b) The variations of the net plant efficiency with lean CO₂ loading. Lines: Solid lines, net plant efficiency with CO₂ capture only; dashed lines, net plant efficiency with CO₂ capture and compression.....	207
Figure 9.8. (a) The variations of the specific reboiler duty and liquid/gas with lean CO₂ loading for 90% CO₂ capture with 40 wt% MEA solution. Lines: Solid lines, specific reboiler duty; dashed lines, liquid/gas ratio. (b) The variations of the net plant efficiency with lean CO₂ loading. Lines: Solid lines, net plant efficiency with CO₂ capture only; dashed lines, net plant efficiency with CO₂ capture and compression.....	208
Figure 9.9. The variations of the heat duty and the heat transfer area of the lean/rich heat exchanger with lean CO₂ loading for 90% CO₂ capture.	210
Figure 10.1. Concentration range of the mixture of MEA and MDEA recommended for investigation.....	216

Nomenclature

Abbreviations

Abbreviation **Meaning**

<i>AAD</i>	<i>Average absolute percent deviation</i>
<i>Am</i>	<i>A tertiary alkanolamine</i>
<i>AmH</i>	<i>A primary (or secondary) alkanolamine</i>
<i>AMP</i>	<i>2-Amino-2-Methyl-1-Propanol</i>
<i>ASU</i>	<i>Air Separation Unit</i>
<i>CAPEX</i>	<i>Capital cost</i>
<i>CCGT</i>	<i>Combined Cycle Gas Turbine</i>
<i>CCS</i>	<i>Carbon Capture and Storage</i>
<i>CCU</i>	<i>CO₂ Compression Unit</i>
<i>CNG</i>	<i>Compressed Natural Gas</i>
<i>COP</i>	<i>Conference of Parties</i>
<i>CPMX</i>	<i>Heat Capacity of a Mixture</i>
<i>DEA</i>	<i>Diethanolamine</i>
<i>DGA</i>	<i>Diglycolamine</i>
<i>DH</i>	<i>Debye-Hückel</i>
<i>DIPA</i>	<i>Diisopropanolamine</i>
<i>DIPPR</i>	<i>Design Institute for Physical Property</i>
<i>DSC</i>	<i>Differential Scanning Calorimeter</i>
<i>ELECNRTL</i>	<i>Electrolyte-Non-Random-Two-Liquid</i>
<i>ENRTL-RK</i>	<i>Electrolyte-Non-Random-Two-Liquid-Redlich-Kwong</i>
<i>EoS</i>	<i>Equation of State</i>
<i>ESP</i>	<i>Electrostatic Precipitator</i>
<i>e-UNIQUAC</i>	<i>Extended Universal-Quasi-Chemical</i>
<i>FEED</i>	<i>Front End Engineering Design</i>
<i>FGD</i>	<i>Flue Gas Desulphurization</i>
<i>FMC</i>	<i>Flow Micro-calorimeter</i>
<i>FTIR</i>	<i>Fourier Transform InfraRed</i>
<i>FWH</i>	<i>Feed Water Heater</i>
<i>GCMS</i>	<i>Gas Chromatography-Mass Spectrometry</i>
<i>G-H</i>	<i>Gibbs-Helmholtz</i>

<i>GHG</i>	<i>Greenhouse Gas</i>
<i>HAZOP</i>	<i>hazard and operability</i>
<i>HFC</i>	<i>Heat Flow Calorimeter</i>
<i>HP</i>	<i>High Pressure</i>
<i>HSS</i>	<i>Heat Stable Salts</i>
<i>IAPWS</i>	<i>International Association for the Properties of Water and Steam</i>
<i>IEA</i>	<i>International Energy Agency</i>
<i>IEA</i>	<i>International Energy Agency</i>
<i>IEAGHG</i>	<i>International Energy Agency Greenhouse Gas</i>
<i>IGCC</i>	<i>Integrated Gasification Combined Cycle</i>
<i>IP</i>	<i>Intermediate Pressure</i>
<i>IPCC</i>	<i>Intergovernmental Panel on Climate Change</i>
<i>KOD</i>	<i>Knock-out Drum</i>
<i>LC</i>	<i>Local Interactions (used interchangeably with SR)</i>
<i>LMTD</i>	<i>Log Mean Temperature Difference</i>
<i>LP</i>	<i>Low Pressure</i>
<i>LPBFW</i>	<i>Low Pressure Boiler Feed Water</i>
<i>LR</i>	<i>Long Range electrostatic interactions</i>
<i>MAD</i>	<i>maximum absolute percent deviation</i>
<i>MDEA</i>	<i>Methyldiethanolamine</i>
<i>MEA</i>	<i>Monoethanolamine</i>
<i>NETL</i>	<i>National Energy Technology Laboratory</i>
<i>NGCC</i>	<i>Natural Gas Combined Cycle</i>
<i>NIST</i>	<i>National Institute of Standards and Technology</i>
<i>NRTL</i>	<i>Non-Random-Two-Liquid</i>
<i>OPEX</i>	<i>operating cost</i>
<i>PACT</i>	<i>Pilot-scale Advanced Capture Technology</i>
<i>PC</i>	<i>Pulverized Coal</i>
<i>PCC</i>	<i>Post Combustion Capture</i>
<i>PC-SAFT</i>	<i>Perturbed Chain Statistical Associating Fluid Theory</i>
<i>PDH</i>	<i>Pitzer-Debye-Hückel</i>
<i>PE</i>	<i>2-Piperidine Ethanol</i>
<i>PLC</i>	<i>Programmable Logic Controller</i>
<i>ppm</i>	<i>parts per million</i>
<i>PR</i>	<i>Peng-Robinson</i>
<i>PVT</i>	<i>Pressure, Volume and Temperature</i>

PZ	Piperizine
R&D	Research and Development
RA	residual's average
RD&D	Research, Development and Deployment
RK	Redlich-Kwong
ROAD	Rotterdam Opslag en Afvang Demonstratieproject (Rotterdam Capture and Storage Demonstration Project)
RSD	residual's standard deviation
SCR	Selective Catalytic Reduction
SIPM	Shell International Petroleum Company
SR	Short Range local interactions
SRK	Soave-Redlich-Kwong
TEA	Triethanolamine
TOTEX	total cost
UKCCSRC	UK CCS Research Centre
UNFCCC	United Nations Framework Convention on Climate Change
UNIQUAC	Universal-Quasi-Chemical
US DOE	United States Department of Energy
VOC	Volatile Organic Compound

Symbols

Symbol	Description	SI Unit
a	One of the parameters in RK, SRK and PR Equations of State	
a_0, a_1, a_2 & a_3	Parameters for pure component heat capacity, Eq. (5.2.6)	
a_i	Activity of species i in a solution	
A_δ	binary interaction parameters	
A_φ	Debye-Hückel parameter	
$A_{\delta,0}$ & $A_{\delta,1}$	Components of excess heat capacity binary interaction parameters, Eq. (5.2.8)	
b	One of the five parameters present in the generalized cubic Equation of State, including RK, SRK and PR Equations of State, Eq. (4.4.10)	
B_δ	ternary interaction parameters	
$B_{\delta,0}$ & $B_{\delta,1}$	Components of excess heat capacity ternary interaction parameters	
$[B]$	Concentration of base	

C_0 & C_1	<i>temperature-dependent parameters</i>	
C_1, C_2, C_3, C_4	<i>Constant parameters in the equation relating equilibrium constant to temperature</i>	
C_{1i} to C_{7i}	<i>Aspen Plus® PLXANT parameters for pure species</i>	
$C_{i,0}, C_{i,1}$ & $C_{i,2}$	<i>Components of excess heat capacity interaction parameters due to CO₂ loading</i>	
[CO ₂]	<i>Concentration of dissolved CO₂ in solution</i>	kmol m ⁻³
c_p	<i>specific heat capacity of a mixture</i>	J kg ⁻¹ K ⁻¹
C_P	<i>molar heat capacity of a mixture</i>	J mol ⁻¹ K ⁻¹
$C_{P,i}$	<i>molar heat capacity of pure species i</i>	J mol ⁻¹ K ⁻¹
C_P^E	<i>excess molar heat capacity of a mixture</i>	J mol ⁻¹ K ⁻¹
$C_{P,12}^E$	<i>excess heat capacity contribution due to AmH–Am interactions</i>	J mol ⁻¹ K ⁻¹
$C_{P,13}^E$	<i>excess heat capacity contribution due to AmH–H₂O interactions</i>	J mol ⁻¹ K ⁻¹
$C_{P,23}^E$	<i>excess heat capacity contribution due to Am– H₂O interactions</i>	J mol ⁻¹ K ⁻¹
$C_{P,123}^E$	<i>excess heat capacity contribution due to AmH–Am–H₂O interactions</i>	J mol ⁻¹ K ⁻¹
$C_{P,\alpha}^E$	<i>excess heat capacity contribution due to CO₂ absorption</i>	J mol ⁻¹ K ⁻¹
$C_{P,ij}^E$	<i>excess heat capacity contribution due to binary interactions</i>	J mol ⁻¹ K ⁻¹
$C_{P,ijk}^E$	<i>excess heat capacity contribution due to ternary interactions</i>	J mol ⁻¹ K ⁻¹
$C_{p,i}^{ig}$	<i>ideal gas heat capacity of component i</i>	J mol ⁻¹ K ⁻¹
d_s	<i>mass density of solvent</i>	kg m ⁻³
[DEA]	<i>Concentration of DEA in solution</i>	kmol m ⁻³
F_{Coal}	<i>Coal feed rate</i>	kg s ⁻¹
$F_{\text{Dry Air}}$	<i>Dry-basis theoretical air required</i>	kg s ⁻¹
F_{FG}	<i>mass flowrate of the flue gas</i>	kg s ⁻¹
f_i	<i>Fugacity of pure species i at the system temperature and pressure</i>	Nm ⁻² (Pa)
f_i^\bullet	<i>Fugacity of species i in a solution at a chosen reference (standard) state</i>	Nm ⁻² (Pa)
\hat{f}_i	<i>Fugacity of species i in solution (gas or liquid)</i>	Nm ⁻² (Pa)
\hat{f}_i^g	<i>Fugacity of species i in the gas-phase of a mixture</i>	Nm ⁻² (Pa)
\hat{f}_i^{id}	<i>Fugacity of species i in an ideal solution at the same conditions as the real solution</i>	Nm ⁻² (Pa)

\hat{f}_i^l	<i>Fugacity of species i in the liquid-phase of a mixture</i>	Nm ⁻² (Pa)
F_{Lean}	<i>mass flowrate of the lean amine solution</i>	kg s ⁻¹
F_{Rich}	<i>mass flowrate of the rich amine solution</i>	kg s ⁻¹
G	<i>Molar Gibbs energy of a solution mixture (gas and/or liquid)</i>	J mol ⁻¹
G_i^\bullet	<i>Gibbs energy of pure species i in its standard state at fixed pressure</i>	J mol ⁻¹
G^α	<i>Molar Gibbs energy of the mixture in α phase</i>	J mol ⁻¹
G^E	<i>Molar Excess Gibbs energy of a liquid solution</i>	J mol ⁻¹
G^E	<i>excess molar Gibbs energy of a mixture</i>	J mol ⁻¹
$G^{E, \text{LR}}$	<i>long-range contribution to excess Gibbs energy</i>	J mol ⁻¹
$G^{E, \text{SR}}$	<i>short-range contribution to excess Gibbs energy</i>	J mol ⁻¹
\bar{G}_i^E	<i>Partial excess Gibbs energy of species i in a solution</i>	J mol ⁻¹
G_i^{ig}	<i>Molar Gibbs energy of species i in an ideal-gas mixture</i>	J mol ⁻¹
G^R	<i>Molar residual Gibbs energy of a gas mixture</i>	J mol ⁻¹
H^E	<i>excess molar enthalpy of a mixture</i>	J mol ⁻¹
h_{ag}^V	<i>vapour phase molar enthalpy of the acid gas</i>	J mol ⁻¹
$H_{\text{CO}_2}^g$	<i>molar enthalpy of gaseous CO₂ absorbed</i>	J mol ⁻¹
H_F	<i>total molar enthalpy of the final solution</i>	J mol ⁻¹
H_{Final}^l	<i>molar enthalpy of the final solution</i>	J mol ⁻¹
H_i	<i>Henry's constant of the dissolved gas component in all solvent components</i>	Nm ⁻² (Pa)
H_I	<i>total molar enthalpy of the initial solution</i>	J mol ⁻¹
H_i^{ig}	<i>ideal gas enthalpy of component i</i>	J
H_i^l	<i>liquid phase enthalpy of component i</i>	J
H_i^\bullet	<i>Enthalpy of pure species i in its standard state at fixed pressure</i>	J
H_{Initial}^l	<i>molar enthalpy of the initial solution</i>	J mol ⁻¹
$H_{i,s}$	<i>Henry's constant of the dissolved gas component in solvent</i>	Nm ⁻² (Pa)
$H_{i,s}(T, P)$	<i>Henry's constant of species i in pure solvent s at the system temperature and pressure</i>	Nm ⁻² (Pa)
$H_{i,s}^o$	<i>reference state Henry's constant of species i at in pure s solvent</i>	Nm ⁻² (Pa)

$H_{i,s}^o(T, P_s^{sat})$	Henry's constant of species i in pure solvent s at the system temperature and the solvent vapour pressure	Nm^{-2} (Pa)
HHV_{Coal}	High heating value of coal	J kg^{-1}
$[H_2O]$	Concentration of H_2O in solution	kmol m^{-3}
$[OH^-]$	Concentration of OH^- in solution	kmol m^{-3}
I_x	ionic strength (on a mole fraction basis) of a mixture	
k	number of reactions	
k	Boltzmann constant	J K^{-1}
K	Mole fraction based equilibrium constant	
K_1	Equilibrium constant of the reaction defined by Eq. (3.1.1)	
K_2	Equilibrium constant of the reaction defined by Eq. (3.1.2)	
K_3	Equilibrium constant of the reaction defined by Eq. (3.1.3)	
K_4	Equilibrium constant of the reaction defined by Eq. (3.1.4)	
K_5	Equilibrium constant of the reaction defined by Eq. (3.1.5)	
K_6	Equilibrium constant of the reaction defined by Eq. (3.1.6)	
K_7	Equilibrium constant of the reaction defined by Eq. (3.1.7)	
K_8	Equilibrium constant of the reaction defined by Eq. (3.1.8)	
k_1	Forward rate constant of the reaction defined by Eq. (3.1.9)	$\text{m}^3 \text{ kmol}^{-1} \text{ s}^{-1}$
k_{-1}	Backward rate constant of the reaction defined by Eq. (3.1.9)	s^{-1}
k_{ap}	Apparent rate constant	s^{-1}
k_B	Forward rate constant of the reaction defined by Eq. (3.1.10)	
k_{H_2O}	Forward rate constant of the reaction defined by Eq. (3.1.2)	
$k_{HCO_3^-}$	Forward rate constant of the reaction defined by Eq. (3.1.4)	s^{-1}
K_m	molality based equilibrium constant	
k_{OH^-}	Forward rate constant of the reaction defined by Eq. (3.1.3)	$\text{m}^3 \text{ kmol}^{-1} \text{ s}^{-1}$
k'_{H_2O}	Rate constant for zwitterion deprotonation by H_2O	s^{-1}
k'_{OH^-}	Rate constant for zwitterion deprotonation by OH^-	$\text{m}^3 \text{ kmol}^{-1} \text{ s}^{-1}$
$k'_{RR/NH}$	Forward rate constant of the reaction defined by Eq. (3.1.5)	$\text{m}^6 \text{ kmol}^{-2} \text{ s}^{-1}$

$k''_{RR'NH}$	Forward rate constant of the reaction defined by Eq. (3.1.6)	s^{-1}
k'	Forward rate constant of the reaction defined by Eq. (3.1.7)	s^{-1}
k''	Forward rate constant of the reaction defined by Eq. (3.1.8)	
k_{-B}	Backward rate constant of the reaction defined by Eq. (3.1.10)	
k_{DEA}	Second-order rate constant of CO ₂ reaction with DEA	$m^3 kmol^{-1} s^{-1}$
$k_{1,MDEA}$	Rate constant of the reaction of CO ₂ with MDEA in a mixed amine system	$m^3 kmol^{-1} s^{-1}$
k_{MDEA}	Rate constant of zwitterion deprotonation by MDEA in a mixed amine system	$m^3 kmol^{-1} s^{-1}$
$k_{1,MEA}$	Rate constant of the reaction of CO ₂ with MEA in a mixed amine system	$m^3 kmol^{-1} s^{-1}$
k_{MEA}	Rate constant of zwitterion deprotonation by MEA in a mixed amine system	$m^3 kmol^{-1} s^{-1}$
k_{obs}	Observed rate constant, based on zwitterion mechanism	s^{-1}
\bar{k}_{obs}	Observed rate constant, based on termolecular mechanism	s^{-1}
M_{AM}	molar mass of the second amine	$kg kmol^{-1}$
M_{AmH}	molar mass of the first amine	$kg kmol^{-1}$
M_{Amine}	molar mass of amine	$kg kmol^{-1}$
m_i	Molality of species i in a solution	$mol kg^{-1}$
m_k	Molality of species k in a solution	$mol kg^{-1}$
M_m	Molecular weight of solvent m	$kg kmol^{-1}$
m_0	Unit molality of a hypothetical ideal solution	$mol kg^{-1}$
M_w	molecular weight of water	$kg kmol^{-1}$
[MDEA]	Concentration of MDEA in solution	$kmol m^{-3}$
[MEA]	Concentration of MEA in solution	$kmol m^{-3}$
n	Total number of moles of all species present in a given system	mol
N_A	Avogadro's number	mol^{-1}
n_{ag}^{total}	total acid gas number of moles (ionic and molecular species)	mol
n_{Final}	the number of moles of the final solution	mol
n_i	Number of moles of species i present in a given system	mol
n_i	loading of the absorbed gas	mol
$n_{Initial}$	the number of moles of the initial solution	mol
$n_{j \neq i}$	Number of moles of all species, excluding the i th species, present in a given	mol

	system	
n_{CO_2}	the number of moles of CO ₂ absorbed	mol
P	Pressure	Nm ⁻² (Pa)
p & q	constant parameters that characterize a given system	
P_F & P_I	the final and initial total pressure, respectively	Nm ⁻² (Pa)
P°	Standard state pressure	Nm ⁻² (Pa)
p^{sat}	Saturation pressure	Nm ⁻² (Pa)
p_i^{sat}	Saturation pressure of pure species i at system temperature	Nm ⁻² (Pa)
P^{vap}	vapour pressure of a pure component	Nm ⁻² (Pa)
P_i^{*l}	vapour pressure of pure species i	Nm ⁻² (Pa)
Q_{Boiler}	Boiler heat rate	J s ⁻¹
Q_e	electron charge	C
$Q_{Turbine}$	Turbine heat rate	J s ⁻¹
R	Gas constant	J mol ⁻¹ K ⁻¹
r_{CO_2}	Apparent rate of CO ₂ reaction with primary or secondary alkanolamine	kmol m ⁻³ s ⁻¹
r'_{CO_2}	Net rate of CO ₂ reaction with water molecule	kmol m ⁻³ s ⁻¹
r''_{CO_2}	Net rate of CO ₂ reaction with hydroxide ions	kmol m ⁻³ s ⁻¹
\bar{r}_{CO_2}	Observed rate of CO ₂ reaction with primary or secondary alkanolamine	kmol m ⁻³ s ⁻¹
r_{CO_2-MDEA}	Rate of CO ₂ reaction with MDEA in a mixed amine system	kmol m ⁻³ s ⁻¹
r_{CO_2-MEA}	Rate of CO ₂ reaction with MEA in a mixed amine system	kmol m ⁻³ s ⁻¹
$r_{CO_2-OH^-}$	Rate of CO ₂ reaction with OH ⁻	kmol m ⁻³ s ⁻¹
r_i	Born radius of the ionic species i	kmol m ⁻³ s ⁻¹
r_{ov}	Overall rate of CO ₂ reaction with mixed amines	kmol m ⁻³ s ⁻¹
$r_{overall}$	Overall rate of CO ₂ reaction with tertiary alkanolamine	kmol m ⁻³ s ⁻¹
$[RR'NH]$	Concentration of primary or secondary alkanolamine	kmol m ⁻³
$[RR'R''N]$	Concentration of tertiary alkanolamine	kmol m ⁻³
T	Temperature	K
T^{ref}	reference temperature (298.15 K)	K
$T_{c,i}$	critical temperature of pure species i in Kelvin	K
T_r	Reduced temperature, defined as the ratio of actual temperature to critical temperature	

V	Molar volume	$\text{m}^3 \text{ kmol}^{-1}$
V_F & V_I	the final and initial total volume, respectively	m^3
\bar{V}_i	Partial molar volume of species i in a gas mixture	$\text{m}^3 \text{ kmol}^{-1}$
V_i^l	Liquid-phase molar volume of pure species i	$\text{m}^3 \text{ kmol}^{-1}$
V_i^v	Vapour-phase molar volume of pure species i	$\text{m}^3 \text{ kmol}^{-1}$
V_i^{BO} and V_s^{BO}	characteristic volume of the supercritical component (i) and the solvent (s), respectively.	$\text{m}^3 \text{ kmol}^{-1}$
$V_{i,s}^\infty$	partial molar volume of species i at infinite dilution in pure s solvent	$\text{m}^3 \text{ kmol}^{-1}$
V_m^l	molar volume of the mixed-solvent mixture	$\text{m}^3 \text{ kmol}^{-1}$
V_m^l	Molar volume of a mixed-solvent mixture	$\text{m}^3 \text{ kmol}^{-1}$
V_{nws}^l	Liquid molar volume for the mixture of all non-water solvents	$\text{m}^3 \text{ kmol}^{-1}$
V_w^l	Molar volume of liquid water	$\text{m}^3 \text{ kmol}^{-1}$
W_s	apparent volume fraction of solvent	
\tilde{x}_1 & \tilde{x}_2	the mole fractions of the amines, AmH and Am, in the unloaded solution	
X_i	Mole fraction of species i in a solution (liquid)	
x_i & x_j	the mole fractions of the amines, AmH and Am, in the unloaded solution	
X_k	Mole fraction of species k in a solution (liquid)	
X_m	Mole fraction of solvent m in a solution	
X'_{nws}	Sum of the mole fractions of all non-water solvents	
X_s	Mole fraction of solvent in a solution (liquid)	
x_{CO_2}	the mass fraction of CO_2 in the flue gas	
y_i	Mole fraction of species i in a gas mixture	
Z	Compressibility factor	
z	number of equivalents per mole of amine	
z_1	number of equivalent per mole of the first amine	
z_2	number of equivalent per mole of the second amine	
z_i	charge number of ion i	
\bar{Z}_i	Partial compressibility factor of species i in a gas mixture	
Z_i^v	Vapour-phase compressibility factor of pure species i	

ΔH	enthalpy change of the chemical equilibrium reaction	J
ΔH^{ex}	excess enthalpy	J
ΔH_{abs}	overall heat of absorption per mole of acid gas	J mol ⁻¹
$\Delta H_{diff}(n_i)$	differential heat of absorption at n_i	J mol ⁻¹
$\Delta H_{dissolution}$	enthalpy of physical dissolution of the acid gas	J mol ⁻¹
ΔH_i	enthalpy of reaction for reaction per mole of key component reacted	J mol ⁻¹
ΔH_i^o	standard enthalpy of reaction for reaction i per mole of key component reacted	J mol ⁻¹
ΔH_i^{vap}	enthalpy of vapourization of pure species i	
$\Delta H_{int}(n_i, T)$	integral heat of absorption at n_i	J mol ⁻¹
ΔH_v	difference between enthalpies of the saturated vapour and the saturated liquid	J
ΔM	the property change of mixing for a real solution.	
ΔM^{id}	the property change of mixing for an ideal solution.	
Δn_i	change in the number of moles of a key component of chemical reaction i	mol
Δn_g^{total}	total number of moles of the acid gas absorbed	mol
ΔZ_v	difference between compressibility factors of the saturated vapour and the saturated liquid	

Greek symbols

Symbol	Description	SI Unit
α	symmetric non-randomness parameters	
α	CO ₂ loading	mol mol ⁻¹
α_{Lean}	lean amine solution CO ₂ loading	mol mol ⁻¹
α_{Rich}	rich amine solution CO ₂ loading	mol mol ⁻¹
δ	One of the five parameters present in the generalized Equation of State	
ε	One of the five parameters present in the generalized Equation of State	
ε_m	Dielectric constant of a single solvent	
ε_s	Dielectric constant of a mixed-solvent	
η	One of the five parameters present in the generalized Equation of State	
η_{Boiler}	Boiler Efficiency	%

γ_i	Symmetrically normalized activity coefficient for species i in a solution	
$\gamma_{i,s}^\infty$	infinite dilution activity coefficient of Henry component i in solvent s	
γ_i^*	Unsymmetrically normalized activity coefficient for species i in a solution	
γ_s	Symmetrically normalized activity coefficient for solvents in a solution	
γ_i^∞	Symmetrically normalized activity coefficient for species i at infinite dilution in a solution	
γ_i^m	Activity coefficient for species i in a solution normalized based on molality	
$\Gamma_i(T)$	A species-dependent function of temperature only	J mol ⁻¹
μ_i	Chemical potential of species i in a solution	J mol ⁻¹
μ_i^g	Chemical potential of species i in the gas phase of a mixture	J mol ⁻¹
μ_i^{id}	Chemical potential of species i in an ideal solution	J mol ⁻¹
μ_i^{ig}	Chemical potential of species i in an ideal-gas mixture	J mol ⁻¹
μ_i^l	Chemical potential of species i in the liquid phase of a mixture	J mol ⁻¹
μ_i^α	Chemical potential of species i in the α phase of a mixture	J mol ⁻¹
μ_i^\bullet	Chemical potential of species i in a solution at a chosen reference (standard) state at which the activity coefficient of species i becomes unity	J mol ⁻¹
μ_i°	A species-dependent function of temperature only and it is the same as $\Gamma_i(T)$	J mol ⁻¹
μ_i^*	Asymmetric reference state chemical potential of species i in a solution	J mol ⁻¹
μ_i^Δ	Molality-based reference state chemical potential of species i in a solution	J mol ⁻¹
μ_s	Chemical potential of solvent in a solution	J mol ⁻¹
μ_s^\bullet	Chemical potential of pure solvent corresponding to unity activity coefficient for the solvent	J mol ⁻¹
$v_{1,k}$ and $v_{2,k}$	correlation parameters for component k in the Brelvi-O'Connell model	
ω	Acentric factor	
ϕ_i^{sat}	Fugacity coefficient of pure species i at its saturation pressure corresponding to solution temperature	

$\hat{\phi}_i$	Fugacity coefficient of species i in a gas mixture	
Ψ_{CO_2}	percentage of CO_2 in the flue gas that is recovered	%
τ	asymmetric binary energy interaction parameters	
θ	a constant parameter whose value is between zero and one	
Θ	One of the five parameters present in the generalized Equation of State	

Superscripts

Symbol	Description
α	Phase, which may be gas or liquid
E	Excess property
g	Gas, or gas phase
l	Liquid, or liquid phase
id	Ideal solution condition
ig	Ideal gas condition
m	molality-based reference state
R	Residual property
sat	Saturation condition
Δ	molality-based reference state
v	Vapour phase condition
ν_i	Stoichiometric number of species i (positive for products and negative for reactants) in a chemical equilibrium reaction equation
•	Reference (standard) state condition
*	Asymmetric (unsymmetric) reference state
∞	Infinite dilution state for solutes in a solvent

Subscripts

Symbol	Description
i, j, k	Species in the gas and/or liquid phase(s)
$j \neq i$	All species, but excluding the i th species, are held constant
ca	ionic components
h	Henry components
ig	ideal gas state
k	All, but the i th species
l	liquid state
m	Solvent present in a solution

<i>nws</i>	<i>Non-water solvent</i>
$P = \sigma$	<i>saturation pressure</i>
<i>s</i>	<i>Mixed-solvent; non-water solvent</i>
<i>s</i>	<i>solvents</i>
<i>w</i>	<i>Water (as solvent)</i>
$\{x_0\}$	<i>constant composition</i>
∞	<i>infinite dilution reference state</i>

Chapter 1

Introduction

This chapter is an introduction to the research work discussed in this thesis. It starts with an overview of the background of the research work, culminating in the motivation for the research and a clear definition of the scope of the research work. Following the scope of the research is a definition of the aims of the research as well as the objectives that lead to the actualization of the research aims. The aims and objectives of the research are followed by a brief discussion of the relevance of the research work. This chapter ends with an outline of the remaining chapters in this thesis.

1.1 Research Background

1.1.1 CO₂ Emissions

Anthropogenic CO₂ emissions have increased greatly over the past 150 years or so, see **Figure 1.1**, leading to a significant increase of the gas in the atmosphere and with an associated increase in the average global temperatures.

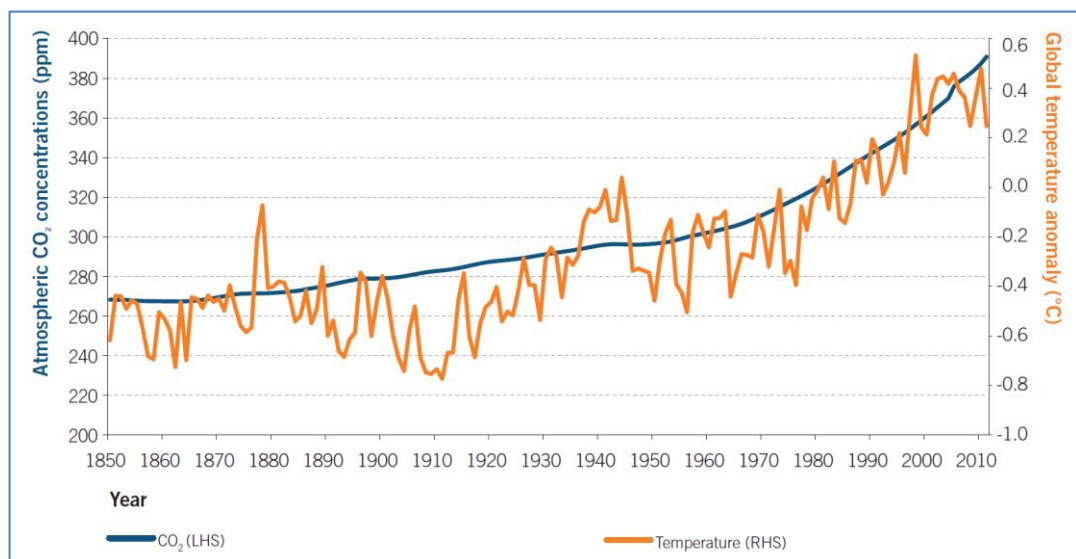


Figure 1.1. Global atmospheric CO₂ concentration and temperature as a function of the year.¹

The International Energy Agency (IEA) gave the total CO₂ emissions for the world in 2011 as 31.3 GtCO₂, with electricity and heat generation contributing 42% followed by transportation with a contribution of 22%.²

Figure 1.2 gives the full sectorial breakdown of global CO₂ emissions for 2011. Also, the IEA has projected that by 2035 the demand for electricity will be approximately 75% higher than the demand for the year 2010, and that global CO₂ emissions from fuel combustion will continue to grow unabated – reaching 35.4 GtCO₂ by 2035.³ The projected increase in electricity demand will be driven by: rapid growth in population and income in developing countries, continuing increase in the number of electrical devices used in homes and commercial buildings, and the growth in electrically driven industrial processes.^{4,5}

On a global scale, the generation of electricity and heat relies heavily on fossil fuels (coal, oil and gas), the main sources of global primary energy consumption with a share of about 81% in 2010.⁶ In the short to medium term, fossil fuels are expected to remain as the main sources of global primary energy consumption with a projected share of about 75% by 2035.⁵ Consequently, CO₂ emissions will continue to increase significantly if mitigation measures are not implemented in the short to medium term. This is better appreciated by considering the fact that about 84% of CO₂ emissions in 2010 were energy related and about 65% of all greenhouse gas (GHG) emissions in 2010 could be attributed to energy supply and consumption.⁷

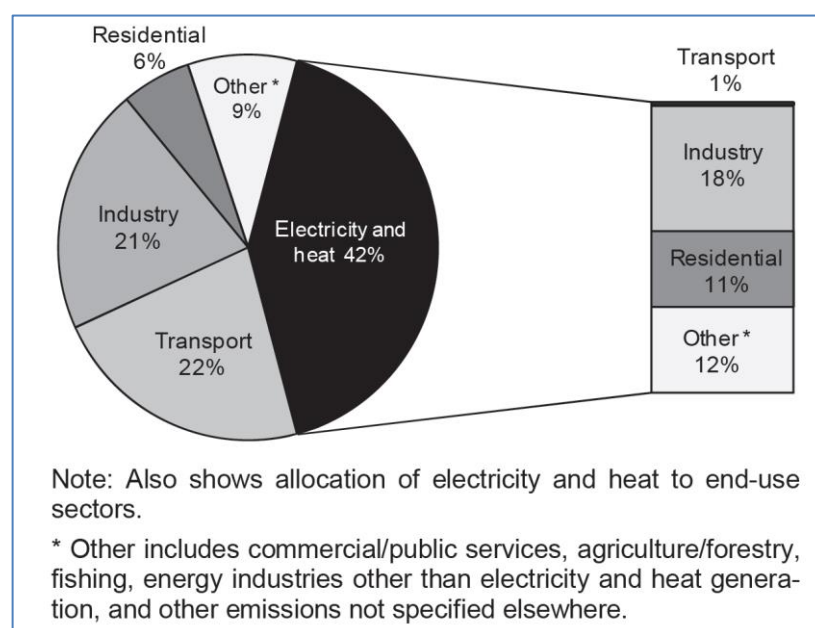


Figure 1.2. Global CO₂ emissions by sector in 2011.²

Table 1.1. Relationship between climate change and CO₂ emissions.⁸

Temperature increase (°C)	All GHGs (ppm CO ₂ -eq.)	CO ₂ (ppm CO ₂)	CO ₂ emissions 2050 (% of 2000 emissions)
2.0-2.4	445-490	350-400	-85 to -50
2.4-2.8	490-535	400-440	-60 to -30
2.8-3.2	535-590	440-485	-30 to +5
3.2-4.0	590-710	485-570	+10 to +60
4.0-4.9	710-885	570-660	+25 to +85
4.9-6.1	885-1 130	660-790	+90 to +140

ppm: parts per million.

1.1.2 CO₂ Emissions and Climate Change

A growing body of evidence has established links between climate change and the anthropogenic CO₂ emissions that arise from energy production and consumption.⁸ In fact, in 2010, the sixteenth session of the United Nations Framework Convention on Climate Change (UNFCCC) Conference of Parties (COP 16) approved a non-legally binding commitment to cap global average temperature rises to 2 °C⁹ because a 2 °C rise is considered consistent with capping atmospheric CO₂ equivalent (CO₂-e) concentration levels to 450ppm by 2050.⁸ **Table 1.1** shows the relationship between CO₂ emissions and temperature increase (a measure of climate change) as revealed by the United Nations Intergovernmental Panel on Climate Change (IPCC).⁸

1.1.3 Resolving the Problem of Climate Change

A portfolio of low-carbon technologies is needed to reduce greenhouse gas (GHG) emissions, and CO₂ in particular, if sustainable development and global energy security are to be achieved.^{1,7} This is underscored by the fact that energy resources are not evenly distributed globally and as such the main source of energy varies from country to country.⁴ For example, in 2009, 84% of the total electricity generation in Brazil came from hydropower, 47% of the total electricity generation in Russia came from gas, while 69% of the total electricity generation in India came from coal.⁴

Technological options for reducing net CO₂ emissions to the atmosphere include:^{1,4,7,10}

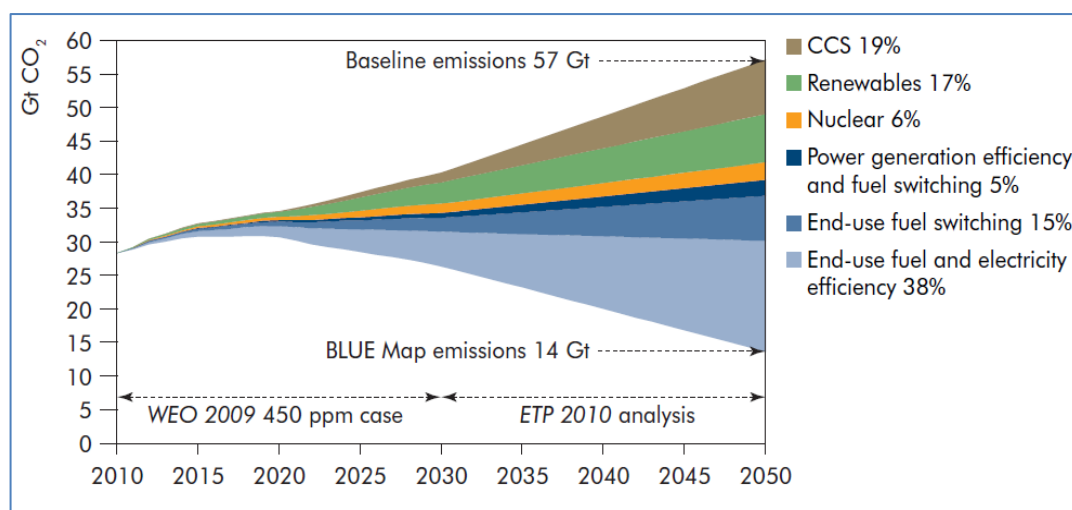


Figure 1.3. Projected contributions of different technology options to global CO₂ emissions reduction.⁷

- i. Reducing energy consumption
- ii. Switching to less carbon intensive fuels (e.g. from coal to gas)
- iii. Increasing the use of renewable energy sources or nuclear energy
- iv. Sequestering CO₂ by enhancing biological absorption capacity in forests and soils
- v. Capturing and storing CO₂ (CCS)

Reducing energy consumption by way of efficient energy conversion and/or utilization, as well as enhancing less energy-intensive economic activities, is expected to dominate global CO₂ emission reduction in the short term (i.e. up to 2020) after which deployment of renewable technologies will begin to play a more significant role in the reduction of global CO₂ emissions.^{1,7} It is expected that between 2025 and 2030, CCS will play a rapidly increasing role alongside with deployment of renewables. In fact, according to the energy emission scenarios developed by IEA (as shown in **Figure 1.3**), CCS is expected to contribute about 19% to global CO₂ emission reduction by 2050.^{7,11,12}

1.1.3.1 CO₂ Capture and Storage (CCS)

Carbon capture and storage (CCS) involves capturing CO₂ produced at large industrial plants using fossil fuels (coal, oil and gas) or other carboniferous fuels (such as biomass), transporting the captured CO₂ to a suitable storage site, and pumping the transported CO₂ into deep

underground rock formations or oceans at great depth for permanent and secured storage.^{1,4,10,13} CCS has an essential role to play in reducing global greenhouse gas emissions as part of a portfolio of low-carbon technologies needed to stabilise atmospheric gas concentrations at levels consistent with limiting projected temperature rises to 2° C by 2050.^{1,4,7,8,10,13} For example, in the electric power generation sector, it has been shown that CCS is a cost-competitive technology with other future large-scale abatement options for avoiding CO₂ emissions.^{1,7,13} In fact, IEA⁷ estimated that without CCS, achieving a 50% emission reduction by 2050 would cost 70% more than if CCS is included. To this end, significant effort is being put into research and development (R&D) of CCS technologies and governments around the world have committed funds (e.g. approximately 23.5 billion US dollars in 2011) to assist in demonstrating CCS technologies at large scale.¹

From the definition of CCS, it is clear that CCS encompasses three main stages, namely: CO₂ Capture, CO₂ Transportation and CO₂ Storage. **Figure 1.4** gives is a schematic representation of possible CCS systems.

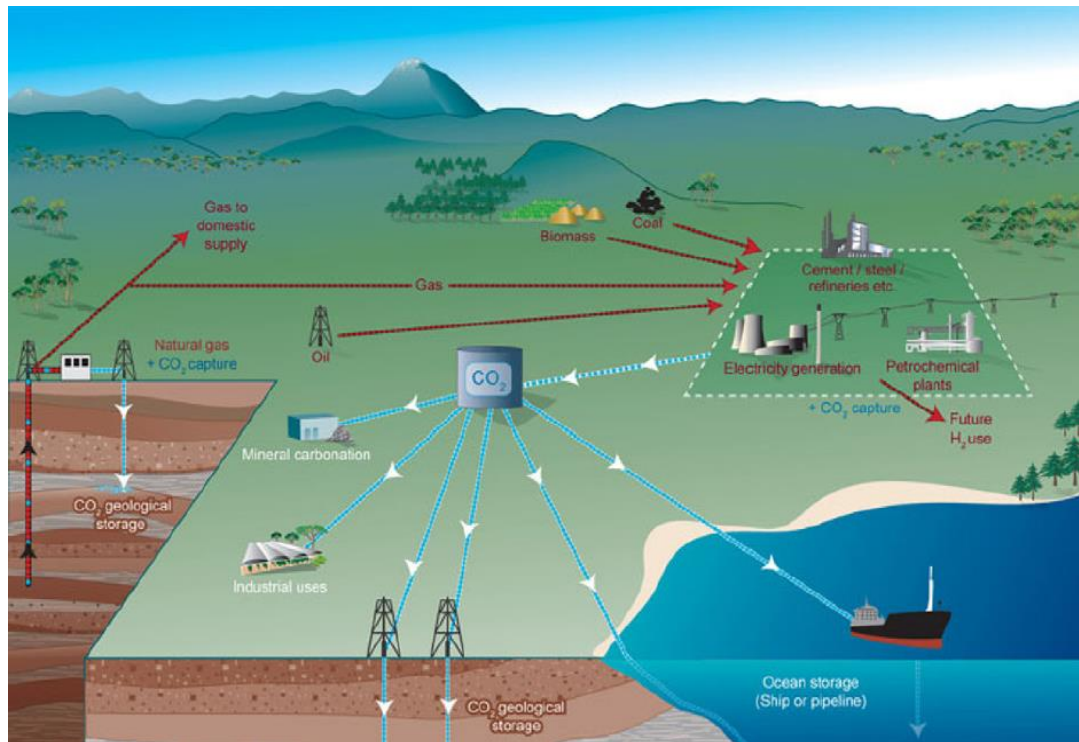


Figure 1.4. Schematic diagram of possible CCS systems.¹⁰

CO₂ Capture

CO₂ capture can be performed following three different technological concepts: post-combustion capture, pre-combustion capture and oxy-fuel combustion capture.^{1,10,13,14} **Figure 1.5** summarises the three different capture technologies with coal as the fossil fuel.

In the post combustion capture process, CO₂ is captured from flue gases that contain 4% to 8% of CO₂ by volume for natural gas-fired power plants, and 12% to 15% by volume for coal-fired power plants.^{10,13} A distinctive advantage of post-combustion capture is that it can easily be retrofitted to existing power plants since it is an “end-of-pipe” retrofit; thus existing power plants, which are mostly fired by air, are very likely to adopt post-combustion capture in a bid to reduce their CO₂ emissions.¹⁰ **Figure 1.6** summarises the separation technologies for CO₂ capture. It is important to state that the separation technologies in **Figure 1.6** cover all the three capture concepts and as such only a few will be suitable for a particular concept. For example, physical absorption is not suitable with post-combustion capture because of the low concentration of CO₂ in the flue gas stream but on the other hand, physical absorption is a very good option for pre-combustion capture because of the high concentration of CO₂ in the stream to be separated.^{10,13}

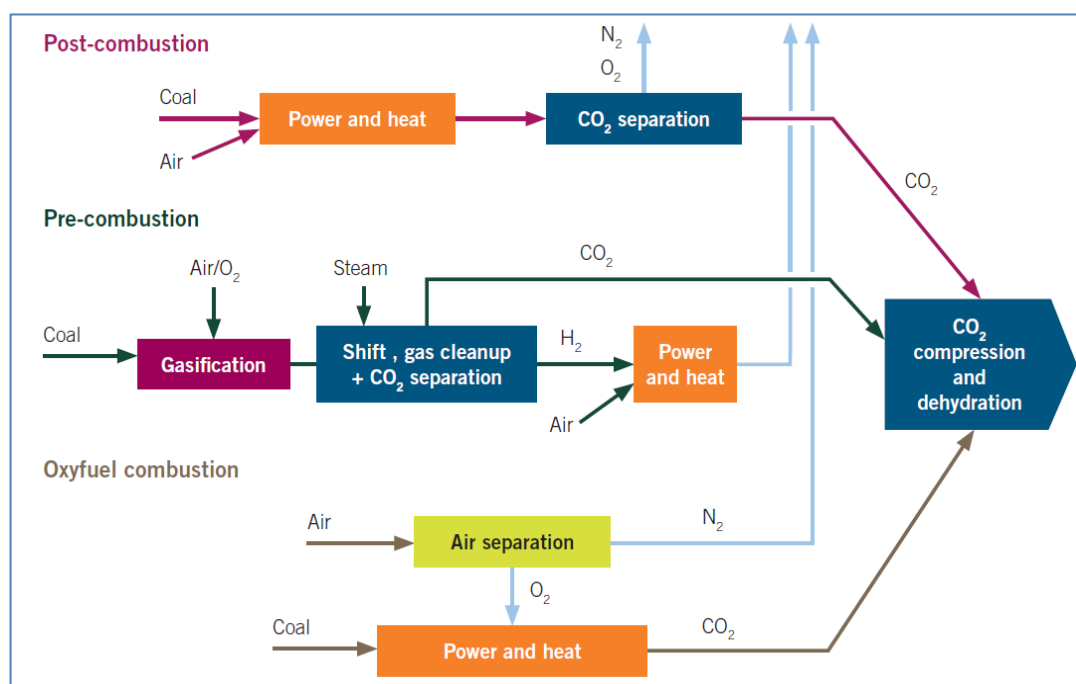


Figure 1.5. Technical options for CO₂ capture from coal-fired power plants.¹

The main separation technologies that could be employed with post-combustion capture are: amine-based chemical absorption (including cryogenic separation using chilled ammonia), adsorption and membranes.^{10,13,15,16} Amine-based chemical absorption is considered to be the proven and the most mature technology for post-combustion CO₂ capture as it has been used on an industrial scale for several decades,^{17,18} but the challenge is to recover the CO₂ with a minimum energy penalty, and at an acceptable cost.^{1,10,13}

In pre-combustion capture processes, which can also be used in coal- or natural gas-fired plant, the fuel is reacted first with air and/or oxygen and then further processed in a shift converter using steam to produce a mixture of hydrogen and CO₂ at a high pressure. After the shift conversion, CO₂ is captured from the high-pressure gas mixture (up to 70 bars) that contains between 15% and 40% CO₂ and the hydrogen is then used to generate electricity and heat in a combined-cycle gas turbine (CCGT).^{10,13} It is pertinent to mention that pre-combustion capture is the ideal technology for integrated gasification combined cycle (IGCC) power plants. Since pre-combustion capture is not the main focus of this research work, reference should be made to the special reports written by the Intergovernmental Panel on Climate Change (IPCC) and the International Energy Agency (IEA) on carbon capture and storage^{10,13} for further details.

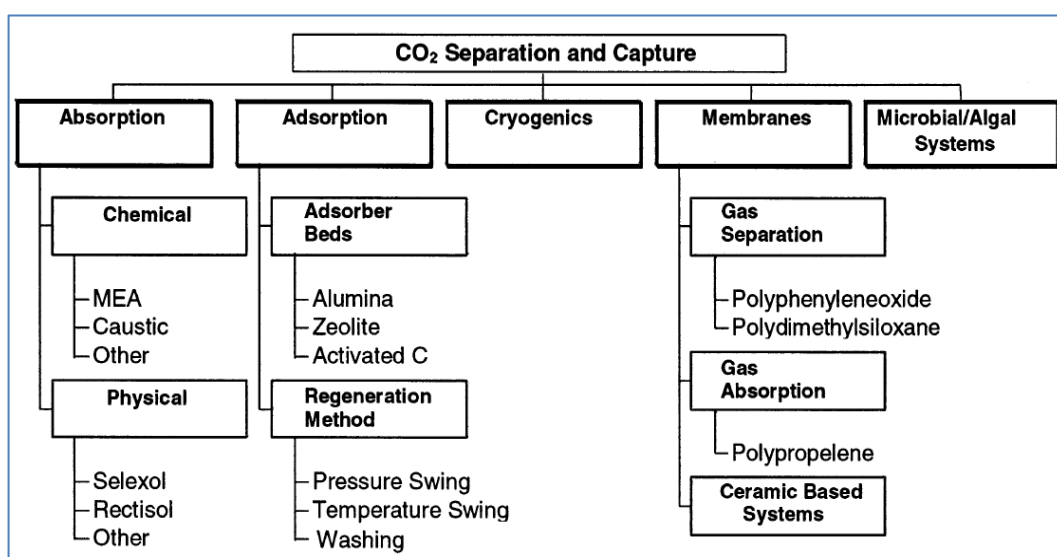


Figure 1.6: Technologies for CO₂ separation and capture.¹⁹

The oxy-fuel combustion process involves the removal of nitrogen from the air in the oxidant stream (i.e. denitrogenation) using an air separation unit (ASU) or membranes. The fossil fuel is then combusted with the near-pure oxygen using recycled flue gas to control the combustion temperature.^{10,13} An air separation unit (ASU), based on cryogenic processes, is the proven and matured technology as of today because the technology of membrane separation is yet to be proven and it is far from being matured with respect to oxy-fuel combustion capture.^{1,13,20} Once again, since oxy-fuel combustion capture is not the main focus of this research work, reference should be made to the special reports written by IPCC and IEA on carbon capture and storage^{10,13} for further details.

CO₂ Transportation

CO₂ transportation is the intermediate stage of CCS that links sources and storage sites and CO₂ can be transported in three states: gas, liquid and solid.^{10,13} CO₂ can be transported as a gas in pipelines and ships and as a liquid in pipelines, ships and road tankers. The transport of supercritical CO₂ in pipelines, which are similar to natural gas pipelines, is an established technology for small quantities of up to a few million tonnes per year.^{1,10,13} Also the intrinsic pressure, volume and temperature (PVT) properties of CO₂ offers easy transportation in semi-refrigerated tanks (at approximately -50 °C and 7 bars) or in compressed natural gas (CNG) carriers.¹³ An advantage of transporting CO₂ by ship is the flexibility that it offers as it allows the collection and combination of products from several small-to-medium size sources and a reduction in capital costs associated with pipelines. Also, it is pertinent to add that transporting CO₂ as a solid is not currently cost-effective from a cost and energy viewpoint.^{10,13} Again, since CO₂ transportation is outside the scope of this work, the reports by the IPCC¹² and the IEA¹³ should be consulted for further details.

CO₂ Storage

The pumping of CO₂ into deep underground geological formations or oceans at great depth for permanent and secured storage is the last stage of a CCS chain. Geological formations that are suitable for CO₂ storage include: depleted oil and gas reservoirs, coal seams that are unminable, and deep saline formations¹⁰. According to IPCC,¹⁰ *“Storage of CO₂ in deep, onshore or offshore geological formations uses many of the same technologies that*

have been developed by the oil and gas industry and has been proven to be economically feasible under specific conditions for oil and gas fields and saline formations, but not yet for storage in unminable coal beds". Also, captured CO₂ could be injected into the ocean at a great depth or on the sea bed, where most of it would remain isolated from the atmosphere for centuries.¹⁰ Again, since CO₂ storage is outside the scope of this thesis, reference should be made to the reports by the IPCC, the IEA and the Global CCS Institute^{10,13,21} for a detailed discussion of CO₂ storage, including the mechanisms involved.

1.2 Motivation of the Thesis

Electricity and heat generation remains the single largest source of CO₂ emissions with a very strong reliance on coal (the most carbon-intensive of fossil fuels) worldwide.^{4,10} For example, in 2009, 43% of CO₂ emissions from fuel combustion were produced from coal while oil and gas contributed 37% and 20%, respectively⁴. In fact, IEA⁵ has projected that emissions from coal will grow to 14.4 GtCO₂ (i.e. approximately 41% of CO₂ emissions from all fossil fuels) by 2035. Thus, intensified use of coal (which is expected because of its fairly even distribution globally and its relatively low cost when compared to oil and gas) would substantially increase CO₂ emissions unless there is a very widespread deployment of CCS.⁷ This clearly shows that CCS has a special role to play in sustainable energy developments in the short to medium term. However, so many issues will have to be resolved before CCS technologies can be deployed at a commercial scale. One such unresolved issue that motivated the work under study in this thesis is the high energy penalty incurred when a post combustion capture (PCC) unit is added as an end-of-pipe retrofit to an existing power plant or as an integral part of a new built power plant.^{14,16,22} In fact, the high parasitic energy associated with post combustion capture technology has led to active research worldwide, with several publications in the open literature within the last decade.²³⁻⁴⁰ However, the issue of high efficiency penalty is far from being resolved and as such substantial effort, by way of research, development and demonstration (RD&D), is required to reduce the energy penalty and associated capital and operating costs.^{1,6,7} This is necessary in order to make PCC competitive with other technological options of CCS (i.e. pre-combustion and oxy-fuel) as well as other options of mitigating CO₂ emissions (e.g. renewable and nuclear).¹

Table 1.2. Carbon dioxide capture technology toolbox.¹³

Capture method	Post-combustion decarbonisation CO ₂ /N ₂		Pre-combustion decarbonisation CO ₂ /H ₂		Oxyfuel conversion O ₂ /N ₂	
	Current	Future	Current	Future	Current	Future
Membranes	Polymeric	Ceramic facilitated transport Carbon molecular sieve	Polymeric	Ceramic Palladium Reactors Contactors	Polymeric	Ion-transport facilitated transport
Solvents / Absorption	Chemical solvents	Improved process design Improved solvents Novel contacting equipment	Chemical solvents Physical solvents	Improved process design Improved solvents Novel contacting equipment	NA	Bio-mimetic solvents
Cryogenic	Liquefaction	Hybrid process Anti-sublimation	Liquefaction	Hybrid process	Distillation	Improved distillation
Solid Sorbents	Zeolites Activated carbon	Carbonates Carbon based solvents	Zeolites Activated carbon Alumina	Dolomites Hydrotalcites Zirconates	Zeolites Activated carbon	Carbonates Hydrotalcites Silicates
Biotechnology		Algae production		High pressure		Bio-mimetic

1.3 Scope

From the earlier discussion in **Section 1.1.3.1**, it was mentioned that CCS encompasses three main areas: Capture, Transportation and Storage, and that there are options within each of them. Although it was earlier mentioned that post-combustion CO₂ capture is the technology being researched in this thesis, it is important to state clearly the specific option of post-combustion CO₂ capture that is being researched. **Table 1.2** gives a summary of the technology options for each of the three technological concepts for CO₂ capture. An indication of the scope of this research work is shown by the light green background in **Table 1.2**.

The scope of this work is limited to post-combustion CO₂ capture based on chemical absorption using aqueous alkanolamines and it is limited to improved process design and system configurations that will optimise the post-combustion capture system bearing in mind the integration of the post-combustion capture (PCC) system with the upstream power plant.

1.4 Aim and Objectives

The main aim of this thesis is to develop an optimized amine-based post-combustion CO₂ capture (PCC) process that can be integrated with a pulverized coal-fired power plant. The objectives that will lead to the actualization of this aim are as follows:

- i. Development of a validated pilot-scale model of an amine-based CO₂ capture process, which will be used as a basis for scale-up.
- ii. Optimal design of the absorption and stripping columns in the amine-based post-combustion CO₂ capture plant, taking into consideration the capital and operating costs of the other unit operation equipment in the PCC plant.
- iii. Optimal integration of the amine-based post-combustion CO₂ capture process, including the associated CO₂ compression unit (CCU), to the upstream coal-fired power plant.
- iv. Simulation of the integrated power plant/PCC-CCU system within a single platform (Aspen Plus[®]), and with the absorber and stripper columns in the PCC plant optimally designed from a systematic approach based on rigorous rate-based calculations.
- v. Quantification of the impact of using different types of coal on the performance of the amine-based PCC plant integrated to a coal-fired power plant and with the absorber and stripper columns designed on the basis of a particular type of coal.

1.5 Relevance

The relevance of this research is best illustrated by considering **Table 1.3** which shows the efficiency penalties of the three technological concepts of CO₂ capture as at 2011 and what is expected by 2020.

It is clear that post-combustion capture, as well as the other two capture technologies, requires continuous and sustained research and development (R&D) in order to meet the target of 2020, which is also the expected time of commercial deployment of amine-based post combustion capture since it is the most mature of all the technologies currently being researched globally. Thus, there is no gainsaying the fact that this research is of high relevance because the aim and objectives of this research are totally aligned with the 2020 targets, especially with respect to reducing the efficiency penalty of post-combustion capture on the upstream power plant.¹³

Table 1.3. Status of CO₂ capture technologies as at 2011.²⁰

Technology	Current	~2020
Unabated coal plant	Efficiency (LCV) ~45%	Efficiency (LCV) ~50-55%
CCS coal – post-combustion capture	~ 12%point efficiency loss	~ 8%point efficiency loss
CCS coal – oxy-fuel combustion	~ 10%point efficiency loss	~ 8%point efficiency loss
CCS coal – pre-combustion decarbonisation	~ 7-9%point efficiency loss	~ 5-6%point efficiency loss
CCS gas – post-combustion capture	~ 8%point efficiency loss	~ 7%point efficiency loss
CCS gas – oxy-fuel combustion	~ 11%point efficiency loss	~ 8%point efficiency loss

1.6 Thesis Outline

This thesis is made up of ten chapters, including this chapter (**Chapter 1**). A brief review of gas purification processes with specific focus on alkanolamines-based gas treating is presented **Chapter 2**, while a review of the chemistry and kinetics of CO₂ reaction with alkanolamines is presented in **Chapter 3**. The theory/review of the thermodynamics of CO₂-alkanolamines-H₂O system is presented in **Chapter 4**, which then leads to **Chapter 5**. The details of a semi-empirical model developed for the estimation of the heat capacity of aqueous solutions of alkanolamines are given in **Chapter 5**. The modelling and simulation of an MEA-based CO₂ capture process at pilot-scale is the subject matter of **Chapter 6**. In **Chapter 7**, the validated model in **Chapter 6** is used as a basis for the optimal design of a commercial-scale MEA-based CO₂ capture plants that can service both coal-fired and gas-fired power plants. **Chapter 8** focuses on the optimal integration of a commercial-scale MEA-based CO₂ capture plant, including the associated CO₂ compression unit, with a pulverized coal-fired power plant. The subject matter of **Chapter 9** is the quantification of the impact of different types of coal on the overall performance of the integrated system in **Chapter 8**, especially when the amine-based CO₂ capture plant is designed on the basis of the flue gas from a particular type of coal. The last chapter of this thesis, **Chapter 10**, contains concluding statements based on the outcome of the research work in this thesis, as well as recommendations for future research work.

Chapter 2

An Introduction to Gas Purification Processes

This chapter is a brief review of gas purification processes but with a specific focus on alkanolamines-based gas treating. The chapter starts with an overview of gas treating processes in **Section 2.1** and then narrows down to a review of the industrial importance of alkanolamines commonly used in gas treating in **Section 2.2**.

2.1 An Overview of Gas Purification Processes

Gas purification (which is also known as *gas treating*) refers to the separation of vapour-phase impurities, such as acidic gases (CO₂, H₂S, SO₂), organic sulphur compounds, etc., from gas streams.^{17,18} The primary operation of gas treating processes generally falls into one of the following five categories:¹⁷

- i. Absorption into a liquid
- ii. Adsorption on a solid
- iii. Permeation through a membrane
- iv. Chemical conversion to another compound
- v. Condensation

2.1.1 Absorption

Absorption, which is the single most important operation in gas treating processes and the most commonly used approach, refers to the transfer of a component of a gas phase to a liquid phase in which it is more soluble than the other components of the gas phase. In the reverse operation, which is called *stripping*, a component that is dissolved in a liquid phase is transferred to a gas phase. There are two types of absorption processes: physical absorption and chemical absorption.^{17,18}

Physical absorption refers to a class of absorption processes in which the absorbed gas (absorbate) does not chemically react with the liquid solvent (absorbent); thus, the liquid absorbent is normally referred to as a physical solvent. Physical absorption is particularly suitable for gas mixtures having a high pressure and/or a high composition of the gas to be absorbed.^{17,18}

Chemical absorption refers to a class of absorption processes in which the absorbed gas chemically reacts with a component in the liquid absorbent. The chemical reaction may be reversible, as in the case of absorption of carbon dioxide (CO₂) and hydrogen sulphide (H₂S) in alkanolamines such as monoethanolamine (MEA), or it may be irreversible, as in the case of absorption of hydrogen sulphide (H₂S) in iron chelate.^{17,18} In other words, chemical absorption processes can further be grouped into: *absorption with a reversible reaction* (e.g. CO₂ absorption with aqueous MEA) and *absorption with an irreversible reaction* (e.g. H₂S absorption with iron chelate).¹⁷

2.1.2 Adsorption

Adsorption, with respect to gas treating, is the selective concentration of one or more components of a gas at the surface of a microporous solid. The adsorbed component, or mixture of adsorbed components is called the adsorbate, while the microporous solid is the adsorbent.^{17,41} In a manner similar to absorption, an adsorption process may be characterised by only the physical attachment of the adsorbate to the surface of the adsorbent (i.e. physical adsorption), or it may involve the chemical reaction of an adsorbed component with the solid adsorbent (i.e. chemical adsorption, which is commonly referred to as *chemisorption*). Since adsorption is outside the scope of this thesis, reference should be made to the book by Kohl and Nielson¹⁷ and Section 16 of Perry's Handbook⁴¹ for further details.

2.1.3 Membrane Separation

The technology of membrane separation, which is relatively new, and less applied in large-scale gas purification processes when compared with absorption and adsorption, uses polymeric membranes to separate gases by selective permeation of one or more gaseous components from one side of a membrane barrier to the other side.¹⁷ The permeating components dissolve in the polymer at one surface and are transported across the membrane as a result of the concentration gradient existing across the membrane. The concentration gradient is maintained by a high partial pressure of the permeating components in the gas mixture on one side of the membrane barrier and a low partial pressure on the other side.^{17,41} Again, since membrane separation is outside the focus of this thesis, reference should be made to Section 22 of Perry's Handbook⁴¹ for a general

discussion of membrane separation processes, and the book by Kohl and Nielson¹⁷ for a more specific discussion of the application of membrane separation in gas purification.

2.1.4 Chemical conversion

Chemical conversion is a principal operation used in the chemical and process industries for both catalytic and non-catalytic reactions, including gas-liquid and gas-solid reactions.^{17,41-43} Typical chemical conversion processes commonly used in gas purification include: thermal conversion of gas impurities (e.g. thermal oxidation of VOCs and odours), which occurs at a relatively high temperature, and catalytic conversion of gas impurities (e.g. catalytic oxidation of VOCs and odours), which occurs at a much lower temperature but in the presence of a catalyst.¹⁷ Chemical conversion is outside the scope of this thesis and therefore, reference should be made to specialized books^{17,41,43} for further details.

2.1.5 Condensation

Condensation is a frequently used process in the chemical industry for the recovery of valuable products from gas streams and, in many cases, it serves as an initial gas purification step for bulk removal of volatile organic compounds (VOCs) from gas streams before the final clean-up process. Condensation as a means of gas purification is primarily used to remove VOCs from exhaust gases. It involves cooling the gas stream to a temperature at which the VOCs will condense and collecting the condensate.¹⁷ Once again, since condensation is outside the scope of this thesis, reference should be made to the book by Kohl and Nielson¹⁷ for further details.

2.2 A Review of Alkanolamines used in Gas Purification

Alkanolamines belong to a general group of organic compounds called amines, which are characterized by their appreciable basicity.^{17,44} Amines may be thought of as an ammonia derivative in which one or more hydrogen atoms have been replaced by organic groups. Depending on the number of hydrogen atoms replaced with respect to an ammonia molecule, amines are generally classified into **primary amines** (if one of the three hydrogen atoms

in ammonia is replaced by an organic group), **secondary amines** (if two of the three hydrogen atoms in ammonia are replaced by organic groups) and **tertiary amines** (if the three hydrogen atoms in ammonia are replaced by organic groups).⁴⁴ However, if the organic group, or one of the organic groups, in an amine has the hydroxyl (-OH) functional group (which is characteristic of alkanols) then the amine is called an alkanolamine.¹⁷

The use of alkanolamines as absorbents for gas treating is an established industrial process which has been in commercial use for several decades.^{17,45} It was Bottoms^{46,47} that first came up with the idea of using alkanolamines for acid gas removal and he was granted a US patent in 1930 for his innovative discovery. Triethanolamine (TEA), the alkanolamine recommended by Bottoms,⁴⁷ was the first alkanolamine to become commercially available and was mainly used in the early gas-treating plants.^{17,45} However, TEA was later displaced as other members of the alkanolamines family were introduced and evaluated as possible acid-gas absorbents.¹⁷ Triethanolamine was displaced largely because of its low capacity (resulting from higher equivalent weight), its low reactivity (as a tertiary amine), and its relatively poor stability.^{17,45}

The alkanolamines that are of commercial interest in gas treating, and which have replaced TEA over the years, include: monoethanolamine (MEA), diethanolamine (DEA), methyldiethanolamine (MDEA), diisopropanolamine (DIPA), and 2-(2-aminoethoxy) ethanol, which is commercially known as Diglycolamine (DGA).^{17,45}

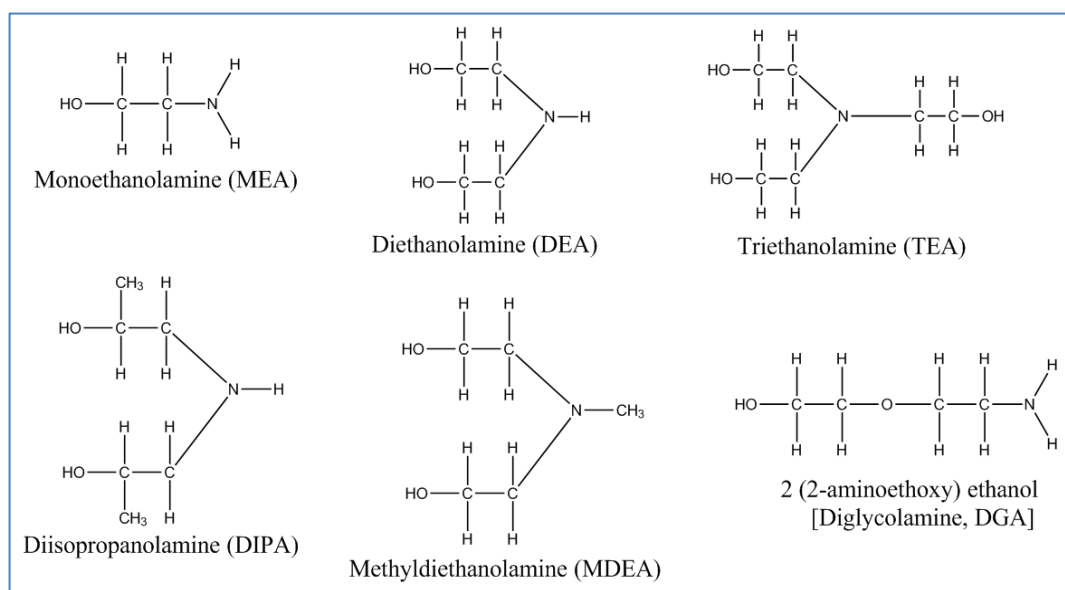


Figure 2.1. Structural formulas of alkanolamines commonly used in gas treating.¹⁷

Figure 2.1 shows the structural formulas of alkanolamines commonly used in gas treating. Also, in addition to simple aqueous solutions of alkanolamines earlier mentioned, proprietary formulations comprising mixtures of the amines with various additives are widely used.¹⁷ Proprietary formulations are offered by companies such as: Fluor[®], Honeywell UOP, Huntsman Corporation, BASF, Cansolv Technologies (Shell Cansolv), Mitsubishi Heavy Industries (MHI), etc.^{17,48-50}

2.2.1 Primary Alkanolamines

Alkanolamines which have two hydrogen atoms directly attached to a nitrogen atom, such as monoethanolamine (MEA) and 2-(2-aminoethoxy) ethanol (DGA), are called primary alkanolamines. They generally have the highest basicity, and by extension are more reactive when compared with secondary and tertiary alkanolamines.

2.2.1.1 Monoethanolamine (MEA)

Aqueous monoethanolamine (MEA) solutions, which were used almost exclusively for many years for the removal of H₂S and CO₂ from natural and certain synthesis gases, have been displaced by other more efficient solvents in the treatment of high pressure natural gases.¹⁷ However, they are still considered as the state-of-the-art solvents for gas streams containing relatively low concentrations of H₂S and CO₂ and essentially no COS and CS₂ contaminants.^{16,17,26,51} The low molecular weight of MEA, resulting in a high solution capacity at moderate concentrations (on a weight basis), its high alkalinity, the relative ease with which it can be reclaimed from contaminated solutions, and its relative cheapness are advantages of MEA.^{17,51} However, the formation of irreversible reaction products (e.g. heat stable salts, HSS) with COS and CS₂ is a serious disadvantage.^{17,52} Also, MEA solutions are appreciably more corrosive than solutions of other amines, particularly if the amine concentrations exceed 20% (by weight) and the solutions are highly loaded with acid gas, and they degrade thermally as well as oxidatively in the presence of O₂.^{17,53-55} Notwithstanding, proprietary formulations that make use of effective corrosion inhibitors have permitted MEA concentrations as high as 30% to be used for CO₂ removal in ammonia and hydrogen plants as well as from sweet natural gas streams.^{17,52} Another disadvantage of MEA is its high heat of reaction with CO₂ and H₂S (about 30% higher than DEA for both acid gases), leading to higher energy

requirements for stripping in MEA systems, and it is this particular disadvantage that has mainly worked against the state-of-the-art 30 wt% MEA solution as a suitable solvent for post-combustion CO₂ capture as it imposes high efficiency penalty on the upstream power plant.^{28,30,32,33,51,56} However, Oexmann and Kather⁵¹ and Meldon⁵⁶ have cautioned against focusing on the heat of absorption only when screening amines for post combustion CO₂ capture. Finally, the relatively high vapour pressure of MEA can cause significant vapourization losses, particularly in low-pressure operations. However, the problem of vapourization losses can be overcome by a simple water wash treatment of the purified gas.¹⁷

2.2.1.2 2-(2-Aminoethoxy) Ethanol (DGA)

The use of an aqueous solution of 2-(2-aminoethoxy) ethanol, which is known commercially as diglycolamine (DGA), was commercialized jointly by the Fluor Daniel and the Huntsman Corporations. The solvent is in many respects similar to monoethanolamine, except that its low vapour pressure permits concentration as high as 60%. Therefore, it requires appreciably lower circulation rates and steam consumption when compared to typical monoethanolamine solutions.^{17,45}

2.2.2 Secondary Alkanolamines

Alkanolamines which have one hydrogen atom directly attached to the nitrogen atom, such as diethanolamine (DEA) and diisopropanolamine (DIPA), are called secondary alkanolamines. They generally have higher basicity and are more reactive when compared with tertiary alkanolamines.

2.2.2.1 Diethanolamine (DEA)

Aqueous solutions of diethanolamine (DEA) have been used for many years for the treatment of refinery gases which normally contain appreciable amounts of COS and CS₂ in addition to H₂S and CO₂.¹⁷ DEA and other secondary amines are the better choice for treating gas streams containing COS and CS₂ because they are much less reactive with COS and CS₂ than primary amines, and the reaction products are not particularly corrosive. Also, the low vapour pressure of DEA makes it suitable for low-pressure operations as vapourization losses are quite negligible.^{17,45} One disadvantage of DEA solutions is that the reclaiming of contaminated

solutions may require vacuum distillation. Another disadvantage of DEA is that it undergoes numerous irreversible reactions with CO₂, forming corrosive degradation products; thus, DEA may not be the optimum choice for treating gases with a high CO₂ content.¹⁷

2.2.2.2 Diisopropanolamine (DIPA)

Diisopropanolamine (DIPA) has been used in the ADIP and sulfinol processes, both licensed by the Shell International Petroleum Company (SIPM), and it has been reported that solutions of DIPA have low regeneration steam requirements and to be noncorrosive.^{17,45} In the sulfinol process, diisopropanolamine is used in conjunction with physical organic solvents, while the ADIP process employs relatively concentrated aqueous solutions of diisopropanolamine. However, SIPM is gradually replacing DIPA with MDEA in both applications.¹⁷

2.2.3 Tertiary Alkanolamines

Alkanolamines which have no hydrogen atom attached directly to the nitrogen atom, such as triethanolamine (TEA) and methyldiethanolamine (MDEA), are called tertiary alkanolamines. They have the least basicity and are less reactive when compared with primary and secondary alkanolamines.

2.2.3.1 Triethanolamine (TEA)

Aqueous solutions of triethanolamine (TEA) were mainly used in the early gas-treating plants because TEA was the first alkanolamine to become commercially available.¹⁷ However, because of its low capacity, low reactivity and relatively poor stability, TEA has been displaced by more suitable alkanolamines, such as MEA, DEA, DGA, MDEA, etc., in gas purification processes.^{17,45}

2.2.3.2 Methyldiethanolamine (MDEA)

Methyldiethanolamine (MDEA) was first reported by Frazier and Kohl⁵⁷ as a potential gas sweetening agent, particularly for selective absorption of H₂S from gas streams in the presence of CO₂. MDEA is also considered as an important non-selective solvent for the bulk removal of CO₂ from gas

streams because of its low energy requirements, high capacity, excellent stability, and other favourable attributes. Also, because of its low vapour pressure, MDEA can be used in concentrations up to 60 wt% in aqueous solution without appreciable evaporation losses.¹⁷ Furthermore, MDEA is highly resistant to thermal and chemical degradation, and it is essentially non-corrosive. However, MDEA has a principal disadvantage of a low rate of reaction with CO₂.^{17,58-61}

2.2.4 Sterically Hindered Amines

In the early 1980s, researchers at EXXON Research and Engineering Company disclosed a different class of acid gas absorbents called sterically hindered amines.⁶²⁻⁶⁴ A sterically hindered amine is defined structurally as a primary amine in which the amino group is attached to a tertiary carbon atom, or a secondary amine in which the amino group is attached to a secondary or tertiary carbon atom.⁶² Sterically hindered amines, some of which are not alkanolamines, use steric hindrance to control the CO₂/amine reaction.^{17,62} Typical examples of sterically hindered amines used in commercial gas treating include: 2-amino-2-methyl-1-propanol (AMP) and 2-piperidine ethanol (PE)⁶². **Figure 2.2** shows the structural formulas of AMP and PE.

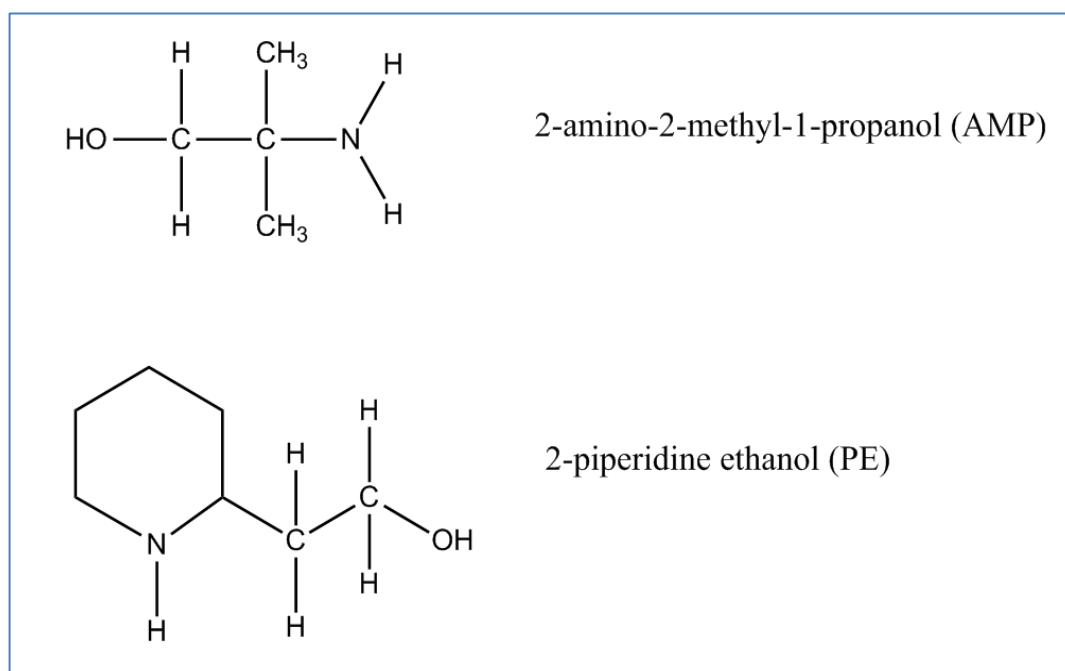


Figure 2.2. Structural formulas of some sterically hindered amines.⁶²

2.2.5 Mixed Amines

As mentioned in **Section 2.2.3.2**, MDEA reacts slowly with CO₂ and that limits the usefulness of an aqueous solution of MDEA for bulk CO₂ removal from gas streams.¹⁷ However, it has been found that the addition of a primary or secondary amine, such as MEA or DEA, to an aqueous solution of MDEA increases its rate of reaction with CO₂ without diminishing the many advantages of MDEA.⁶⁵⁻⁶⁸ The addition of primary and secondary amines to MDEA gives what are commonly referred to as **mixed amines**.^{17,69} Mixed amines, also known as *amine blends*, have been found to be attractive for CO₂ capture.⁶⁹

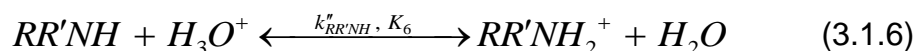
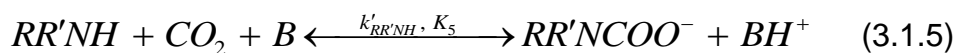
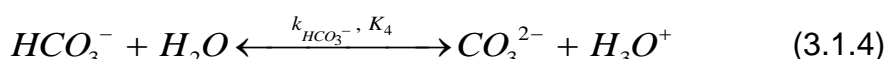
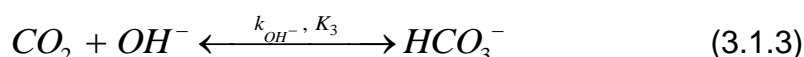
Chapter 3

Chemistry and Kinetics of CO₂ Reaction with Aqueous Solution of Alkanolamines

This chapter presents a review of the chemistry and kinetics of CO₂ reaction with alkanolamines. The importance of this chapter cannot be overemphasised since the subject matter of the research discussed in this thesis is the capture of CO₂ (a weak acidic gas) from the flue gas of coal-fired power plants, and because the idea of using aqueous alkanolamines for acid gas removal is mainly based on their chemical reaction with acidic gases.

3.1 Chemistry of CO₂ Reaction with Aqueous Alkanolamines

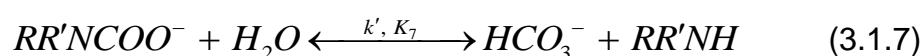
The reactions occurring when an aqueous solution of primary or secondary alkanolamines (including sterically hindered amines) is used to absorb CO₂ from a gas stream may be represented as follows:^{17,68-74}



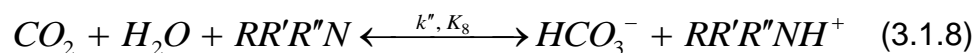
where $RR'NH$ in Eqs. (3.1.5) and (3.1.6) represents a primary amine ($R' = H$), or a secondary amine ($R' \neq H$). The base (B) in Eq. (3.1.5) can be any of H_2O , OH^- , $RR'NH$, or a combination of bases present in the system.^{69,75-77} $RR'NCOO^-$ and $RR'NH_2^+$ are carbamate and protonated amine respectively. Eqs. (3.1.1) and (3.1.6), which describe water ionization, and amine protonation respectively, are normally considered to be instantaneous. On the other hand, Eq. (3.1.2), which represents the direct

reaction of CO₂ with water, is a very slow reaction when compared with Eq. (3.1.5), which represents carbamate formation.^{69,73}

However, Sharma⁷⁸ reported that steric effects reduce the stability of carbamates formed by sterically hindered amines, and Danckwerts⁷⁶ also suggested that the carbamate formed by a sterically hindered amine is only as stable as the zwitterion. Thus, in addition to Eqs. (3.1.1) to (3.1.6), the carbamate of a sterically hindered amine may also undergo hydrolysis to form bicarbonate with the release of free amine molecule as given by the equation:^{69,73}



Also, Eq. (3.1.5) (i.e. carbamate formation) cannot take place if the amine is a tertiary alkanolamine since tertiary alkanolamines do not have any hydrogen atoms directly attached to their nitrogen atom.^{69,73,77,79} Thus, tertiary alkanolamines cannot react directly with CO₂ to form carbamate. However, they are known to catalyse the hydration of CO₂ to bicarbonate as defined by:⁷⁹



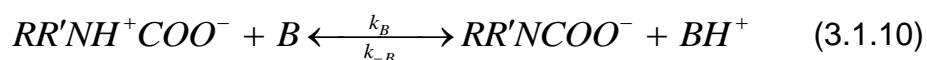
3.1.1 Mechanism of CO₂ Reaction with Aqueous Alkanolamines

The reaction of CO₂ with primary and secondary amines, as described by Eqs. (3.1.5) and (3.1.6), is usually explained using a two-step *zwitterion mechanism* which was originally proposed by Caplow⁸⁰ and later reintroduced by Danckwerts.⁷⁶ However, an alternative one-step *termolecular mechanism* was proposed by Crooks and Donnellan⁸¹ as being capable of explaining the reaction of CO₂ with primary and secondary amines. On the other hand, the reaction of CO₂ with tertiary amines is usually described by the *base-catalysed hydration* of CO₂, as proposed by Donaldson and Nguyen⁷⁹ and later revisited by da Silva and Svendsen.⁸²

3.1.1.1 Zwitterion Mechanism

The two-step zwitterion mechanism suggests that CO₂ reacts reversibly with a primary or secondary amine in the first step to form an unstable zwitterion,

as given by Eq. (3.1.9). The unstable zwitterion may reverse back to the original CO_2 and amine from which it was formed, or it will get deprotonated by a base (or bases) present in the system to form carbamate in the second step as given by the equations.^{68,75-77}



Again, the base (B) in Eq. (3.1.10) can be any of H_2O , OH^- , $\text{RR}'\text{N}'\text{H}$, or a combination of bases present in the system. It is clear that the addition of Eqs. (3.1.9) and (3.1.10) will give Eq. (3.1.5). Also, it is pertinent to add that the zwitterion mechanism is the mechanism that is mostly used for explaining the reaction of CO_2 with primary and secondary amines in both aqueous and non-aqueous solutions, as documented in the literature.^{69,73,75-77}

3.1.1.2 Termolecular Mechanism

Crooks and Donnellan,⁸¹ in their proposed termolecular mechanism, suggested direct combination of CO_2 , the amine and a base to give a loosely-bound encounter complex as an intermediate in a single step. A schematic illustration of the mechanism is shown in **Figure 3.1**.

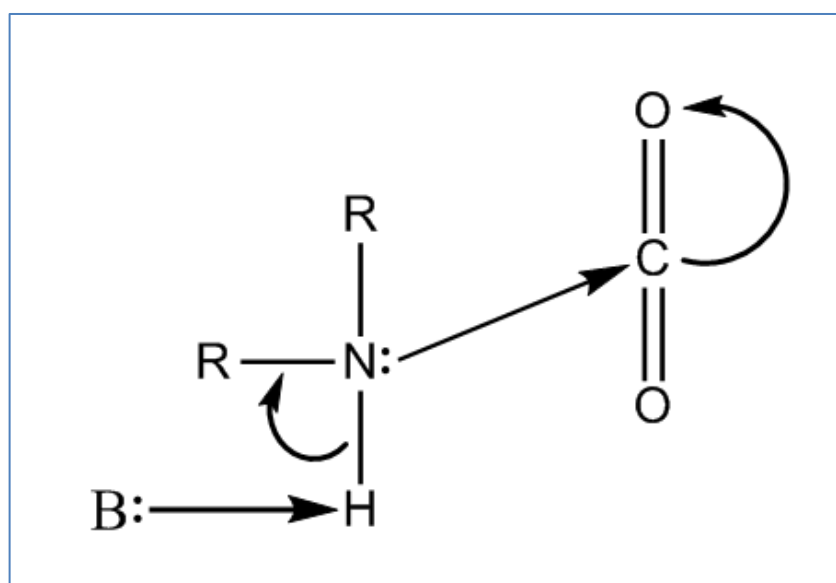


Figure 3.1. Schematic of the termolecular mechanism.⁸¹

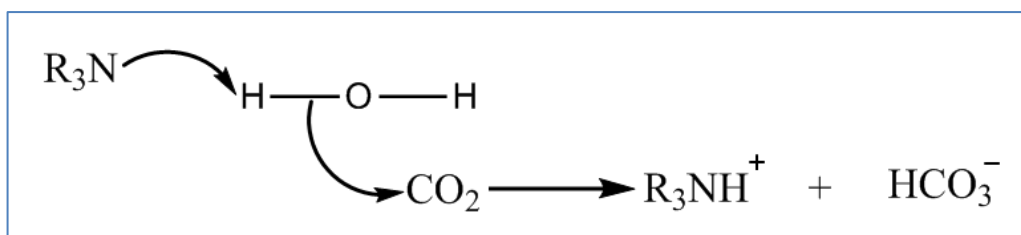


Figure 3.2. Schematic of the base-catalysed mechanism.⁷⁹

The loosely-bound complex breaks up to form the original reactant molecules (i.e. CO_2 , amine and a base), while a small fraction of it reacts with a molecule of the amine or water to give ionic products. The formation of bond and charge separation occur only in the second step.⁸¹ However, Crooks and Donnellan⁸¹ also asserted that their proposed termolecular mechanism may be regarded as a limiting case of the zwitterion mechanism when $k_{-1} \gg k_B[B]$.

3.1.1.3 Base-catalysed Hydration Mechanism

It is now widely accepted that CO_2 cannot react directly with tertiary amines as suggested by Donaldson and Nguyen⁷⁹ in their *base-catalysed hydration mechanism*, although some authors had earlier reported that a direct reaction occurred at extremely high pH.^{69,73} In principle, a direct reaction between CO_2 and tertiary amines may occur at extremely high pH, resulting in monoalkylcarbonate formation⁸³. However, at pH values lower than 12, a direct reaction between CO_2 and tertiary amines can be neglected⁸⁴.

In the based-catalysed hydration mechanism, tertiary amines catalyse the hydration of CO_2 to bicarbonate by acting as a nucleophile and becoming protonated in the process as shown in **Figure 3.2**.

3.1.2 Kinetics of the CO_2 Reaction with Aqueous Alkanolamines

The kinetics of the CO_2 reaction with aqueous primary and secondary alkanolamines will be discussed based on the zwitterion mechanism, since it is the widely accepted mechanism. However, a brief analogy to the termolecular mechanism will be given. On the other hand, the kinetics of CO_2 reaction with tertiary alkanolamines will be discussed based on the based-catalysed hydration mechanism.

3.1.2.1 CO₂ Reaction with Primary and Secondary Alkanolamines

If a quasi-steady state is assumed for the intermediate zwitterion in Eqs. (3.1.9) and (3.1.10), the net rate of reaction of CO₂ with a primary or secondary alkanolamine becomes:⁶⁸

$$r_{CO_2} = \frac{k_1[CO_2][RR'NH] - k_{-1}[RR'NCOO^-] \frac{\sum k_{-B}[BH^+]}{\sum k_B[B]}}{1 + \frac{k_{-1}}{\sum k_B[B]}} \quad (3.2.1)$$

However, the forward reaction in Eq. (3.1.10) is usually assumed to be instantaneous and the backward reaction is usually considered to be negligible^{69,73,75-77}. Therefore, if the second term in the numerator of Eq. (3.2.1) is neglected, the original equation derived by Danckwerts⁷⁶ is obtained as follows:

$$r_{CO_2} = \frac{k_1[CO_2][RR'NH]}{1 + \frac{k_{-1}}{\sum k_B[B]}} = k_{ap}[CO_2] \quad (3.2.2)$$

The reaction rate represented by Eq. (3.2.2) is generally taken to be first-order with respect to the CO₂ concentration. However, Eq. (3.2.2) may exhibit a fractional order between one and two with respect to the amine concentration^{69,73,77}. k_{ap} in Eq. (3.2.2) is the apparent rate constant, and it is the rate constant normally used in the analysis of experimental data.^{69,77} From Eq. (3.2.2) it is clear that:

$$k_{ap} = \frac{k_1[RR'NH]}{1 + \frac{k_{-1}}{\sum k_B[B]}} = \frac{[RR'NH]}{\frac{1}{k_1} + \frac{k_{-1}}{k_1} \frac{1}{\sum k_B[B]}} \quad (3.2.3)$$

where $\sum k_B[B]$ in Eqs. (3.2.2) and (3.2.3) represent the overall contribution towards the zwitterion deprotonation by all the bases present in the solution. In an aqueous amine solution, a combination of H₂O, OH⁻ and the amine (RR'NH) will serve as deprotonation bases.^{75,76} For non-aqueous amine solvents, only the amine can be regarded as a deprotonation base.⁷³ It is

important to state that Eq. (3.2.2) adequately represents the observed rate of reaction of CO₂ with non-aqueous amine solvents.⁷³

In an aqueous solution of primary or secondary alkanolamines, Eqs. (3.1.2) and (3.1.3) give the reaction of CO₂ with H₂O and OH⁻, respectively, in addition to Eq. (3.1.5). The reaction kinetics of Eqs. (3.1.2) and (3.1.3) can be represented as follows:^{69,74,77}

$$r'_{CO_2} = k_{H_2O}[CO_2][H_2O] \quad (3.2.4)$$

$$r''_{CO_2} = k_{OH^-}[CO_2][OH^-] \quad (3.2.5)$$

Thus, taking Eqs. (3.2.4) and (3.2.5) into consideration, Eq. (3.2.2) can be modified to give the observed rate of the CO₂ reaction in aqueous alkanolamines as follows.^{69,77}

$$\bar{r}_{CO_2} = \frac{[RR'NH]}{\frac{1}{k_1} + \frac{k_{-1}}{k_1} \frac{1}{\sum k_B[B]}} + \{k_{H_2O}[H_2O] + k_{OH^-}[OH^-]\}[CO_2] \quad (3.2.6)$$

On writing Eq. (3.2.6) as $\bar{r}_{CO_2} = k_{obs}[CO_2]$, where k_{obs} is the observed rate constant, gives.^{69,77}

$$k_{obs} = \frac{[RR'NH]}{\frac{1}{k_1} + \frac{k_{-1}}{k_1} \frac{1}{\sum k_B[B]}} + \{k_{H_2O}[H_2O] + k_{OH^-}[OH^-]\} \quad (3.2.7)$$

Thus, from Eqs. (3.2.3) and (3.2.7), the observed and apparent rate constants are related as follows:

$$k_{ap} = k_{obs} - \{k_{H_2O}[H_2O] + k_{OH^-}[OH^-]\} \quad (3.2.8)$$

There are two asymptotic cases that can be considered in both Eqs. (3.2.3) and (3.2.7), depending on the relative values of k_{-1} and $k_B[B]$. The two asymptotic cases are as follows.^{69,73}

Case 1: $k_{-1} \gg k_B[B]$

$$k_{ap} = \frac{k_1}{k_{-1}} \left(\sum k_B[B] \right) [RR'NH] \quad (3.2.9)$$

$$k_{obs} = \frac{k_1}{k_{-1}} \left(\sum k_B[B] \right) [RR'NH] + \left\{ k_{H_2O}[H_2O] + k_{OH^-}[OH^-] \right\} \quad (3.2.10)$$

Case 2: $k_{-1} \ll k_B[B]$

$$k_{ap} = k_1[RR'NH] \quad (3.2.11)$$

$$k_{obs} = k_1[RR'NH] + \left\{ k_{H_2O}[H_2O] + k_{OH^-}[OH^-] \right\} \quad (3.2.12)$$

Finally, in order to show the analogy between the zwitterion mechanism and the termolecular mechanism, the reaction of CO_2 with an aqueous primary and secondary alkanolamines based on termolecular mechanism may be represented as follows:^{69,85}



Crooks and Donnellan,⁸¹ while considering only amine and water as dominant bases, gave the observed rate of reaction in their proposed termolecular mechanism as follows:

$$\bar{r}_{CO_2} = \bar{k}_{obs}[CO_2] \quad (3.2.14)$$

where \bar{k}_{obs} is given by:⁸¹

$$\bar{k}_{obs} = \left\{ k_{RR'NH}[RR'NH] + k_{H_2O}[H_2O] \right\} [RR'NH] \quad (3.2.15)$$

However, if the contribution of OH^- to the overall rate of reaction cannot be neglected, then Eq. (3.2.15) can be modified slightly to give:^{69,85}

$$\bar{k}_{obs} = \left\{ k_{RR'NH}[RR'NH] + k_{H_2O}[H_2O] + k_{OH^-}[OH^-] \right\} [RR'NH] \quad (3.2.16)$$

It is pertinent to state that the “observed rate constant” in Eq. (3.2.15), or (3.2.16), is equivalent to the “apparent rate constant” defined by Eq. (3.2.3). A comparison of Eq. (3.2.15), or (3.2.16), with Eq. (3.2.9) shows that the termolecular molecular mechanism may be considered as a limiting case of the zwitterion mechanism when $k_{-1} \gg k_B[B]$.^{69,73,81}

3.1.2.2 CO₂ Reaction with Tertiary Alkanolamines

As mentioned in Section 3.1.1.3, tertiary amines cannot react directly with CO₂; they catalyse the hydration of CO₂ to bicarbonate by acting as a nucleophile and get protonated in the process. Therefore, it follows that the overall rate of reaction of tertiary alkanolamines with CO₂ will be given by the summation of the rates of the reactions defined by Eqs. (3.1.2), (3.1.3) and (3.1.8) as follows:⁶⁹

$$r_{overall} = \{k_{H_2O}[H_2O] + k_{OH^-}[OH^-] + k''[RR'R''N]\}[CO_2] \quad (3.2.17)$$

The observed rate constant and the apparent rate constant are given, respectively, by:⁶⁹

$$k_{obs} = k_{H_2O}[H_2O] + k_{OH^-}[OH^-] + k''[RR'R''N] \quad (3.2.18)$$

$$k_{ap} = k''[RR'R''N] \quad (3.2.19)$$

3.1.2.3 CO₂ Reaction with Mixed Amines

The overall reaction rate of CO₂ with an aqueous solution of mixed amines, such as MDEA-MEA-H₂O, can be expressed as follows:⁵⁹

$$r_{ov} = r_{CO_2-MEA} + r_{CO_2-MDEA} + r_{CO_2-OH^-} + r_{CO_2-H_2O} \quad (3.2.20)$$

Liao and Li⁵⁹ studied the reaction kinetics of CO₂ absorption in a MDEA-MEA-H₂O system and they adopted a zwitterion mechanism for the primary amine (MEA) component combined with a pseudo-first order reaction mechanism for the tertiary amine (MDEA) component. Neglecting the contribution of the reaction of CO₂ with H₂O, the first three terms on the RHS of Eq. (3.2.20) are given as follows:

$$r_{CO_2-MEA} = \frac{k_{1,MEA}[CO_2][MEA]}{1 + \frac{k_{-1}}{k'_{H_2O}[H_2O] + k'_{OH^-}[OH^-] + k_{MEA}[MEA] + k_{MDEA}[MDEA]}} \quad (3.2.21)$$

$$r_{CO_2-MDEA} = k_{1,MDEA}[CO_2][MDEA] \quad (3.2.22)$$

$$r_{CO_2-OH^-} = k_{OH^-}[CO_2][OH^-] \quad (3.2.23)$$

However, contrary to the model proposed by Liao and Li,⁵⁹ Ramachandran et al.⁵⁸ reported that the reaction kinetics of CO₂ absorption in a MDEA-MEA-H₂O system cannot be interpreted by the zwitterion and termolecular mechanisms in their original forms. They adopted a modified termolecular mechanism, which included the contribution of OH⁻ ions, to predict the kinetics of CO₂ absorption into aqueous MDEA-MEA solution as follows:

$$r_{ov} = \left\{ \left(k_{OH^-} [OH^-] + k_{MEA} [MEA] \right) [MEA] + k_{MDEA} [MDEA] \right\} [CO_2] \quad (3.2.24)$$

The reaction rate constants in Eq. (3.2.24) were reported by Ramachandran et al.⁵⁸ as follows:

$$k_{MEA} = 9.56 \times 10^8 \exp \left[\frac{-3802.4}{T} \right] \quad (3.2.25)$$

$$k_{OH^-} = 5.04 \times 10^{12} \exp \left[\frac{-5411.0}{T} \right] \quad (3.2.26)$$

$$k_{MDEA} = 2.58 \times 10^8 \exp \left[\frac{-3736.5}{T} \right] \quad (3.2.27)$$

where k_{MEA} and k_{OH^-} are in L²/(mol s), k_{MDEA} is in L/(mol s) and the temperature, T , is in K.

The reaction kinetics of the absorption of CO₂ into aqueous blends of DEA and MDEA had also been investigated^{60,61}. Rinker et al.⁶¹ developed a comprehensive model based on penetration theory, with the assumption of the zwitterion mechanism for the reaction between CO₂ and DEA, the base-catalyzed mechanism for the reaction between CO₂ and MDEA, and instantaneous proton transfer as the only means of interaction between protonated and unprotonated amines, and concluded that MDEA did not contribute significantly to the zwitterion deprotonation in their laminar-jet experiment. Also, Zhang et al.⁶⁰ experimentally studied the kinetics of absorption of CO₂ into aqueous solutions of MDEA blended with DEA in a disk column under conditions approaching those in industrial processes. They assumed a rapid pseudo-first-order reversible reaction between the CO₂ and free DEA in parallel with that of CO₂ and MDEA, based on the fact that free DEA can transfer CO₂ to MDEA and regenerate itself

simultaneously in the process. The second-order rate constant of the reaction between CO₂ and DEA was given by Zhang et al.⁶⁰ as follows:

$$\ln k_{DEA} = 24.515 - 5411.3 / T \quad (3.2.28)$$

Chapter 4

Thermodynamics of CO₂-Alkanolamines-H₂O Systems

The design of alkanolamines-based gas treating processes, whether equilibrium-based or rate-based, fundamentally depends on the availability of an appropriate thermodynamic model that can accurately interpolate and extrapolate experimental thermodynamic data for the given system.^{71,72,86} If process simulation is envisaged, then the availability of an appropriate thermodynamic model for the system of interest becomes critical and more or less indispensable.^{70,72} The ideal thermodynamic model for a CO₂-alkanolamines-H₂O system should be able to accurately account for the phase equilibria existing between the gas and liquid phases, as well as the chemical-reaction equilibria existing within the liquid phase.⁸⁷ However, it is pertinent to add that the coupling of the chemical-reaction equilibria in the liquid phase with the gas-liquid phase equilibria in CO₂-alkanolamines-H₂O systems complicates their thermodynamic modelling. For example, **Figure 4.1** illustrates the coupling of gas-liquid phase equilibria with liquid phase chemical-reaction equilibria in CO₂-MEA-H₂O system.

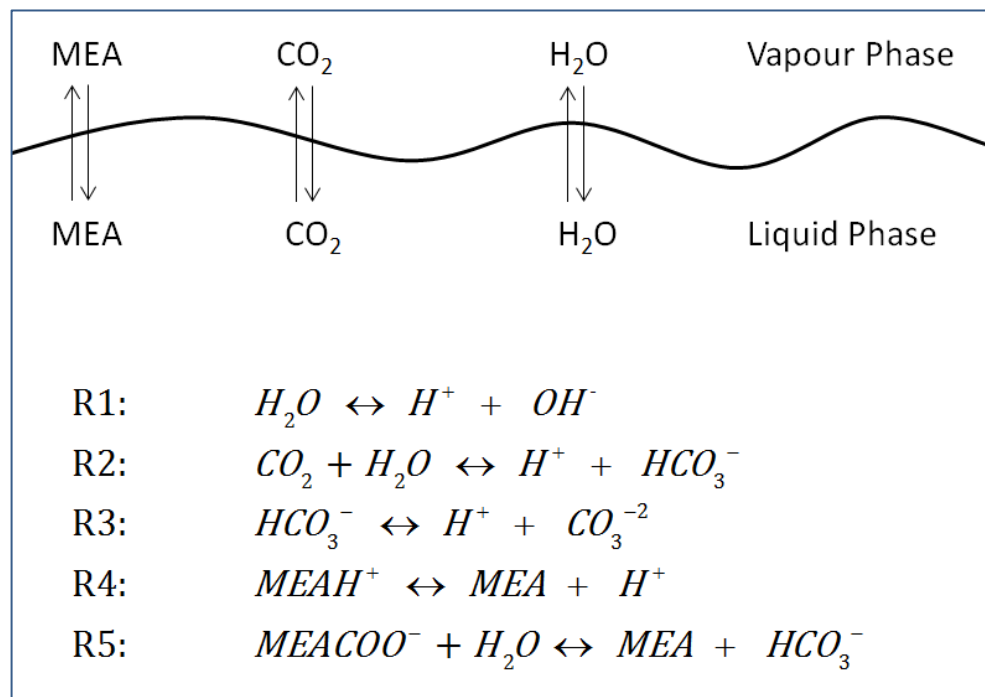


Figure 4.1. A Schematic of the coupling of the chemical and phase equilibria in CO₂-MEA-H₂O system.⁸⁸

In **Figure 4.1**, the molecular species (MEA, CO₂ and H₂O) in the vapour phase are in phase equilibria with their corresponding molecular species (MEA, CO₂ and H₂O) in the liquid phase, and the same molecular species (MEA, CO₂ and H₂O) in the liquid phase are simultaneously in chemical equilibria with the various ionic species in the liquid phase as given by the reactions labelled R1 to R5.

4.1 Gas-Liquid Phase Equilibrium

Phase equilibrium is what governs the distribution of molecular species between the vapour and liquid phases in an equilibrium mixture. However, ionic species are normally treated as non-volatile and they are assumed to be present in the liquid phase only.^{71,89} According to Gibbs,⁹⁰ phase equilibria is said to be attained when the chemical potential of each of the species is the same in all the phases present in a given system, in addition to uniform temperature and pressure. In other words, for a gas-liquid system under isothermal and isobaric conditions, gas-liquid phase equilibria can be expressed mathematically as follows:^{91,92}

$$\mu_i^g = \mu_i^l \quad (4.1.1)$$

where μ_i^g and μ_i^l are, respectively, the chemical potential of species i in the gas and liquid phases.

The chemical potential of species i in a mixture existing in a given phase (α), by definition, is given as follow:^{91,92}

$$\mu_i^\alpha = \left[\frac{\partial(nG^\alpha)}{\partial n_i} \right]_{P, T, n_{j \neq i}} \quad (4.1.2)$$

where G^α is the molar Gibbs energy of the mixture in the α phase, n is the total number of moles in the mixture, P is the uniform and constant pressure of the mixture, and T is the uniform and constant temperature of the mixture. The subscript $n_{j \neq i}$ indicates that the number of moles of all species, except the *ith* species, is held constant. However, Eq. (4.1.2) is not employed in practice because of the following two limitations associated with chemical potential:⁹¹

- I. The Gibbs energy is a function of the internal energy and entropy and, because absolute values are unknown for both internal energy and entropy, only relative values of the chemical potential can be computed.
- II. The chemical potential approaches negative infinity as the mole fraction of a component approaches infinite dilution.

4.1.1 Fugacity and Fugacity Coefficient

As stated in **Section 4.1**, chemical potential is not used in practice to describe gas-liquid phase equilibria because of the limitations associated with it. Consequently, a pragmatic way of describing phase equilibria uses the concepts of *fugacity* introduced by Lewis⁹³, and which he related to chemical potential as follows:

$$\mu_i - \mu_i^\bullet = RT \ln \left(\frac{\hat{f}_i}{f_i^\bullet} \right) = RT \ln (a_i) \quad (4.1.3)$$

where μ_i^\bullet and f_i^\bullet are arbitrary, but not independent, values of the chemical potential and fugacity of component i for some chosen reference state. \hat{f}_i is the fugacity of species i in a mixture. The difference in chemical potentials ($\mu_i - \mu_i^\bullet$) is for an isothermal change between the arbitrary reference state and the actual state for any component in the system. a_i is the activity of species i .

Lewis⁹³ was able to show, from Gibbs definition of phase equilibria and Eq. (4.1.3), that phase equilibria is equally attained when the fugacity of each of the species is the same in all the phases present in a given system, in addition to uniform temperature and pressure. Thus, for a gas-liquid system under isothermal and isobaric conditions, gas-liquid phase equilibria can be expressed mathematically as follows:

$$\hat{f}_i^g = \hat{f}_i^l \quad (4.1.4)$$

where \hat{f}_i^g and \hat{f}_i^l are, respectively, the fugacity of species i in the gas and liquid phases.

The relationship between the chemical potential of species i in an ideal-gas mixture under isothermal condition and its partial pressure can be written as follows:⁹¹

$$\mu_i^{ig} = \Gamma_i(T) + RT \ln(y_i P) \quad (4.1.5)$$

with

$$\Gamma_i(T) = G_i^{ig} - RT \ln P \quad (4.1.6)$$

where $\Gamma_i(T)$ is a species-dependent function of temperature only.

Similarly, fugacity (which is closely related to chemical potential and may be viewed as a corrected partial pressure) is defined as follows for a real gas mixture:⁹¹

$$\mu_i = \Gamma_i(T) + RT \ln \hat{f}_i \quad (4.1.7)$$

such that:

$$\hat{f}_i = \hat{\phi}_i y_i P \quad (4.1.8)$$

where \hat{f}_i is the fugacity of species i in the gas mixture, and $\hat{\phi}_i$ is a dimensionless number called the fugacity coefficient of species i in the gas mixture.

Therefore, subtracting Eq. (4.1.5) from Eq. (4.1.7), and taking Eq. (4.1.8) into consideration, gives:

$$\mu_i - \mu_i^{ig} = RT \ln \hat{\phi}_i \quad (4.1.9)$$

From the equation relating the chemical potential to Gibbs energy, as defined by Eq. (4.1.2), it can be shown that:

$$\ln \hat{\phi}_i = \left[\frac{\partial(nG^R / RT)}{\partial n_i} \right]_{P, T, n_{j \neq i}} \quad (4.1.10)$$

where G^R is the molar residual Gibbs energy of the gas mixture, which is defined as follows:⁹¹

$$G^R = G - G^{ig} \quad (4.1.11)$$

where G is the molar Gibbs energy of the gas mixture and G^{ig} is the ideal-gas value of the molar Gibbs energy at the same conditions as the gas mixture

A useful alternative to Eq. (4.1.10) that allows for the calculation of the $\hat{\phi}_i$ values from the PVT data is given by:^{87,91}

$$\ln \hat{\phi}_i = \int_0^P (\bar{Z}_i - 1) \frac{dP}{P} = \frac{-1}{RT} \int_0^P \left(\frac{RT}{P} - \bar{V}_i \right) dP \quad (4.1.12)$$

where \bar{Z}_i and \bar{V}_i are the *partial compressibility factor* and the *partial molar volume* of species i in the gas mixture under isothermal condition.

An analogous form of Eq. (4.1.5) can be written for an ideal liquid mixture (ideal solution) as follows:⁹¹

$$\mu_i^{id} = \Gamma_i(T) + RT \ln \hat{f}_i^{id} \quad (4.1.13)$$

such that:

$$\Gamma_i(T) = G_i - RT \ln f_i \quad (4.1.14)$$

$$\hat{f}_i^{id} = x_i f_i \quad (\text{Lewis-Randall rule}) \quad (4.1.15)$$

$$f_i = \phi_i^{sat} P_i^{sat} \exp \left[\frac{V_i^l (P - P_i^{sat})}{RT} \right] \quad (4.1.16)$$

In Eqs. (4.1.13) to (4.1.16), \hat{f}_i^{id} is the fugacity of species i in an ideal solution at the same conditions as the real solution, f_i is the fugacity of pure species i at the temperature and pressure of the solution, x_i is the mole fraction of species i in the solution, ϕ_i^{sat} is the fugacity coefficient of pure species i at its saturation pressure corresponding to the solution temperature, and V_i^l is the liquid-phase molar volume of pure species i and it is usually assumed to be constant at the value for saturated liquid. The exponential term in (4.1.16) is known as *Poynting factor*, and it can be neglected with negligible calculation errors when dealing with systems operating at low to moderate pressures.⁹¹

An analogous form of Eq. (4.1.12) can be written for ϕ_i^{sat} as follows:⁹¹

$$\ln \phi_i^{sat} = \int_0^{P^{sat}} (Z_i^v - 1) \frac{dP}{P} = \frac{-1}{RT} \int_0^{P^{sat}} \left(\frac{RT}{P} - V_i^v \right) dP \quad (4.1.17)$$

where Z_i^v and V_i^v are *vapour-phase compressibility factor* and *vapour-phase molar volume* of pure species i under isothermal condition.

It is pertinent to add that Eq. (4.1.7) equally applies to a real liquid mixture (solution) with the fugacity interpreted accordingly and provided Eq. (4.1.14) is used in place of Eq. (4.1.6).^{91,92} Thus, subtracting Eq. (4.1.13) from Eq. (4.1.7) gives:

$$\mu_i - \mu_i^{id} = RT \ln \left(\frac{\hat{f}_i}{\hat{f}_i^{id}} \right) = RT \ln \left(\frac{\hat{f}_i}{x_i f_i} \right) \quad (4.1.18)$$

4.1.2 Activity and Activity Coefficient

The concepts of activity and activity coefficient are derived from Eq. (4.1.18), whose left hand side represents *partial excess Gibbs energy of species i in solution* (\bar{G}_i^E) and the fractional terms in the brackets represent, by definition, *activity coefficient* of species i (γ_i). Thus, mathematically, it follows that:^{91,92}

$$\bar{G}_i^E = RT \ln \gamma_i \quad (4.1.19)$$

where:

$$\bar{G}_i^E = \mu_i - \mu_i^{id} \quad (4.1.20)$$

$$\gamma_i = \frac{\hat{f}_i}{\hat{f}_i^{id}} = \frac{\hat{f}_i}{x_i f_i} \quad (4.1.21)$$

Eq. (4.1.21) clearly shows that the activity coefficient of a species in a solution is the ratio of its actual fugacity to the ideal fugacity value given by the Lewis-Randall rule at the same temperature, pressure, and composition. Also, the *activity* (a_i) of species i in solution is directly related to its activity coefficient as follows.^{91,92,94}

$$a_i = x_i \gamma_i \quad (4.1.22)$$

Furthermore, from the definition of partial property, it follows that: ^{87,91,92,94}

$$\ln \gamma_i = \left[\frac{\partial(nG^E / RT)}{\partial n_i} \right]_{P, T, n_{j \neq i}} \quad (4.1.23)$$

such that:

$$\frac{G^E}{RT} = \sum_i x_i \ln \gamma_i \quad (4.1.24)$$

$$\sum_i x_i d \ln \gamma_i = 0 \quad (\text{Constant } T \text{ and } P) \quad (4.1.25)$$

Eqs. (4.1.24) and (4.1.25) are, respectively, forms of *summability* and *Gibbs-Duhem* equations. It is pertinent to state that Eq. (4.1.25), Gibbs-Duhem equation, is normally used to test for thermodynamic consistency because it imposes a constraint on activity coefficients that may not be satisfied by a set of experimental values derived from *P*-*xy* data. ^{91,92}

4.2 Standard States and Normalization Conventions

The concept of standard states, also referred to as reference states, may be best explained by adopting the following expressions for the chemical potentials of the various components in gases and solutions. ⁹²

$$\mu_i^{ig} = \mu_i^\circ + RT \ln y_i P \quad (\text{for an ideal-gas mixture}) \quad (4.2.1)$$

$$\mu_i = \mu_i^\circ + RT \ln \hat{\phi}_i y_i P \quad (\text{for a real gas mixture}) \quad (4.2.2)$$

$$\mu_i^{id} = \mu_i^\bullet + RT \ln x_i \quad (\text{for an ideal solution}) \quad (4.2.3)$$

$$\mu_i = \mu_i^\bullet + RT \ln \gamma_i x_i \quad (\text{for a real solution}) \quad (4.2.4)$$

where μ_i° is a function of temperature only and it is essentially $\Gamma_i(T)$ in Eq. (4.1.6), while μ_i^\bullet is a function of both temperature and pressure.

It is pertinent to add that subtraction of Eq. (4.2.1) from Eq. (4.2.2) gives Eq. (4.1.9), and subtraction of Eq. (4.2.3) from Eq. (4.2.4) gives Eq. (4.1.19) (with Eq. (4.1.20) taken into consideration). Also, it is clear from Eqs. (4.1.3) and (4.1.22) that:

$$\gamma_i = \frac{a_i}{x_i} = \frac{\hat{f}_i}{x_i f_i^\bullet} \quad (4.2.5)$$

The definition of activity coefficient as given by Eq. (4.2.5) is not complete until a reference state is specified for the species i , and a value is assigned to μ_i^\bullet . Since μ_i^\bullet , by convention, is the chemical potential of species i at the conditions at which γ_i is unity, it follows that conditions of temperature, pressure and composition at which γ_i becomes unity define the reference state of species i in solution. The process of identifying reference states at which the activity coefficients of all species in a solution become unity is referred to as *normalization*, and there are three normalization conventions.^{92,94,95}

4.2.1 Normalization Convention I

This convention, which leads to Raoult's law, is normally applied when all the components of a solution are liquids at the system temperature and pressure. In other words, all components are regarded as solvents. The reference state of each component of the solution is the pure component state at the system temperature and an arbitrary reference pressure, which is often taken as the system pressure or the vapour pressure of the component at the system temperature. It follows therefore that the activity coefficient of each component approaches unity as its mole fraction approaches unity at the system temperature and system reference pressure, and this can be represented mathematically as follows.^{92,94,95}

$$\mu_i = \mu_i^\bullet + RT \ln x_i \gamma_i \quad \gamma_i \rightarrow 1 \text{ as } x_i \rightarrow 1 \quad (4.2.6)$$

Since the normalization convention holds for all the components in solution, it is often referred to as *symmetric normalization*; activity coefficients normalized by this convention are said to be symmetrically normalized.

4.2.2 Normalization Convention II

This convention, which leads to Henry's law for the solutes, is usually applied when some components of the solution are solids or gases at the system temperature and pressure. For such solutions, it is convenient to distinguish between the solvents and the solutes. The reference state of the

solvent, which is the component present in excess and whose mole fraction can be varied up to unity without change of phase, is the same as that defined by Eq. (4.2.6). On the other hand, the reference state for a solute is taken to be the hypothetical state of pure solute found by extrapolating its chemical potential from infinite dilution in the solvent to the pure solute at the solution temperature and reference pressure. The mathematical representation of this normalization convention can be written as follows:^{92,94,95}

$$\begin{aligned} \mu_s &= \mu_s^\bullet + RT \ln x_s \gamma_s & \gamma_s &\rightarrow 1 \text{ as } x_s \rightarrow 1 \\ \mu_i &= \mu_i^* + RT \ln x_i \gamma_i^* \quad (\gamma_i^* = \gamma_i / \gamma_i^\infty) & \gamma_i^* &\rightarrow 1 \text{ as } x_i \rightarrow 0 \end{aligned} \quad (4.2.7)$$

$$\sum_k x_k = 1$$

where $\gamma_i^\infty = \lim_{x \rightarrow 0} \gamma_i$ is the infinite dilution activity coefficient of solute i in the solution.

Since different reference states are used for the solvent and the solutes in this normalization convention, it is often referred to as *rational asymmetric (or rational unsymmetric) normalization*; activity coefficients normalized by this convention are said to be asymmetrically (or unsymmetrically) normalized^{92,94}. The relationship between the symmetric standard state for the solvents and the asymmetric standard state for the solutes is given as follows⁹⁴:

$$\mu_i^* = \mu_i^\bullet + RT \ln \gamma_i^\infty \quad (4.2.8)$$

4.2.3 Normalization Convention III

Molality is often used to represent the concentration of solids and gases in electrolyte solutions and, as a consequence, there is a normalization convention based on molality as follows:^{92,94,95}

$$\begin{aligned} \mu_s &= \mu_s^\bullet + RT \ln x_s \gamma_s & \gamma_s &\rightarrow 1 \text{ as } x_s \rightarrow 1 \\ \mu_i &= \mu_i^\Delta + RT \ln \left[\frac{m_i \gamma_i^m}{m_0} \right] \quad (\gamma_i^m = x_w \gamma_i^*) & \gamma_i^m &\rightarrow 1 \text{ as } m_i \rightarrow 0 \end{aligned} \quad (4.2.9)$$

$$\sum_k m_k = 0$$

where $m_i = x_i / (x_w M_w)$. μ_i^Δ in Eq. (4.2.9) is loosely referred to as the chemical potential of the solute in a hypothetical ideal solution of unit molality (m_0) at the same temperature and pressure as the solution under discussion.

It is clear that this normalization, which is sometimes referred to as *practical asymmetric normalization*, is closely related to the rational asymmetric normalization defined under normalization convention II. In fact, the standard states for normalization conventions II and III are related as follows:⁹⁴

$$\mu_i^\Delta = \mu_i^* + RT \ln(M_w m_0) \quad (4.2.10)$$

4.3 Liquid Phase Chemical-Reaction Equilibria

The criterion for chemical-reaction equilibrium state, which is characterized by minimum total Gibbs energy, is generally given by:^{91,92}

$$\sum_i \nu_i \mu_i = 0 \quad (4.3.1)$$

where ν_i is the *stoichiometric number* of species i (positive for products and negative for reactants) in the chemical-equilibrium reaction equation.

Once again, the limitations of chemical potential preclude direct utilization of Eq. (4.3.1). Therefore, an equivalent equation in terms of fugacity is given as follows:⁹¹

$$\prod_i \left(\frac{\hat{f}_i}{f_i^\bullet} \right) = \exp\left(\frac{-\Delta G^\bullet}{RT} \right) = K \quad (4.3.2)$$

with

$$\Delta G^\bullet = \sum_i \nu_i G_i^\bullet \quad (4.3.3)$$

K , the equilibrium constant, is a function of temperature only since G_i^\bullet , the Gibbs energy of pure species i in its standard state at fixed pressure, depends only on temperature. The fundamental relationship between equilibrium constant and temperature is given as follows:^{91,92}

$$\frac{d \ln K}{dT} = \frac{\Delta H^\bullet}{RT^2} \quad (4.3.4)$$

with

$$\Delta H^\bullet = \sum_i \nu_i H_i^\bullet \quad (4.3.5)$$

However, the commonly used functional relationship between equilibrium constant, K , and temperature, T , is usually expressed as follows:^{70-72,96}

$$\ln K = C_1 + C_2 / T + C_3 \ln T + C_4 T \quad (4.3.6)$$

Furthermore, Eq. (4.3.2) can be expressed in terms of activity coefficient as follows:⁹¹

$$\prod_i (x_i \gamma_i)^{\nu_i} = K \exp \left[\frac{(P^\circ - P)}{RT} \sum_i \nu_i V_i \right] \quad (4.3.7)$$

The exponential term in Eq. (4.3.7) is close to unity, except for high pressures, and can therefore be omitted to give:^{91,92}

$$\prod_i (x_i \gamma_i)^{\nu_i} = K \quad (4.3.8)$$

If unsymmetric reference state is chosen for the solutes, then Eq. (4.3.8) can be expanded as follows:⁸⁷

$$K = (x_w \gamma_w)^{\nu_w} \prod_s (x_s \gamma_s)^{\nu_s} \prod_i (x_i \gamma_i^*)^{\nu_i} \quad (4.3.9)$$

Also, it is pertinent to add that Eqs. (4.3.8) and (4.3.9) are on the mole fraction scale, including the equilibrium constant. The equivalents of Eqs. (4.3.8) and (4.3.9) on molality scale, with molality-based reference state chosen for the solutes, are given as follows:^{87,92}

$$K_m = \prod_i (m_i \gamma_i^m)^{\nu_i} \quad (4.3.10)$$

$$K_m = (x_w \gamma_w)^{\nu_w} \prod_s (x_s \gamma_s)^{\nu_s} \prod_i (m_i \gamma_i^m)^{\nu_i} \quad (4.3.11)$$

Furthermore, the unsymmetric activity coefficient of the solutes (as well as the equilibrium constant) in Eq. (4.3.9) is related to the molality-based activity coefficient of the solutes (as well as the equilibrium constant) in Eq. (4.3.11) as follows:⁸⁷

$$m_i \gamma_i^m = x_i \gamma_i^* \left(\frac{1000}{M_w} \right) \quad (4.3.12)$$

$$\ln K_m - \ln K = \sum_{\substack{i \neq w \\ i \neq s}} \nu_i \ln \left(\frac{m_i \gamma_i^m}{x_i \gamma_i^*} \right) = \ln \left(\frac{1000}{M_w} \right) \sum_{\substack{i \neq w \\ i \neq s}} \nu_i \quad (4.3.13)$$

where M_w is the molecular weight of water.

4.4 Rigorous Vapour-Liquid-Equilibrium (VLE) Models for CO₂-Alkanolamines-H₂O Systems

In principle, the vapour-liquid equilibrium (VLE) for non-electrolytic gas-liquid systems, which follows from a combination of Eqs. (4.1.8), (4.1.16) and (4.1.21), can be represented by the following equation:^{87,91}

$$\hat{\phi}_i y_i P = x_i \gamma_i \phi_i^{sat} P_i^{sat} \exp \left[\frac{V_i^l (P - P_i^{sat})}{RT} \right] \quad (4.4.1)$$

Although Eq. (4.4.1) accurately describes the VLE of solvent molecules, it is pertinent to add that Eq. (4.4.1) is more or less meaningless for supercritical components (i.e. components which are gases at normal conditions) such as CO₂ because the concept of saturation pressure does not apply to supercritical components.⁸⁷ An equivalent form of Eq. (4.4.1), based on *Henry's constant*, is normally adopted and hence the reason why supercritical components (molecular gases at normal conditions) are often referred to as Henry components.^{87,95}

The Henry's constant of a dissolved gas component in a single solvent is defined as the infinite dilute reference state fugacity of the gas in the liquid-phase and it is given as follows:^{87,91}

$$H_{i,s} = \lim_{x \rightarrow 0} \left(\frac{\hat{f}_i}{x_i} \right) \quad (4.4.2)$$

The Henry's constant of a supercritical component (i) in a given solvent (s) can be calculated from the following equation:^{87,97,98}

$$H_{i,s}(T, P) = H_{i,s}^o(T, P_s^{sat}) \exp \left(\frac{1}{RT} \int_{P_s^{sat}}^P V_{i,s}^\infty dP \right) \quad (4.4.3)$$

where:

$H_{i,s}(T, P)$ is the Henry's constant of species i in pure solvent s at the system temperature and pressure

$H_{i,s}^o(T, P_s^{sat})$ is the Henry's constant of species i in pure solvent s at the system temperature and the solvent vapour pressure

$V_{i,s}^\infty$ is the partial molar volume of species i at infinite dilution in pure solvent s , which can be calculated from the Brelvi-O'Connell model

Brelvi and O'Connell⁹⁹ presented universal empirical correlations relating compressibility of liquids to reduced density, and the partial molal volume of gases at infinite dilution in liquids to reduced density of the solvent and the reducing volumes of the gas and solvent. The general form of the Brelvi-O'Connell model can be expressed as follows:^{87,97}

$$V_{i,s}^\infty = \text{function} \left(V_i^{BO}, V_s^{BO}, V_s^{sat} \right) \quad (4.4.4)$$

with

$$V_k^{BO} = v_{1,k} + v_{2,k} T, \quad (k = i, s) \quad (4.4.5)$$

where V_i^{BO} and V_s^{BO} are, respectively, the characteristic volume of the supercritical component (i) and the solvent (s). V_s^{sat} is the saturated liquid volume of the solvent, which can be obtained from the Rackett¹⁰⁰ model. Also, $v_{1,k}$ and $v_{2,k}$ are the correlation parameters for component k (i.e. both the Henry component and the solvent).

The exponential term in (4.4.3), *Poynting correction*, can be neglected when dealing with systems operating at low to moderate pressures.^{91,98} Also, the

functional relationship between the reference state Henry's constant, $H_{i,s}^o$, and temperature, T , is usually expressed as follows:^{70-72,96-98}

$$\ln H_{i,s}^o = C_1 + C_2 / T + C_3 \ln T + C_4 T \quad (4.4.6)$$

For a mixed-solvent system, the Henry's constant for a dissolved gas component in all solvent components in the mixture can be approximated as follows:^{87,98,101}

$$\ln \left(\frac{H_i}{\gamma_i^\infty} \right) = \sum_s w_s \ln \left(\frac{H_{i,s}}{\gamma_{i,s}^\infty} \right) \quad (4.4.7)$$

with

$$w_s = \frac{x_s (V_s^{*l})^{\frac{2}{3}}}{\sum_{s'} x_{s'} (V_{s'}^{*l})^{\frac{2}{3}}} \quad (4.4.8)$$

where:

H_i is the Henry's constant of the dissolved gas component i in all solvent components

γ_i^∞ is the infinite dilution activity coefficient of Henry component i in the solution

$H_{i,s}$ is the Henry's constant of the dissolved gas component i in solvent s

$\gamma_{i,s}^\infty$ is the infinite dilution activity coefficient of Henry component i in solvent s

w_s is an apparent volume fraction of solvent s

As earlier stated, Eq. (4.4.1) is not applicable to supercritical (Henry) components such as CO₂ because the concept of saturation pressure does not apply to supercritical components. Therefore, the equivalent of Eq. (4.4.1) applicable to supercritical (Henry) components can be written as follows:⁸⁷

$$\hat{\phi}_i y_i P = x_i \gamma_i^* H_i = x_i \gamma_i \left(\frac{H_i}{\gamma_i^\infty} \right), \quad (i = \text{Henry component}) \quad (4.4.9)$$

The VLE of electrolytic systems, such as CO₂-Alkanolamines-H₂O systems, requires simultaneous satisfaction of Eqs. (4.3.8) and (4.4.1), including Eq. (4.4.9) for the Henry components. In other words, the coupled phase and chemical equilibria, characteristic of electrolytic systems must be satisfied simultaneously. It is also clear from Eqs. (4.3.8), (4.4.1) and (4.4.9) that values of fugacity coefficients and activity coefficients for all species, as well as Henry's constants for the Henry components, are needed for accurate description of the VLE behaviour of gas-liquid electrolytic systems.

4.4.1 Models for the Fugacity Coefficient

Fugacity coefficient, as defined by Eq. (4.1.12), can be calculated from PVT data using one of the numerous cubic Equations of State (EoS) available in the literature.^{87,91,102} According to Abbott¹⁰³, the general form of all possible cubic EoS can be represented by a five-parameter equation as follows:

$$P = \frac{RT}{V - b} - \frac{\Theta(V - \eta)}{(V - b)(V^2 + \delta V + \varepsilon)} \quad (4.4.10)$$

The parameters (b , Θ , η , δ and ε) in Eq. (4.4.10) are model dependent, and one or more may be constants (including zero), or they may vary with T and/or composition. Also, from the definition of compressibility factor ($Z = PV / RT$), an equivalent form of Eq. (4.4.10) can be expressed as follows:

$$Z = \frac{V}{V - b} - \frac{(\Theta / RT)V(V - \eta)}{(V - b)(V^2 + \delta V + \varepsilon)} \quad (4.4.11)$$

Although several popular EoS have been reported in the literature^{102,103}, the ones commonly used in the modelling of the gas-phase non-ideal behaviour in CO₂-alkanolamines-H₂O systems are the Redlich-Kwong (RK) equation¹⁰⁴, the Soave's modification of the Redlich-Kwong (SRK) equation¹⁰⁵, and the Peng-Robinson equation (PR)¹⁰⁶. A summary of parameters assignment for the RK, SRK and PR Equations of State, based on either Eq. (4.4.10) or Eq. (4.4.11), is given in **Table 4.1**. It is pertinent to add that application of any of the EoS to gas mixtures requires appropriate mixing rules for the parameters that are involved.^{87,94,102}

Table 4.1. Assignment of Parameters for the RK, SRK and PR Equations of State.¹⁰²

EoS	η	δ	ε	Θ	Unknown parameters
RK	b	0	0	$a / T_r^{0.5}$	2; (a, b)
SRK	b	b	0	$a[\alpha(T_r)]$	3; (a, b, ω)
PR	b	$2b$	$-b^2$	$a[\alpha(T_r)]$	3; (a, b, ω)

$$\text{SRK: } \alpha(T_r) = [1 + (0.48 + 1.574\omega - 0.176\omega^2)(1 - T_r^{0.5})]^2$$

$$\text{PR: } \alpha(T_r) = [1 + (0.37464 + 1.54226\omega - 0.2699\omega^2)(1 - T_r^{0.5})]^2$$

4.4.2 Models for the Activity Coefficient

Activity coefficient, as defined by Eq. (4.1.23), can be calculated if a model for excess Gibbs energy is available for the system of interest. Most of the models for the excess Gibbs energy of electrolytic systems, including CO₂-alkanolamine-H₂O systems, usually combine short-range interactions, such as van der Waals type of interactions, with long-range electrostatic interactions as follows:⁹⁴

$$\frac{G^E}{RT} = \frac{G^{E, \text{SR}}}{RT} + \frac{G^{E, \text{LR}}}{RT} \quad (4.4.12)$$

where $G^{E, \text{SR}}$ and $G^{E, \text{LR}}$ are, respectively, the short-range contribution and the long-range contribution to the excess Gibbs energy of the system.

The short-range interactions are usually accounted for by local composition models, such as the **Non-Random-Two-Liquid** (NRTL) equation of Renon and Prausnitz¹⁰⁷ and the **Universal Quasi-Chemical** (UNIQUAC) equation of Abrams and Prausnitz.¹⁰⁸ However, it is pertinent to add that virial type empirical models, such as the Margules expansions, may also be used to account for short-range interactions as demonstrated in the work of Li and Mather.⁸⁶ On the other hand, electrostatic interactions in most models are usually based on a modified form of the equation originally proposed by Debye and Hückel.¹⁰⁹ The Debye-Hückel (DH) equation was extended by Guggenheim,¹¹⁰ and the extended equation by Guggenheim was further improved upon by Pitzer^{111,112} to give what is commonly referred to as

Pitzer-Debye-Hückel (PDH) equation. Thus, Eq. (4.4.12) may be written as follows:^{86,113}

$$\frac{G^E}{RT} = \frac{G^{E, SR}}{RT} + \frac{G^{E, PDH}}{RT} \quad (4.4.13)$$

such that:

$$\ln \gamma_i = \ln \gamma_i^{SR} + \ln \gamma_i^{PDH} \quad (4.4.14)$$

Two of the widely used rigorous models for the excess Gibbs energy, which combines the local composition model for short range interactions with DH or PDH equation for long range electrostatic interactions, are the extended UNIQUAC model (which is sometimes referred to as electrolyte-UNIQUAC model, e-UNIQUAC) and the electrolyte-NRTL (e-NRTL) model⁹⁴. The extended UNIQUAC model, which was originally introduced by Sander et al.¹¹⁴, will not be discussed further in this thesis since the model adopted in this thesis is the electrolyte-NRTL model. Notwithstanding, reference can be made to the book by Kontogeorgis and Folas⁹⁴ for a detailed discussion of the extended UNIQUAC model, as well as the papers by Kaewsichan et al.,¹¹⁵ Faramarzi et al.¹¹⁶ and Aronu et al.¹¹⁷ for a more specific discussion of the application of the extended UNIQUAC model to CO₂ absorption in aqueous alkanolamine solutions.

4.4.2.1 Electrolyte-NRTL Model

The electrolyte-NRTL (e-NRTL) model, which is the Aspen Plus[®] recommended model for rigorous modelling of electrolyte systems (including CO₂-alkanolamine-H₂O systems), was originally proposed by Chen and co-workers^{113,118} and it was later extended to mixed-solvent electrolyte systems by Mock et al.¹¹⁹. Also, Chen and Song¹²⁰ have generalized the electrolyte-NRTL model for mixed-solvent electrolyte systems using the concept of segment interactions, while Bollas et al.¹²¹ presented a refinement of the electrolyte-NRTL model by deriving general expressions for the activity coefficients. The original electrolyte-NRTL model proposed by Chen and co-workers^{113,118}, including subsequent extension and generalization for mixed-solvent electrolyte systems, is based on two fundamental assumptions as follows:

- i. **The like-ion repulsion assumption:** the local composition of cations around cations is zero, and similarly for anions, which is equivalent to

assuming that repulsive forces between ions of like charge are extremely large.

- ii. **The local electroneutrality assumption:** the distribution of cations and anions around a central solvent molecule is such that the net local ionic charge is zero.

The e-NRTL model, as originally proposed by Chen and Co-workers,^{113,118} uses the NRTL equation to account for short range interactions and the PDH equation for long range electrostatic interactions. However, the state-of-the-art e-NRTL model includes a Born term^{122,123} to account for the excess Gibbs energy of transfer from infinite dilution in mixed-solvent to infinite dilution in aqueous phase. Thus the state-of-the-art e-NRTL model for excess Gibbs energy has three contributions as follows:^{70,72,87}

$$\frac{G^{*E}}{RT} = \frac{G^{*E, PDH}}{RT} + \frac{G^{*E, BORN}}{RT} + \frac{G^{*E, LC}}{RT} \quad (4.4.15)$$

such that:

$$\ln \gamma_i^* = \ln \gamma_i^{*PDH} + \ln \gamma_i^{*BORN} + \ln \gamma_i^{*LC} \quad (4.4.16)$$

where the * notation denotes an unsymmetric reference state.

The PDH equation is used to represent the long-range interaction contribution. The PDH equation, normalized to mole fractions of unity for solvent and zero for electrolytes, is given as follows:¹¹²

$$\frac{G^{*E, PDH}}{RT} = - \left(\sum_i x_i \right) \left(\frac{1000}{M_s} \right)^{1/2} \left(\frac{4A_\varphi I_x}{\rho} \right) \ln \left(1 + \rho I_x^{1/2} \right) \quad (4.4.17)$$

with

$$A_\varphi = \frac{1}{3} \left(\frac{2\pi N_A d_s}{1000} \right)^{1/2} \left(\frac{Q_e^2}{\epsilon_s kT} \right)^{3/2} \quad (4.4.18)$$

$$I_x = \frac{1}{2} \sum_i x_i z_i^2 \quad (4.4.19)$$

where:

x_i is the mole fraction of component i

M_s is the molecular weight of the solvent

A_φ is Debye-Hückel parameter

I_x is ionic strength (on a mole fraction basis) of the mixture

ρ is the “closest approach” parameter

N_A is Avogadro’s number

d_s is the mass density of solvent

Q_e is electron charge

ϵ_s is Dielectric constant of the solvent

k is Boltzmann constant

T is temperature

z_i is charge number of ion i

Taking the derivative of Eq. (4.4.17), in line with the definition of the activity coefficient as given by Eq. (4.1.23), gives the following equation:¹¹²

$$\ln \gamma_i^{*PDH} = -\left(\frac{1000}{M_s}\right)^{1/2} A_\phi \left[\left(\frac{2z_i^2}{\rho}\right) \ln\left(1 + \rho I_x^{1/2}\right) + \frac{z_i^2 I_x^{1/2} - 2I_x^{3/2}}{1 + \rho I_x^{1/2}} \right] \quad (4.4.20)$$

It is important to note that the Debye-Hückel theory, the basis for the PDH equation, is based on the infinite dilution reference state for ionic species in the actual solvent media. Thus, for systems with water as the only solvent, the reference state is the infinite dilution aqueous solution. For mixed-solvent systems, the reference state for which the Debye-Hückel theory remains valid is the infinite dilution solution with the corresponding mixed-solvent composition. Also, the molecular weight (M_s), the mass density (d_s), and the dielectric constant (ϵ_s) for the single solvent can be extended for mixed-solvents by using simple composition average mixing rules as follows⁸⁷:

$$M_s = \sum_m x'_m M_m \quad (4.4.21)$$

$$d_s = \frac{\sum_m x'_m M_m}{V_m^l} \quad (4.4.22)$$

$$\epsilon_s = \frac{\sum_m x'_m M_m \epsilon_m}{\sum_m x'_m M_m} \quad (4.4.23)$$

$$x'_m = \frac{x_m}{\sum_m x_m} \quad (4.4.24)$$

$$V_m^l = x'_w V_w^l + x'_{nws} V_{nws}^l \quad (4.4.25)$$

$$x'_w + x'_{nws} = 1 \quad (4.4.26)$$

where:

x_m is the mole fraction of the solvent m in the solution

M_m is the molecular weight of the solvent m

V_m^l is the molar volume of the mixed-solvent mixture

ε_m is the dielectric constant of the solvent m

V_w^l is the molar volume of liquid water

x'_{nws} is the sum of the mole fractions of all non-water solvents

V_{nws}^l is the liquid molar volume for the mixture of all non-water solvents

Furthermore, the temperature dependency of the dielectric constant of a given solvent can be represented as follows:⁸⁷

$$\varepsilon(T) = A + B \left(\frac{1}{T} - \frac{1}{T^{ref}} \right) \quad (4.4.27)$$

where A and B are parameters, and T is the temperature in Kelvin.

The Born equation^{122,123}, which is used to account for the Gibbs energy of transfer of ionic species from the infinite dilution state in a mixed-solvent to the infinite dilution state in aqueous phase, is given as follows:^{70,72,87,120}

$$\frac{G^{*E, BORN}}{RT} = \frac{Q_e^2}{2kT} \left(\frac{1}{\varepsilon_s} - \frac{1}{\varepsilon_w} \right) \left(\sum_i \frac{x_i z_i^2}{r_i} \right) 10^{-2} \quad (4.4.28)$$

where:

ε_w is the Dielectric constant of water

r_i is the Born radius of the ionic species i

Taking the derivative of Eq. (4.4.28), in line with the definition of activity coefficient as given by Eq. (4.1.23), gives the following equation:⁸⁷

$$\ln \gamma_i^{*BORN} = \frac{Q_e^2}{2kT} \left(\frac{1}{\epsilon_s} - \frac{1}{\epsilon_w} \right) \left(\frac{z_i^2}{r_i} \right) 10^{-2} \quad (4.4.29)$$

The local interaction contribution to the overall excess Gibbs energy of a multicomponent system, based on the NRTL model, is given as follows:^{70,72,87,118}

$$\begin{aligned} \frac{G^{*E, LC}}{RT} &= \sum_m X_m \frac{\sum_j X_j G_{jm} \tau_{jm}}{\sum_k X_k G_{km}} \\ &+ \sum_c X_c \sum_{a'} \left(\frac{X_{a'}}{\sum_{a''} X_{a''}} \right) \frac{\sum_j X_j G_{jc, a'c} \tau_{jc, a'c}}{\sum_k X_k G_{kc, a'c}} \\ &+ \sum_a X_a \sum_{c'} \left(\frac{X_{c'}}{\sum_{c''} X_{c''}} \right) \frac{\sum_j X_j G_{ja, c'a} \tau_{ja, c'a}}{\sum_k X_k G_{ka, c'a}} \end{aligned} \quad (4.4.30)$$

with

$$G_{cm} = \frac{\sum_a X_a G_{ca, m}}{\sum_{a'} X_{a'}} \quad (4.4.31)$$

$$G_{am} = \frac{\sum_c X_c G_{ca, m}}{\sum_{c'} X_{c'}} \quad (4.4.32)$$

$$\alpha_{cm} = \alpha_{mc} = \frac{\sum_a X_a \alpha_{ca, m}}{\sum_{a'} X_{a'}} \quad (4.4.33)$$

$$\alpha_{am} = \alpha_{ma} = \frac{\sum_c X_c \alpha_{ca, m}}{\sum_{c'} X_{c'}} \quad (4.4.34)$$

$$\tau_{jm} = -\frac{\ln G_{jm}}{\alpha_{jm}} \quad (4.4.35)$$

$$\tau_{jc,a'c} = -\frac{\ln G_{jc,a'c}}{\alpha_{jc,a'c}} \quad (4.4.36)$$

$$\tau_{ja,c'a} = -\frac{\ln G_{ja,c'a}}{\alpha_{ja,c'a}} \quad (4.4.37)$$

$$\tau_{mc,ac} = \tau_{cm} - \tau_{ca,m} + \tau_{m,ca} \quad (4.4.38)$$

$$\tau_{ma,ca} = \tau_{am} - \tau_{ca,m} + \tau_{m,ca} \quad (4.4.39)$$

where:

$$X_j = x_j C_j \quad (C_j = z_j \text{ for ions; } C_j = 1.0 \text{ for molecules})$$

α represent the symmetric non-randomness parameters

τ represent the asymmetric binary energy interaction parameters

j and k in Eqs. (4.4.30) to (4.4.39) can be any of the species [anions (a, a'), cations (c, c'), or molecules (m, m')] present in the system. The symmetric non-randomness parameters (α) and the asymmetric binary energy interaction parameters (τ) both exist for molecule-molecule pairs ($\alpha_{mm'} = \alpha_{m'm}$ while $\tau_{mm'} \neq \tau_{m'm}$), molecule-electrolyte pairs ($\alpha_{m,ca} = \alpha_{ca,m}$ while $\tau_{m,ca} \neq \tau_{ca,m}$), and electrolyte-electrolyte pairs ($\alpha_{ca,ca'} = \alpha_{ca',ca}$ and $\alpha_{ca,c'a} = \alpha_{c'a,ca}$ while $\tau_{ca,ca'} \neq \tau_{ca',ca}$ and $\tau_{ca,c'a} \neq \tau_{c'a,ca}$).

The temperature dependency of all symmetric non-random parameters (molecule-molecule pairs, molecule-electrolyte pairs, and electrolyte-electrolyte pairs) is represented as follows:⁸⁷

$$\alpha_{ij} = a_{ij} + d_{ij}(T - 273.15) \quad (4.4.40)$$

where $\alpha_{ij} = \alpha_{mm'}, \alpha_{m,ca}, \alpha_{ca,c'a}$ and $\alpha_{ca,ca'}$

The temperature dependency of the asymmetric binary energy interaction parameters for electrolyte pairs, excluding the molecule-molecule pairs, is represented as follows.⁸⁷

$$\tau_{ij} = C_{ij} + \frac{D_{ij}}{T} + E_{ij} \left[\frac{(298.15 - T)}{T} + \ln \left(\frac{T}{298.15} \right) \right] \quad (4.4.41)$$

where $\tau_{ij} = \tau_{m,ca}, \tau_{ca,m}, \tau_{ca,c'a}, \tau_{c'a,ca}, \tau_{ca,ca'}$ and $\tau_{ca',ca}$.

The temperature dependency of the asymmetric binary energy interaction parameters for the molecule-molecule pairs is represented as follows:⁸⁷

$$\tau_{mm'} = a_{mm'} + \frac{b_{mm'}}{T} + e_{mm'} \ln T + f_{mm'} T \quad (4.4.42)$$

Application of Eq. (4.1.23) to Eq. (4.4.30) gives rise to the following set of equations, which account for the short-range contributions (i.e. local contributions) to the overall activity coefficients:^{87,118}

For molecules:

$$\begin{aligned} \ln \gamma_m^{LC} = & \frac{\sum_j X_j G_{jm} \tau_{jm}}{\sum_k X_k G_{km}} + \sum_{m'} \frac{X_{m'} G_{mm'}}{\sum_k X_k G_{km'}} \left(\tau_{mm'} - \frac{\sum_k X_k G_{km'} \tau_{km'}}{\sum_k X_k G_{km'}} \right) \\ & + \sum_c \sum_{a'} \frac{X_{a'}}{\sum_{a''} X_{a''}} \frac{X_c G_{mc,a'c}}{\sum_k X_k G_{kc,a'c}} \left(\tau_{mc,a'c} - \frac{\sum_k X_k G_{kc,a'c} \tau_{kc,a'c}}{\sum_k X_k G_{kc,a'c}} \right) \\ & + \sum_a \sum_{c'} \frac{X_{c'}}{\sum_{c''} X_{c''}} \frac{X_a G_{ma,c'a}}{\sum_k X_k G_{ka,c'a}} \left(\tau_{ma,c'a} - \frac{\sum_k X_k G_{ka,c'a} \tau_{ka,c'a}}{\sum_k X_k G_{ka,c'a}} \right) \end{aligned} \quad (4.4.43)$$

For cations:

$$\begin{aligned}
 \frac{1}{z_c} \ln \gamma_c^{*LC} &= \sum_{a'} \frac{X_{a'}}{\sum_{a''} X_{a''}} \frac{\sum_k X_k G_{kc,a'c} \tau_{kc,a'c}}{\sum_k X_k G_{kc,a'c}} \\
 &+ \sum_m \frac{X_m G_{cm}}{\sum_k X_k G_{km}} \left(\tau_{cm} - \frac{\sum_k X_k G_{km} \tau_{km}}{\sum_k X_k G_{km}} \right) \\
 &+ \sum_a \sum_{c'} \frac{X_{c'}}{\sum_{c''} X_{c''}} \frac{X_a G_{ca,c'a}}{\sum_k X_k G_{ka,c'a}} \left(\tau_{ca,c'a} - \frac{\sum_k X_k G_{ka,c'a} \tau_{ka,c'a}}{\sum_k X_k G_{ka,c'a}} \right)
 \end{aligned} \tag{4.4.44}$$

For anions:

$$\begin{aligned}
 \frac{1}{z_a} \ln \gamma_a^{*LC} &= \sum_{c'} \frac{X_{c'}}{\sum_{c''} X_{c''}} \frac{\sum_k X_k G_{ka,c'a} \tau_{ka,c'a}}{\sum_k X_k G_{ka,c'a}} \\
 &+ \sum_m \frac{X_m G_{am}}{\sum_k X_k G_{km}} \left(\tau_{am} - \frac{\sum_k X_k G_{km} \tau_{km}}{\sum_k X_k G_{km}} \right) \\
 &+ \sum_c \sum_{a'} \frac{X_{a'}}{\sum_{a''} X_{a''}} \frac{X_c G_{ac,a'c}}{\sum_k X_k G_{kc,a'c}} \left(\tau_{ac,a'c} - \frac{\sum_k X_k G_{kc,a'c} \tau_{kc,a'c}}{\sum_k X_k G_{kc,a'c}} \right)
 \end{aligned} \tag{4.4.45}$$

4.5 Other Thermodynamic Properties

The activity coefficient model is directly related to other thermodynamic properties, such as enthalpy, through fundamental thermodynamic equations in terms of the liquid phase excess properties defined as follows:^{87,91}

$$M^{E,l} = M^l - M^{id} = \Delta M - \Delta M^{id} \quad (M = G, H, U, S, V) \tag{4.5.1}$$

$$\text{with } \Delta M = M^l - \sum_i x_i M_i^l \quad \text{and} \quad \Delta M^{id} = M^{id} - \sum_i x_i M_i^l$$

where ΔM and ΔM^{id} are, respectively, the property change of mixing for a real solution and an ideal solution.

4.5.1 Gibbs Energy

The fundamental relationship between excess Gibbs energy and activity coefficient is given by Eq. (4.1.24), which is repeated below for ease of reference:

$$\frac{G^{E,l}}{RT} = \sum_i x_i \ln \gamma_i \quad [\text{Eq. (4.1.24)}]$$

Also, the relationship between Gibbs energy and excess Gibbs energy is given as follows.^{87,91,98}

$$G^l = G^{E,l} + \sum_i x_i G_i^l + RT \sum_i x_i \ln x_i \quad (4.5.2)$$

such that:

$$\Delta G^{id} = RT \sum_i x_i \ln x_i \quad (4.5.3)$$

$$G^l - G^{ig} = G^{E,l} + \sum_i x_i (G_i^l - G_i^{ig}) + RT \sum_i x_i \ln x_i \quad (4.5.4)$$

$$G_i^{ig} = \Delta_f H_i^{ig} + \int_{T^{ref}}^T C_{p,i}^{ig}(T) dT - T \int_{T^{ref}}^T \frac{C_{p,i}^{ig}(T)}{T} dT \quad (4.5.5)$$

$$- \frac{T(\Delta_f H_i^{ig} - \Delta_f G_i^{ig})}{T^{ref}}$$

However, Eq. (4.5.5) is not directly applicable to mixtures containing ionic components because it is strictly for ideal gas mixture and the ideal gas model is invalid for ionic components. Therefore, a formulation for calculating the Gibbs energy of electrolyte systems, such as CO₂-alkanolamine-H₂O systems, may be written as follows:^{87,98}

$$G^l = \sum_{i=s} x_i G_i^l + \sum_{i=ca} x_i G_i^{\infty,l} + \sum_{i=h} x_i G_i^{\infty,l} + RT \sum_i x_i \ln x_i + G^{E,l} \quad (4.5.6)$$

such that:

$$G_s^l(T) = \Delta_f H_{s,298.15}^{ig} + \int_{298.15}^T C_{p,s}^{ig} dT - T \int_{298.15}^T \frac{C_{p,s}^{ig}(T)}{T} dT \quad (4.5.7)$$

$$- \frac{T(\Delta_f H_s^{ig} - \Delta_f G_s^{ig})}{298.15} + \Delta G_s^{ig \rightarrow l}(T)$$

$$G_{ca}^{\infty,l}(T) = \Delta_f H_{ca,298.15}^{\infty,l} + \int_{298.15}^T C_{p,ca}^{\infty,l} dT - T \int_{298.15}^T \frac{C_{p,ca}^{\infty,l}(T)}{T} dT \quad (4.5.8)$$

$$- \frac{T(\Delta_f H_{ca,298.15}^{\infty,l} - \Delta_f G_{ca,298.15}^{\infty,l})}{298.15} + RT \ln \left(\frac{1000}{M_w} \right)$$

$$G_h^{\infty,l}(T) = \Delta_f G_h^{ig}(T) - RT \ln \left(\frac{H_h}{P^{ref}} \right) \quad (4.5.9)$$

$$G^{E,l} = RT \sum_i x_i \ln \gamma_i \quad (4.5.10)$$

where the subscripts “s”, “h” and “ca” indicate the contributions from solvents, Henry components and ionic components, respectively, and the superscripts “ig”, “l” and “∞” indicate ideal gas state, liquid state, and infinite dilution reference state, respectively.

4.5.2 Enthalpy

The fundamental relationship between activity coefficient and liquid phase excess enthalpy is given as follows.^{87,91}

$$H^{E,l} = -RT^2 \sum_i x_i \frac{\partial \ln \gamma_i}{\partial T} \quad (4.5.11)$$

Also, the relationship between enthalpy and excess enthalpy is given as follows.^{87,91}

$$H^l = H^{E,l} + \sum_i x_i H_i^l \quad (4.5.12)$$

such that:

$$\Delta H^{id} = 0 \quad (4.5.13)$$

$$H^l - H^{ig} = H^{E,l} + \sum_i x_i (H_i^l - H_i^{ig}) \quad (4.5.14)$$

$$H^{ig} = \sum_i x_i H_i^{ig} \quad (4.5.15)$$

$$H_i^{ig} = \Delta_f H_i^{ig} + \int_{T^{ref}}^T C_{p,i}^{ig}(T) dT \quad (4.5.16)$$

where H_i^l and H_i^{ig} are, respectively, the liquid phase enthalpy and ideal gas enthalpy of component i at the system conditions, $\Delta_f H_i^{ig}$ is the ideal gas standard enthalpy of formation of component i at $T^{ref} = 298.15 \text{ K}$, and $C_{p,i}^{ig}$ is the ideal gas heat capacity of component i .

Once again, Eq. (4.5.16) is not directly applicable to mixtures containing ionic components because it is strictly for ideal gas mixture and the ideal gas model is invalid for ionic components. Therefore, a formulation for calculating the enthalpy of electrolyte systems, such as CO₂-alkanolamine-H₂O systems, may be written as follows.^{87,98}

$$H^l = \sum_{i=s} x_i H_i^l + \sum_{i=ca} x_i H_i^{\infty,l} + \sum_{i=h} x_i H_i^{\infty,l} + H^{E,l} \quad (4.5.17)$$

such that:

$$H_s^l(T) = \Delta_f H_{s,298.15}^{ig} + \int_{298.15}^T C_{p,s}^{ig} dT + \Delta H_s^{ig \rightarrow l}(T) \quad (4.5.18)$$

$$H_{ca}^{\infty,l}(T) = \Delta_f H_{ca,298.15}^{\infty,l} + \int_{298.15}^T C_{p,ca}^{\infty,l} dT \quad (4.5.19)$$

$$H_h^{\infty,l}(T) = \Delta_f H_h^{ig}(T) - RT^2 \left[\frac{\partial \ln H_h}{\partial T} \right] \quad (4.5.20)$$

$$H^{E,l} = -RT^2 \sum_i x_i \frac{\partial \ln \gamma_i}{\partial T} \quad (4.5.21)$$

4.5.3 Entropy

Entropy is usually calculated directly from the fundamental relationship relating it to enthalpy and Gibbs energy, which is given as follows.^{87,91}

$$S^l = \frac{H^l - G^l}{T} \quad (4.5.22)$$

The corresponding relationship between their excess properties is given as follows.^{87,91}

$$S^{E,l} = \frac{H^{E,l} - G^{E,l}}{T} = -R \left[T \sum_i x_i \frac{\partial \ln \gamma_i}{\partial T} + \sum_i x_i \gamma_i \right] \quad (4.5.23)$$

4.5.4 Vapour pressure

The fundamental equation upon which most vapour pressure models are based is given by the Clapeyron equation as follows:^{91,102}

$$\frac{d \ln P^{vap}}{d(1/T)} = -\frac{1}{R} \frac{\Delta H_v}{\Delta Z_v} \quad (4.5.24)$$

where P^{vap} is the vapour pressure of a pure component, ΔH_v is the difference between enthalpies of the saturated vapour and the saturated liquid, ΔZ_v is the difference between compressibility factors of the saturated vapour and the saturated liquid. Most vapour pressure models stem from an integration of Eq. (4.5.24) with an assumption regarding the dependency of $\Delta H_v / \Delta Z_v$ on temperature.¹⁰² The extended Antoine equation, which is the default model used by Aspen Plus[®] in the calculation of vapour pressure, is given by Eq. (4.5.25):⁸⁷

$$\ln P_i^{*l} (kPa) = C_{1i} + \frac{C_{2i}}{T + C_{3i}} + C_{4i}T + C_{5i} \ln T + C_{6i}T^{C_{7i}} \quad (4.5.25)$$

Table 4.2. Aspen Plus[®] Default Parameters for the Extended Antoine Equation.

PLXANT Parameters	Symbol	Aspen Default value for MEA	Aspen default value for H ₂ O
PLXANT-1	C_{1i}	165.8722447	65.64224472
PLXANT-2	C_{2i}	-13492.0	-7206.7
PLXANT-3	C_{3i}	0.0	0.0
PLXANT-4	C_{4i}	0.0	0.0
PLXANT-5	C_{5i}	-21.914	-7.1385
PLXANT-6	C_{6i}	1.3779E-5	4.046E-6
PLXANT-7	C_{7i}	2.0	2.0
Temperature range (K)		283.0 – 638.0	273.16 – 647.29

where P_i^{*l} is the vapour pressure of pure species i , C_{1i} to C_{7i} are the model parameters (Aspen Plus® PLXANT parameters) for the pure species, and T is temperature in Kelvin. **Table 4.2** summarises the default Aspen Plus® PLXANT parameters for MEA and H₂O.

4.5.5 Enthalpy of Vapourization

The Clapeyron equation, which is given by Eq. (4.5.24), is an exact thermodynamic relationship between the vapour pressure of a pure species and its enthalpy of vapourization, the temperature at which the vapourization occurs, and the difference between the compressibilities of the saturated vapour and the saturated liquid.^{91,102} However, an approximate relationship known as Clausius-Clapeyron equation, which is only valid at low pressure, is directly obtained if the difference between the compressibilities of saturated vapour and saturated liquid is taken as unity. Therefore, if ΔZ_v , Eq. (4.5.24) is taken as one, the Clausius-Clapeyron equation is given as follows:⁹¹

$$\frac{d \ln P^{vap}}{d(1/T)} = -\frac{\Delta H_v}{R} \quad (4.5.26)$$

Since C_3 and C_4 in Eq. (4.5.25) are both zero for MEA and H₂O, as shown in **Table 4.2**, their elimination from Eq. (4.5.25) gives rise to an equation, which is equivalent to the DIPPR equation for vapour pressure, as follows:⁸⁷

$$\ln P_i^{vap} = C_{1i} + \frac{C_{2i}}{T} + C_{5i} \ln T + C_{6i} T^{C_{7i}} \quad (4.5.27)$$

Thus, from Eqs. (4.5.26) and (4.5.27), it can easily be shown that the enthalpy of vapourization of the pure components is approximately given by:

$$\Delta H_i^{vap} = R \left\{ C_{6i} C_{7i} [T(K)]^{C_{7i}+1} + C_{5i} T(K) - C_{2i} \right\} \quad (4.5.28)$$

Once again, it is pertinent to add that Eq. (4.5.28) is only valid at low pressure since its derivation is based on Eq. (4.5.26).

A widely used model for calculating the enthalpy of vapourization is the model developed by Watson.¹²⁴ The form of the Watson model used by

Aspen Plus[®] in the calculation of enthalpy of vapourisation is given as follows:⁸⁷

$$\Delta H_i^{vap}(T) = \Delta H_i^{vap}(T_1) \left[\frac{1 - T / T_{c,i}}{1 - T_1 / T_{c,i}} \right]^{\{a_i + b_i(1 - T/T_{c,i})\}} \quad [T > T_{\min}] \quad (4.5.29)$$

where $\Delta H_i^{vap}(T_1)$ is the enthalpy of vapourization of pure species i at temperature T_1 , a_i and b_i are the model parameters (Aspen Plus[®] DHVLWT parameters) for the pure species, and $T_{c,i}$ is the critical temperature of pure species i in Kelvin. **Table 4.3** summarises the default Aspen Plus[®] DHVLWT parameters for MEA and H₂O.

An alternative to the Watson model, which is also available in Aspen Plus[®] as an option, is the DIPPR equation for enthalpy of vapourization. The DIPPR equation is given as follows:⁸⁷

$$\Delta H_i^{vap} = C_{1,i}(1 - T_{r,i})^{[C_{2,i} + C_{3,i}T + C_{4,i}T^2 + C_{5,i}T^3]} \quad (4.5.30)$$

where ΔH_i^{vap} is the enthalpy of vapourization of pure species i at temperature T , $C_{1,i}$ to $C_{5,i}$ are the model parameters (Aspen Plus[®] DHVLDP parameters) for the pure species, and $T_{r,i}$ (i.e. $T / T_{c,i}$) is the reduced temperature of pure species i at Temperature T . **Table 4.4** summarises the default Aspen Plus[®] DHVLDP parameters for MEA and H₂O.

Table 4.3. Aspen Plus[®] Default Parameters for the Watson Enthalpy of Vapourization Model.

DHVLWT Parameters	Symbol	Aspen Default value for MEA	Aspen default value for H ₂ O
DHVLWT -1	$\Delta H_i^{vap}(T_1)$	5.48358E+07	4.0683136E+07
DHVLWT -2	$T_1(^{\circ}C)$	126.67	100.05
DHVLWT -3	a_i	0.3288	0.3106
DHVLWT -4	b_i	-0.0857	0.0
DHVLWT -5	$T_{\min}(^{\circ}C)$	-27.37	0.05

Table 4.4. Aspen Plus[®] Default Parameters for the DIPPR Enthalpy of Vapourization Model.

DHVLDP Parameters	Symbol	Aspen Default value for MEA	Aspen default value for H ₂ O
DHVLDP -1	$C_{1,i}$ (J/kmol)	8.5465E+07	5.1546E+07
DHVLDP -2	$C_{2,i}$	0.5102	0.28402
DHVLDP -3	$C_{3,i}$	0.0	-0.15843
DHVLDP -4	$C_{4,i}$	0.0	0.2375
DHVLDP -5	$C_{5,i}$	0.0	0.0

4.5.6 Heat Capacity

The exact thermodynamic equation relating enthalpy to constant-pressure heat capacity is given as follows:^{87,91}

$$C_P = \left(\frac{\partial H}{\partial T} \right)_P \quad (4.5.31)$$

such that:

$$\Delta H_i^v = H_i^v(T) - H_i^v(T^{ref}) = \int_{T^{ref}}^T C_{P,i}^v dT \quad (4.5.32)$$

$$\Delta H_i^l = H_i^l(T) - H_i^l(T^{ref}) = \int_{T^{ref}}^T C_{P,i}^l dT \quad (4.5.33)$$

Aspen Plus[®] calculates the constant-pressure heat capacity of a pure liquid by taking the temperature derivative of its enthalpy according to Eq. (4.5.31) and by evaluating the reference enthalpy in Eq. (4.5.33) as follows:⁸⁷

$$H_i^l(T^{ref}) = H_i^{ig} + (H_i^v - H_i^{ig}) - \Delta H_i^{vap} \quad (4.5.34)$$

It is clear that the connection between the enthalpy of evaporation and the heat capacity of a pure liquid is given by the last term on the right hand side of Eq. (4.5.34). It follows that accurate calculation of constant-pressure heat capacity of a pure liquid is dependent on accurate estimation of the enthalpy of vapourization of the pure liquid. Furthermore, Aspen Plus[®] calculates the liquid phase heat capacity of a mixture (CPMX), in the same manner as for

pure liquid components, by taking the derivative of the liquid mixture enthalpy at constant pressure as follows:^{87,91}

$$C_{P,m}^l = \left(\frac{\partial H_m^l}{\partial T} \right)_P \quad (4.5.35)$$

such that:

$$H_m^l(T + \Delta T) - H_m^l(T) = \int_T^{T+\Delta T} C_{P,m}^l dT \quad (4.5.36)$$

$$H_m^l = \sum_i x_i H_i^l + H^{E,l} \quad (4.5.37)$$

The relationship between the liquid phase excess enthalpy and the activity coefficients of the components of the mixture is given by Eq. (4.5.11), which is repeated below for ease of reference.

$$H^{E,l} = -RT^2 \sum_i x_i \frac{\partial \ln \gamma_i}{\partial T} \quad [\text{Eq. 4.5.11}]$$

It is clear from Eqs. (4.5.11) and (4.5.37) that the liquid phase heat capacity of a mixture is a function of the activity coefficients of the components of the mixture. Also, the activity coefficient of any species in a mixture plays a role in the vapour-liquid-equilibrium of the species as given by Eq. (4.4.1). Therefore, in order to calculate the liquid-phase heat capacity of a mixture, in addition to the prediction of the vapour-liquid-equilibrium (VLE) of the mixture, the interaction parameters of the electrolyte-NRTL model is usually regressed, simultaneously, using VLE data, enthalpy data and/or excess enthalpy data, heat capacity data and/or excess heat capacity data. However, the simultaneous regression of the electrolyte-NRTL model parameters using VLE data, enthalpy data and heat capacity data imposes great constraints on the model parameters and limits the prediction accuracy of the electrolyte-NRTL model, especially the variation of the liquid-phase heat capacity of CO₂-loaded aqueous solution of alkanolamines with temperature.¹²⁵ It is the limitation of the electrolyte-NRTL model in predicting the liquid-phase heat capacity of a CO₂-loaded aqueous solution of alkanolamines accurately, coupled with the fact that the electrolyte-NRTL model cannot be used outside the Aspen Plus software, that motivated the development of a semi-empirical model that can accurately estimate the heat capacity of aqueous solutions of alkanolamines (including blend of two

alkanolamines), both before and after CO₂ absorption. The details of the semi-empirical model are presented in **Chapter 5** of this thesis.

4.6 Heat of Solution (Heat of Absorption)

The heat of solution, which is also known as the *heat of absorption* when referring to gas absorption processes, is essentially the heat effect associated with the dissolution of a unit mole of solute (gas or solid) in a liquid solvent.⁹¹ There are two types of heat of absorption: integral heat of absorption and differential heat of absorption. The integral heat of absorption is the heat effect per mole of gas solute absorbed from an initial gas-free solution to the final gas-loaded solution, while the differential heat of absorption is the heat effect per mole of gas solute absorbed if a very small amount of the gas solute is added into a solution of known concentration.^{98,126,127}

The integral heat of absorption at a given temperature (T) is related to the differential heat of absorption as follows:¹²⁶

$$\Delta H_{\text{int}}(n_i, T) = \frac{1}{n_i} \int_0^{n_i} \Delta H_{\text{diff}}(n_i) dn_i \quad (4.6.1)$$

where

$\Delta H_{\text{int}}(n_i, T)$ is the integral heat of absorption at n_i

$\Delta H_{\text{diff}}(n_i)$ is the differential heat of absorption at n_i

n_i is the loading of the absorbed gas

The differential heat of absorption can be calculated from solubility (VLE) data by application of the Gibbs-Helmholtz (G-H) equation as follows:¹²⁷⁻¹²⁹

$$\Delta H_{\text{diff}} = R \left[\frac{\partial \ln \hat{f}_i}{\partial (1/T)} \right]_{P=\sigma, \{x_0\}} \quad (4.6.2)$$

where the index $P = \sigma$ indicates saturation pressure and the index $\{x_0\}$ indicates constant composition.

For systems operating at low to medium pressure, the fugacity in Eq. (4.6.2) can be replaced with the partial pressure as follows:¹²⁶

$$\Delta H_{diff} = R \left[\frac{\partial \ln P_i}{\partial (1/T)} \right]_{P=\sigma, \{x_0\}} \quad (4.6.3)$$

Mathias and O'Connell¹²⁷ have cautioned against the direct application of Eq. (4.6.2) when estimating differential heat of absorption from VLE data, especially for systems at saturated vapour conditions, because of the inherent assumption of bubble point pressure in the equation. In fact, Mathias and O'Connell¹²⁷ proposed a rigorous equation for all phases at equilibrium as follows:

$$\Delta H_{diff} = R \left[\frac{\partial \ln \hat{f}_i}{\partial (1/T)} \right]_{P=\sigma, \{x_0\}} - \frac{\bar{V}_i}{T} \left[\frac{\partial \ln P}{\partial (1/T)} \right]_{P=\sigma, \{x_0\}} \quad (4.6.4)$$

The heat of absorption can also be calculated from van't Hoff's equation, which is derived from the Gibbs-Helmholtz equation relating changes in enthalpy and Gibbs energy, as follows:^{129,130}

$$\Delta H = RT^2 \left[\frac{d \ln K}{dT} \right]_P \quad (4.6.5)$$

where ΔH is the enthalpy change of the chemical equilibrium reaction.

If there are more than one equilibrium reactions involved in the process, the overall heat of absorption can be calculated as follows:¹²⁹

$$\Delta H_{abs} = \frac{1}{\Delta n_g^{total}} \sum_{i=1}^k \Delta n_i \Delta H_i \quad (4.6.6)$$

where

ΔH_{abs} is the overall heat of absorption per mole of acid gas

ΔH_i is the enthalpy of reaction for reaction i per mole of key component reacted

Δn_i is the change in the number of moles of a key component of chemical reaction i

Δn_g^{total} is the total number of moles of the acid gas absorbed

k is the number of reactions

However, Zhang et al.¹⁰¹ adopted an extended form of Eq. (4.6.6) by including the enthalpy of physical dissolution and excess enthalpy as follows:

$$\Delta H_{abs} = \sum_{i=1}^k \Delta n_i \Delta H_i^o + \Delta H_{dissolution} + \Delta H^{ex} \quad (4.6.7)$$

where

ΔH_i^o is the standard enthalpy of reaction for reaction i per mole of key component reacted

$\Delta H_{dissolution}$ is the enthalpy of physical dissolution of the acid gas

ΔH^{ex} is the excess enthalpy

A third approach for calculating the heat of absorption is based on an internal energy balance or enthalpy balance.^{98,126} Blanchon le Bouhelec et al.¹²⁶ calculated the heat of absorption of acid gases (CO₂ and H₂S) in alkanolamine solutions (MEA, DEA and MDEA solutions) using an internal energy balance for an open system as follows:

$$\Delta H_{abs} = \frac{H_F - H_I - (P_F V_F - P_I V_I) - h_{ag}^V n_{ag}^{total}}{n_{ag}^{total}} \quad (4.6.8)$$

where

H_F is the total molar enthalpy of the final solution

H_I is the total molar enthalpy of the initial solution

h_{ag}^V is the vapour phase molar enthalpy of the acid gas

n_{ag}^{total} is the total acid gas number of moles (ionic and molecular species)

P_F and P_I are, respectively, the final and initial total pressure

V_F and V_I are, respectively, the final and initial total volume

In a similar manner, Zhang and Chen⁹⁸ calculated the heat of absorption of CO₂ in aqueous MDEA solutions from an enthalpy balance of the absorption process as follows:

$$\Delta H_{abs} = \frac{n_{Final} H_{Final}^l - n_{Initial} H_{Initial}^l - n_{CO_2} H_{CO_2}^g}{n_{CO_2}} \quad (4.6.9)$$

where:

- H_{Final}^l is the molar enthalpy of the final solution
- $H_{Initial}^l$ is the molar enthalpy of the initial solution
- $H_{CO_2}^g$ is the molar enthalpy of gaseous CO₂ absorbed
- n_{Final} is the number of moles of the final solution
- $n_{Initial}$ is the number of moles of the initial solution
- n_{CO_2} is the number of moles of CO₂ absorbed

Chapter 5

A Semi-Empirical Model for Estimating the Heat Capacity of Aqueous Solutions of Alkanolamines for CO₂ Capture

5.1 Introduction

The heat capacity of aqueous solutions of alkanolamines, whether as a single amine or as blended amines, is a fundamental requirement for the calculation of the heat duty in condensers, heat exchangers and reboilers. Over the years, experimental heat capacity data has been reported for pure alkanolamines,¹³¹⁻¹³⁷ binary mixtures of water and alkanolamines,^{88,134-136,138-142} binary mixtures of two alkanolamines,^{134,135,142-144} and aqueous solutions of mixed alkanolamines.^{88,134,135,140,142-144} Weiland et al.¹⁴⁰ reported some heat capacity data for CO₂-loaded aqueous solutions of MEA, DEA, MDEA, MEA/MDEA blend, and DEA/MDEA blend, at various concentrations of the alkanolamines and for CO₂ loadings up to 0.64 mol·mol⁻¹, but at a fixed temperature of 298.15 K. Similarly, Hilliard⁸⁸ reported some heat capacity data for CO₂-loaded aqueous solutions of MEA with molal concentrations of 3.5 mol·kg⁻¹ and 7.0 mol·kg⁻¹, and aqueous solutions of PZ with concentrations of 2.0 mol·kg⁻¹ and 3.6 mol·kg⁻¹, for temperatures ranging from 313.15 K to 393.15 K. Hilliard⁸⁸ also reported some heat capacity data for CO₂-loaded aqueous solution blends comprising 2.0 mol·kg⁻¹ of PZ and 3.5 mol·kg⁻¹ of MEA, and for blends comprising 2.0 mol·kg⁻¹ of PZ and 7.0 mol·kg⁻¹ of MEA, over a temperature range from 313.15 K to 393.15 K.

The main aim of this chapter is the development of a model that can be used to accurately estimate the heat capacity of aqueous solutions of alkanolamines (solutions of single amines and blends of two amines) both before and after CO₂ absorption. Also, being a requirement for the actualization of the main aim of this chapter, the heat capacity data for pure MEA, DEA, MDEA, AMP, PZ, and pure H₂O, as well as the heat capacity data for aqueous solutions of the alkanolamines that have been reported in the open literature have been analyzed in this chapter. The analysis of the pure components data was based on the direct comparisons of the data reported by several different authors, while the analysis of both the aqueous and non-aqueous solutions was based on key statistics of the model

predictions against the different sets of experimental data that have been simultaneously used, without any weighting, in the fitting of the model parameters.

The systems, as well as the possible sub-systems that can be derived from them, modelled in this work include PZ-MDEA-H₂O, PZ-AMP-H₂O, MEA-AMP-H₂O, CO₂-MEA-MDEA-H₂O, CO₂-DEA-MDEA-H₂O and CO₂-PZ-MEA-H₂O.

5.2 Modelling

The fundamental thermodynamic equation relating the liquid-phase molar heat capacity of a mixture to the molar heat capacity of the individual components present in the mixture is given by:⁹¹

$$C_P = \sum_i x_i C_{P,i} + C_P^E \quad (5.2.1)$$

where C_P is the molar heat capacity of the mixture, x_i is the mole fraction of species i , $C_{P,i}$ is the molar heat capacity of pure species i , and C_P^E is the excess molar heat capacity of the mixture.

Also, the fundamental equation relating the excess heat capacity of a mixture to the excess enthalpy and excess Gibbs energy of the mixture is given by:⁹¹

$$C_P^E = \left(\frac{\partial H^E}{\partial T} \right)_{P,x} = T \left(\frac{\partial^2 G^E}{\partial T^2} \right)_{P,x} \quad (5.2.2)$$

Furthermore, the excess Gibbs energy is fundamentally related to the mixture composition, the mixture temperature, and the activity coefficients of the components in the mixture as follows:⁹¹

$$G^E = RT \sum_i x_i \ln \gamma_i \quad (5.2.3)$$

Therefore, it follows that before Eqs. (5.2.2) and (5.2.3) can be applied, a model for the excess Gibbs energy or activity coefficient must be available.

Although, over the past decades, rigorous local composition models have been developed for predicting the excess Gibbs energy (and activity coefficient by extension),⁹⁴ the simultaneous regression of the model parameters using both vapour-liquid-equilibrium (VLE) data and enthalpy data and/or heat capacity data imposes great constraints on the model parameters and limits the prediction accuracy of the models, especially the variation of the liquid-phase heat capacity of a mixture with temperature. The direct application of Eqs. (5.2.2) and (5.2.3) is even more complicated when dealing with electrolyte systems, such as CO₂-loaded aqueous solutions of alkanolamines, because of the presence of ions and the highly non-ideal behaviour of electrolyte systems. Therefore, in view of the complications associated with the direct application of Eqs. (5.2.2) and (5.2.3), a different approach is adopted for the modelling work presented in this chapter.

Where “AmH” denotes a primary (or secondary) alkanolamine and “Am” loosely denotes a tertiary alkanolamine, a general model that is capable of representing the molar heat capacity of the binary AmH–Am, AmH–H₂O, Am–H₂O systems, the ternary AmH–Am–H₂O, CO₂–AmH–H₂O, CO₂–Am–H₂O systems, and the quaternary CO₂–AmH–Am–H₂O system may be represented as follows:

$$C_P = \sum_i x_i C_{P,i} + C_P^E \quad (i \neq CO_2) \quad (5.2.4)$$

with the excess heat capacity, C_P^E , expressed as:

$$C_P^E = C_{P,12}^E + C_{P,13}^E + C_{P,23}^E + C_{P,123}^E + C_{P,\alpha}^E \quad (5.2.5)$$

The binary indices “12”, “13” and “23” in Eq. (5.2.5) denote, respectively, the excess heat capacity contribution due to AmH–Am interactions, AmH–H₂O interactions and Am–H₂O interactions, while the ternary index “123” denotes the excess heat capacity contribution due to AmH–Am–H₂O interactions. $C_{P,\alpha}^E$ is the excess heat capacity contribution due to CO₂ absorption.

The application of Eq (5.2.4) depends on the availability of appropriate and accurate models for the heat capacity of pure H₂O and pure alkanolamines. The heat capacity of pure H₂O is assumed to be related to temperature by a third-order polynomial as follows:^{41,102}

$$C_{P,i} / (\text{J mol}^{-1} \text{K}^{-1}) = a_0 + a_1 (T / \text{K}) + a_2 (T / \text{K})^2 + a_3 (T / \text{K})^3 \quad (5.2.6)$$

On the other hand, the heat capacity of the pure alkanolamines is assumed to be a linear function of the temperature.^{132,133} Thus, only the first two terms in Eq (5.2.6) apply to the pure alkanolamines (i.e. a_2 and a_3 are set to zero for the pure alkanolamines).

The excess heat capacity contributions from the binary interactions are modelled using a Redlich-Kister-type equation as follows:^{134,137,141-144}

$$C_{P,ij}^E / (\text{J mol}^{-1} \text{K}^{-1}) = x_i x_j \sum_{\delta=0}^n A_{\delta} (x_i - x_j)^{\delta} \quad (5.2.7)$$

and all the parameters, A_{δ} , in Eq (5.2.7) are assumed to be linearly related to temperature as follows.^{134,141-144}

$$A_{\delta} = A_{\delta,0} + A_{\delta,1} (T / \text{K}) \quad (5.2.8)$$

The excess heat capacity contribution due to the ternary AmH(i)–Am(j)–H₂O(k) interaction is modelled using the following equation:

$$C_{P,ijk}^E / (\text{J mol}^{-1} \text{K}^{-1}) = x_i x_j x_k \sum_{\delta=0}^n B_{\delta} \left(\theta [x_i - x_k] + (1 - \theta) [x_j - x_k] \right)^{\delta} \quad (5.2.9)$$

where θ is a constant parameter whose value is between zero and one, while the B_{δ} parameters are assumed to be linearly related to the temperature as follows:

$$B_{\delta} = B_{\delta,0} + B_{\delta,1} (T / \text{K}) \quad (5.2.10)$$

The excess heat capacity contribution due to CO₂ loading was found to be adequately accounted for by the following equation:

$$C_{P,\alpha}^E / (\text{J mol}^{-1} \text{K}^{-1}) = \alpha^{\{p+q(\tilde{x}_1+\tilde{x}_2)\}} \left[C_0 + C_1 (\tilde{x}_1 + \tilde{x}_2) \right] \quad (5.2.11)$$

where α denotes the CO₂ loading of the solution, which is defined as the mole of CO₂ in the solution per the total mole equivalent of the amine(s) in the solution; \tilde{x}_1 and \tilde{x}_2 are the mole fractions of the amines, AmH and Am, in the unloaded solution; p and q are constant parameters that characterize a given system, while C_0 and C_1 are temperature-dependent parameters assumed to be given by the following equation:

$$C_i = C_{i,0} + C_{i,1} (T / \text{K}) + C_{i,2} \ln (T / \text{K}) \quad (5.2.12)$$

For ease of conversion from molar heat capacity to specific heat capacity, it can be shown that the relationship between the molar heat capacity and the corresponding specific heat capacity is given by the following equation (see **Appendix A** for details):

$$\frac{c_p / (\text{J kg}^{-1} \text{K}^{-1})}{C_p / (\text{J mol}^{-1} \text{K}^{-1})} = \frac{[(1 + z_1\alpha)\tilde{x}_1 + (1 + z_2\alpha)\tilde{x}_2 + \tilde{x}_3] \times 10^3}{[44.009\alpha(z_1\tilde{x}_1 + z_2\tilde{x}_2) + M_{AmH}\tilde{x}_1 + M_{AM}\tilde{x}_2 + 18.015\tilde{x}_3]} \quad (5.2.13)$$

where z_1 is the number of equivalent per mole of the first amine, z_2 is the number of equivalent per mole of the second amine, M_{AmH} is the molar mass of the first amine and M_{AM} is the molar mass of the second amine.

5.3 Data Regression and Parameters Estimation

A progressive approach was adopted for the data regression and parameters estimation. The data regression and parameters estimation started with the pure components before considering the binary systems, the ternary systems, and the systems involving CO₂ loading, in that order. Also, before commencing with the data regression analysis, experimental data of the pure components that have been reported by different authors were compared and any set of data with relatively large deviations from others were excluded from the data used in the regression and parameters estimation. **Table 5.1** summarizes the experimental heat capacity data for pure MEA, DEA, MDEA, AMP, PZ and pure H₂O, while the experimental heat capacity data for the various binary systems and ternary systems are

summarized in **Table 5.2** and **Table 5.3**, respectively. The few available heat capacity data for the CO₂-loaded systems are summarized in **Table 5.4**.

The regression of the pure components parameters was achieved using only a consistent set of data from several different authors. After completing the pure components regression, the pure components parameters were fixed at their regressed values and the parameters for the binary interactions were regressed, one binary system at a time, and the binary interaction parameters were then fixed at their regressed values before proceeding to the regression of the ternary interaction parameters for the ternary systems. Finally, with the ternary interaction parameters fixed at their regressed values, the parameters accounting for CO₂ loading effect were regressed for the systems with available experimental data.

In regressing each of the binary and ternary systems, all the available data sets were included in the regression since most of the data reported by the different authors were at different concentration and/or temperature, except in a few cases which have the same concentration and/or temperature conditions. The binary interaction parameters were regressed using Eqs. (5.2.7) and (5.2.8) after fixing the pure components parameters at their previously regressed values. Similarly, with the parameters of the pure components and the binary interaction parameters fixed at their regressed values, the ternary interaction parameters were regressed using Eqs. (5.2.9) and (5.2.10). Furthermore, with the parameters of the pure components and the binary and ternary interaction parameters fixed at their regressed values, Eqs. (5.2.11) and (5.2.12) were used to regress the parameters accounting for the CO₂ loading effect.

It is important to state that the heat capacity data for the mixtures were regressed directly as against the regression of the excess heat capacity. The reason for regressing the heat capacity data directly is because most authors used different parameter values for the pure components when estimating the excess heat capacity values reported by them, and some authors did not report any data for excess heat capacity. Furthermore, in order to retain the minimum number of digits, and yet maintain accuracy, a sensitivity analysis was performed on the regressed parameters. From the sensitivity analysis performed, all the regressed parameter values have to be approximated to at least 4 d.p.

5.4 Results and Discussion

5.4.1 Pure Components

Figure 5.1 to Figure 5.5 show a direct comparison of the molar heat capacity data reported by different authors for pure MEA, MDEA, DEA, AMP and PZ, respectively, and each of the figures includes the model prediction based on the regression analysis performed. The regressed values of the model parameters are given in **Table 5.5**. The standard error and confidence levels of the regressed values of the model parameters are given in **Table B.1, Appendix B**, while the correlation matrices for the model parameters are given in **Table B.5, Appendix B**.

The heat capacity data reported by Maham et al.¹³² were excluded from the model fitting for pure MEA due to their relatively large deviations from those of Chiu et al.¹³³ and Mundhwa and Henni,¹³⁷ as can be seen in **Figure 5.1**. Similarly, the data reported by Chiu et al.¹³³ were excluded from the model fitting for pure MDEA because of their relatively large deviations from the data reported by other authors as shown in **Figure 5.2**.

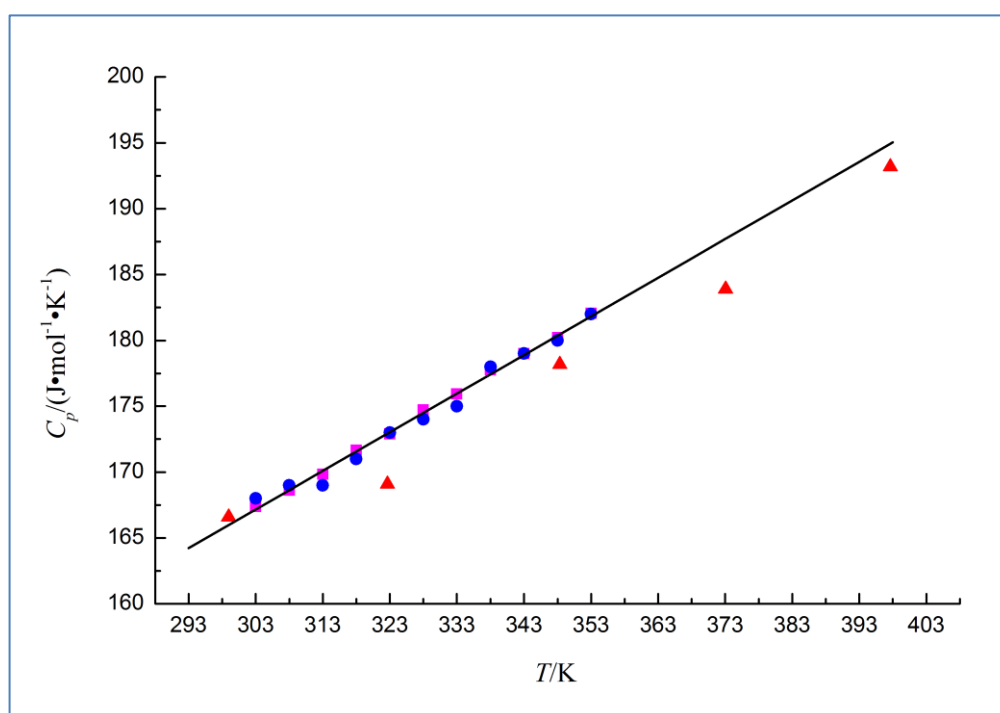


Figure 5.1. Molar heat capacity of pure MEA: ▲, Maham et al.¹³²; ■, Chiu et al.¹³³; ●, Mundhwa and Henni¹³⁷; line, Model prediction. The data reported by Maham et al.¹³² have been excluded from the model fitting.

Table 5.1. Heat Capacity Data used in the Regression of the Parameters for Pure Alkanolamines and Pure Water.

Pure Component	T/K	Data points	Exp. Method ^b (Uncertainty)	References	Comments
MEA	299.10 – 397.80	5	HFC ($\pm 0.9\%$)	Maham et al. ¹³²	Excluded from fitting
	303.15 – 353.15	11	DSC ($\pm 2\%$)	Chiu et al. ¹³³	
	303.15 – 353.15	11	HFC ($\pm 0.23\%$)	Mundhwa and Henni ¹³⁷	
DEA	299.10 – 397.80	5	HFC ($\pm 0.9\%$)	Maham et al. ¹³²	Uncertainty is with respect to Chiu et al. ¹³³
	303.15 – 353.15	11	DSC ($\pm 2\%$)	Chiu et al. ¹³³	
MDEA	299.10 – 397.80	5	HFC ($\pm 0.9\%$)	Maham et al. ¹³²	Excluded from fitting
	303.15 – 353.15	11	DSC ($\pm 2\%$)	Chiu et al. ¹³³	
	303.15 – 353.15	11	DSC ($\pm 2\%$)	Chen et al. ¹³⁴	
	278.15 – 368.15	19	DSC ($\pm 2\%$)	Zhang et al. ¹³⁶	
	303.15 – 353.15	11	HFC ($\pm 0.23\%$)	Mundhwa and Henni ¹³⁷	
AMP	322.8 – 397.80	4	HFC ($\pm 0.9\%$)	Maham et al. ¹³²	Uncertainty is with respect to Chen et al. ¹³⁴
	303.15 – 353.15	11	DSC ($\pm 2\%$)	Chiu et al. ¹³³	
	303.15 – 353.15	11	DSC ($\pm 2\%$)	Chen and Li ¹³⁵	
	303.15 – 368.15	14	DSC ($\pm 2\%$)	Zhang et al. ¹³⁶	
PZ ^a	393.20 – 450	12	DSC ($\pm 1\%$)	Steele et al. ¹³¹	
	393.20 – 413.20	5	DSC ($\pm 2\%$)	Chen et al. ¹⁴²	
H ₂ O	273.15 – 473.15	189	IAPWS ($\pm 0.2\%$)	Wagner and Kretzschmar ¹⁴⁵	0.1 MPa – 2.0 MPa

^aData from Steele et al.¹³¹ were calculated using the equation given by them.

^bHFC stands for Heat Flow Calorimeter; DSC stands for Differential Scanning Calorimeter.

Table 5.2. Heat Capacity Data used in the Regression of the Parameters for the Excess Heat Capacity contribution due to Binary Interactions.

Binary system	T/K	Mole fraction, x_1	Data points	Exp. Method ^c (Uncertainty)	References
MEA (1) – H ₂ O (2)	283.15 – 313.15	0 – 1.0	54	FMC (not reported)	Page et al. ¹³⁹
	298.15	0.0317 – 0.1643	4	HFC ($\pm 1\%$)	Weiland et al. ¹⁴⁰
	303.15 – 353.15	0.2 – 0.8	44	DSC ($\pm 2\%$)	Chiu and Li ¹⁴¹
	313.15 – 393.15	0.0495, 0.1122	34	DSC ($\pm 2\%$)	Hilliard ⁸⁸
DEA (1) – H ₂ O (2)	298.15	0.0187 – 0.1025	4	HFC ($\pm 1\%$)	Weiland et al. ¹⁴⁰
	303.15 – 353.15	0.2 – 0.8	44	DSC ($\pm 2\%$)	Chiu and Li ¹⁴¹
MDEA (1) – H ₂ O (2)	298.15 – 348.15	0.0432 – 0.1313	6	HFC ($\pm 0.85\%$)	Hayden et al. ¹³⁸
	298.15	0.0609 – 0.1849	4	HFC ($\pm 1\%$)	Weiland et al. ¹⁴⁰
	303.15 – 353.15	0.0432 – 0.8	66	DSC ($\pm 2\%$)	Chiu and Li ¹⁴¹
	303.15 – 353.15	0.2 – 0.8	44	DSC ($\pm 2\%$)	Chen et al. ¹³⁴
	278.15 – 368.15	0.03 – 0.9381	228	DSC ($\pm 2\%$)	Zhang et al. ¹³⁶
AMP (1) – H ₂ O (2)	303.15 – 353.15	0.2 – 0.8	44	DSC ($\pm 2\%$)	Chiu and Li ¹⁴¹
	303.15 – 353.15	0.2 – 0.8	44	DSC ($\pm 2\%$)	Chen and Li ¹³⁵
	278.15 – 368.15	0.06209 – 0.9024	200	DSC ($\pm 2\%$)	Zhang et al. ¹³⁶
PZ (1) – H ₂ O (2)	313.15 – 393.15	0.0348, 0.0609	34	DSC ($\pm 2\%$)	Hilliard ⁸⁸
	303.20 – 353.20	0.05 – 0.2	44	DSC ($\pm 2\%$)	Chen et al. ¹⁴²
MEA (1) – MDEA (2)	303.15 – 353.15	0.2 – 0.8	44	DSC ($\pm 2\%$)	Chen et al. ¹³⁴
DEA (1) – MDEA (2)	303.20 – 353.20	0.1 – 0.9	99	DSC ($\pm 15 \text{ J}\cdot\text{kg}^{-1}\cdot\text{K}^{-1}$)	Shih et al. ¹⁴³
PZ (1) – MDEA (2)	303.20 – 353.20	0.1 – 0.4	44	DSC ($\pm 2\%$)	Chen et al. ¹⁴²
MEA (1) – AMP (2)	303.15 – 353.15	0.2 – 0.8	44	DSC ($\pm 2\%$)	Chen and Li ¹³⁵
PZ (1) – AMP (2)	303.20 – 353.20	0.05 – 0.2	44	DSC ($\pm 2\%$)	Chen et al. ¹⁴⁴

^cFMC stands for Flow Micro-calorimeter.

Table 5.3. Heat Capacity Data used in the Regression of the Parameters for the Excess Heat Capacity contribution due to Ternary Interactions.

Ternary system	T/K	H ₂ O mole fraction, x_3	Data points	Exp. Method (Uncertainty)	Reference
MEA (1) – MDEA (2) – H ₂ O (3)	298.15	0.8273 – 0.8579	3	HFC ($\pm 1\%$)	Weiland et al. ¹⁴⁰
	303.15 – 353.15	0.2 – 0.8	176	DSC ($\pm 2\%$)	Chen et al. ¹³⁴
DEA (1) – MDEA (2) – H ₂ O (3)	298.15	0.8626 – 0.8672	3	HFC ($\pm 1\%$)	Weiland et al. ¹⁴⁰
	303.20 – 353.20	0.2 – 0.8	176	DSC ($\pm 15 \text{ J}\cdot\text{kg}^{-1}\cdot\text{K}^{-1}$)	Shih et al. ¹⁴³
PZ (1) – MDEA (2) – H ₂ O (3)	303.20 – 353.20	0.6 – 0.9	165	DSC ($\pm 2\%$)	Chen et al. ¹⁴²
MEA (1) – AMP (2) – H ₂ O (3)	303.15 – 353.15	0.2 – 0.8	176	DSC ($\pm 2\%$)	Chen and Li ¹³⁵
PZ (1) – AMP (2) – H ₂ O (3)	303.20 – 353.20	0.6 – 0.9	154	DSC ($\pm 2\%$)	Chen et al. ¹⁴⁴
PZ (1) – MEA (2) – H ₂ O (3)	313.15 – 393.15	0.8605, 0.9098	34	DSC ($\pm 2\%$)	Hilliard ⁸⁸

Table 5.4. Heat Capacity Data used in the Regression of the Parameters for the Excess Heat Capacity contribution due to CO₂ Loading Effect.

CO ₂ -loaded System	T/K	CO ₂ loading (mol·mol ⁻¹)	Data points	Exp. Method (Uncertainty)	Reference
CO ₂ – MEA – H ₂ O	298.15	0.05 – 0.5	20	HFC (±1%)	Weiland et al. ¹⁴⁰
	313.15 – 393.15	0.097 – 0.583	102	DSC (±2%)	Hilliard ⁸⁸
CO ₂ – DEA – H ₂ O	298.15	0.05 – 0.5	35	HFC (±1%)	Weiland et al. ¹⁴⁰
CO ₂ – MDEA – H ₂ O	298.15	0.05 – 0.64	35	HFC (±1%)	Weiland et al. ¹⁴⁰
CO ₂ – PZ – H ₂ O	313.15 – 393.15	0.157 – 0.401	85	DSC (±2%)	Hilliard ⁸⁸
CO ₂ – MEA – MDEA – H ₂ O	298.15	0.1 – 0.5	15	HFC (±1%)	Weiland et al. ¹⁴⁰
CO ₂ – DEA – MDEA – H ₂ O	298.15	0.1 – 0.5	15	HFC (±1%)	Weiland et al. ¹⁴⁰
CO ₂ – PZ – MEA – H ₂ O	313.15 – 393.15	0.098 – 0.432	102	DSC (±2%)	Hilliard ⁸⁸

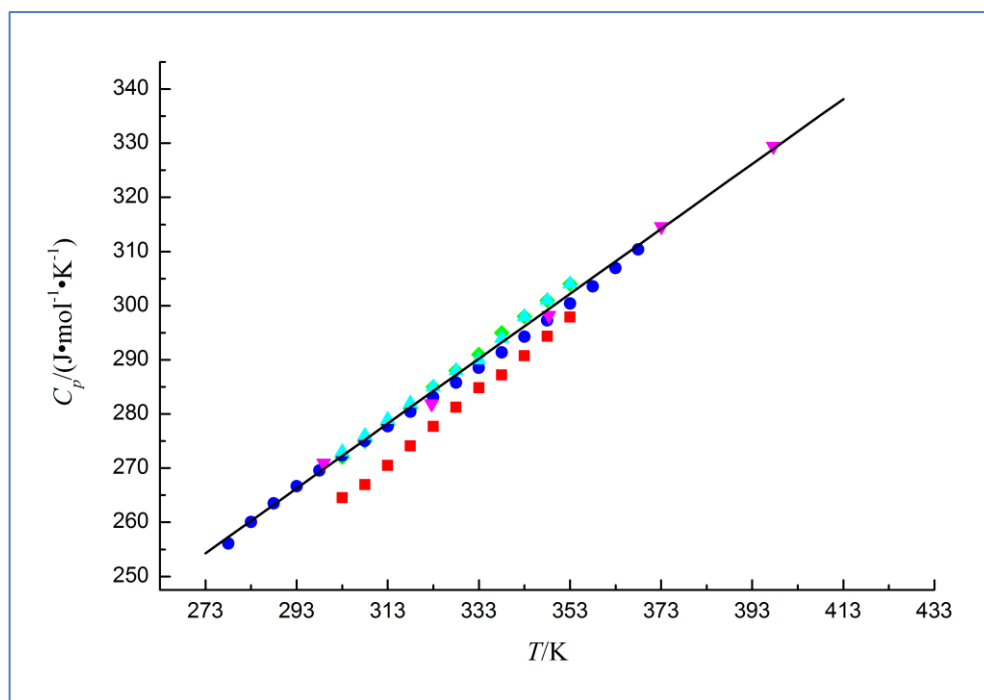


Figure 5.2. Molar heat capacity of pure MDEA: \blacktriangledown , Maham et al.¹³²; \blacksquare , Chiu et al.¹³³; \blacklozenge , Chen et al.¹³⁴; \bullet , Zhang et al.¹³⁶; \blacktriangle , Mundhwa and Henni¹³⁷; line, Model prediction. The data reported by Chiu et al.¹³³ have been excluded from the model fitting.

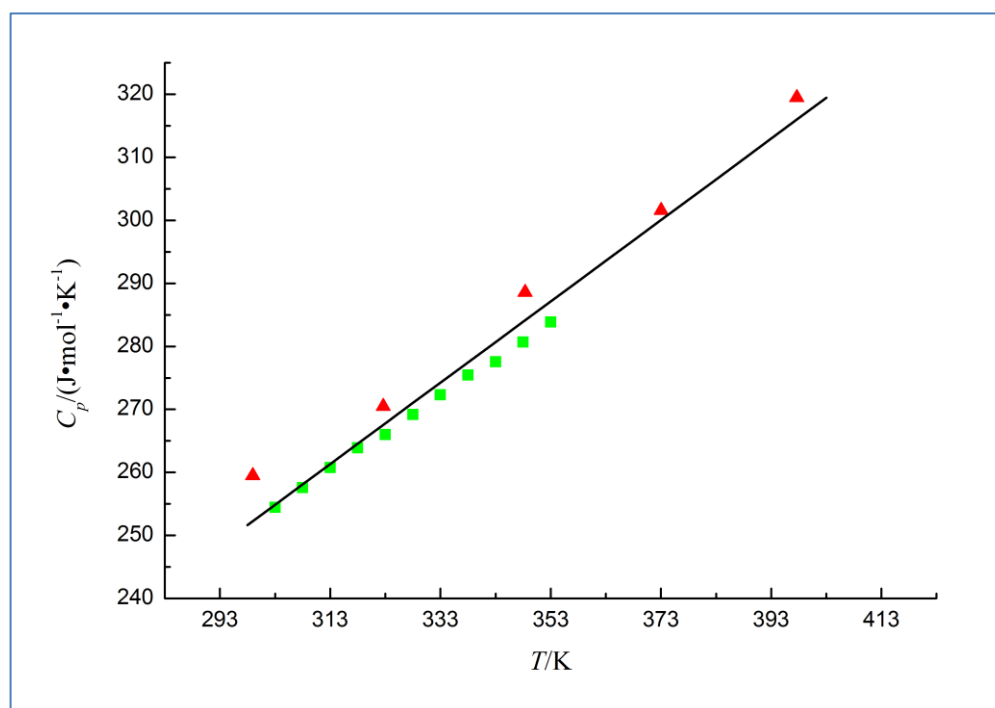


Figure 5.3. Molar heat capacity of pure DEA: \blacktriangle , Maham et al.¹³²; \blacksquare , Chiu et al.¹³³; line, Model prediction.

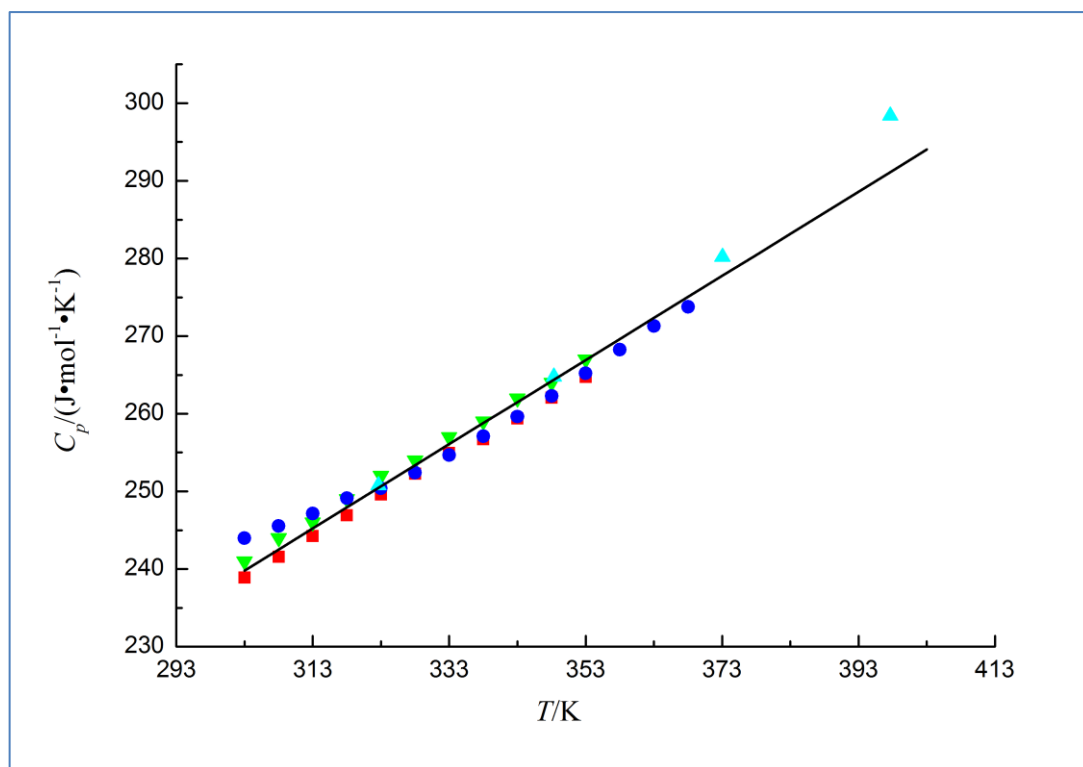


Figure 5.4. Molar heat capacity of pure AMP: ▲, Maham et al.¹³²; ■, Chiu et al.¹³³; ▼, Chen and Li¹³⁵; ●, Zhang et al.¹³⁶; line, Model prediction.

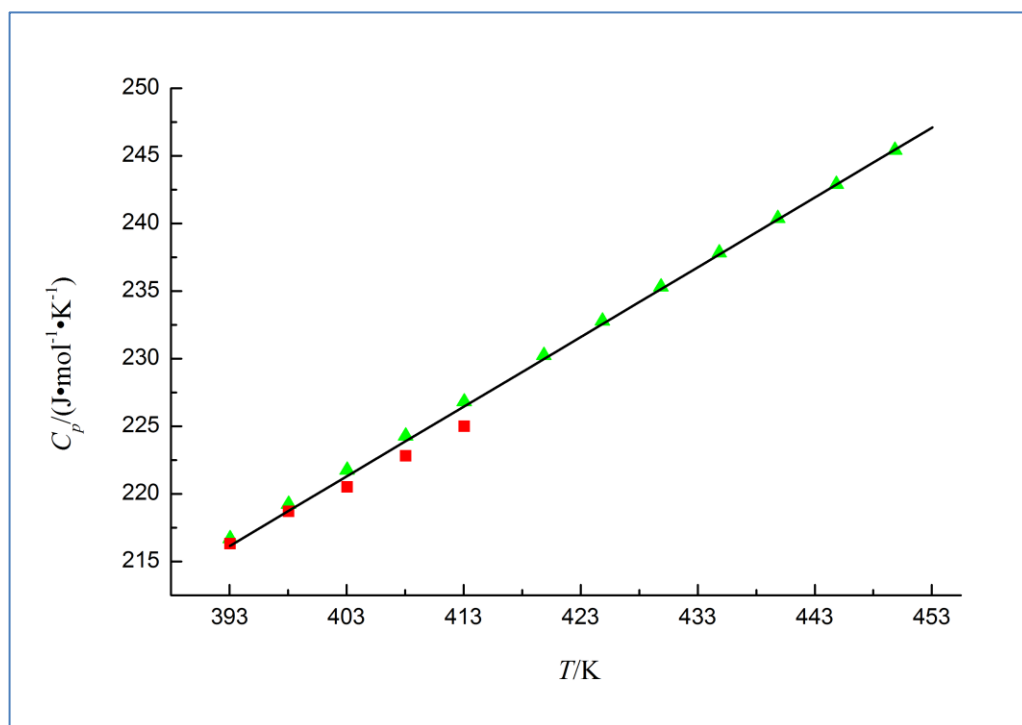


Figure 5.5. Molar heat capacity of Pure PZ: ▲, Steele et al.¹³¹; ■, Chen et al.¹⁴²; line, Model prediction.

Table 5.5. Parameters for the Heat Capacity of Pure Water and Pure Alkanolamines based on Eq. (5.2.6).

	a_0	a_1	$a_2 \times 10^4$	$a_3 \times 10^8$
H ₂ O	96.3170	-1241	1.5981	6.9827
MEA	78.2498	0.293		
DEA	59.238	0.6454		
MDEA	90.6224	0.5991		
AMP	75.4034	0.5423		
PZ	13.3859	0.5157		

Although the heat capacity data for pure DEA reported by Maham et al.¹³² are slightly higher than those reported by Chiu et al.,¹³³ as shown in **Figure 5.3**, both data sets have been used in the model fitting for pure DEA since it is difficult to distinguish which of the two data sets is more accurate considering the fact that the data reported by Maham et al.¹³² for pure MEA appear to be in error, while the data reported by Chiu et al.¹³³ for pure MDEA also appear to be in error.

All the available heat capacity data for pure AMP have been used in the model fitting for pure AMP, although the data reported by Maham et al.¹³² appear to be in error at temperatures higher than about 373.15 K when compared with those obtained by other authors as shown in **Figure 5.4**. As for the case of DEA, the heat capacity data for pure PZ reported by Steele et al.¹³¹ and Chen et al.¹⁴² were both used in the model fitting of pure PZ and **Figure 5.5** shows a comparison of the model prediction against the data reported by Steele et al.¹³¹ and Chen et al.¹⁴²

A third-order polynomial of the temperature was used to model the heat capacity of pure water. **Figure 5.6** shows the uncertainties of the pure H₂O model predictions against the data from the International Association for the Properties of Water and Steam (IAPWS),¹⁴⁵ as well as the data from the National Institute of Standards and Technology (NIST).¹⁴⁶

It is clear from **Figure 5.6** that the pure H₂O model in this chapter accurately predicts the heat capacity of pure H₂O, within an uncertainty of $\pm 0.2\%$ reported by the IAPWS, up to a temperature of about 473 K (corresponding to a saturation temperature of approximately 1.5 MPa), which is far above the operating temperature of amine-based CO₂ capture processes. It is

important to add that the model for pure H₂O, a third-order polynomial of the temperature, was fitted to the IAPWS data only since the IAPWS is generally considered as the most accurate source of data for pure H₂O properties.

Overall, a simple linear function of temperature was more than adequate in representing the heat capacity of the pure alkanolamines, while a third-order polynomial of the temperature was able to accurately predict the heat capacity of pure water. Furthermore, from the pure components parameters values, it appears that the functional dependence of the heat capacity of the pure alkanolamines on the temperature increases with molecular weight.

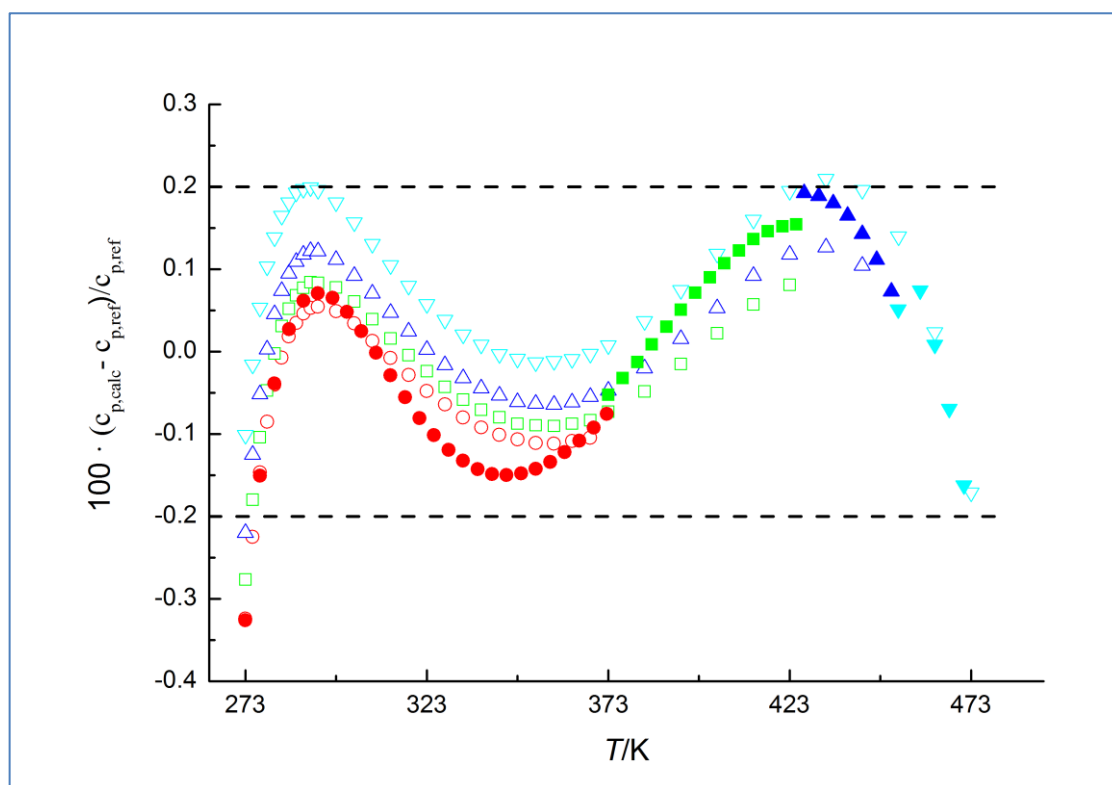


Figure 5.6. Percentage uncertainties of the model predictions of the heat capacity of pure H₂O against the pure H₂O heat capacity data from the International Association for the Properties of Water and Steam (IAPWS)¹⁴⁵ and the National Institute of Standards and Technology (NIST) database.¹⁴⁶
 ○, IAPWS at 0.1 MPa; □, IAPWS at 0.5 MPa; △, IAPWS at 1.0 MPa; ▽, IAPWS at 2.0 MPa; ●, NIST at 0.1 MPa; ■, NIST at 0.5 MPa; ▲, NIST at 1.0 MPa; ▼, NIST at 2.0 MPa.

5.4.2 Binary Systems

In this chapter, a total of ten binary systems, comprising five systems of aqueous mixtures of water and alkanolamines and five systems of non-aqueous mixtures of two alkanolamines, have been modelled. The parameters accounting for the binary interactions are given in **Table 5.6**, while **Table 5.7** summarizes the key statistics, the maximum absolute percent deviation (MAD) and the average absolute percent deviation (AAD), of the heat capacity model predictions against the experimental data set used in the model fitting. It is important to note that no generalization can be made with respect to the behavior of the excess heat capacity of the alkanolamine/water binary systems because the set of parameters accounting for the excess heat capacity vary from one system to another. In order to give a sense of the under-prediction or over-prediction of each data set by the models, the residual's average (RA) and residual's standard deviation (RSD) have been included in **Table 5.7**. The standard error and confidence levels of the regressed values of the parameters, and the correlation matrices for the model parameters are given in **Table B.2** and **Table B.6** in **Appendix B**, respectively.

Table 5.6. Parameters for the Excess Heat Capacity contribution due to Binary Interactions based on Eqs. (5.2.7) and (5.2.8).

	$A_{0,0}$	$A_{0,1}$	$A_{1,0}$	$A_{1,1}$	$A_{2,0}$	$A_{2,1}$
MEA-H ₂ O	-112.4265	0.3962	199.2343	-0.5955	424.5643	-1.3143
DEA-H ₂ O	-123.5135	0.4463	73.5547	-0.2430	169.9517	-0.5052
MDEA-H ₂ O	-159.5189	0.5951	72.9519	-0.3235		
AMP-H ₂ O	-89.8771	0.3741	-61.1080	0.1115		
PZ-H ₂ O	-901.8356	3.1638	-1092.1672	3.6316		
MEA-MDEA	-43.4098	0.0368	33.8159	-0.1303		
DEA-MDEA	-100.5740	0.2348	114.2166	-0.3880		
PZ-MDEA	-83.0434	0.4019	-182.1514	0.6263	-458.8218	1.4792
MEA-AMP	62.5100	-0.1998	-33.8900	0.1015		
PZ-AMP	-165.4484	0.5479	-254.0804	0.7130		

Table 5.7. Statistics of the Heat Capacity Model Predictions for the Binary Systems against the Experimental Data used in the Fitting.

Data source(s)	Data points	C_p (J·mol ⁻¹ ·K ⁻¹)	Av. C_p (J·mol ⁻¹ ·K ⁻¹)	MAD ^d (%)	AAD ^e (%)	RA (J·mol ⁻¹ ·K ⁻¹)	RSD (J·mol ⁻¹ ·K ⁻¹)
<u>MEA(1)–H₂O(2)</u>							
Page et al. ¹³⁹	54	75.28 – 180.79	110.87	5.96	1.31	1.58	2.78
Weiland et al. ¹⁴⁰	4	78.71 – 91.18	84.31	1.15	0.44	-0.23	0.54
Chiu and Li ¹⁴¹	44	93.8 – 128	127.56	2.87	0.76	-0.63	1.33
Hilliard ⁸⁸	34	78.69 – 90.80	84.44	2.81	0.92	-0.53	0.84
Overall	136	75.28 – 180.79	108.88	5.96	1.01	0.29	2.21
<u>DEA(1)–H₂O(2)</u>							
Weiland et al. ¹⁴⁰	4	79.49 – 85.56	87.68	1.86	1.05	0.93	0.56
Chiu and Li ¹⁴¹	44	113 – 249	177.86	0.98	0.17	-0.04	0.38
Overall	48	79.49 – 249	170.35	1.86	0.24	0.04	0.48
<u>MDEA(1)–H₂O(2)</u>							
Hayden et al. ¹³⁸	6	83.61 – 110.39	96.08	4.38	2.48	-1.99	1.65
Weiland et al. ¹⁴⁰	4	91.53 – 116.52	103.12	2.37	1.50	1.49	0.76
Chiu and Li ¹⁴¹	66	85.2 – 261	157.68	1.74	0.74	-0.82	1.03
Chen et al. ¹³⁴	44	117 – 258	183.80	3.41	2.64	-4.63	0.99
Zhang et al. ¹³⁶	228	83.08 – 298.79	177.94	2.51	1.04	1.54	0.81
Overall	348	83.08 – 298.79	172.57	4.38	1.22	0.25	2.29
<u>AMP(1)–H₂O(2)</u>							

Chiu and Li ¹⁴¹	44	113 – 236	171.52	1.82	0.97	0.60	1.76
Chen and Li ¹³⁵	44	112 – 236	171.11	2.99	1.24	0.19	2.14
Zhang et al. ¹³⁶	200	90.39 – 258.97	157.60	5.12	1.27	0.34	1.99
Overall	288	90.39 – 258.97	161.79	5.12	1.22	0.36	1.98
<u>PZ(1)–H₂O(2)</u>							
Hilliard ⁸⁸	34	78.84 – 86.34	82.67	2.31	1.35	-0.84	0.89
Chen et al. ¹⁴²	44	82.5 – 115.3	96.75	2.54	0.83	0.55	0.87
Overall	78	78.8396 – 115.3	90.61	2.54	1.06	-0.05	1.11
<u>MEA(1)–MDEA(2)</u>							
Chen et al. ¹³⁴	44	182 – 274	224.55	0.35	0.13	-0.03	0.34
<u>DEA(1)–MDEA(2)</u>							
Shih et al. ¹⁴³	99	252 – 302	274.70	0.82	0.22	-0.15	0.77
<u>PZ(1)–MDEA(2)</u>							
Chen et al. ¹⁴²	44	240.1 – 297.7	268.95	0.03	0.01	0.00	0.04
<u>MEA(1)–AMP(2)</u>							
Chen and Li ¹³⁵	44	182 – 248	213.22	0.27	0.11	0.0211	0.2932
<u>PZ(1)–AMP(2)</u>							
Chen et al. ¹⁴⁴	44	229.7 – 264.7	247.59	0.39	0.07	0.0201	0.2281

^dMaximum absolute percent deviation, $Maximum \left[\left(\left| C_{p, calc} - C_{p, expt} \right| / C_{p, expt} \right) \times 100 \right]$

^eAverage absolute percent deviation, $\left[\sum_n \left(\left| C_{p, calc} - C_{p, expt} \right| / C_{p, expt} \right) / n \right] \times 100$

5.4.2.1 MEA-H₂O System

The experimental heat capacity data reported by Weiland et al.¹⁴⁰ for an aqueous solution of MEA gave the lowest values for both the MAD and AAD, while the data reported by Page et al.¹³⁹ gave the highest values for both the MAD and AAD. The MAD for the data reported by Chiu and Li¹⁴¹ is slightly higher than the MAD for the data reported by Hilliard,⁸⁸ while the AAD for the data reported by Chiu and Li¹⁴¹ is a little lower than the AAD for the data reported by Hilliard.⁸⁸ Thus, it is difficult to confirm which of the two data sets is more accurate since Chiu and Li¹⁴¹ reported ten more data points than Hilliard,⁸⁸ which might have manifested in the lower AAD. Also, approximately 0.76% AAD obtained in this work for the data of Chiu and Li¹⁴¹ is higher than the 0.2% AAD reported in their work. The slight difference is reasonable since Chiu and Li¹⁴¹ only used the data they generated for pure MEA and MEA-H₂O mixture in their regression.

Overall, with all the data sets taken together, the AAD obtained in this chapter is approximately 1.0% and hence the values of the parameters are sufficiently accurate in predicting the experimental data reported by the different authors.

5.4.2.2 DEA-H₂O System

In contrast to the results obtained for the MEA-H₂O system, the experimental heat capacity data reported by Chiu and Li¹⁴¹ for the DEA-H₂O system gave lower values for both the MAD and AAD than the data reported by Weiland et al.¹⁴⁰ Since the AAD for the data reported by Weiland et al.¹⁴⁰ is higher than the MAD for the data reported by Chiu and Li,¹⁴¹ it is reasonable to assume that the data reported by Chiu and Li¹⁴¹ are more accurate than those reported by Weiland et al.¹⁴⁰ Also, approximately 0.17% AAD obtained in this work for the data of Chiu and Li¹⁴¹ is higher than the 0.07% AAD reported in their work. The reason for the difference can be attributed to the inclusion of the data reported by Maham et al.¹³² in the fitting of the parameters for pure DEA as well as the inclusion of the data reported by Weiland et al.¹⁴⁰ in the fitting of the parameters for the DEA-H₂O mixture.

5.4.2.3 MDEA-H₂O System

The experimental heat capacity data reported by Chiu and Li¹⁴¹ for the MDEA-H₂O system gave the lowest values for both the MAD and AAD, while the data reported by Hayden et al.¹³⁸ and Chen et al.¹³⁴ gave the highest values for MAD and AAD, respectively. Also, although the MAD for the data reported by Zhang et al.¹³⁶ is slightly higher than the MAD for the data reported by Weiland et al.,¹⁴⁰ the AAD for the data reported by Zhang et al.¹³⁶ is only higher than that of Chiu and Li.¹⁴¹ Thus, it is difficult to establish if the data reported by Zhang et al.¹³⁶ is more accurate than the data reported by Weiland et al.¹⁴⁰ since Zhang et al.¹³⁶ reported 224 more data points than Weiland et al.,¹⁴⁰ and this may have manifested in the lower AAD obtained for their data.

A comparison of the model predictions against the experimental data reported by Chiu and Li¹⁴¹ and Chen et al.¹³⁴ is fascinating and revealing since both data sets were generated using the same equipment and experimental procedures. Chen et al.¹³⁴ reported higher values for the heat capacity of pure MDEA than did Chiu and Li¹⁴¹ on the basis of using purer MDEA in their experiment. However, contrary to expectation, they also reported lower values for the heat capacity of MDEA-H₂O mixtures under the same conditions of concentration and temperature used by Chiu and Li.¹⁴¹ Since the MAD and AAD for the data reported by Chiu and Li¹⁴¹ is lower than those of Chen et al.,¹³⁴ and considering the fact that five different data sets were used together in the regression of the model parameters without any weightings, it is probable that the data reported by Chiu and Li¹⁴¹ is more accurate than that of Chen et al.¹³⁴

5.4.2.4 AMP-H₂O System

The experimental heat capacity data reported by Zhang et al.¹³⁶ for the AMP-H₂O system gave the highest values for both the MAD and AAD, while the data reported by Chiu and Li¹⁴¹ gave the lowest values for both the MAD and AAD. Also, as for the case of MDEA-H₂O, and contrary to expectation, Chen and Li¹³⁵ reported slightly lower values for some data points under the same conditions of concentration and temperature used by Chiu and Li.¹⁴¹ However, from the range and mean value of the data reported by them, it is clear that the data reported by Chen and Li¹³⁵ are in general agreement with those of Chiu and Li.¹⁴¹ Overall, since the MAD and AAD for the three data

sets follow the same trend, it may be assumed that the order of accuracy for the data sets is Chiu and Li¹⁴¹ > Chen and Li¹³⁵ > Zhang et al.¹³⁶

5.4.2.5 PZ-H₂O System

The MAD for the heat capacity data reported by Hilliard⁸⁸ for the PZ-H₂O system is slightly lower than the MAD for the data reported by Chen et al.¹⁴² On the other hand, the AAD for the data reported by Chen et al.¹⁴² is lower than the AAD for the data reported by Hilliard.⁸⁸ It is difficult to say which of the two data sets is more accurate since Chen et al.¹⁴² reported 10 more data points than Hilliard,⁸⁸ which may have manifested itself in the lower AAD obtained for the data reported by Chen et al.¹⁴² Approximately 0.83% AAD obtained in this work for the data reported by Chen et al.¹⁴² is higher than the 0.3% AAD reported in their work. The reason for the difference can be attributed to the inclusion of the data reported by Steele et al.¹³¹ in the fitting of the parameters for pure PZ, as well as the inclusion of the data reported by Hilliard⁸⁸ in the fitting of the parameters for the PZ-H₂O mixture.

5.4.2.6 Non-aqueous Binary Systems

The AAD obtained in this work for the heat capacity data reported by Chen et al.¹³⁴ for the MEA-MDEA binary system is approximately 0.13%, which is close to the 0.1% value that they obtained. The MAD obtained in this work for the MEA-MDEA binary is approximately 0.35%. Similarly, the AAD obtained in this work for the heat capacity data reported by Shih et al.¹⁴³ for the DEA-MDEA binary system is approximately 0.22%, which is slightly higher than the 0.1% value that they obtained, and the MAD obtained in this work is approximately 0.82%. Furthermore, the AAD obtained in this work for the heat capacity data reported by Chen et al.¹⁴² for the PZ-MDEA binary system is approximately 0.01%, which is smaller than the 0.1% value that they obtained. In fact, the MAD obtained in this work for the PZ-MDEA binary system, which is approximately 0.03%, is smaller than the 0.1% AAD obtained by Chen et al.¹⁴²

For the MEA-AMP binary system, the AAD obtained in this work for the heat capacity data reported by Chen and Li¹³⁵ is approximately 0.11%, which is approximately the same as the 0.1% value that they obtained. Also, the MAD obtained in this work for the MEA-AMP binary system is approximately

0.27%. Similarly, for the PZ-AMP binary system, the AAD obtained in this work for the heat capacity data reported by Chen et al.¹⁴⁴ is approximately 0.07%, which is smaller than the 0.1% value that they obtained. Also, the MAD obtained in this work for the MEA-AMP is approximately 0.39%.

5.4.3 Ternary Systems (without CO₂ Loading)

Six ternary systems, without CO₂ loading, have been modelled in this chapter. The parameters accounting for ternary interactions are given in **Table 5.8**, while **Table 5.9** summarizes the key statistics of the heat capacity model predictions against the experimental data set used in the model fitting. As for the binary systems, no generalization can be made with respect to the behavior of the excess heat capacity of the ternary systems because the set of parameters accounting for the excess heat capacity vary from one system to another. In order to give a sense of the under-prediction or over-prediction of each data set by the models, the residual's average (RA) and residual's standard deviation (RSD) have been included in **Table 5.9**. The standard error and confidence levels of the regressed values of the model parameters, and the correlation matrices for the model parameters are given in **Table B.3** and **Table B.7** in **Appendix B**, respectively.

Based on the key statistics of the model predictions, it appears that the heat capacity data reported by Weiland et al.¹⁴⁰ for MEA-MDEA-H₂O and DEA-MDEA-H₂O ternary systems are likely to be less accurate than the data reported by Chen et al.¹³⁴ for the MEA-MDEA-H₂O system and Shih et al.¹⁴³ for the DEA-MDEA-H₂O system. However, the relatively large number of data points reported by Chen et al.¹³⁴ and Shih et al.¹⁴³ may have manifested in the lower values of MAD and AAD obtained for their data. Also, approximately 0.45% AAD obtained for the MEA-MDEA-H₂O system in this work is slightly smaller than the 0.5% obtained by Chen et al.¹³⁴ On the other hand, approximately 0.67% AAD obtained for the DEA-MDEA-H₂O system is higher than the 0.2% AAD obtained by Shih et al.¹⁴³ The reason for the difference between the AAD obtained in this work and the AAD obtained by Shih et al.¹⁴³ for the DEA-MDEA-H₂O system can be attributed to the inclusion of the data reported by Maham et al.¹³² in the fitting of the parameters for pure DEA as well as the inclusion of the data reported by Weiland et al.¹⁴⁰ in the fitting of the parameters for the DEA-H₂O mixture.

The approximately 0.9% AAD obtained in this work for the ternary PZ-MDEA-H₂O system is three times the 0.3% AAD obtained by Chen et al.¹⁴² and the reason for the difference can be attributed to the inclusion of the data reported by Steele et al.¹³¹ in the fitting of the parameters for pure PZ as well as the inclusion of the data reported by Hilliard⁸⁸ in the fitting of the parameters for the PZ-H₂O mixture. Also, the same reason is likely to be responsible for approximately 0.74% AAD in this work and the 0.1% AAD obtained by Chen et al.¹⁴⁴ for the ternary PZ-AMP-H₂O system. Similarly, the difference between approximately 0.56% AAD obtained in this work and the 0.2% AAD obtained by Chen and Li¹³⁵ for the MEA-AMP-H₂O system can be attributed to the fact that Chen and Li¹³⁵ used the parameters obtained by Chiu and Li¹⁴¹ for the MEA-H₂O subsystem.

The approximately 0.90% MAD and 0.2% AAD obtained in this work for the PZ-MEA-H₂O ternary system are far lower than the 3.93% MAD and 2.84% MAD obtained by Hilliard.⁸⁸ Since Hilliard⁸⁸ simultaneously regressed the vapour-liquid-equilibrium (VLE) data and the heat capacity data for PZ-MEA-H₂O ternary system, it gives credence to the statement made earlier with respect to accuracy when VLE and heat capacity data are regressed together simultaneously.

Overall, the model developed in this chapter accurately predicts the experimental data reported by the various authors for the six ternary systems.

Table 5.8. Parameters for the Excess Heat Capacity contribution due to Ternary Interactions based on Eqs. (5.2.9) and (5.2.10).

	θ^e	$B_{0,0}$	$B_{0,1}$	$B_{1,0}$	$B_{1,1}$	$B_{2,0}$	$B_{2,1}$
MEA–MDEA–H ₂ O	0.5		-0.3430				-0.5646
DEA–MDEA–H ₂ O	0.5		-0.2322		0.2792		-0.9997
PZ–MDEA–H ₂ O	0.5		1.8657		9.7302		9.0556
MEA–AMP–H ₂ O	0.5		-0.2786		0.1100		
PZ–AMP–H ₂ O	0.5		-1.7060				-0.5940
PZ–MEA–H ₂ O ^d	0.5	35422.4165	-182.6914	48133.6931	-234.5192		

^dParameters for PZ–MEA interaction were set to zero due to non-availability of binary PZ–MEA data.

^eThe value of θ was fixed at 0.5 for all the ternary systems.

Table 5.9. Statistics of the Heat Capacity Model Predictions for the Ternary Systems against the Experimental Data used in the Fitting.

Data source(s)	Data points	C_p (J·mol ⁻¹ ·K ⁻¹)	Av. C_p (J·mol ⁻¹ ·K ⁻¹)	MAD (%)	AAD (%)	RA (J·mol ⁻¹ ·K ⁻¹)	RSD (J·mol ⁻¹ ·K ⁻¹)
<u>MEA(1)–MDEA(2)–H₂O(3)</u>							
Weiland et al. ¹⁴⁰	3	102.69 – 106.36	104.12	2.76	2.16	2.25	0.93
Chen et al. ¹³⁴	176	98.1 – 237	154.30	2.062	0.45	-0.12	0.79
Overall	179	98.1 – 273	153.46	2.76	0.48	-0.08	0.85
<u>DEA(1)–MDEA(2)–H₂O(3)</u>							
Weiland et al. ¹⁴⁰	3	105.98 – 106.57	106.30	2.76	2.48	2.63	0.44
Shih et al. ¹⁴³	176	114 – 255	180.24	1.93	0.67	-0.14	1.47
Overall	179	105.98 – 255	180.00	2.76	0.70	-0.10	1.50
<u>PZ(1)–MDEA(2)–H₂O(3)</u>							
Chen et al. ¹⁴²	165	91.4 – 170.8	124.82	3.55	0.90	-0.15	1.49
<u>MEA(1)–AMP(2)–H₂O(3)</u>							
Chen and Li ¹³⁵	176	97.1 – 219	147.76	1.77	0.56	-0.12	0.97
<u>PZ(1)–AMP(2)–H₂O(3)</u>							
Chen et al. ¹⁴⁴	154	90.4 – 153.8	116.86	3.18	0.74	-0.08	1.18
<u>PZ(1)–MEA(2)–H₂O(3)</u>							
Hilliard ⁸⁸	34	85.00 – 92.20	89.03	0.90	0.20	0.00	0.24

5.4.4 CO₂-Loaded Systems

Seven different CO₂-loaded aqueous systems of alkanolamines, comprising of four systems of single amines and three systems of mixed amines and for which limited data have been reported in the open literature, are modelled. The absorption of CO₂ generally leads to a decrease in the heat capacity of the aqueous systems. The parameters that account for the CO₂ loading effect in the CO₂-loaded systems modelled are summarized in **Table 5.10**. Also, from the values of the parameters in **Table 5.10**, it is clear that the set of parameters accounting for the CO₂ loading effect do vary from one system to another. The key statistics of the heat capacity model predictions against the experimental data set used in the model fitting are given in **Table 5.11**. In order to give a sense of the under-prediction or over-prediction of each data set by the models in this chapter, the residual's average (RA) and residual's standard deviation (RSD) have been included in **Table 5.11**. The standard error and confidence levels of the regressed values of the model parameters, and the correlation matrices for the model parameters are given in **Table B.4** and **Table B.8** in **Appendix B**, respectively.

5.4.4.1 CO₂-MEA-H₂O System

The effect of CO₂ loading on the heat capacity of an aqueous solution of MEA is shown in **Figure 5.7** to **Figure 5.9**. The data points in **Figure 5.7** are the experimental data reported by Weiland et al.¹⁴⁰ for four different concentrations of MEA but at a fixed temperature of 298.15 K, while the lines are the predictions of the model. Also, the data points in **Figure 5.8** and **Figure 5.9** are the experimental data reported by Hilliard⁸⁸ for 3.5 mol·kg⁻¹ and 7.0 mol·kg⁻¹ aqueous solutions of MEA, respectively, while the lines in the figures are the predictions of the model. It is important to add that the data reported by Weiland et al.¹⁴⁰ and Hilliard⁸⁸ have been used simultaneously in the regression of the model parameters.

The MAD and AAD obtained in this work for the data reported by Weiland et al.¹⁴⁰ are 2.67% and 0.66%, respectively. Similarly, the MAD and AAD for the data reported by Hilliard⁸⁸ are 2.10% and 0.60%, respectively, and the 0.60% AAD obtained in this work is lower than the 0.79% AAD value obtained by Hilliard.⁸⁸

Table 5.10. Parameters for the Excess Heat Capacity contribution due to CO₂ Loading Effect based on Eqs. (5.2.11) and (5.2.12).

	p	q	$C_{0,0}$	$C_{0,1}$	$C_{0,2}$	$C_{1,0}$	$C_{1,1}$	$C_{1,2}$
CO ₂ -MEA-H ₂ O	0.4173		1098.8042	0.7711	-233.5587	202.3859	-0.8662	
CO ₂ -DEA-H ₂ O	1.0809					-102.0025		
CO ₂ -MDEA-H ₂ O	2.3860	-7.67435	-15.6976					
CO ₂ -PZ-H ₂ O	0.4668		-28.1435	0.0813		-142.9250		
CO ₂ -MEA-MDEA-H ₂ O	1.5592		-21.3664					
CO ₂ -DEA-MDEA-H ₂ O	2.5199		-22.2567					
CO ₂ -PZ-MEA-H ₂ O	0.8506		-25.7353	0.0188		70.2695		

Table 5.11. Statistics of the Heat Capacity Model Predictions for the CO₂ loaded Systems against the Experimental Data used in the Fitting.

Data source(s)	Data points	C_p (J·mol ⁻¹ ·K ⁻¹)	Av. C_p (J·mol ⁻¹ ·K ⁻¹)	MAD (%)	AAD (%)	RA (J·mol ⁻¹ ·K ⁻¹)	RSD (J·mol ⁻¹ ·K ⁻¹)
<u>CO₂-MEA-H₂O</u>							
Weiland et al. ¹⁴⁰	20	76.24 – 89.09	80.80	2.67	0.66	0.43	0.63
Hilliard ⁸⁸	102	75.09 – 85.98	80.85	2.10	0.60	-0.06	0.58
Overall	122	75.09 – 89.09	79.65	2.67	0.61	0.02	0.61
<u>CO₂-DEA-H₂O</u>							
Weiland et al. ¹⁴⁰	35	77.94 – 95.56	86.27	3.16	0.36	0.06	0.56
<u>CO₂-MDEA-H₂O</u>							
Weiland et al. ¹⁴⁰	35	84.86 – 113.86	97.06	1.83	0.70	0.24	0.79
<u>CO₂-PZ-H₂O</u>							
Hilliard ⁸⁸	85	75.29 – 85.40	79.91	2.31	0.59	-0.23	0.65
<u>CO₂-MEA-MDEA-H₂O</u>							
Weiland et al. ¹⁴⁰	15	92.57 – 104.92	98.42	1.99	0.52	0.11	0.74
<u>CO₂-DEA-MDEA-H₂O</u>							
Weiland et al. ¹⁴⁰	15	99.55 – 106.11	102.57	1.82	0.74	0.41	0.85
<u>CO₂-PZ-MEA-H₂O</u>							
Hilliard ⁸⁸	102	78.99 – 91.42	85.64	1.53	0.51	0.04	0.57

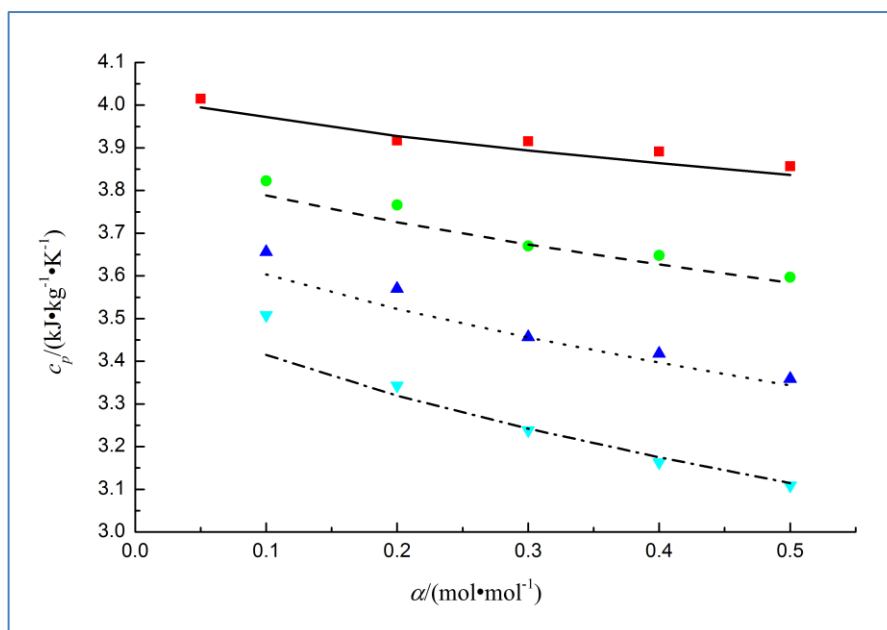


Figure 5.7. The variations of the heat capacity of aqueous solutions of MEA, $c_p/(\text{kJ}\cdot\text{kg}^{-1}\cdot\text{K}^{-1})$, with CO_2 loading, $\alpha/(\text{mol}\cdot\text{mol}^{-1})$, at a fixed temperature of 298.15 K: \blacksquare , 1.819 $\text{mol}\cdot\text{kg}^{-1}$; \bullet , 4.092 $\text{mol}\cdot\text{kg}^{-1}$; \blacktriangle , 7.015 $\text{mol}\cdot\text{kg}^{-1}$; \blacktriangledown , 10.913 $\text{mol}\cdot\text{kg}^{-1}$. Lines: —, Model (1.819 $\text{mol}\cdot\text{kg}^{-1}$); - -, Model (4.092 $\text{mol}\cdot\text{kg}^{-1}$); \cdots , Model (7.015 $\text{mol}\cdot\text{kg}^{-1}$); - · -, Model (10.913 $\text{mol}\cdot\text{kg}^{-1}$). The experimental data are from Weiland et al.¹⁴⁰

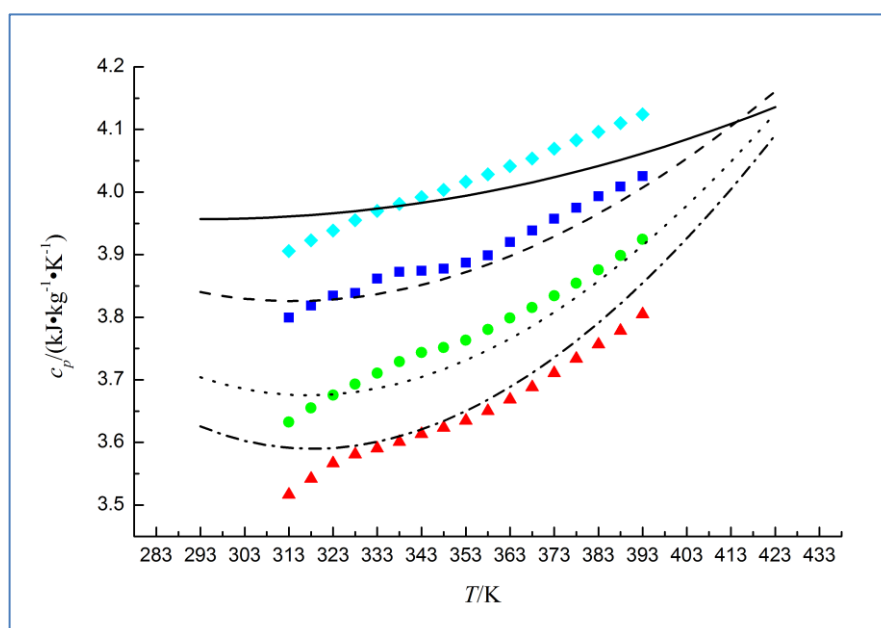


Figure 5.8. The variations of the heat capacity of 3.5 $\text{mol}\cdot\text{kg}^{-1}$ aqueous solutions of MEA, $c_p/(\text{kJ}\cdot\text{kg}^{-1}\cdot\text{K}^{-1})$, with temperature, T/K , for zero CO_2 loading and for three different CO_2 loadings: \blacklozenge , zero CO_2 loading; \blacksquare , 0.097 CO_2 loading; \bullet , 0.375 CO_2 loading; \blacktriangle , 0.583 CO_2 loading. Lines: —, Model (zero CO_2 loading); - -, Model (0.097 CO_2 loading); \cdots , Model (0.375 CO_2 loading); - · -, Model (0.583 CO_2 loading). The experimental data are from Hilliard.⁸⁸

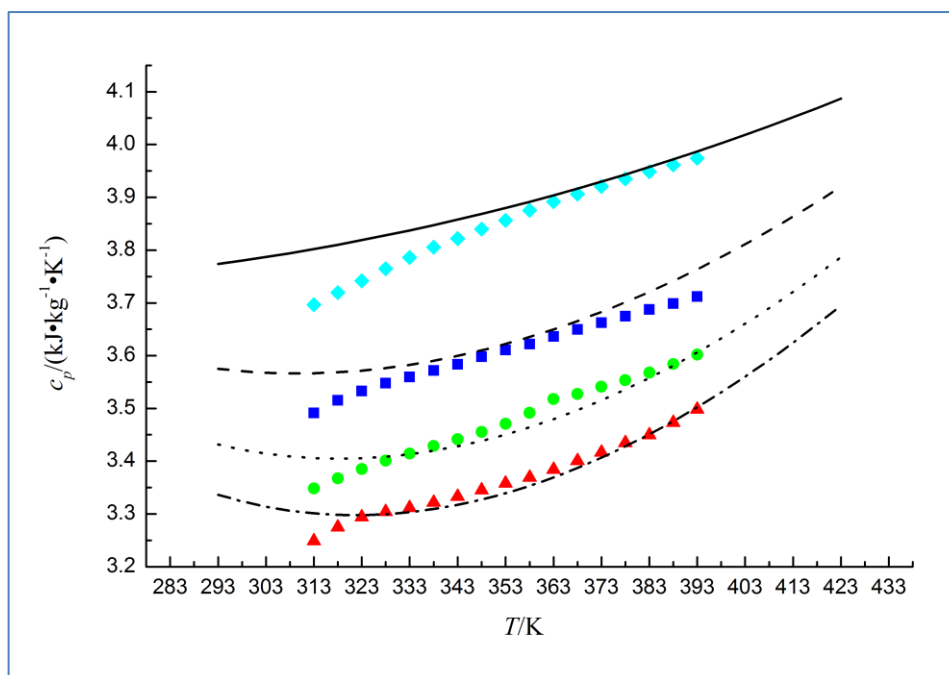


Figure 5.9. The variations of the heat capacity of $7.0 \text{ mol}\cdot\text{kg}^{-1}$ aqueous solutions of MEA, $c_p/(\text{kJ}\cdot\text{kg}^{-1}\cdot\text{K}^{-1})$, with temperature, T/K , for zero CO_2 loading and for three different CO_2 loadings: \blacklozenge , zero CO_2 loading; \blacksquare , 0.139 CO_2 loading; \bullet , 0.358 CO_2 loading; \blacktriangle , 0.541 CO_2 loading. Lines: —, Model (zero CO_2 loading); - -, Model (0.139 CO_2 loading); \cdots , Model (0.358 CO_2 loading); - · -, Model (0.541 CO_2 loading). The experimental data are from Hilliard.⁸⁸

Furthermore, the AAD for the combined data set is approximately 0.61%. Thus, the model accurately predicts the variation of the heat capacity of CO_2 -loaded aqueous solution of MEA with CO_2 loading, as well as the variation of the heat capacity of CO_2 -loaded aqueous solution of MEA with temperature at different CO_2 loadings.

5.4.4.2 CO_2 -DEA- H_2O System

The only experimental data for CO_2 -loaded aqueous solutions of DEA available in the open literature are those reported by Weiland et al.¹⁴⁰ The data points in **Figure 5.10** are the experimental data reported by Weiland et al.¹⁴⁰ for four different concentrations of DEA and at a fixed temperature of 298.15 K, while the lines are the predictions of the model. The MAD and AAD obtained in this work for the data reported by Weiland et al.¹⁴⁰ are 3.16% and 0.36%, respectively, and it is clear from **Figure 5.10** that the data point corresponding to the MAD is an outlier. Overall, as can be seen from

Figure 5.10, the model developed in this chapter accurately captures the variation of the heat capacity with CO₂ loading for the four different concentrations reported by Weiland et al.¹⁴⁰

5.4.4.3 CO₂-MDEA-H₂O System

The only experimental data for CO₂-loaded aqueous solutions of MDEA available in the open literature are those reported by Weiland et al.¹⁴⁰ The data points in **Figure 5.11** are the experimental data reported by Weiland et al.¹⁴⁰ for four different concentrations of MDEA, at a fixed temperature of 298.15 K, while the lines are the predictions of the model. The MAD and AAD for the data reported by Weiland et al.¹⁴⁰ are 2.0% and 0.73%, respectively. It is clear from **Figure 5.11** that the model accurately captures the variation of the heat capacity with CO₂ loading for the four different concentrations reported by Weiland et al.¹⁴⁰

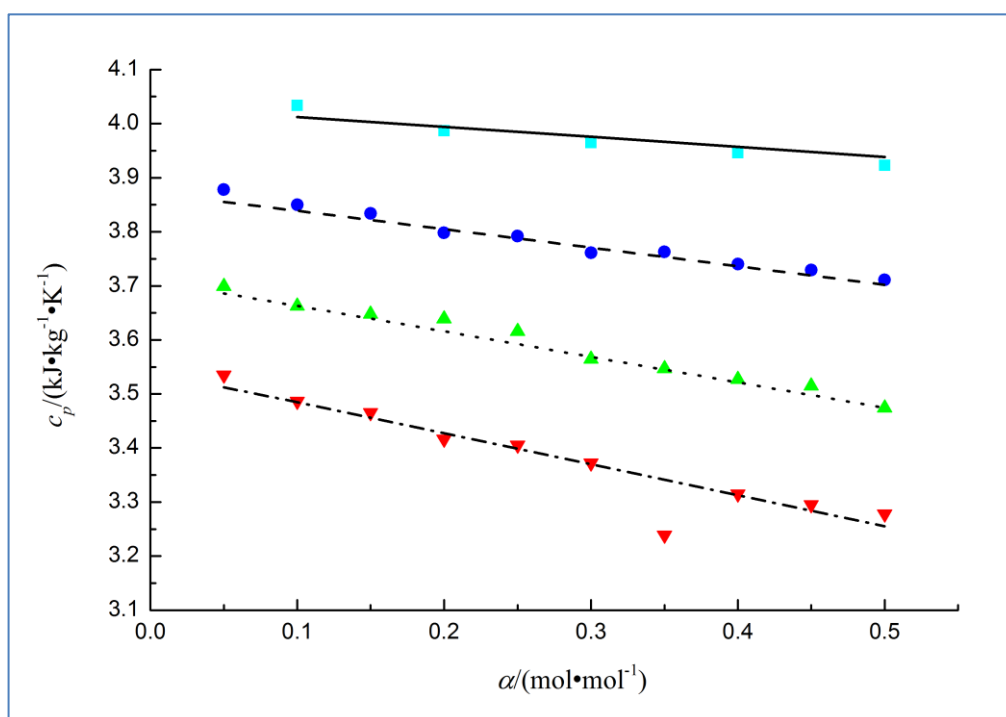


Figure 5.10. The variations of the heat capacity of aqueous solutions of DEA, c_p /(kJ·kg⁻¹·K⁻¹), with CO₂ loading, α /(mol·mol⁻¹), at a fixed temperature of 298.15 K: ■, 1.057 mol·kg⁻¹; ●, 2.378 mol·kg⁻¹; ▲, 4.076 mol·kg⁻¹; ▼, 6.341 mol·kg⁻¹. Lines: —, model (1.057 mol·kg⁻¹); - -, model (2.378 mol·kg⁻¹); ···, model (4.076 mol·kg⁻¹); -·-, model (6.341 mol·kg⁻¹). The experimental data are from Weiland et al.¹⁴⁰

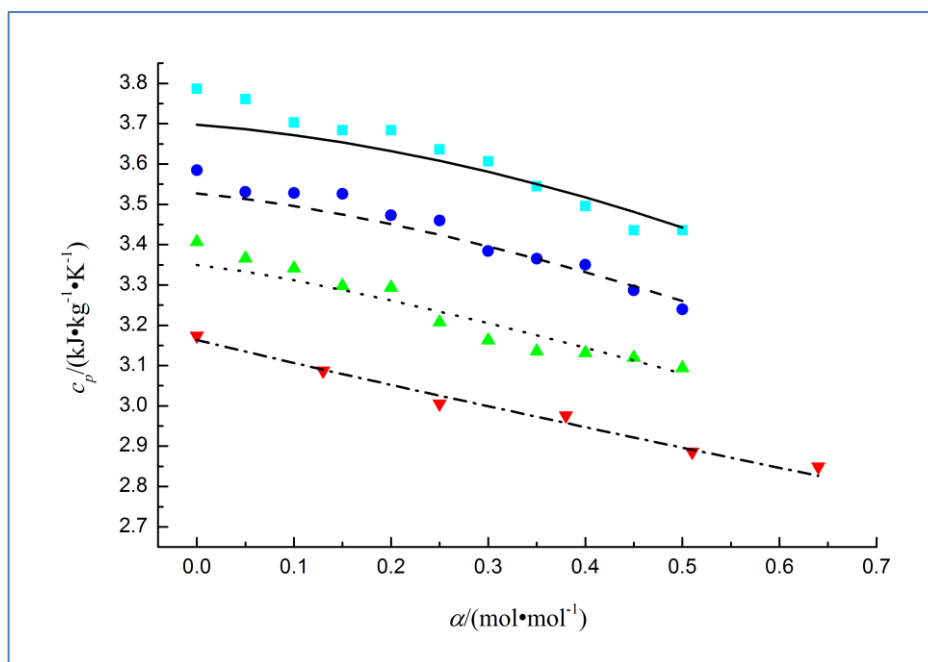


Figure 5.11. The variations of the heat capacity of aqueous solutions of MDEA, $c_p/(\text{kJ}\cdot\text{kg}^{-1}\cdot\text{K}^{-1})$, with CO_2 loading, $\alpha/(\text{mol}\cdot\text{mol}^{-1})$, at a fixed temperature of 298.15 K: \blacksquare , 3.596 $\text{mol}\cdot\text{kg}^{-1}$; \bullet , 5.594 $\text{mol}\cdot\text{kg}^{-1}$; \blacktriangle , 8.391 $\text{mol}\cdot\text{kg}^{-1}$; \blacktriangledown , 12.587 $\text{mol}\cdot\text{kg}^{-1}$. Lines: —, Model (3.596 $\text{mol}\cdot\text{kg}^{-1}$); - -, Model (5.594 $\text{mol}\cdot\text{kg}^{-1}$); \cdots , Model (8.391 $\text{mol}\cdot\text{kg}^{-1}$); - · -, Model (12.587 $\text{mol}\cdot\text{kg}^{-1}$). The experimental data are from Weiland et al.¹⁴⁰

5.4.4.4 CO_2 -PZ- H_2O System

The only experimental data for CO_2 -loaded aqueous solution of PZ available in the open literature are those reported by Hilliard⁸⁸ for 2.0 $\text{mol}\cdot\text{kg}^{-1}$ and 3.5 $\text{mol}\cdot\text{kg}^{-1}$ aqueous solution of PZ. **Figure 5.12** shows comparisons of the model predictions with the experimental data for three different CO_2 loadings of the 2.0 $\text{mol}\cdot\text{kg}^{-1}$ aqueous solutions of PZ. Similarly, **Figure 5.13** shows comparisons of the model predictions with the experimental data for three different CO_2 loadings of the 3.6 $\text{mol}\cdot\text{kg}^{-1}$ aqueous solutions of PZ. It is clear from both figures that the model predictions are in a very good agreement with the experimental data reported by Hilliard.⁸⁸

The MAD and AAD for the data reported by Hilliard⁸⁸ are 1.19% and 0.28%, respectively, and the 0.28% AAD is far lower than the 3.37% AAD value obtained by Hilliard.⁸⁸ Again, since Hilliard⁸⁸ simultaneously regressed the vapour-liquid-equilibrium (VLE) data and the heat capacity data for the CO_2 -PZ- H_2O system, it further confirms the statement made earlier with respect to accuracy when VLE and heat capacity data are regressed together simultaneously.

5.4.4.5 CO₂-MEA-MDEA-H₂O System

Weiland et al.¹⁴⁰ reported some experimental data for CO₂-loaded aqueous solutions of MEA/MDEA blends, with three different ratios of the amines. A comparison of the predictions of the model with the experimental data reported by Weiland et al.¹⁴⁰ is shown in **Figure 5.14**, and it is clear that the predictions of the model developed in this chapter adequately capture the variation of the heat capacity of the mixed system with CO₂ loading. This clearly shows that the model is not limited to solution of single amines, although the combination of the model parameters accounting for the CO₂ loading effect varies from one system to the other. The MAD and AAD obtained for the data reported by Weiland et al.¹⁴⁰ are 1.99% and 0.52%, respectively.

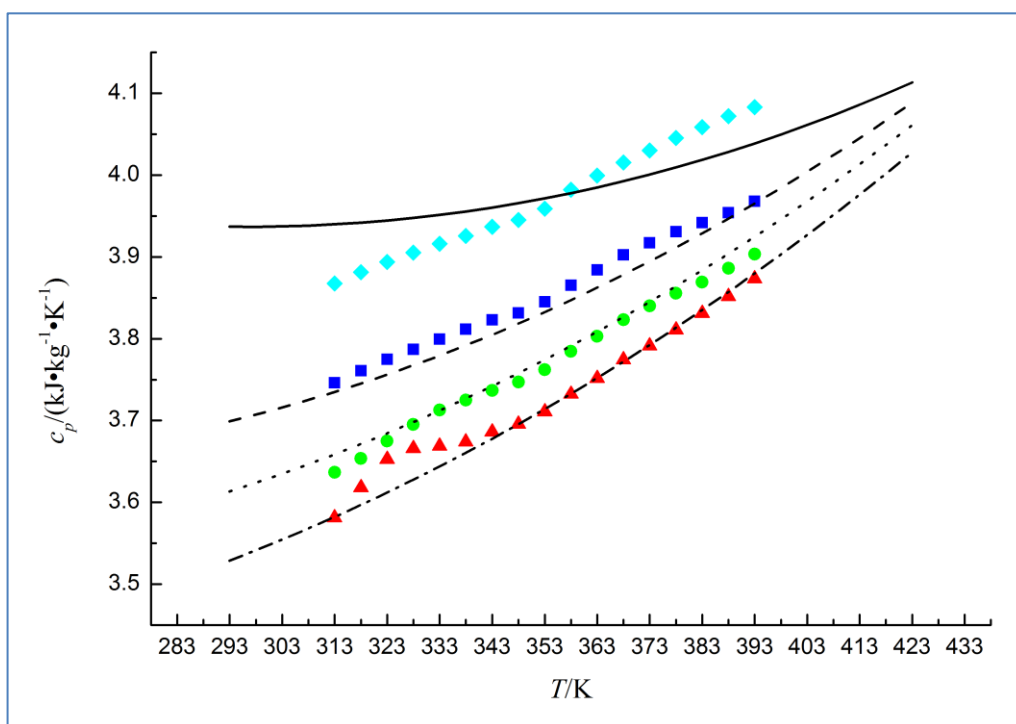


Figure 5.12. The variations of the heat capacity of 2.0 mol·kg⁻¹ aqueous solutions of PZ, c_p /(kJ·kg⁻¹·K⁻¹), with temperature, T/K, for zero CO₂ loading and for three different CO₂ loadings: \blacklozenge , zero CO₂ loading; \blacksquare , 0.157 CO₂ loading; \bullet , 0.269 CO₂ loading; \blacktriangle , 0.401 CO₂ loading. Lines: —, Model (zero CO₂ loading); - - -, Model (0.157 CO₂ loading); ···, Model (0.269 CO₂ loading); - · -, Model (0.401 CO₂ loading). The experimental data are from Hilliard.⁸⁸

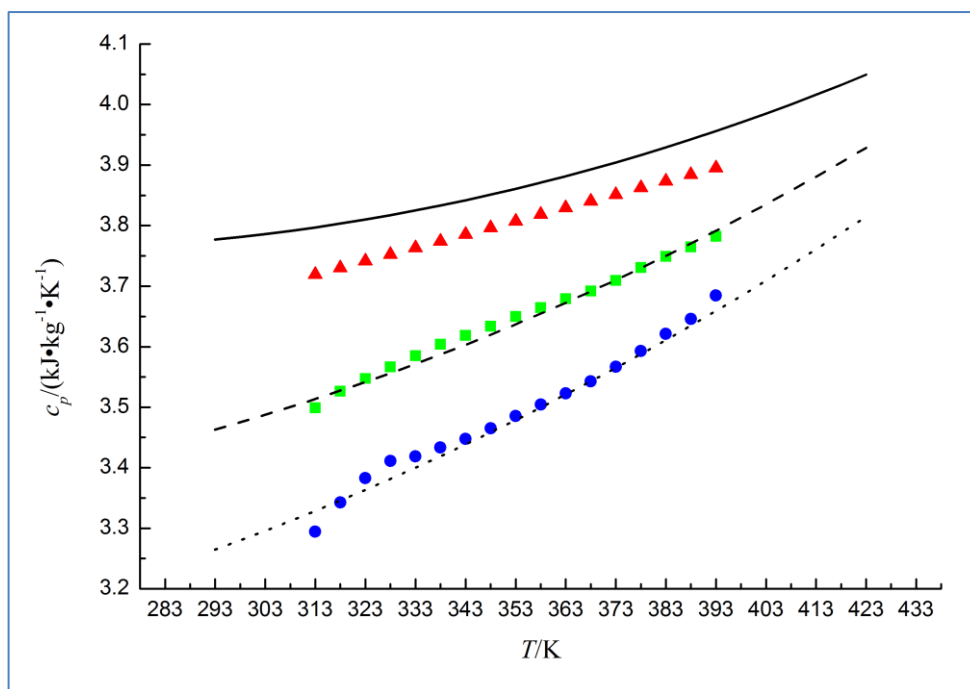


Figure 5.13. The variations of the heat capacity of $3.6 \text{ mol}\cdot\text{kg}^{-1}$ aqueous solutions of PZ, $c_p/(\text{kJ}\cdot\text{kg}^{-1}\cdot\text{K}^{-1})$, with temperature, T/K , for zero CO_2 loading and for two different CO_2 loadings: \blacktriangle , zero CO_2 loading; \blacksquare , 0.159 CO_2 loading; \bullet , 0.375 CO_2 loading. Lines: —, Model (zero CO_2 loading); - -, Model (0.159 CO_2 loading); \cdots , Model (0.375 CO_2 loading). The experimental data are from Hilliard.⁸⁸

5.4.4.6 CO_2 -DEA-MDEA- H_2O System

Some experimental data have been reported by Weiland et al.¹⁴⁰ for CO_2 -loaded aqueous solutions of DEA/MDEA blends, with three different ratios of the amines. **Figure 5.15** shows a comparison of the model predictions with the experimental data reported by Weiland et al.,¹⁴⁰ and it is clear that the predictions of the model adequately captures the variation of the heat capacity of the mixed system with CO_2 loading. The MAD and AAD obtained for the data reported by Weiland et al.¹⁴⁰ are 1.32% and 0.54%, respectively.

5.4.4.7 CO_2 -PZ-MEA- H_2O System

The only experimental data for CO_2 loaded aqueous solutions of PZ/MEA blends available in the open literature are those reported by Hillard⁸⁸ for aqueous solution blends comprising $2.0 \text{ mol}\cdot\text{kg}^{-1}$ of PZ and $3.5 \text{ mol}\cdot\text{kg}^{-1}$ of MEA, and blends comprising $2.0 \text{ mol}\cdot\text{kg}^{-1}$ of PZ and $7.0 \text{ mol}\cdot\text{kg}^{-1}$ of MEA.

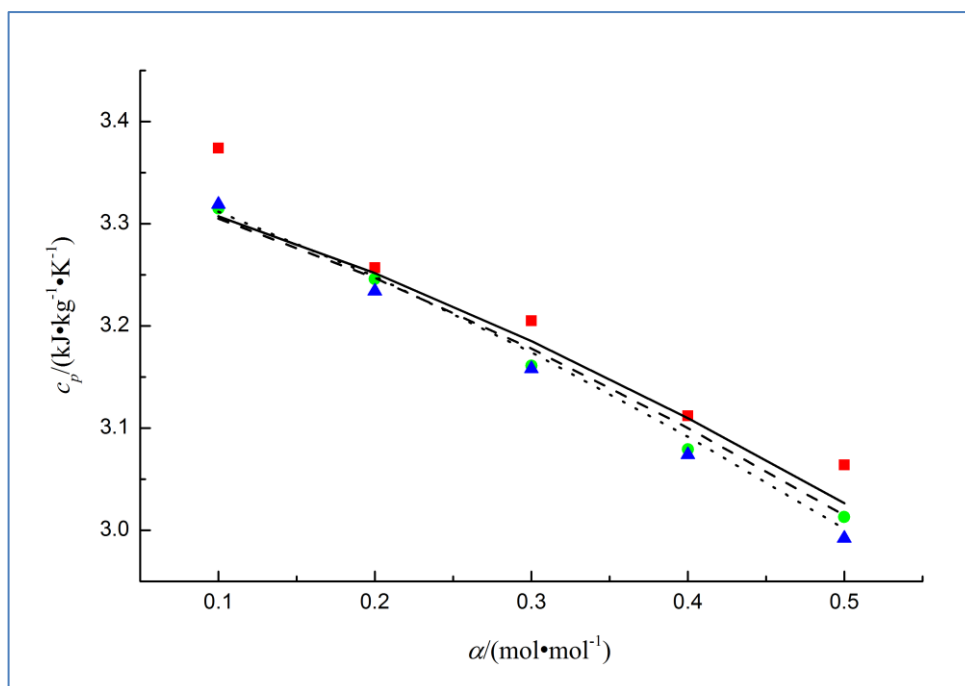


Figure 5.14. The variations of the heat capacity of aqueous solutions of MEA/MDEA blends, $c_p/(\text{kJ}\cdot\text{kg}^{-1}\cdot\text{K}^{-1})$, with CO_2 loading, $\alpha/(\text{mol}\cdot\text{mol}^{-1})$, at a fixed temperature of 298.15 K: ■, 1.637 $\text{mol}\cdot\text{kg}^{-1}$ MEA/7.552 $\text{mol}\cdot\text{kg}^{-1}$ MDEA; ●, 3.274 $\text{mol}\cdot\text{kg}^{-1}$ MEA/6.713 $\text{mol}\cdot\text{kg}^{-1}$ MDEA; ▲, 6.548 $\text{mol}\cdot\text{kg}^{-1}$ MEA/5.035 $\text{mol}\cdot\text{kg}^{-1}$ MDEA. Lines: —, Model (1.637 $\text{mol}\cdot\text{kg}^{-1}$ /7.552 $\text{mol}\cdot\text{kg}^{-1}$); - -, Model (3.274 $\text{mol}\cdot\text{kg}^{-1}$ /6.713 $\text{mol}\cdot\text{kg}^{-1}$); ···, Model (6.548 $\text{mol}\cdot\text{kg}^{-1}$ /5.035 $\text{mol}\cdot\text{kg}^{-1}$). The experimental data are from Weiland et al.¹⁴⁰

Figure 5.16 shows the comparison of the model predictions with the experimental data for three different CO_2 loadings of the aqueous solution blends comprising 2.0 $\text{mol}\cdot\text{kg}^{-1}$ of PZ and 3.5 $\text{mol}\cdot\text{kg}^{-1}$ of MEA, while **Figure 5.17** shows the comparison of the model predictions with the experimental data for three different CO_2 loadings of the aqueous solution blends comprising 2.0 $\text{mol}\cdot\text{kg}^{-1}$ of PZ and 7.0 $\text{mol}\cdot\text{kg}^{-1}$ of MEA. It is clear from both figures that the model predictions are in a very good agreement with the experimental data reported by Hilliard.⁸⁸

The MAD and AAD obtained for the data reported by Hilliard⁸⁸ are 1.53% and 0.51%, respectively, and both values are far lower than the 40.0% and 5.1% values obtained by Hilliard,⁸⁸ respectively. Again, since Hilliard⁸⁸ simultaneously regressed the vapour-liquid-equilibrium (VLE) data and the heat capacity data for the CO_2 -PZ-MEA- H_2O system, it further confirms the statement made earlier with respect to accuracy when VLE and heat capacity data are regressed together simultaneously.

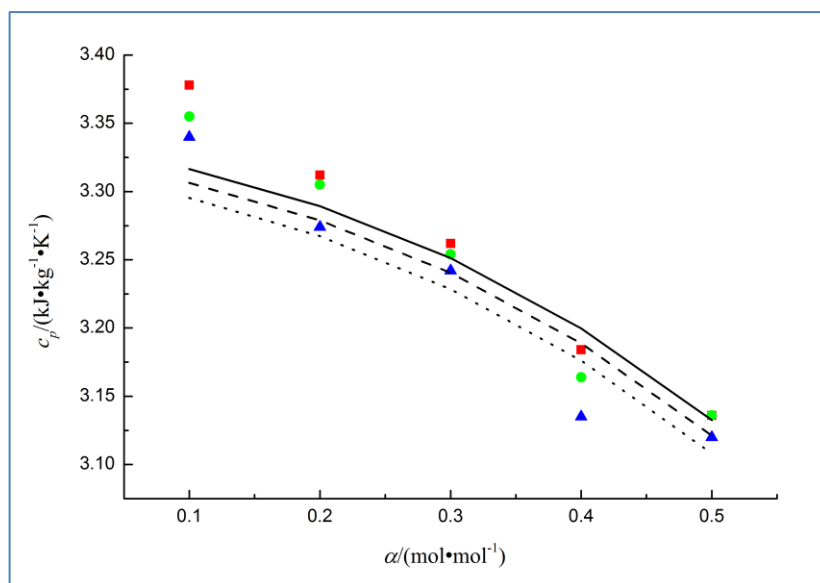


Figure 5.15. The variations of the heat capacity of aqueous solutions of DEA/MDEA blends, $c_p/(\text{kJ}\cdot\text{kg}^{-1}\cdot\text{K}^{-1})$, with CO_2 loading, $\alpha/(\text{mol}\cdot\text{mol}^{-1})$, at a fixed temperature of 298.15 K: ■, 0.951 $\text{mol}\cdot\text{kg}^{-1}$ DEA/7.552 $\text{mol}\cdot\text{kg}^{-1}$ MDEA; ●, 1.902 $\text{mol}\cdot\text{kg}^{-1}$ DEA/6.713 $\text{mol}\cdot\text{kg}^{-1}$ MDEA; ▲, 3.804 $\text{mol}\cdot\text{kg}^{-1}$ DEA/5.035 $\text{mol}\cdot\text{kg}^{-1}$ MDEA. Lines: —, Model (0.951 $\text{mol}\cdot\text{kg}^{-1}$ /7.552 $\text{mol}\cdot\text{kg}^{-1}$); - -, Model (1.902 $\text{mol}\cdot\text{kg}^{-1}$ /6.713 $\text{mol}\cdot\text{kg}^{-1}$); ···, Model (3.804 $\text{mol}\cdot\text{kg}^{-1}$ /5.035 $\text{mol}\cdot\text{kg}^{-1}$). The experimental data are from Weiland et al.¹⁴⁰

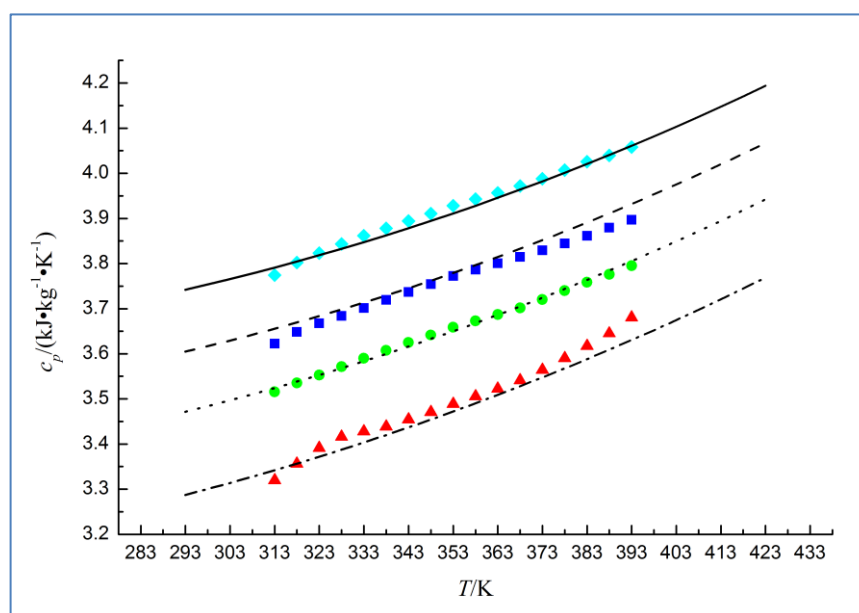


Figure 5.16. The variations of the heat capacity of aqueous solutions made up of 2.0 $\text{mol}\cdot\text{kg}^{-1}$ of PZ and 3.5 $\text{mol}\cdot\text{kg}^{-1}$ of MEA, $c_p/(\text{kJ}\cdot\text{kg}^{-1}\cdot\text{K}^{-1})$, with temperature, T/K , for zero CO_2 loading and for three different CO_2 loadings: ◆, zero CO_2 loading; ■, 0.109 CO_2 loading; ●, 0.236 CO_2 loading; ▲, 0.432 CO_2 loading. Lines: —, Model (zero CO_2 loading); - -, Model (0.109 CO_2 loading); ···, Model (0.236 CO_2 loading); - · -, Model (0.432 CO_2 loading). The experimental data are from Hilliard.⁸⁸

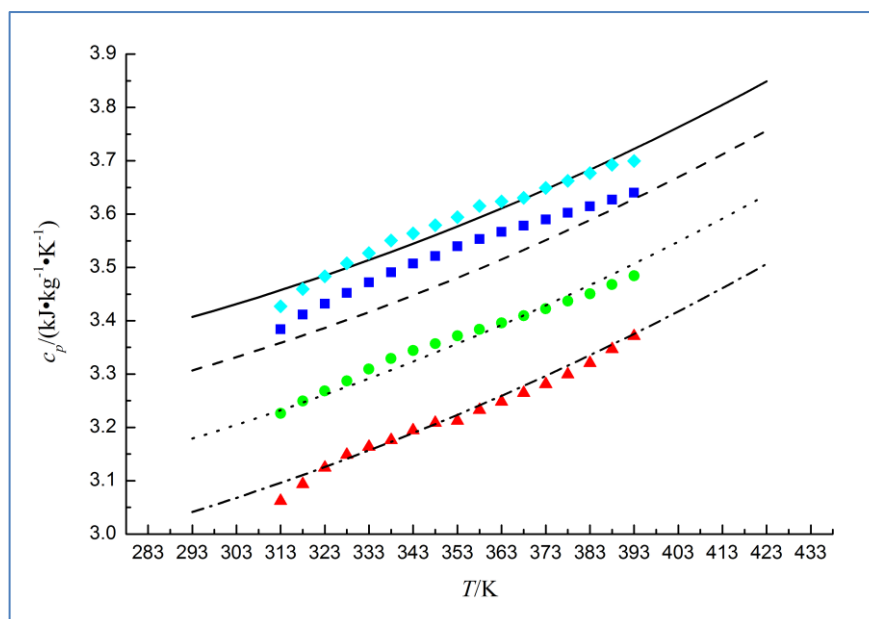


Figure 5.17. The variations of the heat capacity of aqueous solutions made up of 2.0 mol·kg⁻¹ of PZ and 7.0 mol·kg⁻¹ of MEA, c_p /(kJ·kg⁻¹·K⁻¹), with temperature, T/K, for zero CO₂ loading and for three different CO₂ loadings: ◆, zero CO₂ loading; ■, 0.098 CO₂ loading; ●, 0.248 CO₂ loading; ▲, 0.430 CO₂ loading. Lines: —, Model (zero CO₂ loading); - - -, Model (0.098 CO₂ loading); ···, Model (0.248 CO₂ loading); - · -, Model (0.430 CO₂ loading). The experimental data are from Hilliard.⁸⁸

5.5 Conclusions

The semi-empirical model presented in this chapter can accurately estimate the heat capacity of aqueous solutions of alkanolamines, including aqueous solutions of two alkanolamines, both before and after CO₂ absorption. Further, the model predictions provide some insights on the relative accuracy of the experimental data reported by different authors for the same system. Overall, the model predictions are in excellent agreement with most of the experimental data reported by the different authors for all the systems modelled.

The model, along with the parameters regressed for the various systems, can serve as a valuable tool for design engineers involved in the design of amine-based gas purification plants, especially the heat exchange equipment in such plants. It is also postulated that the model equations can be used by researchers in the regression of new sets of data generated for aqueous solutions of alkanolamines, especially the solutions loaded with CO₂, other than the ones presented in this chapter.

Chapter 6

Modelling and Simulation of MEA-based CO₂ Capture Process at Pilot-scale

6.1 Introduction

In this chapter, MEA-based CO₂ capture process is modelled using the rate-based model in Aspen plus[®] and the models developed for two different pilot plants have been validated with pilot plant data reported for the pilot plants. One of the pilot plants is the UK CCS Research Centre (UKCCSRC)/Pilot-scale Advanced Capture Technology (PACT) pilot plant, which is located at Beighton, Sheffield, while the second pilot plant is the University of Kaiserslautern pilot plant, which is located in Kaiserslautern, Germany.

6.2 Pilot Plants and Process Description

6.2.1 The UKCCSRC/PACT Pilot Plant

The UKCCSRC/PACT pilot plant consists of an SO₂ removal tower and the CO₂ removal section. The SO₂ removal tower is used to condition the flue gas entering the absorber when burning high sulphur-containing fuel such as coal, and it can be put offline when burning low or no sulphur-containing fuel such as natural gas. The CO₂ removal section has an absorber, a water-wash section, a stripper with an air-cooled condenser and a reflux drum at the top. The key information about the columns in the CO₂ removal section is summarized in **Table 6.1**. Heat integration is achieved in a plate lean/rich heat exchanger, and further cooling of the lean amine solution leaving the lean/rich heat exchanger is achieved in an air-cooled plate-type lean amine cooler. The flue gas needed by the CO₂ capture plant is provided by a coal/biomass burner or by mixing a fraction of the flue gas from a micro-turbine with pure CO₂ from a CO₂ storage tank. It is also possible to supply synthetic flue gas to the absorber by mixing CO₂, O₂, and N₂ from their respective storage tanks. A schematic of the CO₂ capture plant, excluding the SO₂ removal tower, is shown in **Figure 6.1**.¹⁴⁷

Table 6.1. Key data for the columns in the UKCCSRC/PACT Pilot Plant.¹⁴⁷

	Absorber column	Stripper column	Water wash column
Diameter	0.303 m	0.303 m	0.303 m
Packed height	6.0 m	6.0 m	1.2 m
Packing type	IMTP #40	IMTP #40	IMTP #40

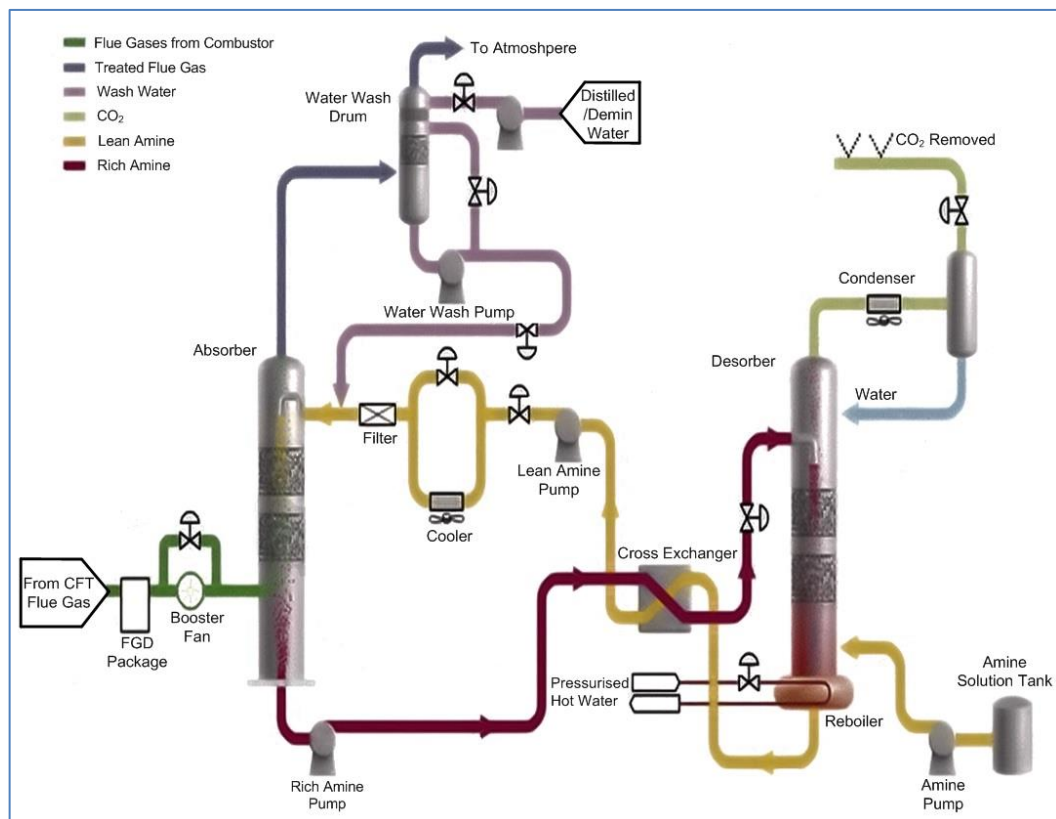


Figure 6.1. A Schematic of the UKCCSRC/PACT CO₂ Capture Pilot Plant.¹⁴⁷

The pressure of the flue gas is boosted by a booster fan before introducing it to the bottom of the absorber in order to overcome pressure drop in the absorber and water-wash columns. The countercurrent contact of the flue gas entering the bottom of the absorber with the lean MEA solution entering the top of the absorber column results in the absorption of CO₂ from the upward-flowing flue gas into the downward-flowing MEA solution. A demister at the top of the absorber limits carryover of water/MEA vapour by the treated gas exiting the top of the absorber, and the treated gas exiting the absorber is further washed in the water-wash column using demineralized

water before exiting to the atmosphere. The rich MEA solution exiting the bottom of the absorber column, after recovering some heat from the lean MEA solution in the lean/rich heat exchanger, is regenerated in the stripper column. The heat duty of the stripper reboiler is supplied by pressurized hot water. The mass flowrate, the inlet temperature and the outlet temperature of the pressurized hot water are used for the estimation of the reboiler heat duty of the stripping process.¹⁴⁷

The measurement of the conditions and compositions of the flue gas entering the absorber, the treated gas exiting the top of the absorber, and the clean gas exiting the top of the water-wash column is performed by a combination of experimental techniques consisting of gas analysers (Horiba VS3000/VA3000), FTIR (Gasmeter DX4000) and GCMS (PerkinElmer Clarus SQ8). The alkalinity of the amine solution is determined analytically by titrating samples with HCl solution, while the CO₂ loadings of the lean MEA and rich MEA solutions are determined by titrating samples of the solution with NaOH solution. The control of the CO₂ capture plant is via programmable logic controllers (PLCs) while data acquisition and logging is performed with LABVIEW[®] interfaced with MS Excel[®].¹⁴⁷

6.2.2 The University of Kaiserslautern Pilot Plant

The Process and Instrumentation Diagram (P&ID) of the Pilot Plant at the University of Kaiserslautern is shown in **Figure 6.2** and the key data characterizing the pilot plant is summarized in **Table 6.2**. The complete pilot plant and process description is available in Notz et al.¹⁴⁸ An abridged description of the pilot plant culled from Notz et al.¹⁴⁸ is given as follows:

“The flue gas from the burner first passes a blower. Before entering the pre washer and the absorber the flue gas flow is split as the amount of flue gas produced by the burner cannot be freely specified. Only a part enters the pre washer, the rest is directly fed to the chimney. The flue gas temperature after the blower is approx. 70 – 80 °C. For setting a typical flue gas temperature at the absorber inlet of 45 – 50 °C a pre washer, which is realized as direct contact cooler, is used. The heat is removed in a plate heat exchanger, which is installed in the washing water loop, cooled by cooling water. For the whole pilot plant cooling water of approx. 5 – 10 °C is available. The condensate is removed discontinuously through valve V10. The flue gas mass flow at the absorber inlet can be controlled in three ways: by the valve in the

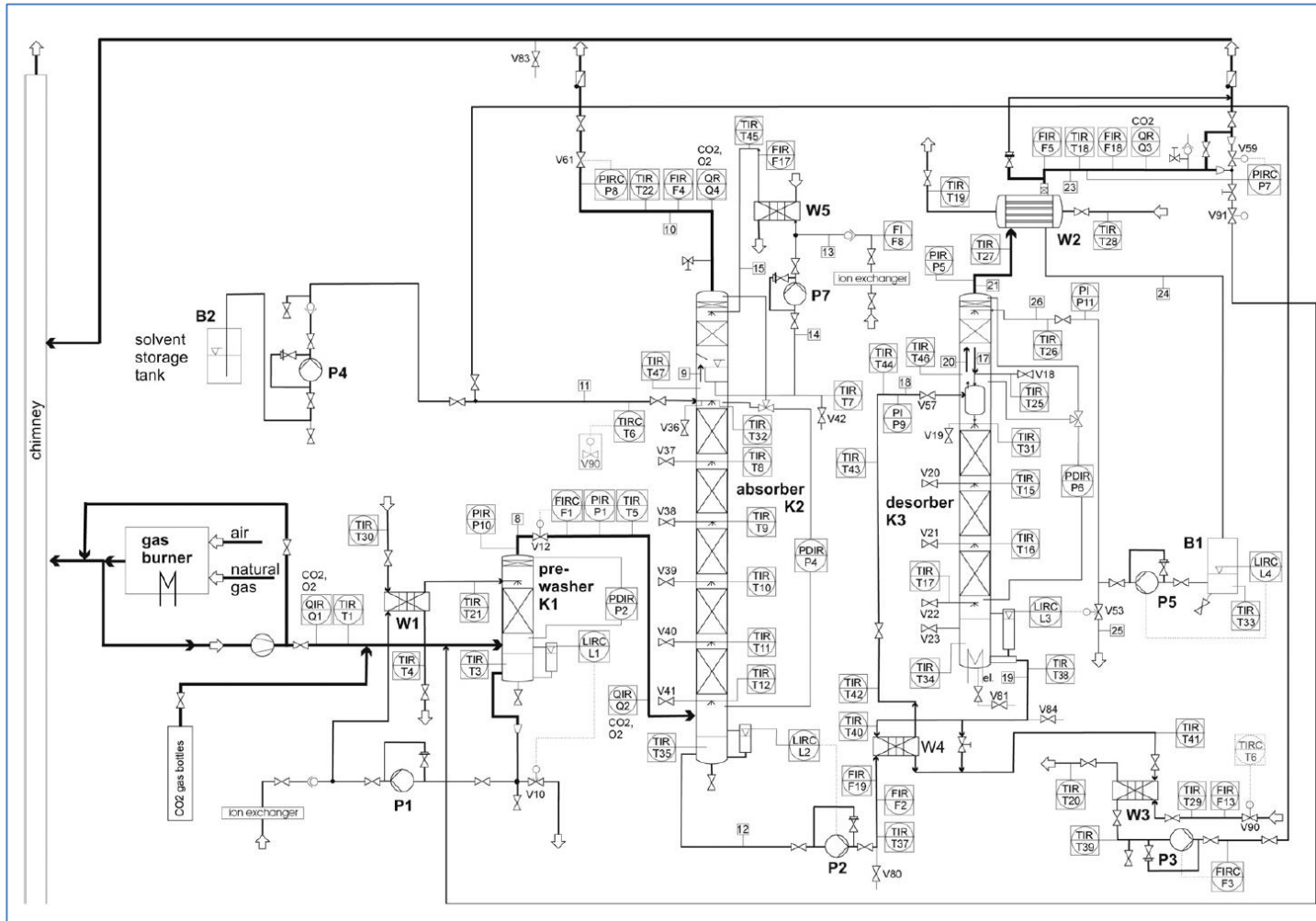


Figure 6.2. Process and Instrumentation Diagram (P&ID) of the Pilot Plant at the University of Kaiserslautern. ¹⁴⁸

Table 6.2. Survey data for the University of Kaiserslautern Pilot Plant.¹⁴⁸

Flue gas source	Natural gas burner + CO ₂ feed from gas bottles + CO ₂ recycle from desorber
CO ₂ partial pressure in the flue gas	36 – 134 mbar
Diameter of columns (absorber, desorber, washing section, pre washer)	125 mm
Column internals in absorber, desorber, washing sections, pre washer	Structured packing (Sulzer Mellapak 250.Y™)
Height of packing	
Absorber	4.20 m
Desorber	2.52 m
Washing sections in absorber and desorber	0.42 m
Pre washer	0.84 m
Material of apparatus and piping	Stainless steel (1.4571, 1.4401, 1.4404)
Flue gas flow rate in the absorber	30 – 110 kg/h
F-factor in the absorber	0.6 – 2.4 \sqrt{Pa}
Solvent flow rate	50 – 350 kg/h
Liquid load in the absorber	4 – 28.5 m ³ /(m ² h)
Pressure in the absorber	Atmospheric pressure
Pressure in the desorber	1 – 2.5 bar (absolute)
Electrical heat duty of the evaporator	0 – 30 kW
Temperature of cooling water	5 – 10 °C

bypass flow into the chimney, by the frequency of the blower, and by the throttle valve V12 in the main flue gas line. The flue gas flow rate through the absorber is limited due to fluid dynamic reasons. At a solvent flow rate of 300 kg/h, the maximum F-factor is approx. 2.4 Pa^{0.5} corresponding to a flue gas flow rate of approx. 110 kg/h. The amount and condition of the flue gas at the absorber inlet are determined in the following way: measurement of volume flow (F1, vortex flow meter), pressure (P1) and temperature (T5), online gas analysis of CO₂ and O₂ concentration in the dry gas (Q2, CO₂ by IR absorption, O₂ by paramagnetism), determination of the water partial pressure assuming that the flue gas leaves the pre washer saturated at the outlet temperature, calculation of the N₂ concentration from the concentration summation equation neglecting trace components. From a

measurement it is known that the NO_x concentrations are approx. 13 vol ppm NO and 3 vol ppm NO_2 .

The absorber has five packing sections, each of which contains a liquid redistributor at the top and a collector at the bottom. Each collector contains a sampling line and a Pt 100 thermometer so that the temperature and concentration profiles can be determined. The liquid distributor at the bottom of the collector is realized as horizontal tubing, which contains a horizontal slot over the whole length. Each packing section is equipped with four elements of the structured packing Sulzer Mellapak 250.YTM, the overall packing height in each section is 0.84 m. The flue gas is fed into the absorber below the lowest of the five packing sections, the lean solvent above the highest. For reducing amine losses a washing section is installed at the top of the absorber above the lean solvent feed. This sixth packing section is identical with the five others except of the packing height of 0.42 m. Before the treated gas leaves the absorber column above the washing section, it has to pass a demister to retain liquid droplets. For monitoring the fluid dynamic behaviour in the absorber, the differential pressure over the whole column is measured (P4).

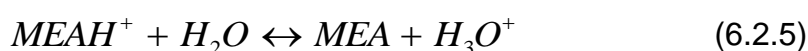
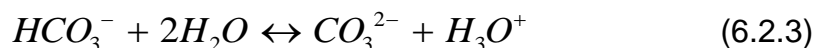
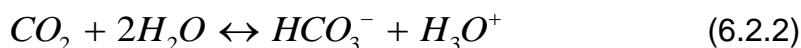
The rich solvent leaving the absorber is pumped through the heat exchanger W4 (so called rich-lean heat exchanger) in which it is heated up by the hot lean solvent from the desorber bottom. To avoid evaporation of CO_2 in the heat exchanger and in the feed line to the desorber, the throttle valve V57 is installed at the desorber inlet and set so that the pressure P9 is sufficiently high. After passing the throttle valve the solvent enters a flash vessel, which is located directly above the desorber packing inside the desorber column. From there the liquid solvent is directly distributed on the top of the desorber packing. The released gas leaves the flash vessel at the top outlet, where it is combined with the vapour flow from the desorber packing sections. The desorber is built up of three packing sections which are constructed in the same way as in the absorber. The stripping steam is generated in the desorber bottom by partial evaporation of the liquid solvent with electrical heating elements, for which the electrical power is measured. The hot lean solvent at the desorber bottom flows through the rich-lean heat exchanger W4 and through the heat exchanger W3 before entering the absorber top. The composition of the lean solvent can be determined by analysis of a liquid sample from valve V84.”

6.3 Modelling Framework

The Aspen Plus® RadFrac column model, a second generation rate-based model for multistage separation operations, was used for the modelling of the absorption and stripping columns in the MEA-based CO₂ capture process. Being a pre-requisite for accurate process modelling of the CO₂ capture process, validated high fidelity models were used for thermodynamic and transport properties.¹⁴⁹

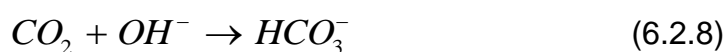
6.3.1 Thermodynamic Model

The model adopted for the thermodynamic properties is based on the work by Zhang et al.¹⁰¹ The model uses the electrolyte-NRTL activity coefficient model for the liquid phase properties and PC-SAFT equation of state for vapour phase properties. The model has been validated by Zhang et al.¹⁰¹ against experimental data in the open literature. The equilibrium reactions describing the solution chemistry of CO₂ absorption with MEA, which are integral components of the thermodynamic model, include:¹⁰¹



6.3.2 Reaction Kinetics Model

The formation of carbamate and bicarbonate are kinetically limited and the forward and reverse reactions are given as follows:¹⁵⁰



In Aspen Plus[®], the reaction rates for the above kinetically limited reactions are described by power law expressions as follows:¹⁵⁰

$$r_j = k_j^0 \exp\left(-\frac{\varepsilon_j}{R} \left[\frac{1}{T} - \frac{1}{298.15}\right]\right) \prod_{i=1}^N a_i^{\alpha_{ij}} \quad (6.2.10)$$

where r_j is the reaction rate for reaction j , k_j^0 is the pre-exponential factor, ε_j is the activation energy, R is the gas constant, T is the system temperature in Kelvin, a_i is the activity of species i , and α_{ij} is the reaction order of species i in reaction j . The kinetic expressions for the carbamate and bicarbonate reactions, including the rate constant parameters, were obtained from the work by Zhang and Chen¹⁵⁰ and they are summarized in **Table 6.3**.

6.3.3 Transport Property Models

The Aspen Plus[®] RadFrac model requires quantitative values of the transport properties that are part of the correlations for heat transfer, mass transfer, interfacial area, liquid holdup, pressure drop, etc.

Table 6.3. Kinetic expressions for MEA carbamate and bicarbonate reactions in the absorber and stripper.¹⁵⁰

Related Specie	Reaction Direction	Reaction Kinetics ^a
MEACOO ⁻	Forward	$r_6 = 3.02 \times 10^{14} \exp\left(-\frac{41.20}{R} \left[\frac{1}{T} - \frac{1}{298.15}\right]\right) a_{MEA} a_{CO_2}$
MEACOO ⁻	Reverse (Absorber)	$r_7 = 5.52 \times 10^{23} \exp\left(-\frac{69.05}{R} \left[\frac{1}{T} - \frac{1}{298.15}\right]\right) \frac{a_{MEACOO^-} a_{H_3O^+}}{a_{H_2O}}$
MEACOO ⁻	Reverse (stripper)	$r_7 = 6.56 \times 10^{27} \exp\left(-\frac{95.24}{R} \left[\frac{1}{T} - \frac{1}{298.15}\right]\right) \frac{a_{MEACOO^-} a_{H_3O^+}}{a_{H_2O}}$
HCO ₃ ⁻	Forward	$r_8 = 1.33 \times 10^{17} \exp\left(-\frac{55.38}{R} \left[\frac{1}{T} - \frac{1}{298.15}\right]\right) a_{CO_2} a_{OH^-}$
HCO ₃ ⁻	Reverse	$r_9 = 6.63 \times 10^{16} \exp\left(-\frac{107.24}{R} \left[\frac{1}{T} - \frac{1}{298.15}\right]\right) a_{HCO_3^-}$

^aThe reaction rate and the pre-exponential factor are in kmol/(m³ s), while the activation energy is in kJ/mol

Table 6.4. Summary of the models in Aspen Plus® that were used for transport properties calculations.⁸⁷

Property	Gas phase	Liquid phase
Density	PC-SAFT equation of state model	Clarke density model
Viscosity	Chapman-Enskog model with Wilke approximation	Jones-Dole model
Surface tension	-	Onsager-Samaras model
Thermal conductivity	Stiel-Thodos model with Wassiljewa-Mason-Saxena mixing rule	Reidel model
Binary diffusivity	Chapman-Enskog Wilke-Lee model	Nernst-Hartley model

The transport properties include density, viscosity, surface tension, thermal conductivity, and binary diffusivity¹⁵¹. A summary of the models in Aspen Plus® that were adopted for the transport properties calculations is given in **Table 6.4**.

6.3.4 Implementation of the Pilot Plant Models in Aspen Plus®

Figure 6.3 and **Figure 6.4** show the process flow diagrams (PFDs) of the pilot plants models as implemented in Aspen Plus®. A summary of the key parameters and sub-models used in setting up the absorber and stripper columns in the pilot plant models is given in **Table 6.5**.

Table 6.5. The key parameters and sub-models used in setting up the pilot plants models.

Parameter or Sub-model	UKCCSRC/PACT		University of Kaiserslautern	
	Absorber	Stripper	Absorber	Stripper
Calculation Mode	Rate-based	Rate-based	Rate-based	Rate-based
Number of Stages	20	20	20	20

Top Pressure (bar)	~ 1.0	1.2	~ 1.0	1 – 2.5
Packing Type	IMTP #40	IMTP #40	Mellapak 250.Y™	Mellapak 250.Y™
Diameter (m)	0.303	0.303	0.125	0.125
Total Height (m) ^b	6.0	6.0	4.62	2.94
Wash section height (m)	-	-	0.42	0.42
Absorber section height (m) ^c	6.0	6.0	4.2	2.52
Mass transfer coefficient method	HanleyIMTP (2010) ¹⁵²	HanleyIMTP (2010) ¹⁵²	Bravo (1985) ¹⁵³	Bravo (1985) ¹⁵³
Interfacial area method	HanleyIMTP (2010) ¹⁵²	HanleyIMTP (2010) ¹⁵²	Bravo (1985) ¹⁵³	Bravo (1985) ¹⁵³
Liquid holdup method	Stichlmair et al. (1989) ¹⁵⁴	Stichlmair et al. (1989) ¹⁵⁴	Bravo (1992) ¹⁵⁵	Bravo (1992) ¹⁵⁵
Flooding method (pressure drop)	Stichlmair et al. (1989) ¹⁵⁴	Stichlmair et al. (1989) ¹⁵⁴	Vendor (Sulzer)	Vendor (Sulzer)
Heat transfer coefficient method	Chilton and Colburn ¹⁵⁶			
Film resistance options	“Discrxn” for liquid film; “film” for vapour film	“Discrxn” for liquid film; “film” for vapour film	“Discrxn” for liquid film; “film” for vapour film	“Discrxn” for liquid film; “film” for vapour film
Liquid film discretization	discretization points = 5; discretization ratio = 5	discretization points = 5; discretization ratio = 5	discretization points = 5; discretization ratio = 5	discretization points = 5; discretization ratio = 5
Flow model	VPlug	VPlug	VPlug	VPlug

^bTotal height refers to the summation of the absorber (or stripper) height and the wash section height.

^cStripper section height when referring to the stripper.

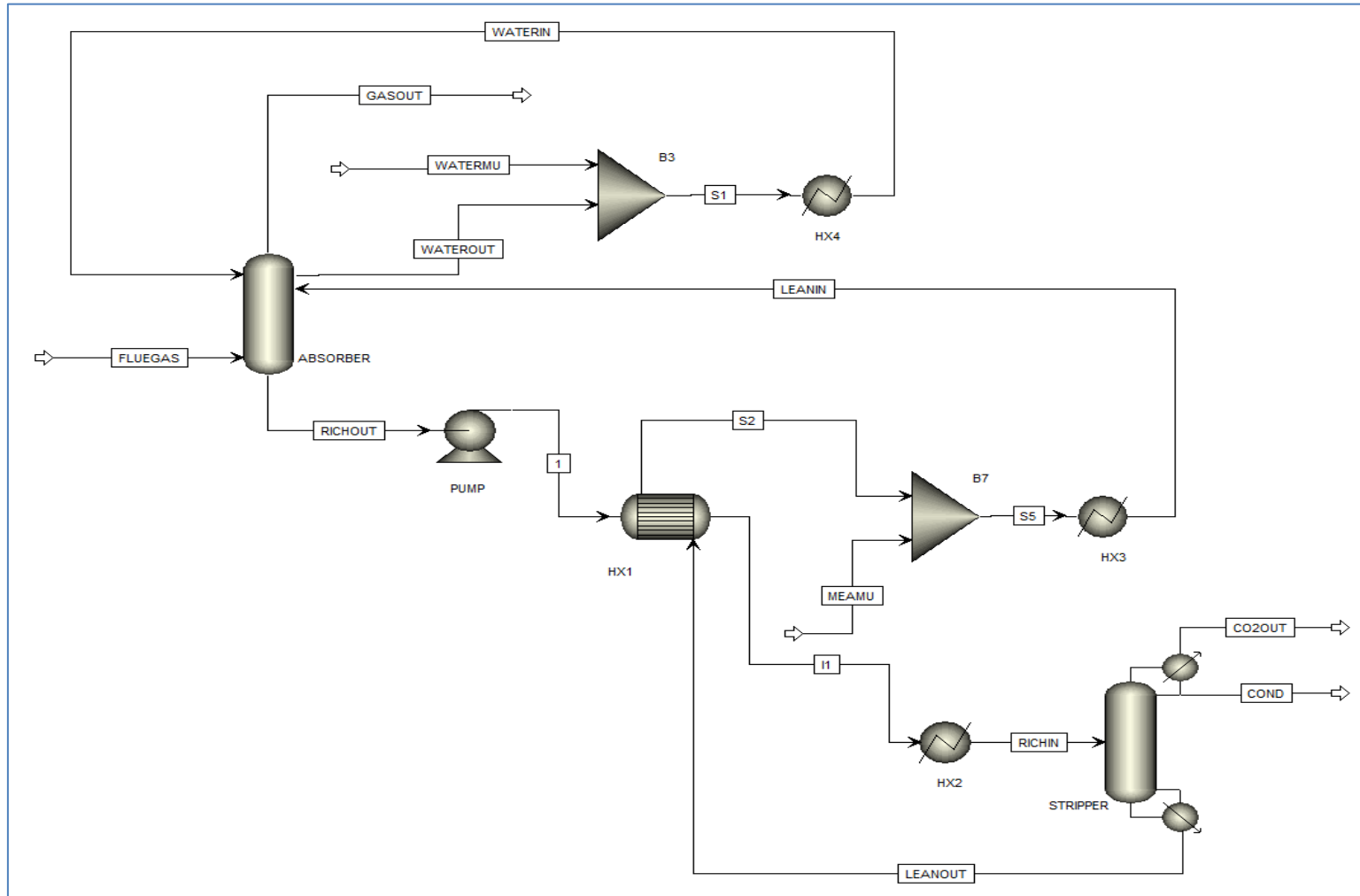


Figure 6.4. Process flow diagram of the model of the University of Kaiserslautern pilot plant as implemented in Aspen Plus®.

6.4 Model Validation

6.4.1 Validation of the UKCCSRC/PACT Pilot Plant Model

The comparison between pilot plant results and simulation results for the CO₂ capture plant is given in **Table 6.6**, which also includes the uncertainties in the pilot plant values. The average values of some of the experimental data logged over a period of 24 hours were used in setting up the Aspen plus model for the CO₂ capture plant. The set of values in **Table 6.6** with shaded background are calculated values after the closed-loop model of the CO₂ capture plant converged. As may be seen from **Table 6.6**, the model results are in good agreement with the experimental results. The relatively high values obtained for the specific reboiler duty is due to the liquid/gas ratio used in the experiments. The experimental liquid/gas ratios for the two cases presented in **Table 6.6** are sub-optimal and this fact underscores the need for some modelling work to be carried out before experiments are conducted so that effort and time will be targeted at the optimal operating regime. It also goes to show that modelling and experiment complement each other and both should run concurrently if possible.¹⁴⁷

Table 6.6. Comparison of experimental and simulation results for the UKCCSRC/PACT CO₂ capture pilot plant.¹⁴⁷

	L/G = 1.86 kg/kg		L/G = 3.77 kg/kg	
	Experiment	Simulation ^e	Experiment	Simulation ^e
Flue gas flowrate (Nm ³ /hr) ^d	207.3±1.8	207.3	192.1±1.6	192.1
Flue gas temperature (°C) ^d	41.3±0.5	41.3	39.4±0.3	39.4
Flue gas pressure (barg) ^d	0.17±0.02	0.17	0.19±0.01	0.19
Flue gas composition ^d				
CO ₂ (mol%)	4.48±0.11	4.48	4.55±0.11	4.55
H ₂ O (mol%)	-	2.96	-	2.96
O ₂ (mol%)	-	17.04	-	17.04
N ₂ (mol%)	-	75.52	-	75.45
CO ₂ in flue gas (kg/hr)	18.23±0.16	18.23	17.17±0.14	17.17

MEA concentration (wt%)	28.2±0.1	28.2	25.6±0.1	25.6
Lean MEA flowrate (kg/hr)	515.6±5.4	515.6	964.3±8.5	964.3
Lean MEA temperature (°C)	39.9±0.9	39.9	40±0.5	40
Lean MEA CO ₂ loading (mol/mol)	0.246±0.001	0.246	0.153±0.001	0.153
Condenser pressure (barg)	0.20±0.02	0.20	0.20±0.02	0.20
Rich MEA CO ₂ loading (mol/mol)	0.409±0.001	0.416	0.247±0.001	0.249
CO ₂ injected (kg/hr)	12.00±0.5	11.86	12.00±0.5	11.25
CO ₂ captured (kg/hr)	16.47±0.40	16.98	16.30±0.59	16.35
CO ₂ capture efficiency (%)	90.35±3.00	93.14	94.93±4.20	95.23
Specific reboiler duty (MJ/kg CO ₂)	5.92±0.80	5.47	13.27±2.21	17.25

^dAbsorber inlet

^eValues in shaded background are calculated values

6.4.2 Validation of the University of Kaiserslautern Pilot Plant Model

The validation of the University of Kaiserslautern pilot plant model was accomplished using the comprehensive pilot plant results reported by Notz et al.¹⁴⁸ The model validation strategy targeted the CO₂ capture rate reported and by varying the stripper reboiler duty. **Table 6.7** shows how the key pilot plant results compare with the model results for the 47 experiments reported by Notz et al.¹⁴⁸ Furthermore, **Figure 6.5** to **Figure 6.17** show how the temperature profiles in the absorber and stripper calculated by the model compare with the pilot plant data for the complete set of parametric studies reported by Notz et al.¹⁴⁸

Figure 6.5 to **Figure 6.8** show the changes in the temperature profiles in the absorber and stripper with the variation of the solvent flowrate. **Figure 6.5** to **Figure 6.7** show the temperature profiles in the absorber and stripper for gas-fired condition, while **Figure 6.8** shows the temperature profiles in the

absorber and stripper for coal-fired condition. It is clear from **Figure 6.5** to **Figure 6.8** that the model captures the temperature profile in the absorber and stripper better for coal-fired condition than it did for gas-fired condition. The reason for the better prediction of the temperature profile in the absorber and stripper for coal-fired condition is because of the higher lean CO₂ loading associated with coal-fired condition when compared with that of gas-fired condition. The changes in the temperature profile in the absorber with the variation of the solvent flowrate are shown in **Figure 6.5(a)** to **Figure 6.8(a)**, while the changes in the temperature profile in the stripper with the variation of the solvent flowrate are shown in **Figure 6.5(b)** to **Figure 6.8(b)**. From **Figure 6.5(a)** to **Figure 6.8(a)**, it is clear that the temperature bulge shifts from the top of the column (packed height = 0) towards the bottom of the column as the solvent flowrate (i.e. L/G, since the gas flow rate is held constant) increases and this observation is in line with the paper by Kvamsdal and Rochelle.¹⁵⁷ Also, from **Figure 6.5(b)** to **Figure 6.8(b)**, the temperature profile in the stripper is approximately constant across the stripper column for a given solvent flowrate and the accuracy of the model prediction increases as the solvent flowrate increases because of the high lean CO₂ loading associated with high solvent flowrate for a given CO₂ capture rate.

Figure 6.9 shows the changes in the temperature profile in the absorber and stripper with the variation of the stripper pressure. It is clear from **Figure 6.9(a)** that the temperature profile in the absorber is more or less independent of the stripper pressure. On the other hand, the temperature profile in the stripper depends on the operating pressure of the stripper as shown in **Figure 6.9(b)**. Furthermore, it is clear from **Figure 6.9(b)** that the temperature in the stripper increases as the operating pressure of the stripper is increased, and the reason is because of the increase in the boiling temperature of the solvent in the reboiler as the operating pressure of the stripper is increased.

The changes in the temperature profile in the absorber with the variation of MEA mass fraction are shown in **Figure 6.10(a)** and **Figure 6.11(a)** for gas-fired condition and coal-fired condition, respectively, while the changes in the temperature profile in the stripper with the variation of MEA mass fraction are shown in **Figure 6.10(b)** and **Figure 6.11(b)** for gas-fired condition and coal-fired condition, respectively. From **Figure 6.10(a)** and **Figure 6.11(a)**, it is clear that the temperature bulge shifts slightly from the bottom of the column towards the top of the column as the mass fraction of MEA

increases. Furthermore, the magnitude of the temperature bulge increases with an increase in the MEA mass fraction because of the increase in the heat of CO₂ absorption as the MEA mass fraction increases. The temperature in the stripper decreases as the MEA mass fraction increases as shown in **Figure 6.10(b)** and **Figure 6.11(b)**, and the reason for the decrease is because of the increase in the lean CO₂ loading as MEA mass fraction increases for a given CO₂ capture rate. Furthermore, it is clear from **Figure 6.10(b)** to **Figure 6.11(b)** that the model captures the temperature profile in the stripper better for coal-fired condition than it did for gas-fired condition and the reason is because of the higher lean CO₂ loading associated with coal-fired condition when compared with that of gas-fired condition.

The changes in the temperature profile in the absorber and stripper with the variation of the lean solvent temperature is shown **Figure 6.12**. It is clear from **Figure 6.12(a)** that the temperature in the absorber increases as the lean solvent temperature is increased; thus the increase in the heat of CO₂ absorption as the lean solvent temperature is decreased is not enough to compensate for the decrease in the lean solvent temperature. On the other hand, the temperature profile in the stripper is more or less independent of the lean solvent temperature as shown in **Figure 6.12(b)**.

Figure 6.13 shows the changes in the temperature profile in the absorber and stripper with the variation of the CO₂ partial pressure in the flue gas. It is clear from **Figure 6.13(a)** that the temperature in the absorber increases as the CO₂ partial pressure in the flue gas increases, and the reason for the temperature increase is because of the increase in the heat of CO₂ absorption as the CO₂ partial pressure in the flue gas is increased. On the other hand, the temperature in the stripper decreases as the CO₂ partial pressure in the flue gas is increased as shown in **Figure 6.9(b)**. The reason for the temperature decrease is because, for a given percent CO₂ capture level, the required lean CO₂ loading increases as the CO₂ partial pressure in the flue gas is increased. Furthermore, the model captures the temperature profile in the absorber and stripper better as the CO₂ partial pressure in the flue gas is increased, and the reason for the better prediction of the temperature profile is because the required lean CO₂ loading increases as the CO₂ partial pressure in the flue gas is increased.

Figure 6.14 shows the changes in the temperature profile in the absorber and stripper with the variation of the mass flowrate of the flue gas entering the bottom of the absorber and at a constant liquid/gas ratio of 2.8. From

Figure 6.14(a) it is clear that the temperature profile in the absorber does not change much when the mass flowrates of the flue gas and the lean solvent are simultaneously increased by the same factor. On the other hand, the temperature profile in the stripper depends on the mass flowrates of the flue gas and the lean solvent as shown in **Figure 6.14(b)**. Furthermore, it is clear from **Figure 6.14(b)** that the temperature in the stripper increases as the mass flowrates of the flue gas and the lean solvent are increased, and the reason is because the required lean CO₂ loading decreases as the mass flowrates of the flue gas and the lean solvent increase.

Figure 6.15 and **Figure 6.16** show the changes in the temperature profiles in the absorber and stripper with the variation of the CO₂ removal rate. The changes in the temperature profile in the absorber with the variation of the CO₂ removal rate are shown in **Figure 6.15(a)** and **Figure 6.16(a)** for gas-fired condition and coal-fired condition, respectively, while the changes in the temperature profile in the stripper with the variation of the CO₂ removal rate are shown in **Figure 6.15(b)** and **Figure 6.16(b)** for gas-fired condition and coal-fired condition, respectively. From **Figure 6.15(a)** and **Figure 6.16(a)**, it is clear that the temperature in the absorber increases as the CO₂ removal rate is increased, and the reason for the temperature increase is because of the increase in the heat of CO₂ absorption. Similarly, the temperature in the stripper increases as the CO₂ removal rate is increased as shown in **Figure 6.15(b)** and **Figure 6.16(b)**, and the reason for the increase is because of the decrease in the required lean CO₂ loading as the CO₂ removal rate is increased. Again, it is clear from a comparison of **Figure 6.15** and **Figure 6.16** that the model captures the temperature profiles in the absorber and the stripper more accurately for coal-fired condition than for gas-fired condition.

The changes in the temperature profile in the absorber and stripper with the variation of the flue gas temperature is shown **Figure 6.17**. It is clear from **Figure 6.17(a)** that the temperature in the absorber increases as the flue gas temperature is increased; thus the increase in the heat of CO₂ absorption as the flue gas temperature is decreased is not enough to compensate for the decrease in the flue gas temperature. Similarly, the temperature in the stripper increases as the flue gas temperature is increased as shown in **Figure 6.17(b)**. The reason for the increase is because the required lean CO₂ loading decreases, due to the decrease in the rich CO₂ loading, as the flue gas temperature is increased.

In summary, it is clear from **Table 6.7** and **Figure 6.5** to **Figure 6.17** that the model predictions are in good agreement with the reported pilot plant results. The average percent absolute deviations of the model results for the lean CO₂ loading, the rich CO₂ loading, and the specific reboiler duty, when compared with the 47 experimental cases reported by Notz et al.¹⁴⁸, are 7.99%, 4.19%, and 7.14%, respectively. The percent absolute deviations of the model results are in good agreement with the maximum uncertainties (6% for the reboiler duty, and 2% for the CO₂ loading) in the pilot plant results reported by Notz et al.¹⁴⁸. It is important to note that Notz et al.¹⁴⁸ reported a maximum uncertainty of 5% for the CO₂ capture rate, which may have manifested in the relatively high uncertainties of the CO₂ loadings calculated by the model. Since the 2% uncertainty in the CO₂ loading is smaller than the 5% uncertainty in the CO₂ capture rate, a different simulation approach which targeted the reported lean CO₂ loading as against the CO₂ capture rate was investigated and more satisfactory results were obtained (see **Section 7.4.1, Chapter 7**).

Table 6.7. Comparison of the key pilot plant and simulation results for the University of Kaiserslautern CO₂ capture pilot plant.

Exp No.	Lean Loading (mol/mol)		Rich Loading (mol/mol)		Specific Reboiler Duty (MJ/kg CO ₂)	
	Pilot plant	Model	Pilot plant	Model	Pilot plant	Model
1	0.265	0.282	0.386	0.400	5.01	4.88
2	0.308	0.326	0.464	0.477	3.98	3.77
3	0.230	0.217	0.308	0.299	7.18	8.29
4	0.268	0.283	0.397	0.404	5.05	5.20
5	0.306	0.325	0.446	0.463	4.19	3.79
6	0.317	0.333	0.464	0.485	3.85	3.77
7	0.356	0.363	0.478	0.483	3.91	3.88
8	0.228	0.238	0.444	0.453	4.22	4.03
9	0.147	0.151	0.393	0.398	5.49	5.73
10	0.299	0.315	0.402	0.425	5.65	5.14
11	0.28	0.304	0.396	0.420	5.12	4.76
12	0.256	0.289	0.372	0.409	4.91	4.49
13	0.287	0.307	0.400	0.424	4.52	4.53
14	0.253	0.242	0.369	0.362	5.48	5.66

15	0.241	0.223	0.359	0.341	5.81	6.05
16	0.096	0.115	0.414	0.421	7.38	6.07
17	0.166	0.172	0.371	0.384	5.47	5.28
18	0.215	0.192	0.387	0.362	5.35	5.39
19	0.247	0.195	0.354	0.296	6.27	7.91
20	0.261	0.259	0.395	0.386	5.10	5.17
21	0.270	0.263	0.400	0.378	5.18	5.10
22	0.263	0.269	0.389	0.399	5.10	4.95
23	0.274	0.273	0.393	0.401	5.11	5.10
24	0.251	0.242	0.392	0.386	5.11	5.28
25	0.166	0.071	0.435	0.352	5.46	8.49
26	0.288	0.285	0.474	0.474	4.13	4.21
27	0.169	0.131	0.501	0.468	4.77	5.09
28	0.266	0.275	0.470	0.481	3.68	3.93
29	0.306	0.322	0.465	0.477	3.92	4.10
30	0.316	0.313	0.459	0.463	4.38	3.94
31	0.338	0.324	0.454	0.460	4.3	3.83
32	0.335	0.325	0.449	0.454	4.57	4.48
33	0.360	0.339	0.441	0.452	4.35	4.26
34	0.146	0.175	0.417	0.456	4.85	4.23
35	0.208	0.222	0.411	0.445	4.27	4.22
36	0.252	0.266	0.393	0.419	4.68	4.57
37	0.296	0.283	0.398	0.399	5.11	4.85
38	0.308	0.292	0.385	0.386	5.40	5.04
39	0.319	0.292	0.400	0.379	5.23	5.23
40	0.111	0.129	0.297	0.310	10.24	9.26
41	0.130	0.146	0.297	0.302	9.76	8.83
42	0.190	0.216	0.310	0.331	7.16	6.77
43	0.200	0.223	0.318	0.336	6.87	6.54
44	0.209	0.223	0.314	0.320	7.18	7.00
45	0.219	0.221	0.324	0.313	7.09	7.31
46	0.318	0.324	0.417	0.427	4.68	4.40
47	0.255	0.256	0.366	0.376	5.50	5.31

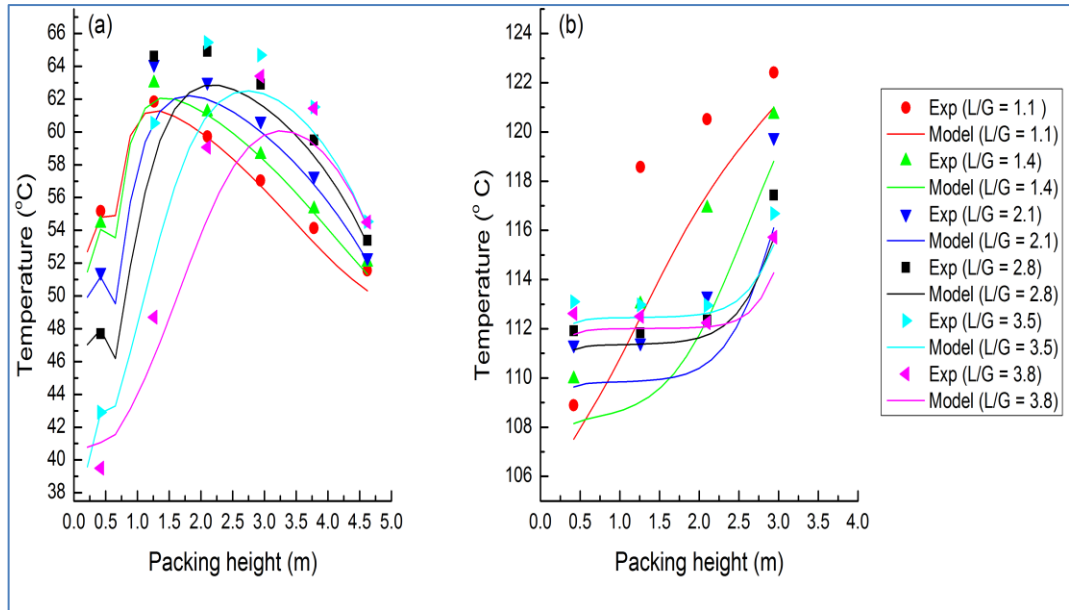


Figure 6.5. Variation of the solvent flowrate at constant flue gas rate of approximately 71.2 kg/h, constant CO₂ partial pressure of approximately 54.7 mbar in the flue gas, and constant CO₂ capture rate of approximately 76%. (a) Temperature profile in the absorber. (b) Temperature profile in the stripper.

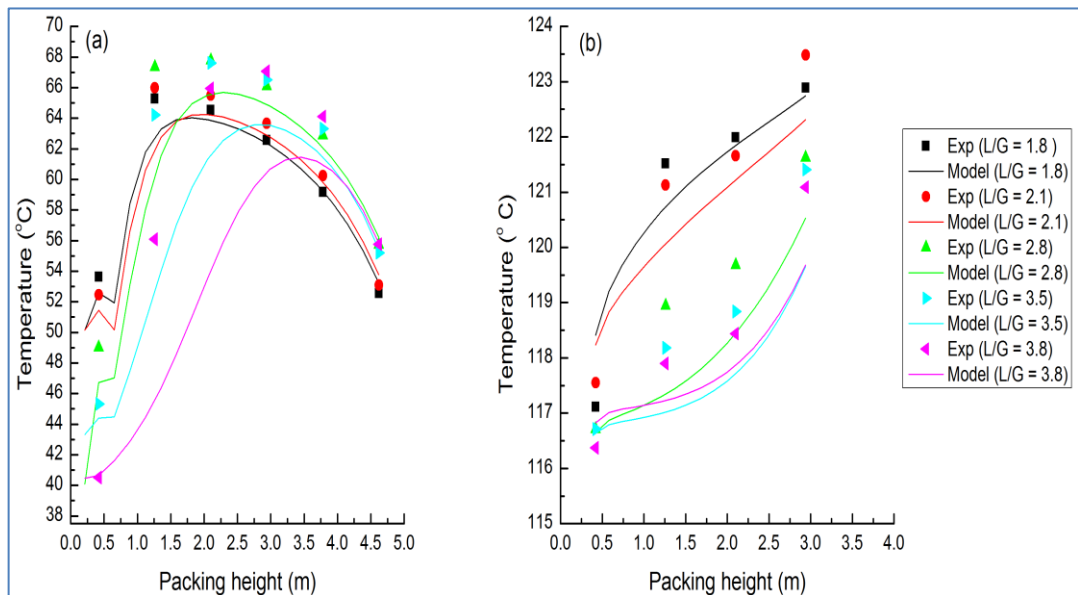


Figure 6.6. Variation of the solvent flowrate at constant flue gas rate of approximately 70.8 kg/h, constant CO₂ partial pressure of approximately 53.7 mbar in the flue gas, and constant CO₂ capture rate of approximately 88%. (a) Temperature profile in the absorber. (b) Temperature profile in the stripper.

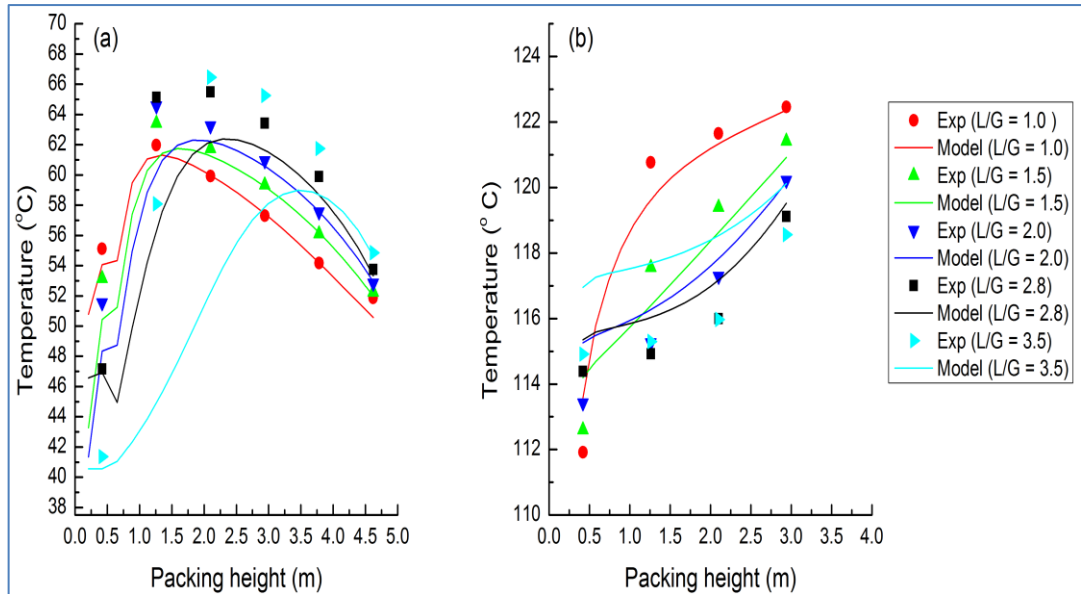


Figure 6.7. Variation of the solvent flowrate at constant flue gas rate of approximately 99.6 kg/h, constant CO₂ partial pressure of approximately 57.1 mbar in the flue gas, and constant CO₂ capture rate of approximately 75%. (a) Temperature profile in the absorber. (b) Temperature profile in the stripper.

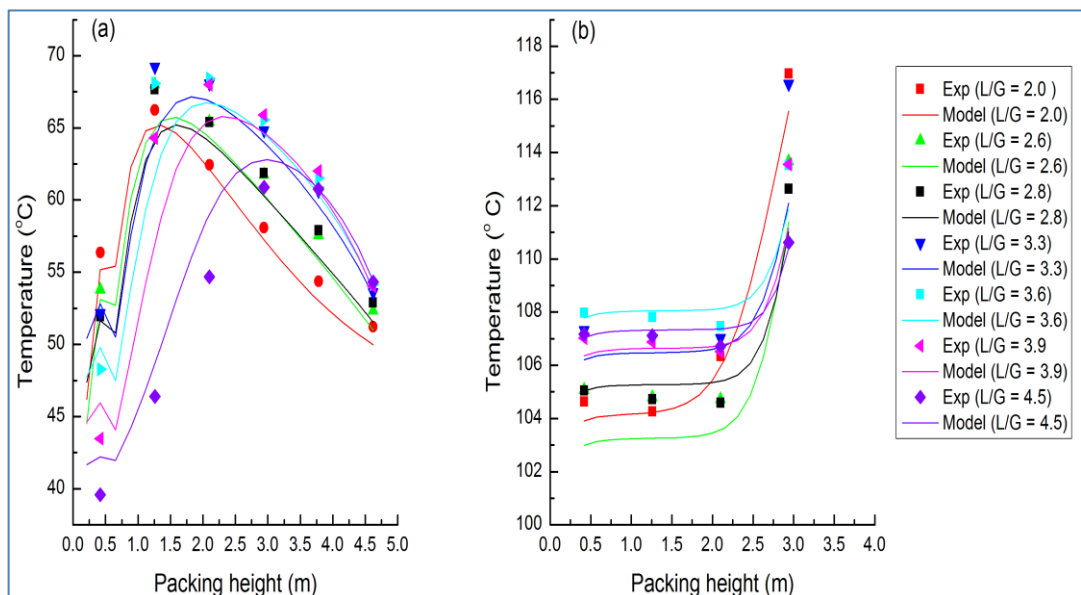


Figure 6.8. Variation of the solvent flowrate at constant flue gas rate of approximately 75.5 kg/h, constant CO₂ partial pressure of approximately 107.5 mbar in the flue gas, and constant CO₂ capture rate of approximately 54%. (a) Temperature profile in the absorber. (b) Temperature profile in the stripper.

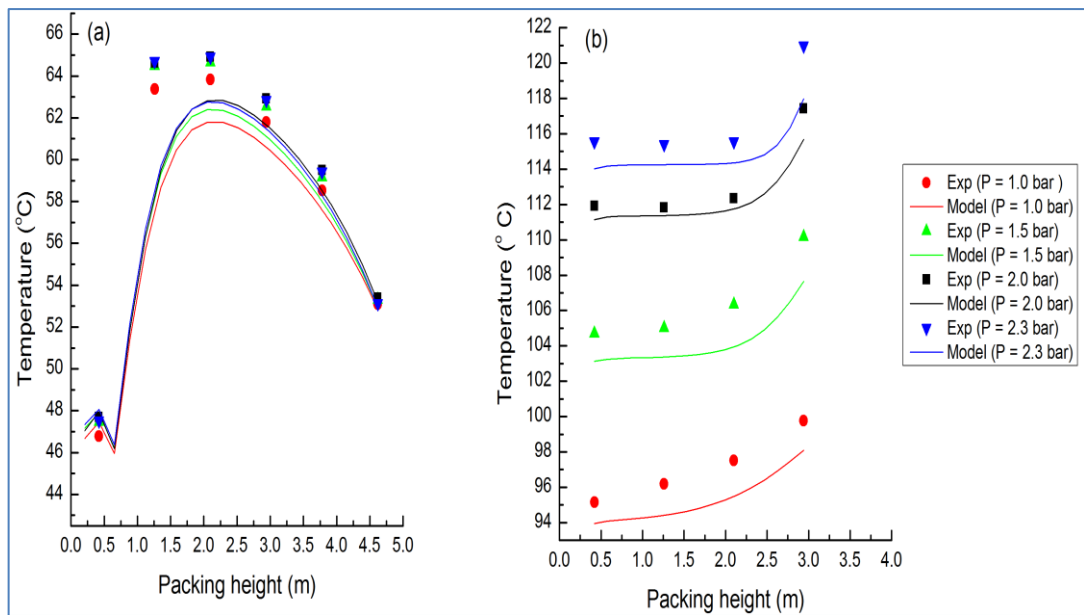


Figure 6.9. Variation of the stripper pressure. (a) Temperature profile in the absorber. (b) Temperature profile in the stripper.

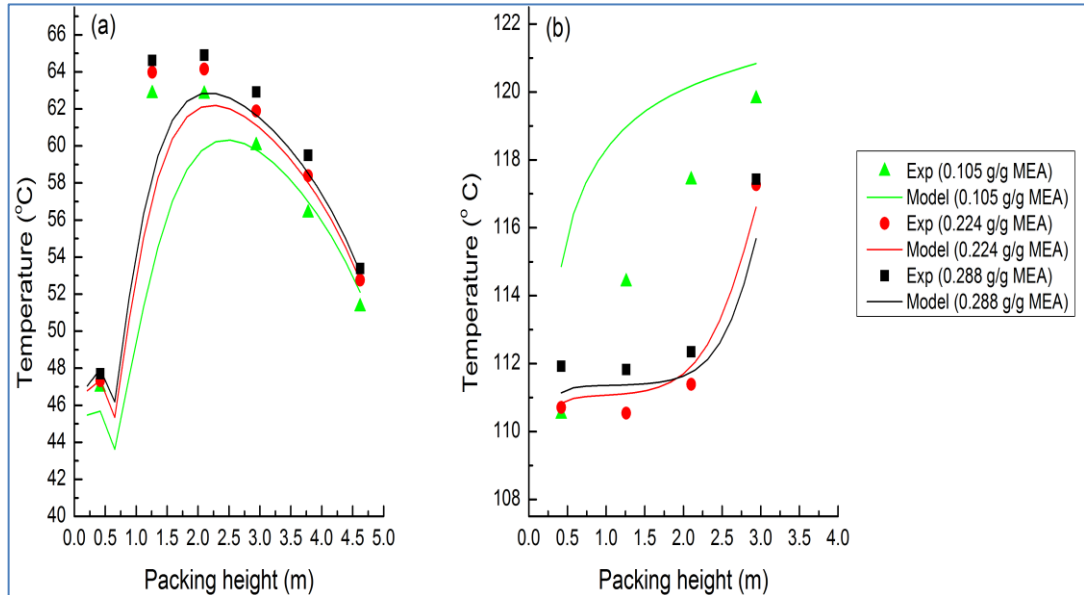


Figure 6.10. Variation of MEA mass fraction at a constant CO₂ partial pressure of approximately 55.5 mbar in the flue gas. (a) Temperature profile in the absorber. (b) Temperature profile in the stripper.

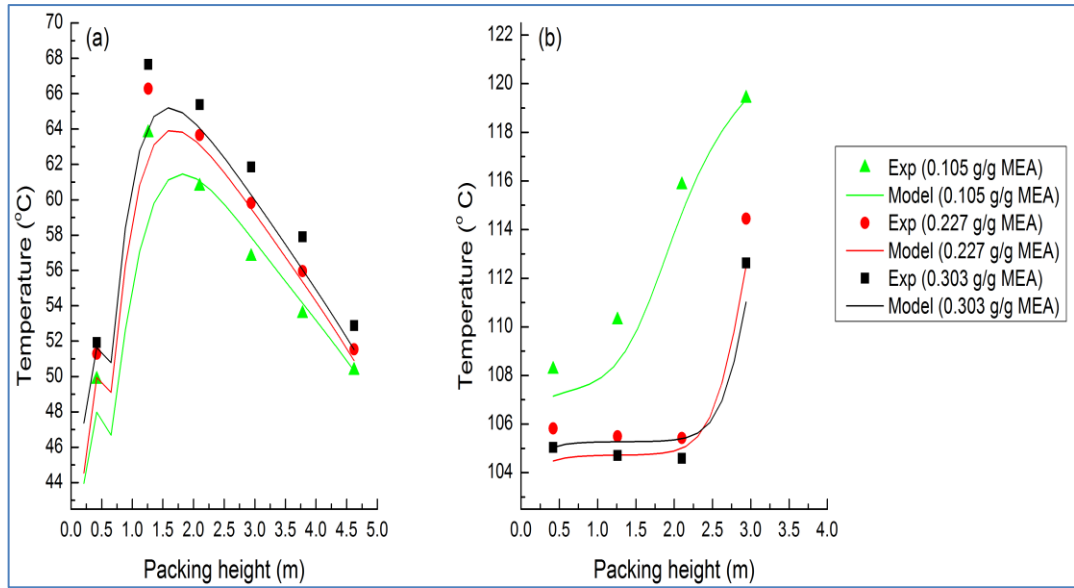


Figure 6.11. Variation of MEA mass fraction at a constant CO₂ partial pressure of approximately 109.5 mbar in the flue gas. (a) Temperature profile in the absorber. (b) Temperature profile in the stripper.

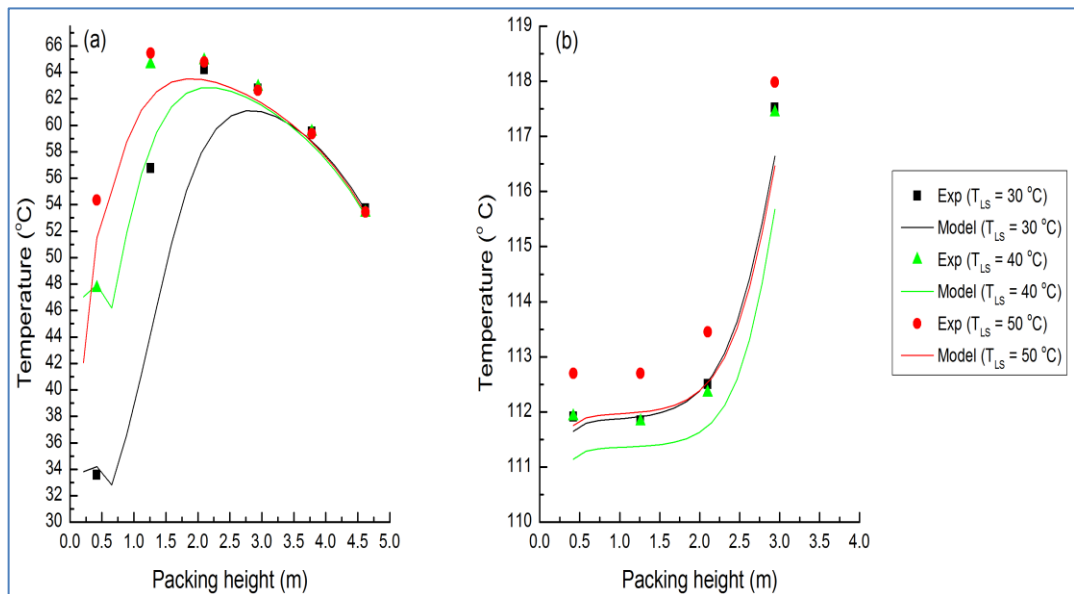


Figure 6.12. Variation of the lean solvent temperature. (a) Temperature profile in the absorber. (b) Temperature profile in the stripper.

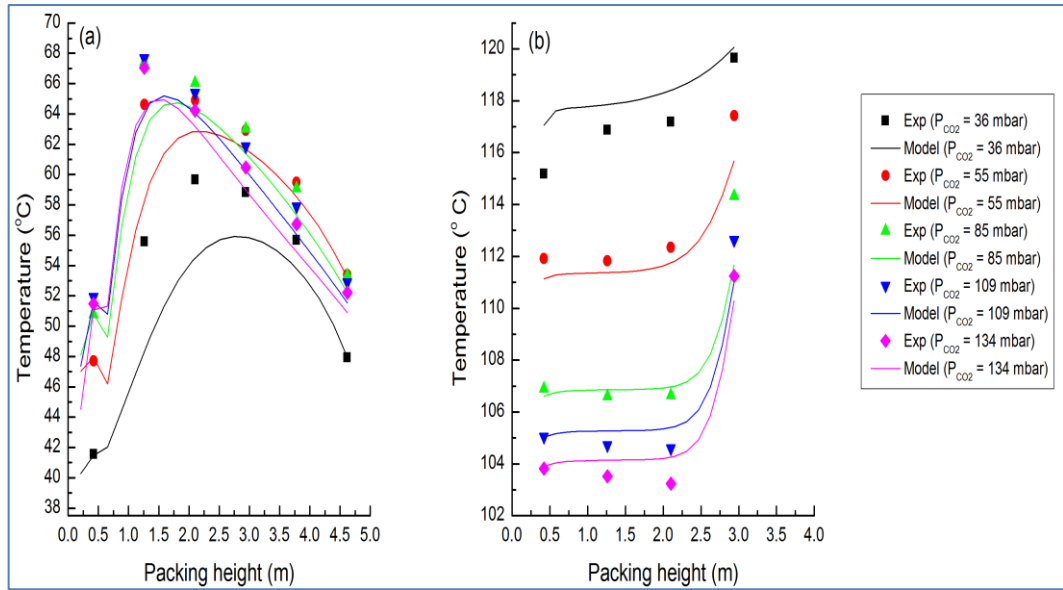


Figure 6.13. Variation of the CO₂ partial pressure in the flue gas. (a) Temperature profile in the absorber. (b) Temperature profile in the stripper.

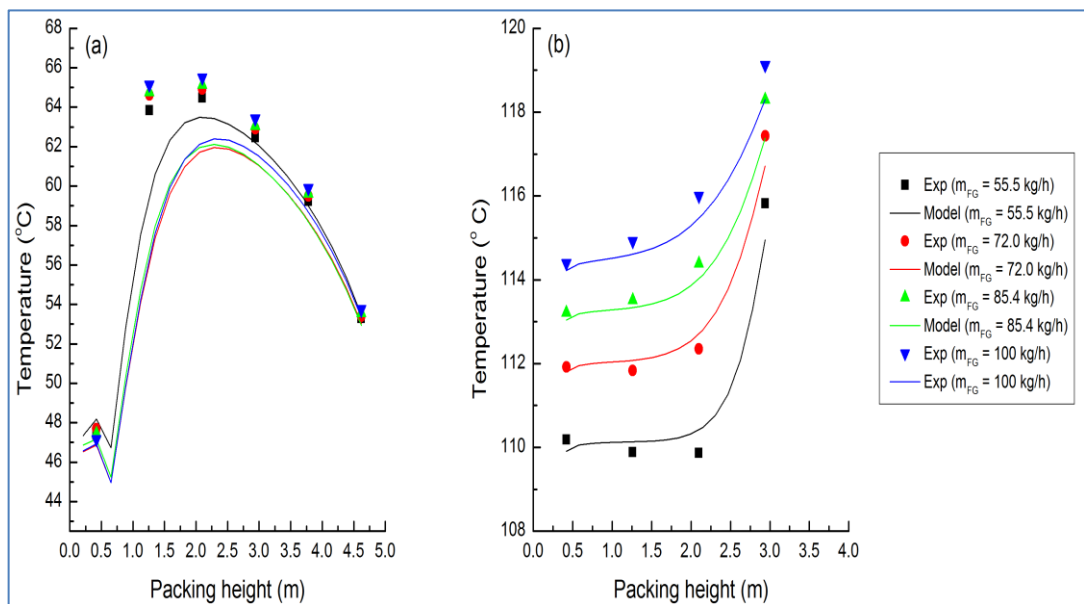


Figure 6.14. Variation of the fluid dynamic load (F-factor) in the absorber at a constant liquid/gas ratio of 2.8. (a) Temperature profile in the absorber. (b) Temperature profile in the stripper.

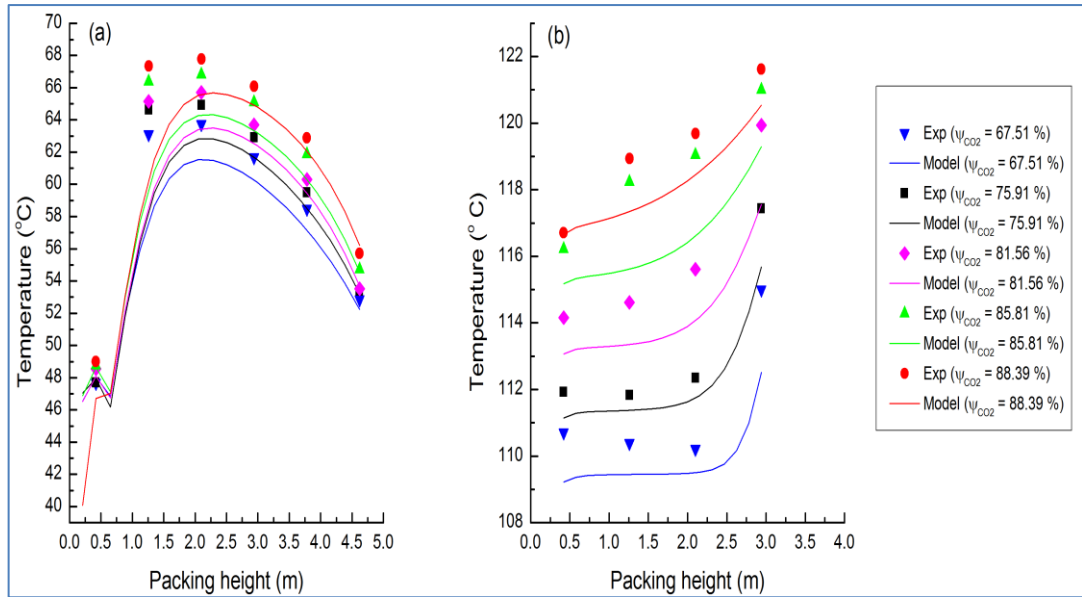


Figure 6.15. Variation of the CO₂ removal rate at a CO₂ partial pressure of approximately 54.6 mbar. (a) Temperature profile in the absorber. (b) Temperature profile in the stripper.

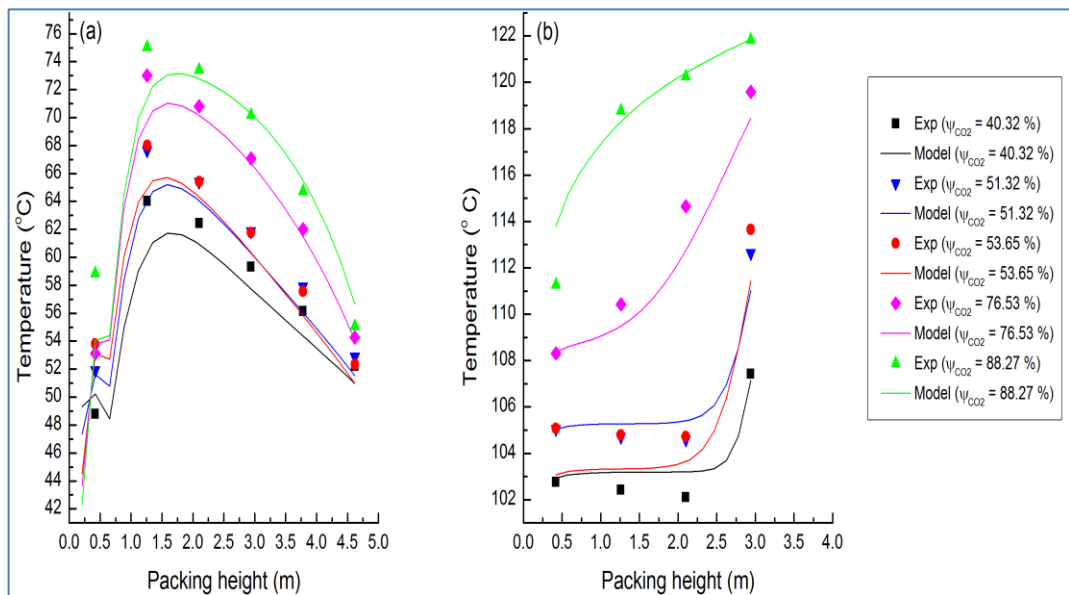


Figure 6.16. Variation of the CO₂ removal rate at a CO₂ partial pressure of approximately 109.6 mbar. (a) Temperature profile in the absorber. (b) Temperature profile in the stripper.

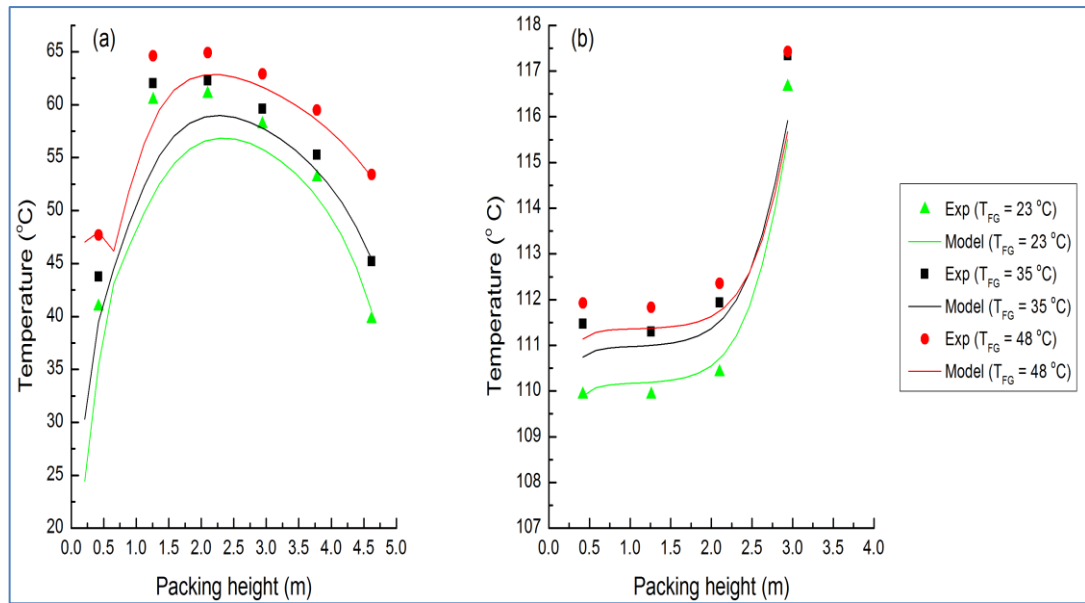


Figure 6.17. Variation of the flue gas temperature. (a) Temperature profile in the absorber. (b) Temperature profile in the stripper.

6.5 Conclusions

The UKCCSRC/PACT pilot plant and the University of Kaiserslautern pilot plant have been modelled in Aspen Plus[®] using rate-based calculation approach. The developed models of the pilot plants have been validated against pilot plant data from the pilot plants and the model results are in good agreement with the pilot plant data.

The experimental liquid/gas ratios for the UKCCSRC/PACT pilot plant cases are sub-optimal, which underscores the need for some modelling work before experiments are conducted so that effort and time will be targeted at the optimal operating regime.

The University of Kaiserslautern pilot plant model predictions are in good agreement with the reported pilot plant data. The average percent absolute deviations of the model results for the lean CO₂ loading, the rich CO₂ loading, and the specific reboiler duty, when compared with the 47 experimental cases reported by Notz et al.¹⁴⁸, are 7.99%, 4.19%, and 7.14%, respectively.

A different simulation approach which target the lean CO₂ loading as against the CO₂ capture rate is used in the model validation presented in **Chapter 7** and the validated model is used for scale-up design of commercial-scale amine-based CO₂ capture plants discussed in **Chapter 7**.

Chapter 7

Optimal Process Design of Commercial-scale Amine-based CO₂ Capture Plants

7.1 Introduction

Reactive absorption with aqueous solutions of amines in an absorber/stripper loop is the most mature technology for post combustion CO₂ capture (PCC).¹⁵⁸ The main barrier that remains unresolved is the huge energy requirement for solvent regeneration in the stripper. In fact, the reduction of solvent regeneration energy is the focus of most of the amine-based PCC research currently being performed globally. From the view point of current research and development (R&D) activities worldwide, three main areas are being investigated in order to reduce the regeneration energy requirement of amine-based PCC, namely: (a) development of new solvents with better overall performance than 30 wt% monoethanolamine (MEA) aqueous solution, which is generally considered as the base-line solvent for solvent-based PCC, (b) PCC process optimization, including modifications of PCC plant configuration, and (c) optimal integration of the PCC Plant, including the associated CO₂ compression system, to the upstream power plant.

In recent years, research activities aimed at testing new solvents, as well as the optimisation of solvent-based PCC, have resulted in several projects with the setting up of pilot plants globally.^{148,159-163} In most of the studies that have been reported, aqueous MEA solution is usually taken as the reference solvent to which new solvents are compared. Among the pilot-scale studies that have been reported for MEA, Notz et al.¹⁴⁸ have reported a very comprehensive set of results based on systematic studies of CO₂ capture with aqueous MEA solutions in a pilot plant and they also gave a fairly detailed description of the pilot plant with sufficient information and data to permit successful modelling of it.

Process modelling is critical in the scale-up of a pilot plant to a commercial-scale plant during design. There are several rigorous process modelling studies of the MEA-based CO₂ capture process at pilot-scale in the open literature, with many of them focusing on the absorber as a stand-alone

unit,^{27,151,164,165} or the stripper as a stand-alone unit,^{25,26,166} and some of them have considered the absorber and the stripper in a closed loop.^{150,167,168} However, in spite of the numerous process modelling and simulation studies of the MEA-based CO₂ capture process at pilot-scale that have been reported in the open literature, there is nothing freely available with complete information on the optimal design of amine-based CO₂ capture plants that can service commercial-scale coal-fired power plants, as well as onshore-based commercial-scale gas-fired power plants. It is important to state that some work on the design of commercial-scale MEA-based CO₂ capture plants for coal-fired and gas-fired power plants have been reported in the open literature¹⁶⁹⁻¹⁸² with minimal or incomplete information on the design process, and/or with partial or non-disclosure of the design results by most of them. However, the paper by Kvamsdal et al.,¹⁷³ which reported an optimised design of an MEA-based CO₂ capture plant for a 540 MWe (gross) NGCC power plant in an offshore application, is an exception because complete information on the design process was given in addition to full disclosure of the optimised design results. Apart from the paper by Kvamsdal et al.¹⁷³ most of the commercial-scale CO₂ capture plant designs that have been reported in the open literature are based on values of CO₂ loadings and/or solvent circulation rates without an openly available techno-economic consideration. As a consequence, most of the reported designs may be sub-optimal, and some of them appear to be unrealistic from practical and operational viewpoints when compared with the design data in the non-confidential report of the front end engineering design (FEED) study undertaken by Fluor[®] for the “ROAD project” (Rotterdam Opslag en Afvang Demonstratieproject; Rotterdam Capture and Storage Demonstration Project),¹⁸³ as well as statements in process licensor reports.^{48,184,185} For example, Lawal et al.,¹⁷⁷ while adopting CO₂ loadings of 0.29 mol/mol and 0.47 mol/mol for the lean MEA and the rich MEA solutions, respectively, used the generalized pressure drop correlation (GPDC) for packed columns to scale-up the pilot plant model that they developed with gPROMS[®], and they ended up with a commercial-scale CO₂ capture plant that can service a 500 MWe (net power without CO₂ capture) subcritical coal-fired power plant. Their design comprised of two absorbers, each with a diameter of 9 m based on an assumed pressured drop of 42 mm-H₂O/m, and a single stripper with a diameter of 9 m. The pressure drop they assumed as a basis for diameter sizing is about two times the maximum pressure drop that is recommended for amine systems, which are known to

be moderately foaming.^{186,187} Furthermore, based on the work by Cifre et al.,¹⁷¹ Lawal et al.¹⁷⁷ assumed a preliminary height of 17 m for each of the absorbers and ended up with a packed height of 27 m by varying the absorber height, but they did not report the stripper height. Their design results appear to be sub-optimal when compared with Fluor's design data for the ROAD demonstration project, and there may be operational issues with their design because of the large pressure drop they assumed for the absorber diameter sizing. Similarly, Sipocz and Tobiesen¹⁷⁸ adopted 0.132 mol/mol and 0.473 mol/mol for the CO₂ loadings of the lean MEA and rich MEA solutions as the basis for scaling up the pilot plant model that they developed with the CO2SIM software to a commercial-scale CO₂ capture plant that can service a 410.6 MWe (gross power without CO₂ capture) natural gas combined-cycle (NGCC) power plant. Their design comprised of a single absorber with a 9.13 m diameter and a height of 26.9 m, and a single stripper with a diameter of 5.5 m and a height of 23.5 m. Their design results appear to be unrealistic because it is very unlikely that a single absorber with 9.13 m diameter can handle the amount of flue gas they used as the basis for their design. Furthermore, Biliyok and Yeung¹⁷⁹ adopted CO₂ loadings of 0.234 mol/mol and 0.4945 mol/mol for the lean MEA and rich MEA solutions, respectively, and they used the method used by Lawal et al.¹⁷⁷ to design a commercial-scale CO₂ capture plant that can service a 440 MWe (gross power without CO₂ capture) NGCC power plant. They ended up with four absorbers, each having a diameter of 10 m and a height of 15 m, and a single stripper having a diameter of 9 m and a height of 15 m. The choice of four absorbers by Biliyok and Yeung¹⁷⁹ most likely followed the design reported by Hetland et al.,¹⁷² and/or Kvamsdal et al.,¹⁷³ which was a special design case for an offshore application where balanced distribution of structural weight is an important design factor since local concentration of dead weight could affect the stability of an offshore platform. Also, both Hetland et al.¹⁷² and Kvamsdal et al.¹⁷³ noted that operational flexibility informed their choice of four absorbers and a single stripper in their design, with one absorber servicing each of the four trains that make up the offshore NGCC power plant they used as a basis for their design. Therefore, the design by Biliyok and Yeung¹⁷⁹ is unlikely to be adopted in an onshore application because a 440 MWe (gross) NGCC power plant should require no more than two absorbers if optimally designed. **Table 7.1** summarizes and compares the commercial-scale designs reported by various authors in the open literature. It is clear from

Table 7.1 that, with the exception of the special design case by Kvamsdal et al.¹⁷³ for an offshore application, complete information on the optimal design of absorption and stripping columns for commercial-scale amine-based CO₂ capture plants is still lacking in the open literature, and it is this lack of information on the optimal design of the absorption and stripping columns for amine-based CO₂ capture plants in the open literature that motivated the work presented in this chapter.

7.2 Process Description

The basic flowsheet of an amine-based CO₂ capture process is shown in **Figure 7.1**. The process consists of countercurrent contact of the flue gas coming from a direct contact cooler (DCC) unit with an amine solution in a packed absorber. The rich flue gas enters the absorber at the bottom while the lean amine solution is introduced into the top of the absorber. The treated flue gas leaves the top of the absorber and is normally washed in a water-wash section (not shown in **Figure 7.1**) so as to remove entrained solvent droplets and, in turn, limit the loss of valuable solvents in addition to meeting environmental regulations on solvent emissions into the atmosphere. The rich solvent from the bottom of the absorber is sent to the stripper for CO₂ stripping after absorbing some of the heat in the lean solvent exiting the stripper bottom in a cross heat-exchanger.

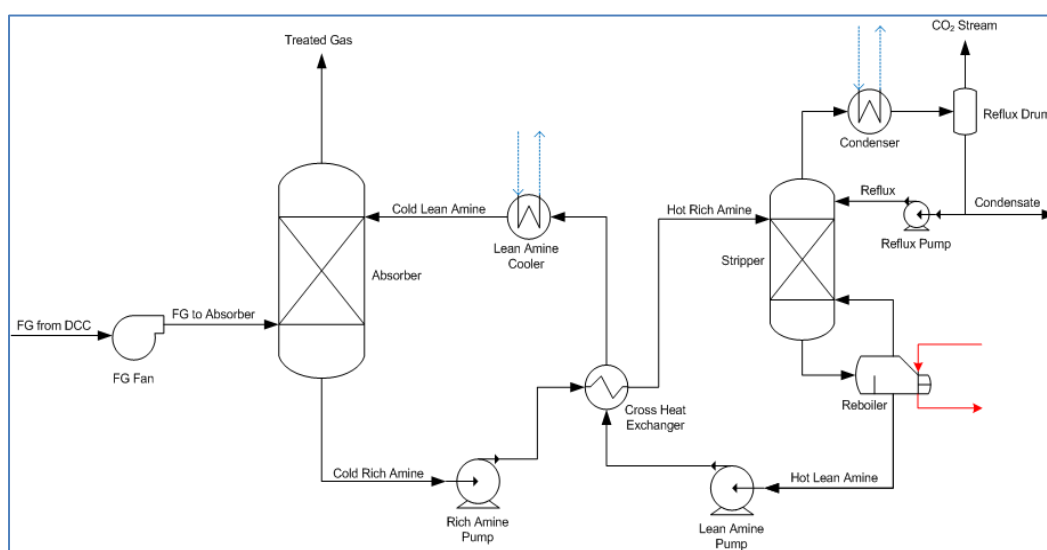


Figure 7.1. The basic flowsheet for an amine-based CO₂ capture process.

Table 7.1. Summary of the design data for the standard configuration of an MEA-based CO₂ capture process, including the key assumptions made, as reported by different authors in the open literature.

	Heuzeling and van den Weijde ¹⁸³	Cifre et al. ¹⁷¹	Lawal et al. ¹⁷⁷	Khalilpour and Abbas ¹⁸⁸	Hanak et al. ¹⁸²	Mac Dowell and Shah ¹⁸¹	Kvamdsdal et al. ¹⁷³	Sipocz and Tobiesen ¹⁷⁸	Biliyok and Yeung ¹⁷⁹
Power Plant type	Coal-fired (slip stream) ^a	Coal-fired (hard coal)	Coal-fired (subcritical)	Coal-fired (brown coal)	Coal-fired (supercritical)	Coal-fired (subcritical)	Gas-fired (NGCC)	Gas-fired (NGCC)	Gas-fired (NGCC)
Power plant size (MWe), Gross	250	600	500	300	660	660	540	410.6	440
Flue Gas Flowrate (kg/s)	>254	-	589.6	353.3	635.2	969.94	1045.6	639.61	693.6
Liquid Flowrate (kg/s)	-	2236.1	3122	590.132 ^b	3211.2	3879.76	908.40	433 ^b	721.6
Liquid/Gas Ratio (kg/kg)	-	-	5.30	1.67	5.06	4.0	0.87	0.68	1.04
Number of Absorber	1	1	2	2	3	1	4	1	4
Absorber Packing	-	IMTP50	IMTP40	50mm ceramic Berl Saddle	Mellapak 350X	50 mm ceramic Berl Saddle	Mellapak 250X	Mellapak 250	Mellapak 250X
Absorber Diameter (m)	12.8	-	9	10.32	12	20	9.6	9.13	10

Absorber Packed Height (m)	40.3	18	27	18.2	30	60	13.6	26.9	15
Number of Stripper	1	-	1	1	1	1	1	1	1
Stripper Packing	-	IMTP50	Flexipac 1Y	50 mm ceramic Berl Saddle	Mellapak 350X	50 mm ceramic Berl Saddle	Mellapak 250X	Mellapak 250	Mellapak 250X
Stripper Diameter (m)	7.5	-	9	9.67	15	10	6.2	5.5	9
Stripper Packed Height (m)	26.3	-	-	18.8	30	20	7.6	23.5	15
Lean Loading (mol/mol)	-	0.217	0.29	0.28	0.295	0.24	0.216	0.132	0.234
Rich Loading (mol/mol)	-	0.447	0.47	0.45	0.473	0.55	0.470	0.473	0.4945
Reboiler Duty (MW)	-	523.67	352.67	182.58	625.76	786.17	193.00	154.63	156.91
Sp. Reb Duty (MJ/kg CO ₂)	-	4.07	3.18	2.90	4.937	3.865	3.77	3.97	4.003

CO ₂ in Flue Gas (mol% wt%)	13.7 -	- -	14.05 20.9	13.00 19.80	- 22.17	15.87 23.05	3.50 5.43	4.20 -	3.996 -
MEA Conc. (kg/kg)	-	0.30	0.3048	0.3	0.3048	0.3	0.30	0.30	0.30
CO ₂ Capture Rate (%)	90	90	90	90	90	90.97	90	90	90
Stripper Pressure (bar)	-	2	1.62	1.62	1.7	1.85	1.912	1.92 ^c	1.5

^aThis is the non-confidential report for the FEED study undertaken by Fluor for the ROAD demonstration project.

^bLiquid circulation was calculated with a molar mass of 23.5 kg/kmol for the MEA solution.

^cRegenerator temperature of 122 °C was reported.

In the stripper, the downward flowing rich solvent is stripped of its absorbed CO₂ by the upward flowing steam generated by the reboiler. The vapour stream from the top of the stripper, which is essentially a mixture of CO₂, steam and some traces of the amine used, is partially condensed in a condenser and a fraction or all of the condensed liquid is returned to the top of the stripper as reflux. The uncondensed stream, which is mainly CO₂, is sent for compression, transportation and sequestration.

7.3 Process Design of Absorption and Stripping Columns

The process design of packed absorber and stripper columns entails the determination of the column diameter and the packed height needed to achieve a given separation, having chosen the solvent and packing type to be used. The design process is not a clear cut science but more of a combination of science and art based on experience. The column diameter for a given gas flowrate and liquid flowrate is usually determined based on two criteria: (i) the maximum pressure drop that can be tolerated and (ii) the approach to maximum capacity. The approach to maximum capacity can range from 70 to 86 percent of the flooding point velocity,^{186,187} but packed columns are more usually designed within 70 to 80 percent of the flood point velocity.¹⁸⁷ The column height needed to achieve a given separation is determined using the concept of height of transfer unit (HTU) or the height equivalent to a theoretical plate (HETP), but the use of HETP is usually the preferred approach.¹⁸⁷

7.3.1 Column Diameter Sizing

The column diameter (D) is related to the superficial velocity of the gas stream as follows:

$$D = \sqrt{\frac{4G}{\pi U_s}} \quad (7.3.1)$$

where G is the gas flowrate and U_s is the superficial velocity of the gas.

The superficial velocity of the gas stream is related to the packed column capacity factor by the following equation:^{41,186,187}

$$C_0 = U_s \left(\frac{\rho_G}{\rho_L - \rho_G} \right)^{0.5} F_p^{0.5} \nu^{0.05} \quad (7.3.2)$$

where C_0 is the capacity factor; ρ_G and ρ_L are the gas density and the liquid density, respectively; F_p is the packing factor of the packing in the column, and ν is the kinematic viscosity of the liquid.

The capacity factor for a packed column is a function of the flow parameter, X , and the pressured drop per unit height of the packing, ΔP . The flow parameter is defined by the following equation:^{41,186,187}

$$X = \frac{L}{G} \left(\frac{\rho_G}{\rho_L} \right)^{0.5} \quad (7.3.3)$$

where L is the liquid flowrate.

Although generalized pressure drop correlation (GPDC) charts have been developed for both random and structured packings,^{41,186,187} the more accurate vendor-developed pressure drop correlation for each specific packing is considered proprietary and is usually not disclosed by vendors. However, Aspen Tech has a special arrangement with packing vendors and, as a consequence, vendor correlations for pressure drop are built into Aspen Plus for several packings.

7.3.2 Packed Height based on HETP

The height equivalent to a theoretical plate (HETP) in a packed column for a stage designated by subscript j is given by:^{189,190}

$$\begin{aligned} HETP_j &= \frac{\ln \lambda_j}{\lambda_j - 1} \left(HTU_{G,j} + \lambda_j HTU_{L,j} \right) \\ &= \frac{\ln \lambda_j}{\lambda_j - 1} \left(\frac{u_{Gs}}{k_{G,j} a_{e,j}} + \lambda_j \frac{u_{Ls}}{k_{L,j} a_{e,j}} \right) \end{aligned} \quad (7.3.4)$$

with

$$\lambda_j = \frac{m_j G_j}{L_j} \quad (7.3.5)$$

where $HTU_{G,j}$ and $HTU_{L,j}$ are, respectively, the heights of transfer units for the gas and liquid phases in stage j ; λ_j is the stripping factor for stage j ; $k_{G,j}$ and $k_{L,j}$ are, respectively, the local mass-transfer coefficients for the gas and liquid phases; $a_{e,j}$ is the effective interfacial area per unit volume of the packed section in stage j ; u_{Gs} and u_{Ls} are, respectively, the superficial velocities for the gas and liquid phases; m_j is the local slope of the equilibrium line for stage j ; G_j and L_j are, respectively, the local flowrates of the gas and liquid streams to stage j . It is clear that the accuracy of the HETP calculated by Eq. (7.3.4) is a function of the accuracy of the correlations used for the mass-transfer coefficients, the effective interfacial area, the pressure drop, as well as the model for vapour-liquid-equilibrium (VLE).

The packed height required for a given separation is the summation of the HETPs of the stages in the packed column. Thus, for a column with N number of stages, the packed heights for an absorber (without condenser and reboiler) and a stripper (with a condenser and reboiler) are given as follows:

$$Z_{Absorber} = \sum_{j=1}^N HETP_j \quad (7.3.6)$$

$$Z_{Stripper} = \sum_{j=2}^{N-1} HETP_j \quad (7.3.7)$$

7.4 Model Validation at Pilot-scale and Design Philosophy

7.4.1 Aspen Plus Rate-based Model Validation at Pilot-scale

As previously explained in **Chapter 6**, the Aspen Plus[®] rate-based model was used to model the absorber and the stripper columns in the CO₂ capture plants. Although the model had previously been validated by Zhang et al.,^{150,151} there was a need to revalidate the rate-based model for the Sulzer Mellapak 250Y[™] structured packing used in the scale-up design cases

considered in this chapter. This was accomplished using the comprehensive pilot plant results reported by Notz et al.¹⁴⁸ The model validation strategy targeted the lean CO₂ loading by varying the stripper reboiler duty.

Figure 7.2(a) to Figure 7.2(c) show the parity plots for the CO₂ capture level, the stripper reboiler duty and the rich CO₂ loading, respectively, while **Figure 7.2(d)** shows the variation of the specific reboiler duty with liquid/gas ratio. The average percent absolute deviations of the model results for the CO₂ capture level, the stripper reboiler duty, and the rich CO₂ loading, when compared with the 47 experimental cases reported by Notz et al.,¹⁴⁸ are 3.75%, 5.08%, and 2.68%, respectively.

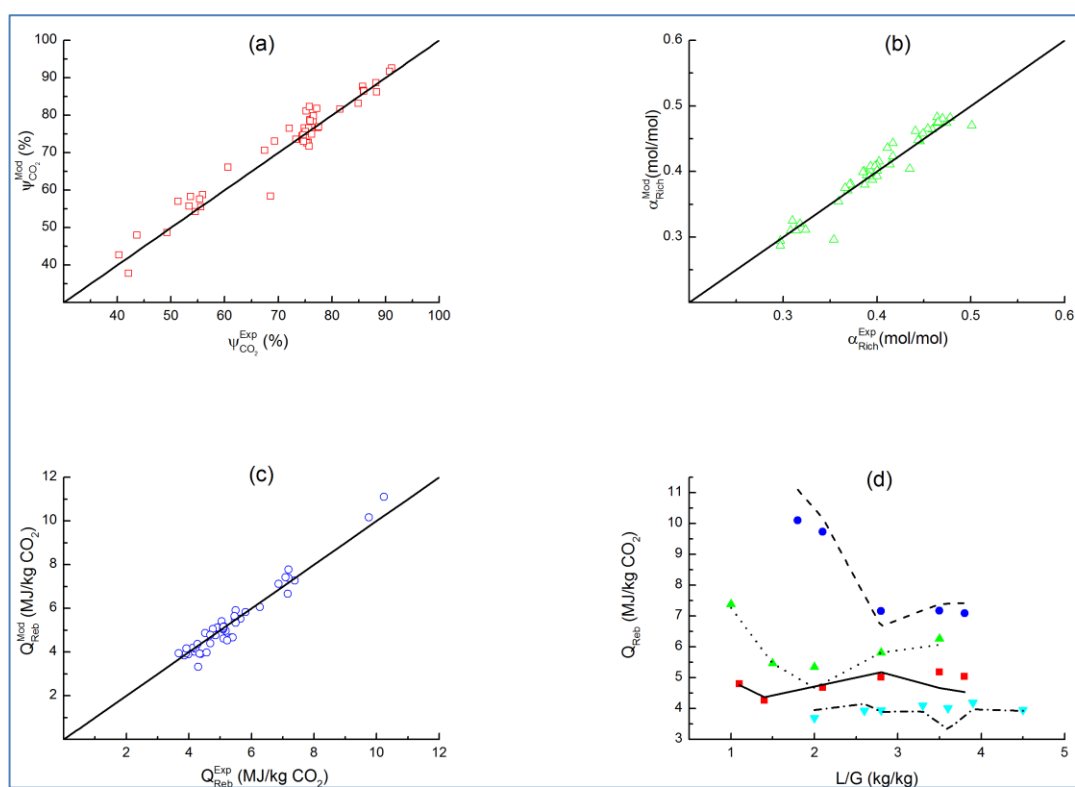


Figure 7.2. Comparison of key simulation results with the pilot plant results reported by Notz et al.¹⁴⁸ (a) CO₂ capture rate parity plot. (b) Rich CO₂ loading parity plot. (c) Specific reboiler duty parity plot. (d) Variations of specific reboiler duty with liquid/gas ratio for the sets of experiments designated as A.1 ($G = 71.2$ kg/h, $P_{CO_2} = 54.7$ mbar, and $\psi_{CO_2} = 76\%$), A.2 ($G = 70.8$ kg/h, $P_{CO_2} = 53.7$ mbar, and $\psi_{CO_2} = 88\%$), A.3 ($G = 99.6$ kg/h, $P_{CO_2} = 57.1$ mbar, and $\psi_{CO_2} = 75\%$), and A.4 ($G = 75.5$ kg/h, $P_{CO_2} = 107.5$ mbar, and $\psi_{CO_2} = 54\%$). ■, (A.1); ●, (A.2); ▲, (A.3); ▼, (A.4). Lines: —, Model (A.1); - -, Model (A.2); ···, Model (A.3); - · -, Model (A.4).

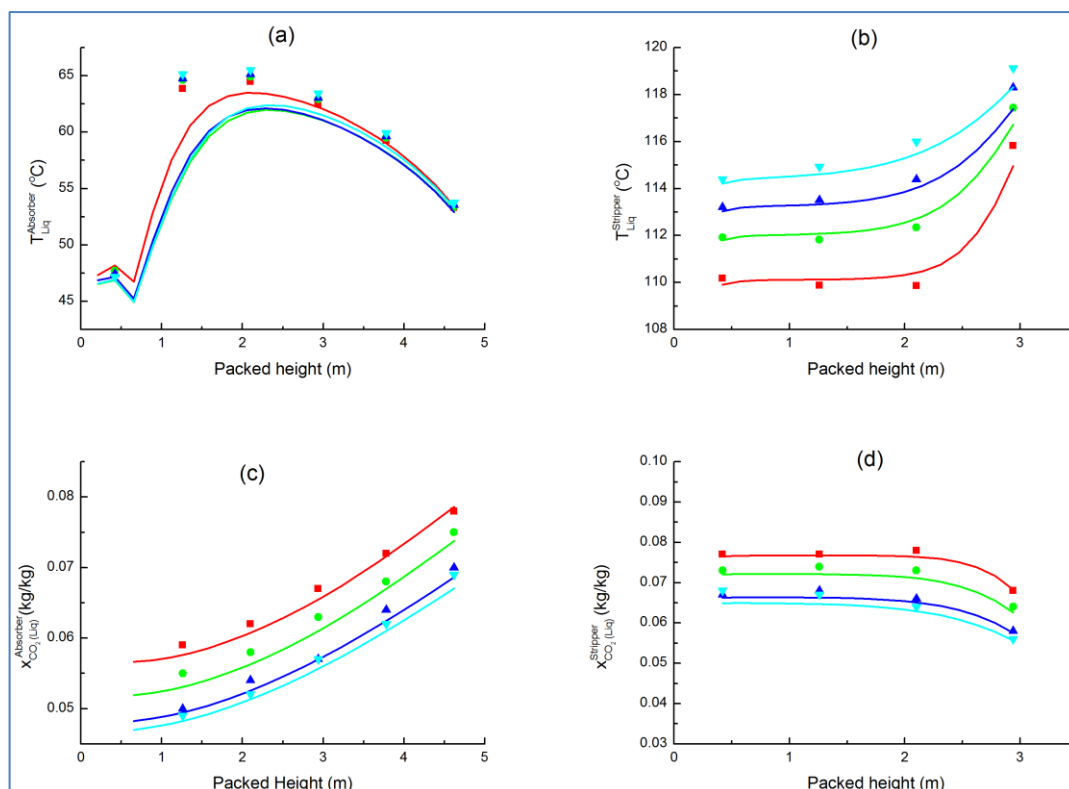


Figure 7.3. Comparison of absorber and stripper profile results at constant liquid/gas ratio ($L/G = 2.8$) with the pilot plant results reported by Notz et al.¹⁴⁸ (a) Liquid phase temperature profile in the absorber. (b) Liquid phase temperature profile in the stripper. (c) Liquid phase apparent CO_2 mass fraction in the absorber. (d) Liquid phase apparent CO_2 mass fraction in the stripper. ■, $G = 55.5$ kg/hr; ●, $G = 72.0$ kg/hr; ▲, $G = 85.4$ kg/hr; ▼, $G = 100.0$ kg/hr. Lines: —, Model ($G = 55.5$ kg/hr); —, Model ($G = 72.0$ kg/hr); —, Model ($G = 85.4$ kg/hr); —, Model ($G = 100.0$ kg/hr).

The percent absolute deviations of the model results are in good agreement with the maximum uncertainties (5% for the CO_2 capture level, 6% for the reboiler duty, and 2% for the CO_2 loading) in the pilot plant results reported by Notz et al.¹⁴⁸ Also, **Figure 7.3** shows how the temperature profiles in the absorber and stripper, as well as the CO_2 composition profiles in the absorber and stripper, compare with the experimental values reported by Notz et al.¹⁴⁸ for the set of experiments with a constant liquid/gas ratio. It is clear from **Figure 7.2** and **Figure 7.3** that the model predictions are in very good agreement with the experimental pilot plant results and hence the model may be confidently used as a basis for scale-up design within a conservative margin of $\pm 10\%$.

7.4.2 Design Philosophy Implementation in Aspen Plus®

The design philosophy for the commercial-scale plants uses two criteria to determine the diameters of the absorber and stripper columns for different liquid flowrates and lean amine CO₂ loadings, while Eqs. (7.3.6) and (7.3.7) are, respectively, used for the absorber height and the stripper height needed for 90% CO₂ capture. A capture rate of 90% was adopted for the design cases in this chapter because it is a commonly used basis for amine-based CO₂ capture plant design and evaluation in publications found in the open literature, including special and FEED study reports. The optimum designs were achieved based on economic analysis using Aspen Plus® Economic Analyzer, V8.4, which is based on the industry-standard Icarus Systems.¹⁹¹

The design philosophy was first implemented at pilot-scale, using the Mellapak 250Y structured packing in the absorber and stripper, and the pilot-scale design results were compared with the openly available design information for the pilot plant used by Notz et al.¹⁴⁸ Having validated the design philosophy at pilot-scale, it was then used directly for the commercial-scale design cases discussed in **Section 7.5**.

The column diameter for a given liquid flowrate was determined based on two recommended criteria for the design of aqueous amine systems, which are known to be moderately foaming. The criteria are a maximum fractional approach to flooding (or maximum operational capacity, MOC) of 0.8, and a maximum pressure drop per unit height of 20.83 mm-H₂O/m.^{186,187} The vendor correlation for Mellapak 250Y structured packing was used for pressure drop calculation. Further, the 1985 correlation of Bravo et al.¹⁵³ was used to calculate mass transfer coefficients and interfacial area for Mellapak 250Y structured packing, while the 1992 correlation of Bravo et al.¹⁵⁵ was used to calculate liquid holdup. The Chilton and Colburn correlation¹⁵⁶ was used to predict the heat transfer coefficient for the Mellapak 250Y structured packing. The correlations used for the pressure drop, mass transfer coefficients, liquid holdup, and heat transfer coefficient calculations are built into Aspen Plus®. Furthermore, with a rate-based calculation approach, the HETPs of the stages are calculated directly based on mass transfer theory. The calculated HETPs are the heights of the stages if they were to be assumed as equilibrium stages; thus, the summation of the HETPs for the stages gives the packed height of the column. An alternative way of determining the packed height is to multiply the average value of the HETPs

of the stages in the packed section by the number of stages in the packed section.

The packed height needed to achieve a given degree of separation is the sum of the HETPs of the stages that will achieve the given separation, starting from the top stage (stage 1 for the absorber or stage 2 for the stripper) and ending at the stage corresponding to the extent of separation specified. However, Aspen Plus requires that the total number of stages and the inlet stream stages be specified a priori before any calculation can be executed. In order to overcome this unavoidable limitation, a calculator block was used to automatically adjust the ending stage number of the packed section to the number of stages while fixing the starting stage of the packed section at 1 for the absorber or 2 for the stripper. Furthermore, the calculator block automatically adjusts the flue gas (feed) stage, the ending stage number for the reactions, and the ending stage number for the reaction holdup. Starting with a total stage number of 2, the number of stages in the absorber was automatically increased in steps of 1, using a sensitivity block until the desired CO₂ capture level was achieved, which was taken as 90%. Data logging of the calculated results of interest in each “pass” was realized using the same sensitivity block that increased the number of stages. Also, with the lean CO₂ loading specified as a design specification for the stripper and starting with a total stage number of 10, the number of stages in the stripper was automatically stepped by 1, using another sensitivity block. In each pass, the reboiler duty was manipulated to achieve the specified lean CO₂ loading and the optimum stripper height was arrived at when there was negligible (less than 0.001%) or no change in the reboiler duty with further increase in the number of stages. As for the absorber, data logging of the calculated results of interest in each pass was realized using the same sensitivity block that increased the number of stages.

7.4.3 Design Philosophy Validation at Pilot-Scale

The design philosophy validation at pilot-scale followed the explanation given in the previous section and, in contrast to the model validation with explicit specification of the absorber and stripper heights, the absorber and stripper heights needed to achieve the experimentally reported CO₂ capture rate were determined and compared with the actual heights of the absorber and stripper.

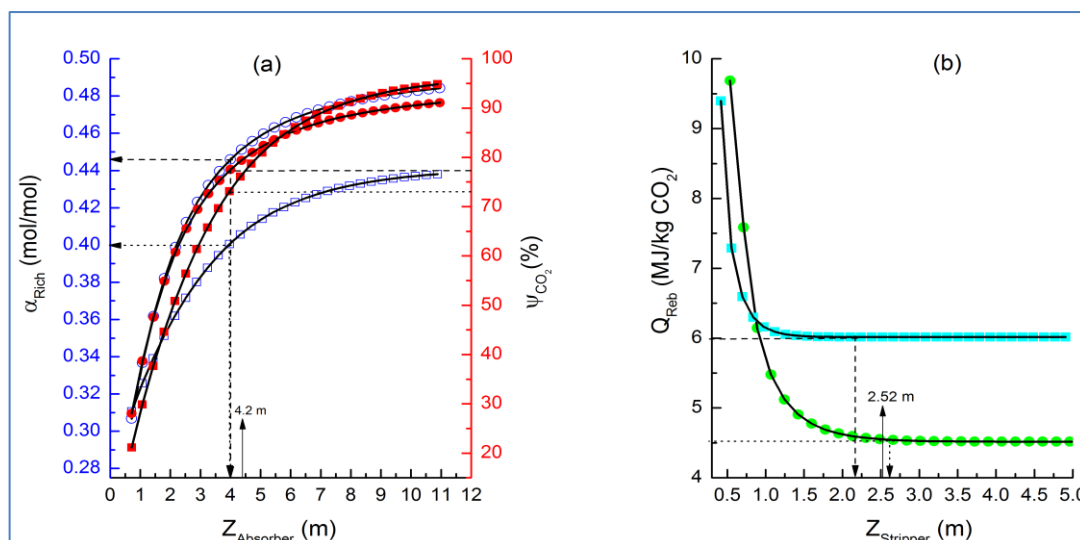


Figure 7.4. Design philosophy validation at pilot scale. (a) Comparison of the calculated absorber height needed for a given CO₂ capture level, as well as the corresponding rich CO₂ loading, with the actual absorber height of the pilot plant. [Symbol: □, rich CO₂ loading for a gas-fired case (Exp 23 in Notz et al.¹⁴⁸); ○, rich CO₂ loading for a coal-fired case (Exp 8 in Notz et al.¹⁴⁸); ■, CO₂ captured level for Exp 23; ●, CO₂ captured level for Exp 8]. (b) Comparison of the calculated stripper height with the actual stripper height of the pilot plant. [Symbol: ■, Exp 23; ●, Exp 8].

Figure 7.4(a) and **Figure 7.4(b)**, respectively, show how the calculated absorber and stripper heights compare with the actual heights of the absorber and stripper. The calculated heights are within $\pm 5\%$ accuracy when compared with the actual heights; thus, the validated mode is deemed to be sufficiently accurate for scale-up design, especially if the calculated results are interpreted with respect to the uncertainties in the experimental values.

7.5 Scale-up Applications

It can be shown that the equation relating the lean amine solution mass flowrate to the amount of CO₂ recovered from the flue gas stream, the mass fraction of the amine in the unloaded solution (ω_{Amine}), and the lean amine solution CO₂ loading is given by (refer to **Appendix C** for details):

$$F_{Lean} = \frac{F_{FG} x_{CO_2} \Psi_{CO_2}}{100z(\alpha_{Rich} - \alpha_{Lean})} \left(\frac{M_{Amine}}{44.009} \left\{ 1 + \frac{1 - \omega_{Amine}}{\omega_{Amine}} \right\} + z\alpha_{Lean} \right) \quad (7.5.1)$$

where F_{Lean} is the mass flowrate of the lean amine solution, F_{FG} is the mass flowrate of the flue gas, x_{CO_2} is the mass fraction of CO_2 in the flue gas, Ψ_{CO_2} is the percentage of CO_2 in the flue gas that is recovered, M_{Amine} is the molar mass of the amine, α_{Lean} and α_{Rich} are, respectively, the lean amine solution CO_2 loading and the rich amine solution CO_2 loading, and z is the number of equivalents per mole of the amine (z is one for MEA).

The stripper reboiler duty needed for CO_2 stripping consists of four parts, namely: (i) the heat of CO_2 desorption, (ii) the heat needed for stripping steam generation, (iii) the heat needed for solvent heating, and (iv) the heat needed for condensate reflux heating, which is often neglected. Their relative contributions to the stripper reboiler duty needed for a given CO_2 capture rate depend on the amine flowrate and the lean amine CO_2 loading.

The scale-up and optimisation question that requires an answer is what combination of lean amine flowrate and lean amine CO_2 loading will optimize the absorber and stripper sizes as well as the stripper reboiler duty at 90% CO_2 capture rate? In order to answer this question for the benchmark amine for solvent-based post-combustion CO_2 capture, which is 30 wt% aqueous solution of monoethanolamine (MEA), a total of four commercial-scale CO_2 capture plants, each of which can service a 400MWe (gross) natural gas combined cycle (NGCC) power plant, a 450MWe (gross) natural gas combined cycle (NGCC) power plant, a 673 MWe (gross) subcritical pulverized coal (PC) power plant, and a 827 MWe (gross) ultrasupercritical pulverized coal (PC) power plant, were optimally designed. The flue gas composition and flowrate for the 673 MWe (gross) subcritical PC power plant were obtained from a 2010 report by the US Department of Energy (DOE),¹⁹² while the composition and flowrate for the 827 MWe (gross) ultrasupercritical PC power plant were obtained from a 2004 report by the International Energy Agency Greenhouse Gas R&D Programme (IEAGHG).¹⁹³ The composition for the two NGCC cases was taken to be the same as the NGCC case in the 2010 US DOE report,¹⁹² and it has a CO_2 composition of approximately 4%, which is essentially the same as the CO_2 composition of the flue gas used by Sipocz and Tobiesen¹⁷⁸ and Biliyok and Yeung.¹⁷⁹ The flue gas flowrates for the two NGCC cases were estimated based on the values reported for different MWe (gross) NGCC power plants. It is important to state that the composition of the flue gas from a NGCC power plant will normally depend on the composition of the natural gas that is used, while the flowrate of the flue gas from a NGCC power plant will

depend on the composition of the natural gas used, the pressure ratio of the air compressor, the temperature and pressure conditions of the main steam and reheat steam in the steam cycle, etc. The two NGCC design cases presented in this chapter provide meaningful comparisons with the designs reported by Sipocz and Tobiesen¹⁷⁸ and Biliyok and Yeung.¹⁷⁹

Table 7.2 summarizes the conditions and compositions of the flue gas used as bases for the four design cases in this chapter, while **Table 7.3** summarizes the basic design and economic assumptions adopted for the four design cases. The optimum design of the absorber and stripper columns for the four cases are summarized in **Table 7.4**, and they were arrived at based on process and economic analyses. It is important to note that, in line with what can be delivered by the state-of-the-art technology as documented in the publications by Reddy et al.,^{48,184,185} a maximum diameter of 18 m was used as the criterion for arriving at the number of columns needed.

Table 7.2. Flue gas conditions and compositions adopted for the design cases.

	Gas-fired (NGCC)	Gas-fired (NGCC)	Coal-fired (Sub- critical)	Coal-fired (Ultra- supercritical)
Flue Gas Pressure (bara), absorber inlet	1.2	1.2	1.2	1.2
Flue Gas Temperature (°C), absorber inlet	40	40	40	40
	<u>Flue Gas Composition</u>			
CO ₂ (mol/mol)	0.0404	0.04	0.1350	0.1238
H ₂ O (mol/mol)	0.0867	0.0867	0.1537	0.1221
N ₂ (mol/mol)	0.7432	0.7432	0.6793	0.7108
O ₂ (mol/mol)	0.1209	0.1209	0.0238	0.0433
Ar (mol/mol)	0.0089	0.0089	0.0081	0.0000

Table 7.3. Design and economic analysis assumptions used for the design cases in this chapter.

Design Assumptions	
Lean MEA inlet temperature (°C)	40
MEA Concentration (kg/kg), without CO ₂	0.30
Stripper Condenser temperature (°C)	35
Stripper Condenser Pressure (bara)	1.62
CO ₂ Capture Rate (%)	90
Cross Heat Exchanger Temperature Approach (°C), hot end	10
Cross Heat Exchanger pressure drop (bar)	0.1
Lean Amine Cooler Pressure drop (bar)	0.1
Lean Amine Pump Discharge Pressure (bara)	3.0
Lean Amine Pump Efficiency (%)	75
Rich Amine Pump Discharge Pressure (bara)	3.0
Rich Amine Pump Efficiency (%)	75
Cooling water temperature rise (°C)	5
Economic Analysis Assumptions^b	
Steam Cost (£/ton)	17.91
Cooling Water Cost (£/m ³)	0.0317
Electricity Cost (£/MWh)	77.5
Plant equipment metallurgy	316L stainless steel

However, the choice of two absorbers for the 400 MWe NGCC case was arrived at based on the need for operational flexibility. The complete optimum design data, which include data for the pumps and heat exchangers, can be found in **Table D.1, Appendix D**.

The capital cost of the plant (CAPEX) and the operating cost of the plant (OPEX) were calculated using the Aspen Plus Economic Analyser[®]. The basic flowsheet shown in **Figure 7.1** and the Costing Template for the UK in the Aspen Plus Economic Analyser[®], with default values, were adopted for

the economic analyses performed. It is important to note that the CAPEX and OPEX will be higher for an actual plant because of the other equipment (including spares) that must be installed based on a hazard and operability (HAZOP) study.

Table 7.4. Summary of the key design results for the absorber and stripper columns.

	Gas-fired (NGCC)	Gas-fired (NGCC)	Coal-fired (Subcritical)	Coal-fired (Ultra- supercritical)
Gross Power plant size (MWe)	400	450	673	827
Flue Gas Flowrate (kg/s)	622.2	725	892.57	932.42
Liquid/Gas Ratio (kg/kg)	0.96	0.96	2.93	2.68
Absorber				
Number of Absorber ^c	2	2	2	2
Absorber Packing	Mellapak 250Y	Mellapak 250Y	Mellapak 250Y	Mellapak 250Y
Diameter (m)	11.93	12.88	16.67	16.92
Optimum Height (m)	19.06	19.99	23.04	23.74
Stripper				
Number of Stripper	1	1	1	1
Stripper Packing	Mellapak 250Y	Mellapak 250Y	Mellapak 250Y	Mellapak 250Y
Diameter (m)	6.76	7.74	14.25	13.89
Optimum Height (m)	28.15	28.15	25.62	25.36
Specific Reboiler Duty (MJ/kg CO ₂)	3.96	3.96	3.69	3.72

Furthermore, it is important to add that the costing of commercial-scale CO₂ capture plants could be associated with high uncertainty since there is no currently operating CO₂ capture plant with the same capacity as the ones considered in this chapter. However, in line with a recent publication by Rubin et al.,¹⁹⁴ if costing assumptions are applied consistently and systematically in screening technologies for CO₂ capture or in screening design and operation parameters for a given CO₂ capture technology, we are very likely to arrive at a valid conclusion. That explains the reason for adopting default values in Aspen Plus Economic Analyser[®] since our primary focus is not really the accuracy of the cost values but rather, the variations of the cost values with important design and operation parameters such as the absorber and stripper sizes, the lean CO₂ loading, and the solvent circulation rate.

In each of the four cases, the optimum design was taken to be the one with the least OPEX. In order to confirm the validity of using the least OPEX as a basis for the optimum design selection, further economic comparisons were performed based on annualized total cost (TOTEX), which takes both the CAPEX and the OPEX into consideration. The annualized total cost (TOTEX) is given by the following equation:

$$TOTEX = C_1(OPEX) + C_2(CAPEX) \left(\frac{i(1+i)^n}{(1+i)^n - 1} \right) \quad (7.5.2)$$

where C_1 and C_2 are scaling factors.

The annualized total cost (TOTEX) for each of the four CO₂ capture plants considered in this chapter was calculated by assuming 20 years ($n=20$) of plant service life and 10% interest rate ($i=0.1$) for three different scenarios as follows:

- TOTEX calculated without scaling CAPEX and OPEX ($C_1 = 1.0$ and $C_2 = 1.0$)
- TOTEX calculated with CAPEX scaled up by 50% without scaling the OPEX ($C_1 = 1.0$ and $C_2 = 1.5$)
- TOTEX calculated with OPEX reduced by 50% without scaling the CAPEX ($C_1 = 0.5$ and $C_2 = 1.0$)

The 50% CAPEX scale-up in the second scenario is assumed to be sufficient to account for the other equipment that needs to be installed based on a hazard and operability (HAZOP) study, as well as the uncertainty that may be present in the CAPEX value calculated by the Aspen Plus Economic Analyzer. Also it is assumed that the reduction of the OPEX by 50% in the third scenario will reduce the weight of the OPEX on the TOTEX, especially if the CO₂ capture plant is to operate in a location where utilities are relatively cheaper than the values used in this chapter.

7.5.1 Commercial-scale MEA-based CO₂ Capture plants for Natural Gas Combined Cycle (NGCC) Power Plants

Figure 7.5(a) and **Figure 7.5(b)** summarize the design results for an MEA-based CO₂ capture plant that can service a 400 MWe (gross) NGCC power plant, while **Figure 7.6(a)** and **Figure 7.6(b)** summarize the design results for an MEA-based CO₂ capture plant that can service a 450 MWe (gross) NGCC power plant. As the liquid/gas ratio is reduced below the optimum value it becomes increasingly difficult to achieve the rich CO₂ loading required for 90% CO₂ capture; hence the reason for the sharp increase in the absorber height for liquid/gas ratio below the optimum value. Also, the change in the absorber height with liquid/gas ratio is less pronounced as the lean CO₂ loading increases. These observations clearly show that arbitrary assumption of liquid/gas ratio, directly or indirectly, will most likely lead to a sub-optimal design. On the other hand, the stripper height is relatively unaffected by the liquid/gas ratio but the stripper height increases as the lean CO₂ loading of the MEA solution decreases, which will have an implication for the overall capital cost of the plant.

The variations of the steam required by the stripper reboiler and the cooling water (C.W.) required by the stripper condenser and lean amine cooler with liquid/gas ratio are shown in **Figure 7.5(b)** and **Figure 7.6(b)**, respectively, for the 400 MWe NGCC plant and the 450 MWe NGCC plant. From **Figure 7.5(b)** and **Figure 7.6(b)**, it is clear that the both the steam and cooling water required for each lean CO₂ loading decreases only marginally if the liquid/gas ratio reduces beyond the optimum liquid/gas ratio. The marginal decrease in the steam and cooling water required cannot compensate for the sharp increase in the absorber height; thus, the optimum design is not given by the liquid/gas ratio that has the minimum steam and cooling water requirement.

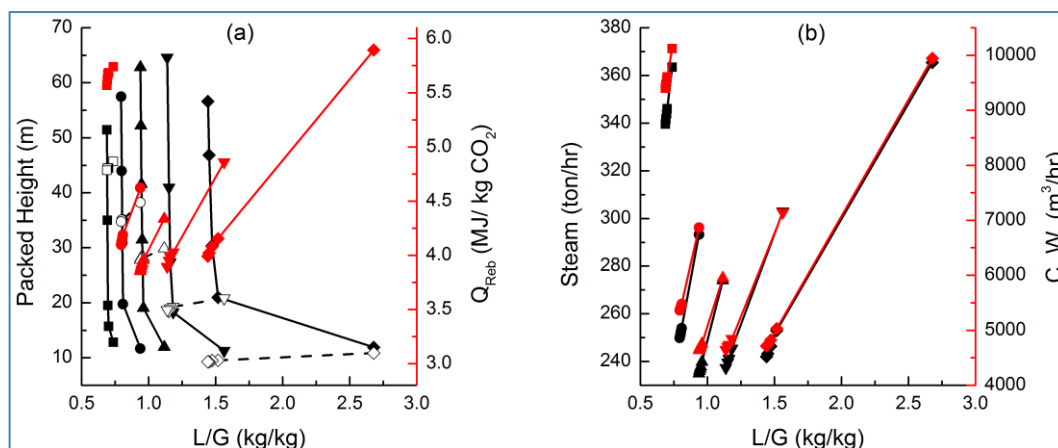


Figure 7.5. Design results for an MEA-based CO₂ capture plant that can service a 400 MWe (gross) NGCC power plant at 90% CO₂ capture rate. (a) Variations of absorber height (black solid lines), stripper height (black dash lines) and specific reboiler duty (red lines) with liquid/gas ratio for different lean CO₂ loadings. (b) Variations of steam requirement (black lines) and cooling water requirement (red lines) with liquid/gas ratio for different lean CO₂ loadings. [Symbols: (■, □, ■), 0.1 CO₂ loading; (●, ○, ●), 0.15 CO₂ loading; (▲, △, ▲), 0.2 CO₂ loading; (▼, ▽, ▼), 0.25 CO₂ loading; (◆, ◇, ◆), 0.3 CO₂ loading].

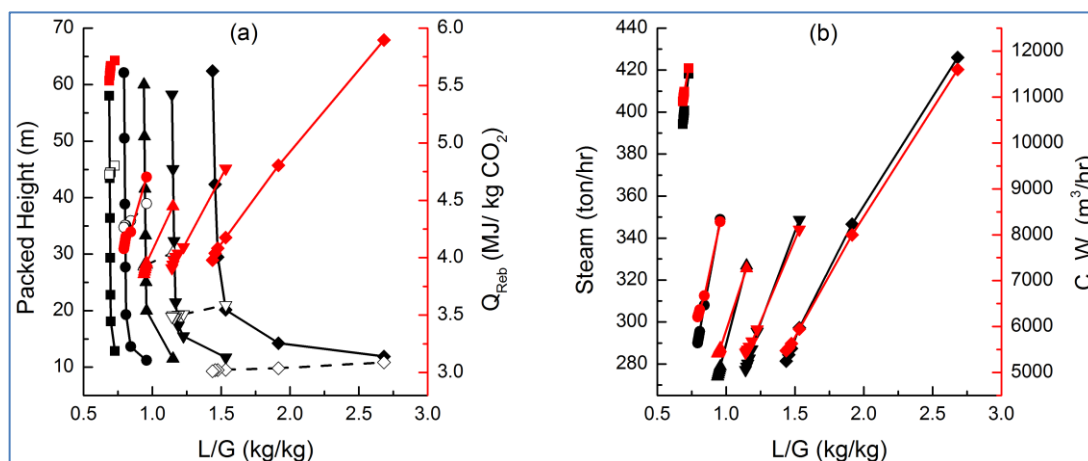


Figure 7.6. Design results for an MEA-based CO₂ capture plant that can service a 450 MWe (gross) NGCC power plant at 90% CO₂ capture rate. (a) Variations of absorber height (black solid lines), stripper height (black dash lines) and specific reboiler duty (red lines) with liquid/gas ratio for different lean CO₂ loadings. (b) Variations of steam requirement (black lines) and cooling water requirement (red lines) with liquid/gas ratio for different lean CO₂ loadings. [Symbols: (■, □, ■), 0.1 CO₂ loading; (●, ○, ●), 0.15 CO₂ loading; (▲, △, ▲), 0.2 CO₂ loading; (▼, ▽, ▼), 0.25 CO₂ loading; (◆, ◇, ◆), 0.3 CO₂ loading].

Since there is a direct relationship between the steam requirement and the specific reboiler duty, it follows therefore that the optimum design for a given lean CO₂ loading does not correspond with the liquid/gas ratio that has the minimum specific reboiler duty.

The economics of the plant, which includes the overnight capital cost (CAPEX) and the operating cost (OPEX) are shown in **Figures 7.7(a) and 7.8(a)**, respectively, for the 400 MWe and the 450MWe NGCC plants. From **Figures 7.7(a) and 7.8(a)**, it is clear that CAPEX increases sharply when the liquid/gas ratio is reduced below an optimum value, and the sharp increase in CAPEX is due to the increase in the cost of the absorbers. Also, the OPEX increases slightly as the liquid/gas ratio is reduced below the optimum value as a result of the increase in maintenance costs, which is tied to CAPEX, despite the decrease in the total cost of the utilities (steam, cooling water and electricity) consumed. On the other hand, as the liquid/gas ratio is increased beyond the optimum value, the CAPEX decreases slightly while the OPEX increases sharply because of the sharp increase in the cost of the utilities consumed.

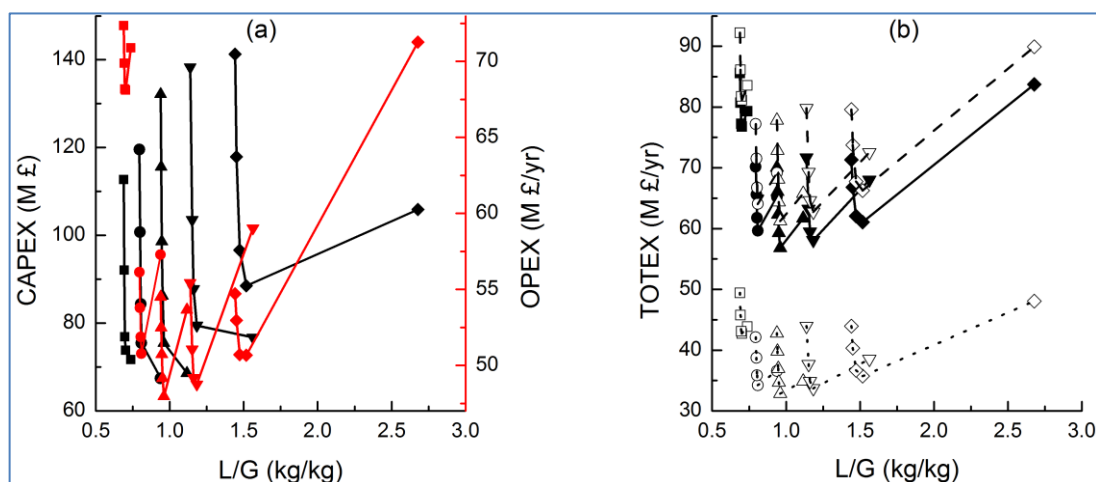


Figure 7.7. Economic results for an MEA-based CO₂ capture plant that can service a 400 MWe (gross) NGCC power plant at 90% CO₂ capture rate. (a) Variations of overnight capital expenditure (black lines) and annual operating expenditure (red lines) with liquid/gas ratio for different lean CO₂ loadings. (b) Variations of annualized total expenditure with liquid/gas ratio for different lean CO₂ loadings: solid line, OPEX + A. CAPEX; dash line, OPEX + 1.5(A. CAPEX); dotted line, 0.5(OPEX) + A. CAPEX. [Symbols: (■, □, ■), 0.1 CO₂ loading; (●, ○, ●), 0.15 CO₂ loading; (▲, △, ▲), 0.2 CO₂ loading; (▼, ▽, ▼), 0.25 CO₂ loading; (◆, ◇, ◆), 0.3 CO₂ loading].

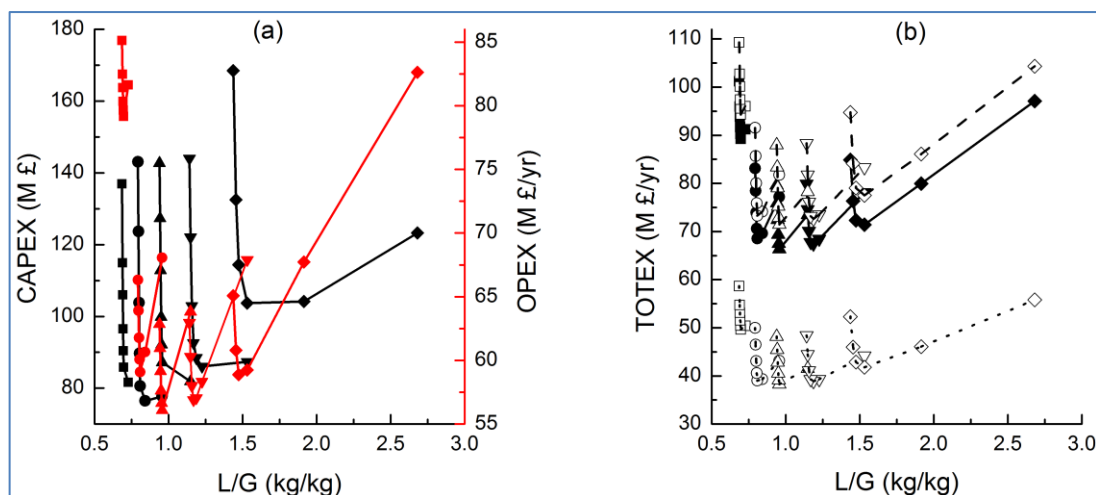


Figure 7.8. Economics results for an MEA-based CO₂ capture plant that can service a 450 MWe (gross) NGCC power plant at 90% CO₂ capture rate. (a) Variations of overnight capital expenditure (black lines) and annual operating expenditure (red lines) with liquid/gas ratio for different lean CO₂ loadings. (b) Variations of annualized total expenditure with liquid/gas ratio for different lean CO₂ loadings: solid line, OPEX + A. CAPEX; dash line, OPEX + 1.5(A. CAPEX); dotted line, 0.5(OPEX) + A. CAPEX. [Symbols: (■, □, ■), 0.1 CO₂ loading; (●, ○, ●), 0.15 CO₂ loading; (▲, △, ▲), 0.2 CO₂ loading; (▼, ▽, ▼), 0.25 CO₂ loading; (◆, ◇, ◆), 0.3 CO₂ loading].

The sharp increase in the costs of the utilities is because more electricity is consumed by the rich and lean pumps with increasing liquid/gas ratio, more steam is consumed in heating up the increasing mass of the solvent from the top inlet temperature to the bottom reboiler temperature in addition to the generation of more stripping steam as the solvent mass flow rate increases, and more cooling water is consumed in the stripper condenser and lean amine cooler. These observations clearly show that there is a trade-off between CAPEX and OPEX in the design of amine-based CO₂ capture plant and hence there is a need for economic analysis before the optimum design of amine-based CO₂ capture plant can be arrived at. Furthermore, from **Figure 7.7(a)** and **Figure 7.8(a)**, it is clear that the overall optimum design depends on the value of the lean CO₂ loading in addition to the value of the liquid/gas ratio, and that both values must be carefully chosen since the optimum liquid/gas ratios are quite different for the different lean CO₂ loadings.

From **Figure 7.7(a)** and **Figure 7.8(a)**, the optimum design with minimum OPEX is given by 0.2 lean CO₂ loading and 0.96 liquid/gas ratio for both plants. To further confirm the optimum selection based on minimum OPEX,

economic evaluations that take both CAPEX and OPEX into consideration were used. **Figure 7.7(b)** and **Figure 7.8(b)** show the annualized total cost (TOTEX), which is a combination of the OPEX and an annualized cost for the CAPEX. The results of the three different scenarios that were considered for the TOTEX are shown in **Figure 7.7(b)** and **Figure 7.8(b)**, respectively, for the 400 MWe NGCC plant and the 450 MWe NGCC plant. Interestingly, the three scenarios follow the same trend as the OPEX and they confirm the optimum design arrived at on the basis of least OPEX.

The total cost of the plants, which include both CAPEX and OPEX, per gross MWh are 16.21 £/MWh and 16.81 £/MWh for the 400MWe NGCC plant and the 450 MWe NGCC plant, respectively, which are more or less the same. Additionally, the total cost of the plants per ton of CO₂ captured are 51.35 £/ton CO₂ and 51.44 £/ton CO₂ for the 400MWe NGCC plant and the 450 MWe NGCC plant, respectively, which are also more or less the same.

7.5.2 Commercial-scale MEA-based CO₂ Capture plants for Pulverized Coal (PC) Power Plants

Figure 7.9(a) and **Figure 7.9(b)** summarize the design results for an MEA-based CO₂ capture plant that can service a 673 MWe (gross) subcritical PC power plant, while **Figure 7.10(a)** and **Figure 7.10(b)** summarize the design results for an MEA-based CO₂ capture plant that can service a 827 MWe (gross) ultra-supercritical PC power plant. The design results for the two cases cover lean CO₂ loadings ranging from 0.1 mol/mol to 0.3 mol/mol. The liquid/gas ratios range from 2.09 to 5.29 for the subcritical plant, and 1.91 to 5.06 for the ultra-supercritical plant. The absorber and stripper heights, as well as the specific reboiler duties, are shown in **Figure 7.9(a)** and **Figure 7.10(a)**, respectively, for the subcritical plant and the ultra-supercritical plant. From **Figure 7.9(a)** and **Figure 7.10(a)**, it is clear that the absorber height required for 90% CO₂ capture increases sharply with liquid/gas ratio when the liquid/gas ratio is reduced below a certain optimum value for each lean CO₂ loading, and the absorber height decreases gradually if the liquid/gas ratio increases beyond the optimum value. Also, as for the NGCC cases, the change in the absorber height with liquid/gas ratio is less pronounced as the lean CO₂ loading increases. Again, these observations clearly show that the arbitrary assumption of liquid/gas ratio, directly or indirectly, will most likely lead to a sub-optimal design. On the other hand, as for the NGCC cases, the stripper height is relatively unaffected by the liquid/gas ratio but the stripper

height increases as the lean CO₂ loading decreases, which will have an implication on the overall capital cost of the plant.

The variations of the steam required by the stripper reboiler and the cooling water (C.W.) required by the stripper condenser and lean amine cooler with liquid/gas ratio are shown in **Figure 7.9(b)** and **Figure 7.10(b)**, respectively, for the subcritical plant and the ultra-supercritical plant. From **Figure 7.9(b)** and **Figure 7.10(b)**, it is clear that both the steam and cooling water required for each lean CO₂ loading decreases only marginally if the liquid/gas ratio is reduced beyond the optimum liquid/gas ratio.

The marginal decrease in the steam and cooling water required cannot compensate for the increase in the absorber height, especially if the large diameter of the absorber is taken into consideration; thus, the optimum design is not given by the liquid/gas ratio that has the minimum steam and cooling water requirement. As for the NGCC cases, since there is a direct relationship between the steam requirement and the specific reboiler duty it follows therefore that the optimum design for a given lean CO₂ loading does not correspond with the liquid/gas ratio that has the minimum specific reboiler duty.

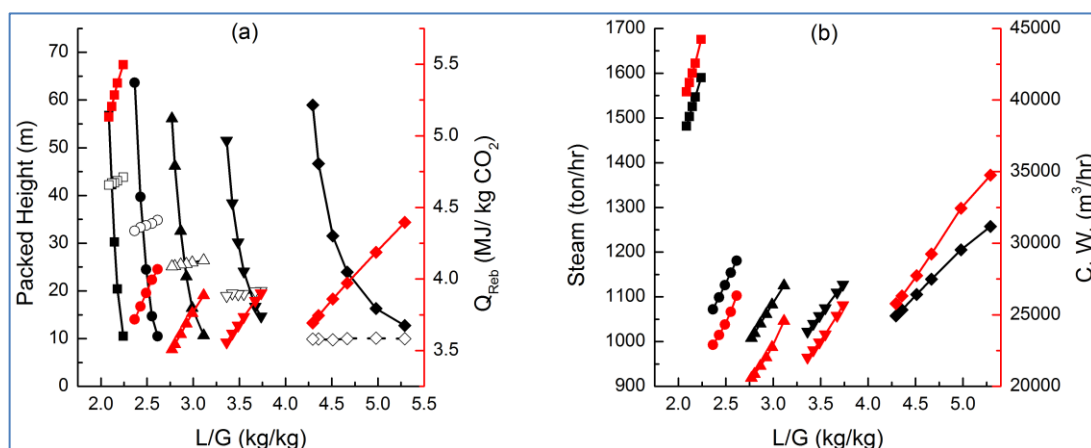


Figure 7.9. Design results for an MEA-based CO₂ capture plant that can service a 673 MWe (gross) subcritical PC power plant at 90% CO₂ capture rate. (a) Variations of absorber height (black solid lines), stripper height (black dash lines) and specific reboiler duty (red lines) with liquid/gas ratio for different lean CO₂ loadings. (b) Variations of steam requirement (black lines) and cooling water requirement (red lines) with liquid/gas ratio for different lean CO₂ loadings. [Symbols: (■, □, ■), 0.1 CO₂ loading; (●, ○, ●), 0.15 CO₂ loading; (▲, △, ▲), 0.2 CO₂ loading; (▼, ▽, ▼), 0.25 CO₂ loading; (◆, ◇, ◆), 0.3 CO₂ loading].

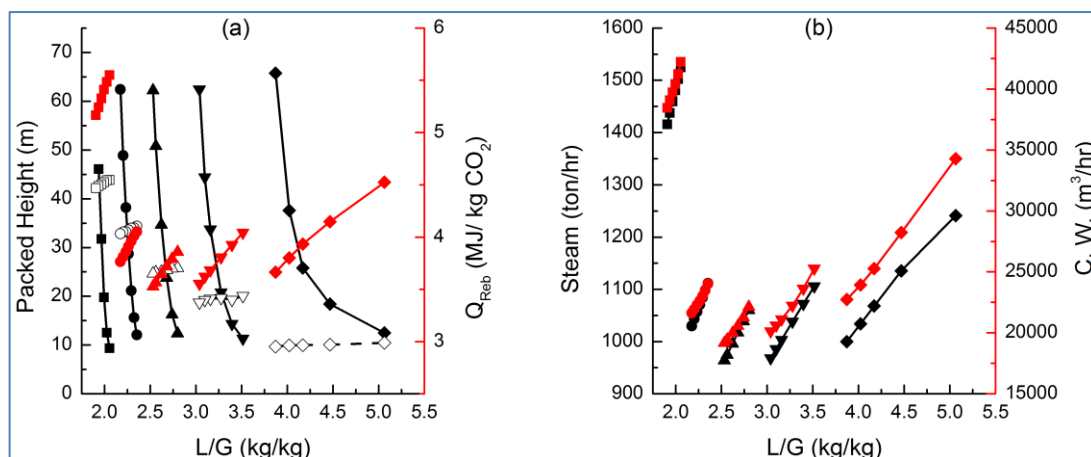


Figure 7.10. Design results for an MEA-based CO₂ capture plant that can service an 827 MWe (gross) ultra-supercritical PC power plant at 90% CO₂ capture rate. (a) Variations of absorber height (black solid lines), stripper height (black dash lines) and specific reboiler duty (red lines) with liquid/gas ratio for different lean CO₂ loadings. (b) Variations of steam requirement (black lines) and cooling water requirement (red lines) with liquid/gas ratio for different lean CO₂ loadings. [Symbols: (■, □, ■), 0.1 CO₂ loading; (●, ○, ●), 0.15 CO₂ loading; (▲, △, ▲), 0.2 CO₂ loading; (▼, ▽, ▼), 0.25 CO₂ loading; (◆, ◇, ◆), 0.3 CO₂ loading].

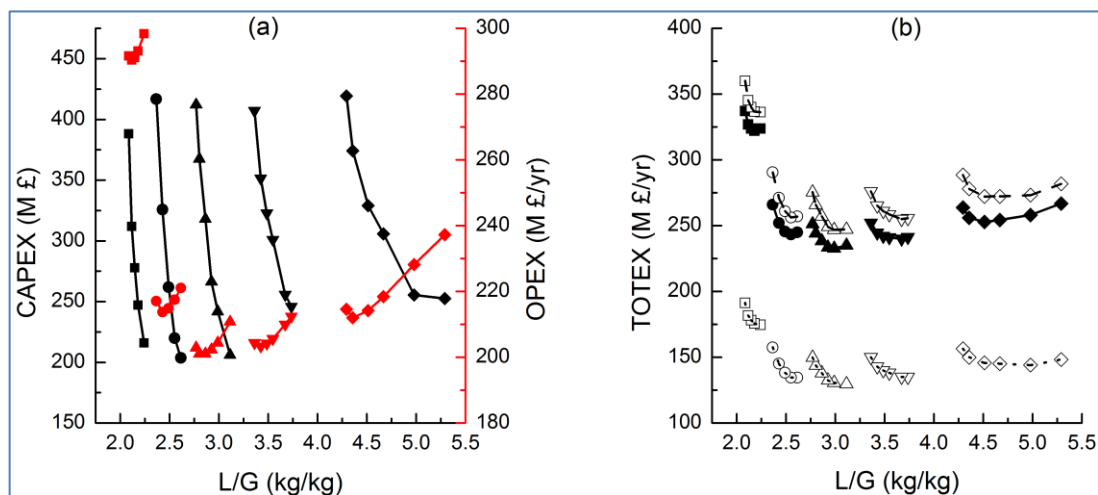


Figure 7.11. Design results for an MEA-based CO₂ capture plant that can service a 673 MWe (gross) subcritical PC power plant at 90% CO₂ capture rate. (a) Variations of overnight capital expenditure (black lines) and annual operating expenditure (red lines) with liquid/gas ratio for different lean CO₂ loadings. (b) Variations of annualized total expenditure with liquid/gas ratio for different lean CO₂ loadings: solid line, OPEX + A. CAPEX; dash line, OPEX + 1.5(A. CAPEX); dotted line, 0.5(OPEX) + A.CAPEX.[Symbols: (■, □, ■), 0.1 CO₂ loading; (●, ○, ●), 0.15 CO₂ loading; (▲, △, ▲), 0.2 CO₂ loading; (▼, ▽, ▼), 0.25 CO₂ loading; (◆, ◇, ◆), 0.3 CO₂ loading].

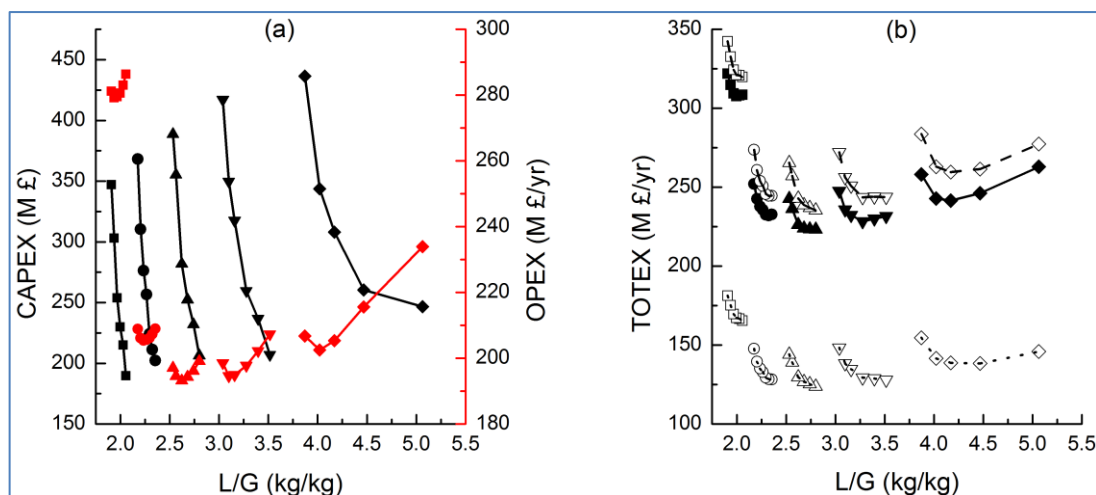


Figure 7.12. Design results for an MEA-based CO₂ capture plant that can service an 827 MWe (gross) ultra-supercritical PC power plant at 90% CO₂ capture rate. (a) Variations of overnight capital expenditure (black lines) and annual operating expenditure (red lines) with liquid/gas ratio for different lean CO₂ loadings. (b) Variations of annualized total expenditure with liquid/gas ratio for different lean CO₂ loadings: solid line, OPEX + A. CAPEX; dash line, OPEX + 1.5(A. CAPEX); dotted line, 0.5(OPEX) + A. CAPEX. [Symbols: (■, □, ■), 0.1 CO₂ loading; (●, ○, ●), 0.15 CO₂ loading; (▲, △, ▲), 0.2 CO₂ loading; (▼, ▽, ▼), 0.25 CO₂ loading; (◆, ◇, ◆), 0.3 CO₂ loading]

The economics of the plants, which includes the overnight capital cost (CAPEX) and the operating cost (OPEX) are shown in **Figure 7.11(a)** and **Figure 7.12(a)**, respectively, for the subcritical plant and the ultra-supercritical plant. As for the NGCC cases, there is trade-off between the CAPEX and OPEX and the explanations previously given for the NGCC cases are equally applicable to the coal-fired cases and it will not be repeated here.

From **Figure 7.11(a)** and **Figure 7.12(a)**, the optimum design with minimum OPEX is given by 0.2 lean CO₂ loading and 2.93 liquid/gas ratio for the subcritical plant, and 0.2 CO₂ loading and 2.68 liquid/gas ratio for the ultra-supercritical plant. The higher liquid/gas ratio for the subcritical plant is because of the higher CO₂ captured when compared with the ultra-supercritical plant. In order to confirm the optimum selection based on minimum OPEX, further economic evaluations that take both CAPEX and OPEX into consideration were used. **Figure 7.11(b)** and **Figure 7.12(b)** show the annualized total cost (TOTEX), which is a combination of the OPEX and an annualized cost for the CAPEX. The results of the three different scenarios that were considered for the TOTEX are shown in **Figure**

7.11(b) and **Figure 7.12(b)**, respectively, for the subcritical plant and the ultra-supercritical plant. The three scenarios followed the same trend as the OPEX, though not exactly, and they give credence to the optimum design arrived at on the basis of least OPEX.

The total cost of the plants, which include both CAPEX and OPEX, per gross MWh are 39.60 £/MWh and 30.90 £/MWh for the subcritical plant and the ultra-supercritical plant, respectively. However, the total cost of the plants per ton of CO₂ captured are 44.71 £/ton CO₂ and 44.19 £/ton CO₂ for the subcritical and ultra-supercritical plants, respectively, which are more or less the same.

7.6 Conclusions

A comparison of the optimal design results in this chapter with some of the previously published designs shows that design based on values of CO₂ loadings and/or solvent circulation rates without techno-economic consideration may lead to a sub-optimal design for an amine-based CO₂ capture plant.

The optimum lean CO₂ loading for MEA-based CO₂ capture plants that can service commercial-scale power plants, whether natural gas-fired or coal-fired, is about 0.2 mol/mol for absorber and stripper columns packed with Sulzer Mellapak 250Y™ structured packing. Also, the optimum liquid/gas ratio for a natural gas combined cycle (NGCC) power plant with a flue gas composition of approximately 4 mol% CO₂ is about 0.96, while the optimum liquid/gas ratio for a coal-fired power plant can range from 2.68 to 2.93 for a flue gas having a CO₂ composition that ranges from 12.38 mol% to 13.5 mol%.

The total cost of building and operating an MEA-based CO₂ capture plant per unit of gross MWh of electricity that is produced by the power plant is far lower for a natural gas combined cycle power plant when compared with that of a pulverized coal-fired power plant. On the other hand, the total cost of building and operating an MEA-based CO₂ capture plant per ton of CO₂ captured from the flue gas is low for a pulverized coal-fired power plant when compared with that of a natural gas combined cycle power plant; thus, the price of electricity and the tax on CO₂ emissions will determine if a natural gas combined cycle power plant with MEA-based post-combustion

CO₂ capture will outperform a coal-fired power plant with MEA-based post-combustion CO₂ capture plant.

Finally, the design method and philosophy developed in this chapter will be used in the design of an MEA-based PCC plant that can service ~550 MWe (net power after CO₂ capture and CO₂ compression) supercritical coal-fired power plant in **Chapter 8** and **Chapter 9**.

Chapter 8

Optimal Integration of Amine-based CO₂ Capture Plant to a Coal-Fired Power Plant

8.1 Introduction

The possibility of reducing the solvent regeneration energy of an amine-based CO₂ capture plant based on its optimal integration with the associated CO₂ compression unit (CCU) and an upstream coal-fired power plant has led to several publications in the open literature in the past few decades.^{37,169-171,174,176,177,181,182,195-203} An important parameter that is critical when integrating a coal-fired power plant to an amine-based post-combustion CO₂ capture is the operating pressure of the stripper. **Table 8.1** summarizes the operating pressure used by several authors, including the operating pressure of the stripper reported for the Econamine FG Plus™ process that is licensed by Fluor®.^{183,192,193} The operating pressure of the stripper used by most of the authors in **Table 8.1** was adopted without a clearly defined basis. Furthermore, from the different values adopted by the various authors, it is clear that there is a lack of consensus on the stripper pressure that will optimize the integration of a coal-fired power plant to a PCC plant and a CCU. Therefore, there is a need for a critical analysis of the operating pressure of the stripper in a PCC plant on the overall performance of the integrated power plant-PCC-CCU system based on rigorous and highly accurate models.

In this chapter, an integrated process comprising ~550MWe (net power with CO₂ capture and compression) pulverized coal-fired power plant firing Illinois No. 6 coal (a high volatile bituminous coal), an MEA-based PCC plant, and a CO₂ compression system, has been modelled using the Aspen Plus® software, V8.4. The boiler, steam cycle and CO₂ compression were modelled based on a 2010 US DOE report,¹⁹² as well as a 2004 IEAGHG report,¹⁹³ while the MEA-based PCC plant was modelled as a rigorous rate-based process. The scale-up of the PCC plant in the integrated power plant-PCC-CCU system is based on the design method and philosophy in our recent paper.¹⁴⁹ The scale-up of the PCC is novel when compared with previous publications in the open literature before our paper was published because, in addition to using recommended rules for the absorber and

stripper column diameter sizing, the column heights needed for 90% CO₂ capture were arrived at systematically based on rate-based calculations. It is pertinent to add that the optimal design of the PCC plant in this chapter takes into consideration the capital and operating costs of the lean amine solution pump, the rich amine solution pump, the lean/rich cross heat exchanger, the lean amine solution cooler, the stripper, the stripper reflux drum and reflux pump, and the stripper reboiler.¹⁴⁹

Table 8.1. A comparison of the stripper pressure adopted for a MEA-based CO₂ capture plant by various authors.

Source	Stripper Pressure (bara)	Reboiler Temperature (°C)	Sp Reboiler Duty (MJ/kg CO ₂)	Comment
Abu-Zahra et al. ¹⁶⁹	2.10	128.0	3.56	CCU considered
Cifre et al. ¹⁷¹	2.00	120.0	4.07	CCU not considered
Sanpasertpanich et al. ¹⁷⁴	1.83	123.0	3.60	CCU considered
Pfaff et al. ¹⁹⁸	2.10	124.1	3.32	CCU considered
Strube and Manfrida ¹⁹⁹	1.60	-	-	CCU considered
Khalilpour and Abbas ¹⁷⁶	2.00	119.6	2.90	CCU considered
Lawal et al. ¹⁷⁷	1.62	-	3.18	CCU not considered
Duan et al. ²⁰²	2.10	> 117.4	2.83	CCU considered
Hanak et al. ¹⁸²	1.70	122.3	4.937	CCU considered
Mac Dowell and Shah ¹⁸¹	1.85	118.0	3.865	CCU not considered
US DOE ^{a192}	1.60	-	-	CCU considered
IEAGHG ^{a193}	1.62	-	3.24	CCU considered
Heuzeling and van den Weijde ^{a183}	1.65	-	-	CCU considered

^aFluor® Econamine FG Plus™ Process.

The coal-fired power plant is integrated to the PCC plant in three ways: (i) boiler flue gas to the PCC absorber, (ii) steam tapping from the IP-LP cross-over or the LP turbine in the steam cycle to the PCC reboiler and (iii) condensate return from the PCC reboiler to the steam cycle deaerator. Extensive parametric studies aimed at optimising the integration of the power plant to the PCC plant have been performed. The parametric studies included the pressure at which steam is tapped from the steam cycle, the use of a steam throttling valve, the use of a let-down turbine, and the pre-heating of boiler feed water with tapped steam. Furthermore, the integration of the steam cycle to the CO₂ compression inter-stage coolers as an option for the elimination of some of the feed water heaters has been investigated.

8.2 Process Description and Modelling Framework

8.2.1 Process Description

The integrated process is comprised of a PC-fired supercritical power plant, an amine-based PCC plant for CO₂ capture and a multistage CO₂ compression system, and it is based on the supercritical PC-fired power plant with CO₂ capture case reported by the US DOE.¹⁹² The PC-fired power plant is comprised of a once-through coal-fired boiler with a selective catalytic reduction (SCR) unit for NO_x reduction, a wet lime-based flue gas desulphurization (wet FGD) unit for SO₂ reduction, an electrostatic precipitator (ESP) unit for particulates removal, and a supercritical steam cycle with a single-reheat. The SCR is stationed between the economizer and air pre-heater while the FGD is located downstream of the EPS. The single-reheat supercritical steam cycle has a main steam with a pressure of 24.1 MPa and a temperature of 593 °C while the reheat steam has a pressure of 4.52 MPa and a temperature of 593 °C. The steam cycle turbine has three sections – a high pressure (HP) turbine section, an intermediate pressure (IP) turbine section and a low pressure (LP) turbine section. Furthermore, the steam cycle has 8 feed water heaters, one of which includes a deaerator. Three feed water heaters are located upstream of the deaerator, with the remaining 4 feed water heaters located downstream of the deaerator. The boiler feed water upstream of the deaerator is heated in the upstream feed water heaters by bleed steam taken from the HP and IP turbine sections while the boiler feed water downstream of the deaerator is heated up in the downstream feed water heaters by bleed steam taken from the LP turbine section. The steam cycle condenser has a pressure of 7.0 kPa, with an associated saturation temperature of ~38 °C. The boiler

feedwater pumps are driven by a boiler feed water turbine and extracted steam from the IP-LP cross-over is expanded in the boiler feed water turbine. The steam needed by the CO₂ capture plant is also tapped from the IP-LP cross-over while the condensate from the stripper reboiler is returned to the steam cycle deareator.

The PCC plant is based on the conventional configuration and it has two absorber columns and a single stripper column. The pressure of the flue gas coming from the FGD is boosted up by a booster fan and the boosted flue gas is divided equally into two streams, with each stream contacted counter-currently with an amine solution in the packed absorbers. The rich flue gas streams enter the absorbers at the bottom while the lean amine solution from the lean amine cooler, which is divided equally into two streams, is introduced into the top of the absorbers. The treated flue gas leaves the top of the absorbers and is normally washed in a water-wash section so as to remove entrained solvent droplets and, in turn, limit the loss of valuable solvents in addition to meeting environmental regulations on solvent emissions into the atmosphere. The rich solvent from the bottom of the absorbers are combined and the combined stream is pumped by the rich pumps via the lean/rich heat exchanger to the top of the stripper for CO₂ stripping. The hot lean solvent exiting the stripper is pumped by the lean pumps through the lean/rich heat exchanger and the lean amine cooler to the top of the absorber. In the stripper, the downward flowing rich solvent is stripped of its absorbed CO₂ by the upward flowing steam generated by the reboiler. The vapour stream from the top of the stripper, which is essentially a mixture of CO₂, steam and some traces of the amine used, is partially condensed in a condenser and a fraction of the condensed liquid is returned to the top of the stripper as reflux. The uncondensed stream, which is mainly CO₂, is compressed by a multi-stage CO₂ compressor to a final pressure of 153 bar. The process flow diagram of the integrated process, with the PCC plant reboiler throttled steam tapped from the IP-LP cross-over pipe, is shown in **Figure 8.1**.

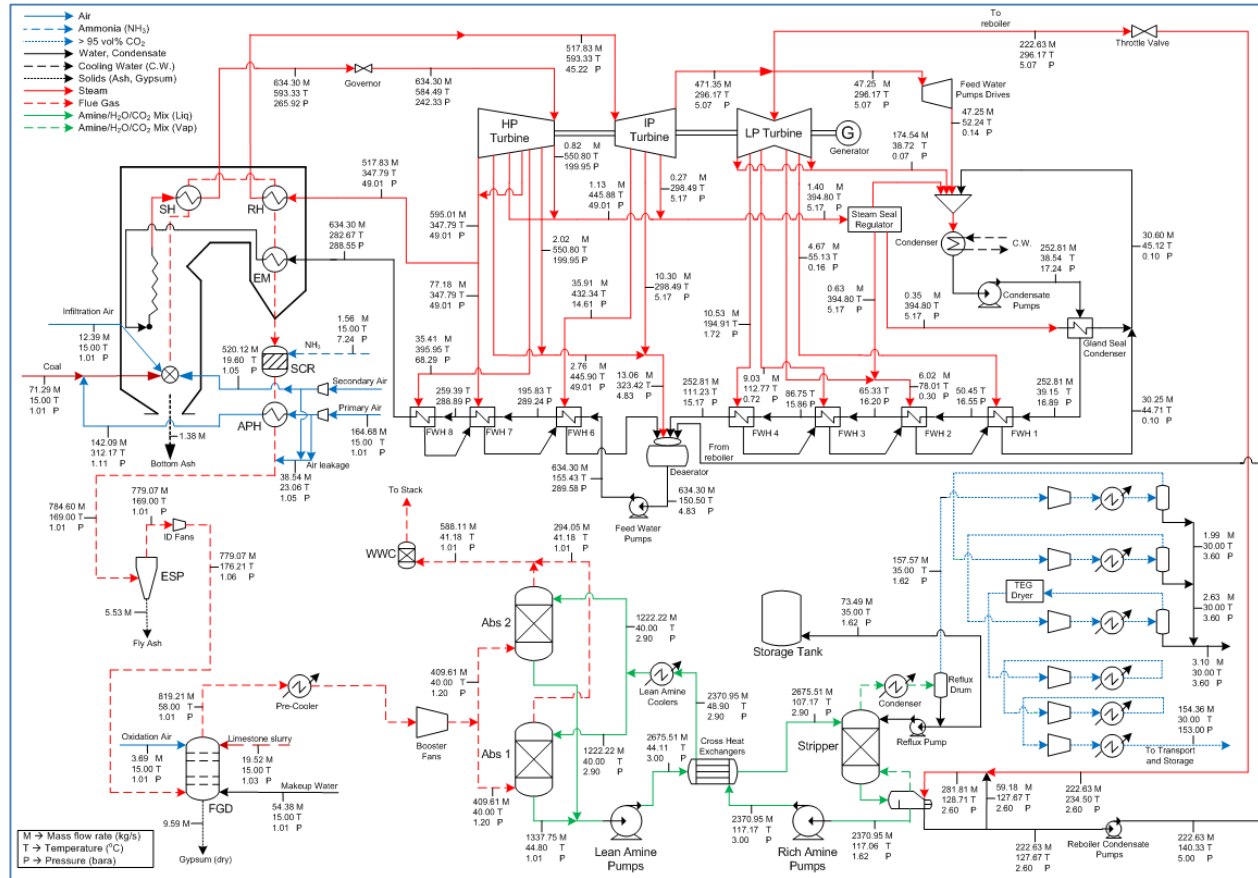


Figure 8.1. The process flow diagram (PFD) of the integrated power plant-PCO-CCU system with a PC-fired boiler firing Illinois No. 6 (bituminous coal), a once-through supercritical single-reheat steam cycle, and with throttled steam tapped from the IP-LP cross-over pipe.

8.2.2 Modelling Framework

The power plant was modelled on the basis of ~1705 MW_{th} turbine thermal input and a boiler efficiency of 88%.¹⁹² The properties of the coal (Illinois No. 6) combusted in the furnace/boiler of the power plant are summarized in **Table 8.2**. The required coal feed rate was calculated as follows:

$$F_{\text{Coal}} = \frac{Q_{\text{Boiler}}}{HHV_{\text{Coal}}} \quad (8.3.1)$$

where

$$Q_{\text{Boiler}} = \frac{Q_{\text{Turbine}}}{\eta_{\text{Boiler}}} = \frac{1705 \text{ MW}_{\text{th}}}{0.88} \quad (8.3.2)$$

Table 8.2. The properties of Illinois No. 6 bituminous coal.²⁰⁴

Proximate Analysis	As-received (wt %)	Dry (wt %)
Moisture	11.12	0.00
Volatile Matter	34.99	39.37
Ash	9.70	10.91
Fixed Carbon	44.19	49.72
Total	100.00	100.00
Ultimate Analysis	As-received (wt %)	Dry (wt %)
C	63.75	71.72
S	2.51	2.82
H ₂	4.50	5.06
H ₂ O	11.12	0.00
N ₂	1.25	1.41
O ₂	6.88	7.75
Ash	9.70	10.91
Cl	0.29	0.33
TOTAL	100.00	100.00
Heating Value	As-received	Dry
HHV (kJ/kg)	27113.00	30506.00
LHV (kJ/kg)	26151.00	29444.00

The theoretical air required, on a dry-basis, was calculated as follows:²⁰⁵

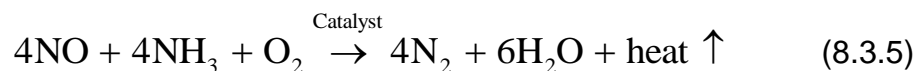
$$F_{\text{Dry Air}} (\text{Ib} / \text{MMBtu}) = \frac{11.52 (\%C) + 34.57 \left(\%H - \frac{\%O}{8} \right) + 4.32 (\%S)}{HHV (\text{Btu} / \text{Ib})} \times 10^4 \quad (8.3.3)$$

The wet-basis theoretical air required was calculated from the dry-basis theoretical air value calculated by Eq (8.3.3) and the moisture content in the air is at ISO conditions. The percent excess air was calculated on the basis of the oxygen content in the flue gas at the economizer outlet by the following equation:²⁰⁶

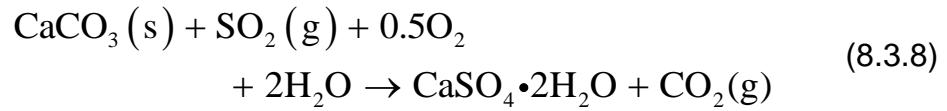
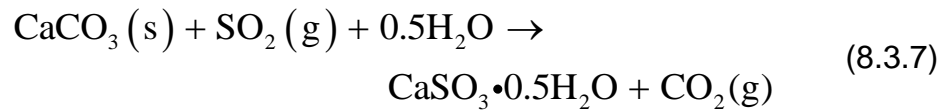
$$\text{Percent Excess Air} = \frac{100 \left(O_2 - \frac{CO}{2} \right)}{0.2682 \times N_2 - \left(O_2 - \frac{CO}{2} \right)} \quad (8.3.4)$$

where N_2 is the volume percent of nitrogen in the flue gas at the economizer outlet, which was taken as 81 as recommended in the literature;²⁰⁶ CO is the volume percent of carbon monoxide in the flue gas at the economizer outlet, which was taken as zero as recommended in the literature;²⁰⁶ O_2 is the volume percent of oxygen in the flue gas at the economizer outlet, which was taken as 2.7 in line with the value in the US DOE report.^{207,208}

The SCR unit was modelled as a reactor. Since the theoretical number of moles of NH_3 required in the SCR unit is equal to the number of moles of NO_x in the flue gas, the amount of NH_3 required in the SCR unit was calculated based on the amount of NO_x in the flue gas and with 2 ppmv NH_3 slip. The predominant reactions in the SCR unit are given as follows:^{17,206}



The FGD unit was modelled by a combination of unit operation blocks, which includes a reactor and a separator. The overall reactions occurring in the FGD unit are given as follows.²⁰⁶



The absorber and stripper columns in the PCC plant were modelled with the Aspen Plus RadFrac model, a second generation rate-based model for multistage separation operations. The model adopted for the thermodynamic properties is based on the work by Zhang et al.¹⁰¹ The framework of the thermodynamic model by Zhang et al.¹⁰¹ can be found in **Section 6.3.1** Error! Reference source not found. and therefore, it is not be repeated here.

The multi-stage CO₂ compression system was modelled as a six-stage compressor with inter-stage coolers and knock-out drums (KODs). The compressed CO₂ stream was cooled to a temperature of 30 °C in the inter-stage coolers and the separation of condensed water was realized in the KODs, with a 2% pressure drop applied to the KODs.^{207,208} The inter-stage pressures are shown in **Table 8.3**. The compressed CO₂ stream from the third-stage of the compressor was dried in a tetraethylene glycol (TEG) unit to give about 20 ppmv H₂O in the compressed CO₂ stream.

A complete documentation of the model parameters assumptions for the boiler, SCR, FGD, steam cycle, and the CO₂ compression system can be found in the quality guidelines published by DOE/NETL.^{207,208}

Table 8.3. Inter-stage pressure of the CO₂ Compressor.¹⁹²

Stage	Outlet Pressure (bar)
1	3.6
2	7.8
3	17.1
4	37.6
5	82.7
6	153

8.3 Optimal Process Design of the PCC Plant in the Integrated System

The optimal process design of the commercial-scale PCC plant in the integrated system is based on the design method and philosophy in the paper that we have published,¹⁴⁹ and which is presented in **Chapter 7**.

The optimum design data for the absorber and stripper columns in the PCC plant are summarized in **Table 8.4**, and they were arrived at based on process and economic analyses. **Figure 8.2(a)** and **Figure 8.2(b)** summarize the design results for the PCC plant. The design results cover lean CO₂ loadings ranging from 0.1 mol/mol to 0.3 mol/mol and a liquid/gas ratio that ranges from 2.09 to 5.29. The absorber and stripper heights, as well as the specific reboiler duties, are shown in **Figure 8.2(a)**.

Table 8.4. Optimal design data for the absorber and stripper columns in the PCC plant.

Flue Gas Flowrate (kg/s)	821.26
Optimum Lean CO ₂ loading (mol/mol)	0.20
Optimum Liquid/Gas Ratio (kg/kg)	2.93
Absorber	
Number of Absorber	2
Absorber Packing	Mellapak 250Y
Diameter (m)	16.13
Optimum Height (m)	23.04
Stripper	
Number of Stripper	1
Packing	Mellapak 250Y
Diameter (m)	14.61 ^b
Optimum Height (m)	25.62
Specific Reboiler Duty (MJ/kg CO ₂)	3.69

^bThe stripper diameter value is based on 0.7 fractional approach to maximum capacity so as to allow for coal flexibility. The stripper diameter is 13.67 m if 0.8 is used in place of 0.7.

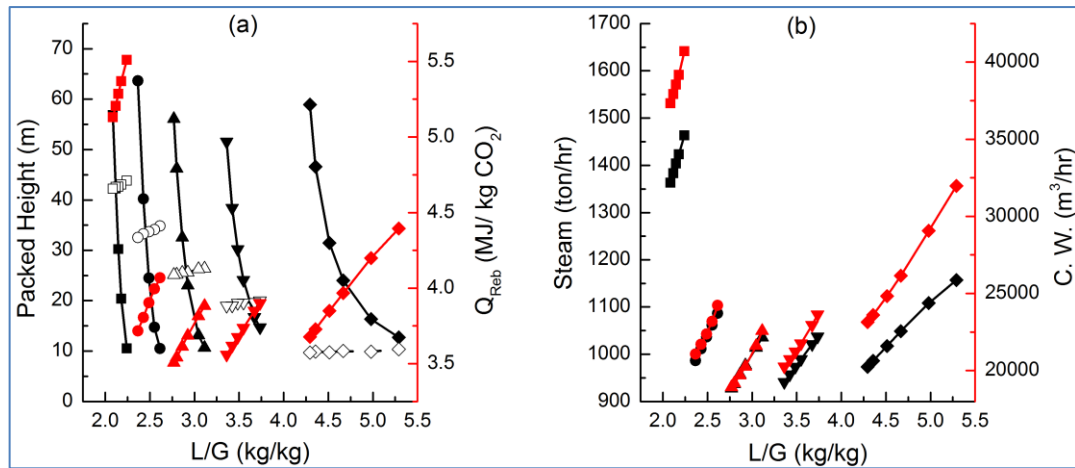


Figure 8.2. Design results for an MEA-based CO₂ capture plant that can service a 663 MWe (gross) supercritical PC power plant at 90% CO₂ capture rate. (a) Variations of absorber height (black solid lines), stripper height (black dash lines) and specific reboiler duty (red lines) with liquid/gas ratio for different lean CO₂ loadings. (b) Variations of steam requirement (black lines) and cooling water requirement (red lines) with liquid/gas ratio for different lean CO₂ loadings. [Symbols: (■, □, ■), 0.1 CO₂ loading; (●, ○, ●), 0.15 CO₂ loading; (▲, △, ▲), 0.2 CO₂ loading; (▼, ▽, ▼), 0.25 CO₂ loading; (◆, ◇, ◆), 0.3 CO₂ loading].

From **Figure 8.2(a)** it is clear that the absorber height required for 90% CO₂ capture increases sharply with liquid/gas ratio when the liquid/gas ratio is reduced below a certain optimum value for each lean CO₂ loading, and the absorber height decreases gradually if the liquid/gas ratio increases beyond the optimum value. Also, the change in the absorber height with liquid/gas ratio is less pronounced as the lean CO₂ loading increases. These observations clearly show that any arbitrary assumption of liquid/gas ratio, directly or indirectly, will most likely lead to a sub-optimal design. On the other hand, the stripper height is relatively unaffected by the liquid/gas ratio but the stripper height increases as the lean CO₂ loading decreases, which will have an implication on the overall capital cost of the plant.¹⁴⁹

The variations of the steam required by the stripper reboiler and the cooling water (C.W.) required by the stripper condenser and lean amine cooler with liquid/gas ratio are shown in **Figure 8.2(b)**. It is clear that the both the steam and cooling water required for each lean CO₂ loading decreases only marginally if the liquid/gas ratio reduces beyond the optimum liquid/gas ratio. The marginal decrease in the steam and cooling water required cannot compensate for the sharp increase in the absorber height; thus, the optimum design is not given by the liquid/gas ratio that has the minimum steam and cooling water requirement.

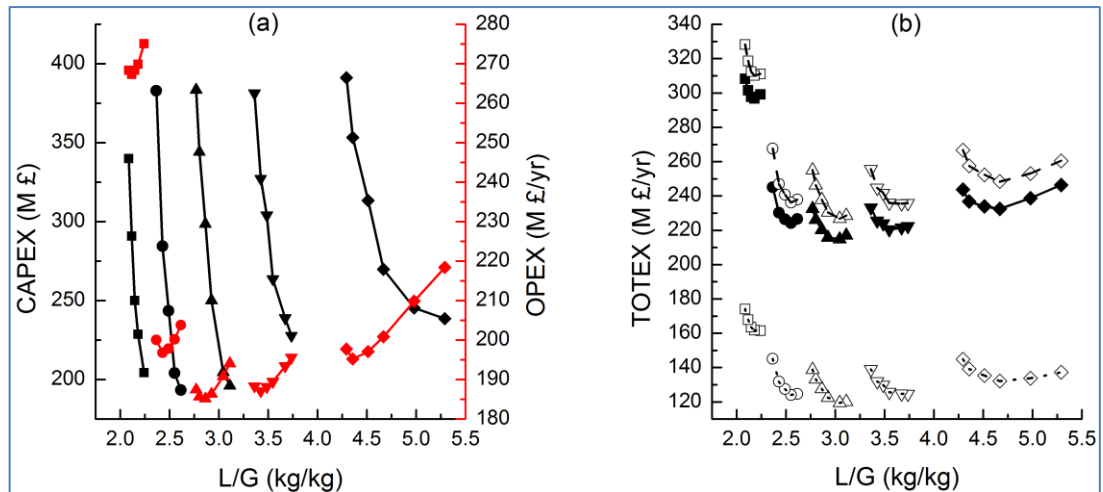


Figure 8.3. Design results for an MEA-based CO₂ capture plant that can service a 663 MWe (gross) supercritical PC power plant at 90% CO₂ capture rate. (a) Variations of overnight capital expenditure (black lines) and annual operating expenditure (red lines) with liquid/gas ratio for different lean CO₂ loadings. (b) Variations of annualized total expenditure with liquid/gas ratio for different lean CO₂ loadings: solid line, OPEX + A. CAPEX; dash line, OPEX + 1.5(A. CAPEX); dotted line, 0.5(OPEX) + A. CAPEX. [Symbols: (■, □, ■), 0.1 CO₂ loading; (●, ○, ●), 0.15 CO₂ loading; (▲, △, ▲), 0.2 CO₂ loading; (▼, ▽, ▼), 0.25 CO₂ loading; (◆, ◇, ◆), 0.3 CO₂ loading].

The economics of the plant, which includes the overnight capital cost (CAPEX) and the operating cost (OPEX) are shown in **Figure 8.3(a)**. **Figure 8.3(b)** shows the annualized total cost (TOTEX), which is a combination of the OPEX and an annualized cost for the CAPEX. The results of the three different scenarios that were considered for the TOTEX are shown in **Figure 8.3(b)**. From **Figure 8.3(a)** and **Figure 8.3(b)**, it is clear that there is trade-off between the CAPEX and the OPEX. The design with a lean CO₂ loading of 0.2 and a corresponding liquid/gas ratio of 2.93 was taken as the optimum. A summary of the optimum performance data for the PCC plant, including the compression and inter-cooling duties of the CCU, is given in **Table 8.5**.

Table 8.5. The optimum performance data for the PCC plant, including the compression and intercooling duties of the CCU.

PCC Plant	
Flue gas, absorber inlet (kg/s bar °C)	819.21 1.20 40.0
Flue gas, absorber outlet (kg/s bar °C)	588.11 1.01 41.2
Lean MEA solution, absorber inlet (kg/s bar °C)	2444.44 3.00 40.0
Lean MEA solution, stripper outlet (kg/s bar °C)	2444.44 1.62 117.2
Rich MEA solution, absorber outlet (kg/s bar °C)	2675.51 1.01 44.8
Rich MEA solution, stripper inlet (kg/s bar °C)	2675.51 3.00 107.2
MEA concentration, CO ₂ free basis (kg/kg)	0.30
Lean CO ₂ loading (mol/mol)	0.20
Rich CO ₂ loading (mol/mol)	0.505
Lean MEA solution cooler inlet temperature (°C)	48.90
CO ₂ captured (kg/s)	154.55
Reboiler heat duty (MW _{th})	569.71
Specific reboiler duty (MJ/kg CO ₂)	3.68
Stripper duty (MW _{th})	231.00
Lean MEA solution cooler duty (MW _{th})	77.98
Lean/Rich heat exchanger duty (MW _{th})	610.44
Lean MEA solution pump duty (kWe)	395.85
Rich MEA solution pump duty (kWe)	561.05
Absorber pressure drop (kPa)	2.72
Absorber fractional approach to flooding	0.71
Stripper pressure drop (kPa)	1.43
Stripper fractional approach to flooding	0.70
Stripper pressure (bar)	1.62
Booster fan duty (MWe)	18.83
CO₂ Compression Unit	
Total compression duty (MWe)	45.697
Total intercooling duty (MW _{th})	78.107

8.4 Integration of the PC-fired Power Plant to the PCC Plant and the CCU

The PC-fired power plant is integrated to the PCC plant in three ways: (i) flue gas from the power plant FGD to the absorbers in the PCC plant, (ii) steam tapping from either the IP-LP cross-over or the LP turbine in the steam cycle of the power plant to the reboiler in the plant and (iii) return of condensate from the reboiler in the PCC plant to the deaerator in steam cycle of the power plant. Since the tapped steam will normally be at a much higher pressure than that required by the reboiler in the PCC plant, the tapped steam will either be throttled using a throttle valve or a let-down turbine could be used to reduce the pressure of the tapped steam to that required by the reboiler in the PCC plant, and with the production of extra power by the let-down turbine. Also, there is a possibility of pre-heating the steam cycle condensate with the tapped steam so as to recover some of the superheat in the tapped steam. Additionally, the steam cycle of the power plant can be integrated to the inter-stage coolers in the CO₂ compressor unit (CCU).

Since the principal focus of this chapter, amongst other objectives, is the identification of the optimum operating pressure of the stripper that will maximize the net plant efficiency of the integrated system, it is important to analyze the impact of the operating pressure of the stripper on the required conditions (e.g. the minimum pressure) of the steam that is tapped, as well as the requirements (e.g. reboiler duty, condenser temperature, etc.) of the PCC plant. **Figure 8.4(a)** shows the variations of the temperature of the lean MEA solution in the reboiler, the condensation temperature of the tapped steam in the reboiler (assuming a minimum temperature difference of 10 °C between the temperature of the lean MEA solution in the reboiler and the condensation temperature of the tapped steam in the reboiler) and the minimum pressure of the steam that is tapped at the point of tapping (assuming a 10% pressure drop between the point of steam tapping in the steam cycle of the power plant and the location of the reboiler in the PCC plant) with the pressure of the stripper. From **Figure 8.4(a)**, it is clear that the lean MEA solution temperature in the reboiler, the condensation temperature of the steam in the reboiler and the minimum pressure of the steam that is tapped increase with the pressure of the stripper. The variation of the maximum operating temperature of the stripper that will give ~96% CO₂ in the stream sent to the CO₂ compressor unit with the pressure of the stripper is shown in **Figure 8.4(b)**.

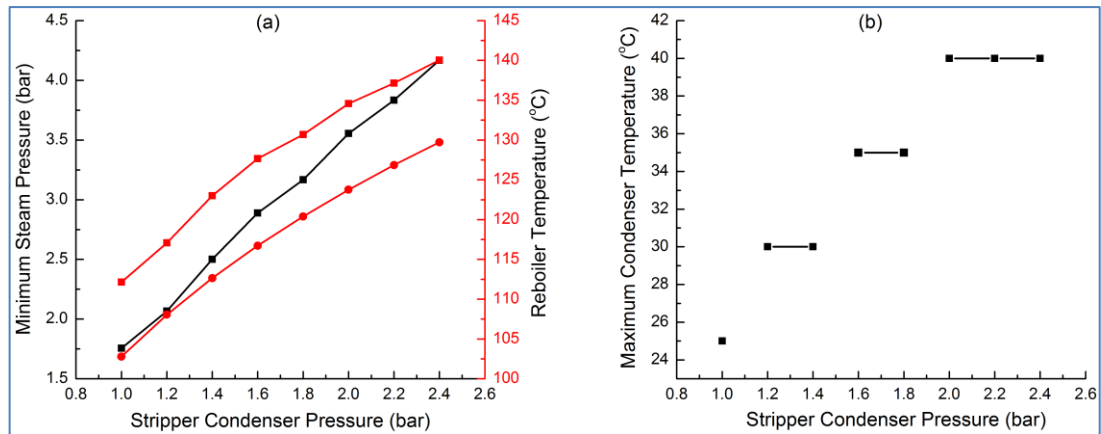


Figure 8.4. The reboiler conditions, tapped steam condition requirement and the maximum stripper temperature at different stripper pressure. (a) The variations of the minimum pressure of tapped steam and the temperature of lean MEA solution in the reboiler, as well as the steam condensation temperature in the reboiler, with stripper pressure. Lines: solid black line, minimum pressure of tapped steam; solid red lines, lean MEA solution temperature and the steam condensation temperature in the reboiler. Symbols: ■, steam condensation temperature; ●, lean MEA solution temperature. (b) The maximum condenser temperature that will give ~96 vol% CO₂ in the stream that is fed to the CCU.

From **Figure 8.4(b)**, it is clear that the maximum condenser temperature decreases as the pressure of the stripper decreases, which will have an implication on the rate of circulation of coolant (e.g. cooling water) in the condenser.

The variations of the specific reboiler duty and the specific condenser duty with the stripper pressure are shown in **Figure 8.5(a)**. Similarly, the variations of the required mass flowrates of tapped steam at different pressures with the stripper pressure are shown in **Figure 8.5(b)**. From **Figure 8.5(a)** and **Figure 8.5(b)**, it is clear that for stripper pressure below 1.6 bar, the specific reboiler duty, the specific condenser duty and the required mass flowrate of tapped steam increase sharply with decreasing stripper pressure. On the other hand, for a stripper pressure above about 1.6 bar, the specific reboiler duty, the specific condenser duty and the required mass flowrate of tapped steam decrease slightly with increasing stripper pressure. Thus, from **Figure 8.5**, operating the stripper at the highest possible pressure will minimize the energy penalty incurred due to CO₂ capture and CO₂ compression, especially if a simple steam throttling is used to reduce the pressure of the tapped steam.

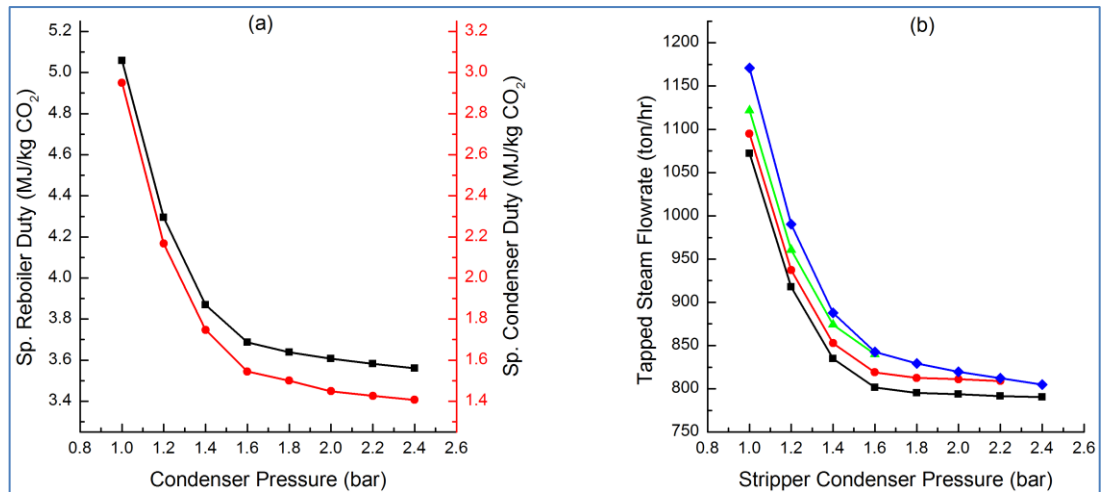


Figure 8.5. The variations of specific reboiler duty, specific condenser duty and the tapped steam mass flowrate with stripper pressure. (a) Specific reboiler duty and specific condenser duty. Symbols: ■, specific reboiler duty; ●, specific condenser duty. (b) Tapped steam mass flowrate at different tapping locations. Symbols: ■, IP-LP crossover and steam throttling; ●, LP at 4 bar and steam throttling; ▲, LP at 3 bar and steam throttling; ◆, let-down turbine.

However, the increasing rate of thermal degradation of the MEA with an increase in the reboiler temperature will normally limit the operating pressure of the stripper below about 2.4 bar because, from **Figure 8.4(a)**, the temperature of the lean MEA solution in the reboiler is about 130 °C if the stripper is operated at 2.4 bar.

8.4.1 Steam tapping from the IP-LP cross-over pipe at 5.07 bar

The overall performance of the integrated power plant-PCC plant-CCU system with steam tapping from the IP-LP cross-over pipe is shown in **Figure 8.6**. **Figure 8.6(a)** shows the variation of the net plant efficiency of the integrated system with the operating pressure of the stripper. The net plant efficiency of the integrated system with the use of a throttle valve or a let-down turbine, for CO₂ capture only and with both CO₂ capture and CO₂ compression, is shown in **Figure 8.6(a)**. From **Figure 8.6(a)**, the net plant efficiency of the integrated system with both CO₂ capture and CO₂ compression increases with the operating pressure of the stripper between 1.0 bar and 1.6 bar and then decreases gradually above 1.6 bar if a let-down turbine is used. Therefore, the optimum pressure at which the stripper should be operated is about 1.6 bar if a let-down turbine is used. On the other hand, the net plant efficiency of the integrated system with both CO₂

capture and CO₂ compression increases with an increase in the operating pressure of the stripper if a throttle valve is used. Therefore, the stripper should be operated at the maximum possible pressure that will minimize excessive thermal degradation of the amine. Nevertheless, from **Figure 8.6(a)** and with steam throttling, the optimal operating pressure range for the stripper is between 1.6 bar and 2.2 bar. The choice of pressure to be used will be dictated by an economic balance between the extra profit gained with increasing pressure and the extra cost incurred due to a more frequent MEA reclamation or a more frequent injection of fresh MEA with increasing pressure of the stripper. A stripper pressure ranging from 1.6 bar (~117 °C Lean MEA temperature) to 1.8 bar (~121 °C Lean MEA temperature) is recommended for the state-of-the-art 30 wt% MEA solution in line with the openly available data on the MEA-based Econamine FG Plus™ process licensed by Fluor®. ^{192,193}

The variations of the power produced by the main steam turbine, the power produced by the let-down turbine and power required by the CO₂ compressor with the operating pressure of the stripper are shown in **Figure 8.6(b)**.

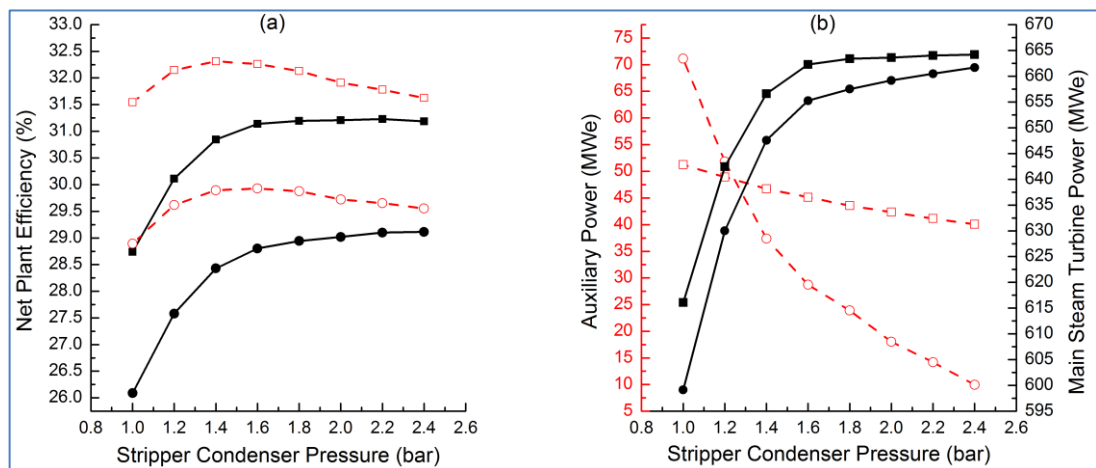


Figure 8.6. The performance of the integrated power plant-PCC plant-CCU system if steam is tapped from the IP-LP cross-over pipe in the steam cycle. (a) The variation of net plant efficiency with stripper pressure. Lines: solid lines, throttle valve; dashed lines, let-down turbine. Symbols: □ and ○, with CO₂ capture only; ■ and ●, with both CO₂ capture and CO₂ compression. (b) The variation of the main steam turbine power and auxiliary power (let-down turbine power and CO₂ compression load) with stripper pressure. Lines: solid line, the main steam turbine power; dashed lines, auxiliary load. Symbols: □, CO₂ compression load; ○, let-down turbine power; ■, the main steam turbine power with throttle valve; ●, the main steam turbine power with let-down turbine.

From **Figure 8.6(b)**, the power output from the main steam turbine increases sharply with an increase in the operating pressure of the stripper up to 1.6 bar, but increases only slightly with increasing pressure of the stripper above 1.6 bar. On the other hand, the power output from the let-down turbine decreases sharply with an increase in the operating pressure of the stripper up to 1.6 bar, but the decrease with further increase in the operating pressure of the stripper is less pronounced for stripper pressure above 1.6 bar. As expected, the power required by the CO₂ compressor decreases as the operating pressure of the stripper increases because of the increase in the pressure of the CO₂ compressor inlet stream with the increasing operating pressure of the stripper.

The extra gain in the net plant efficiency of the integrated system if a let-down turbine is used, as opposed to the use of a simple throttle valve, diminishes with the increasing pressure of the stripper. This is because of the increase in the back-pressure on the let-down turbine as the pressure of the stripper increases, with a consequential reduction in the power produced by the let-down turbine as shown in **Figure 8.6(b)**. The maximum efficiency of the integrated system with the use of a let-down turbine is 32.3% for CO₂ capture only, which corresponds to a stripper pressure of 1.4 bar, and 29.9% for both CO₂ capture and CO₂ compression, which corresponds to a stripper pressure of 1.6 bar. Similarly, the net plant efficiency of the integrated system with the use of a throttle valve and based on the recommended maximum pressure of 1.8 bar for the stripper is 31.2% for CO₂ capture only and 28.9% for both CO₂ capture and CO₂ compression. Thus, the extra gain in the net plant efficiency of the integrated system with the use of a let-down turbine when compared with steam throttling along with a stripper pressure of 1.8 bar is 1.1% for CO₂ capture only and 1.0% for both CO₂ capture and CO₂ compression. It remains unclear if the extra gain in the net plant efficiency of the integrated system with the use of a let-down turbine over a simple steam throttling is worth the investment in the let-down turbine. However, the conditions of the electricity market coupled with the economics of CO₂ emissions may give a clue as to whether it is worth investing in a let-down turbine or not.

8.4.2 Steam tapping from the LP turbine at 4 bar

The overall performance of the integrated power plant-PCC plant-CCU system with steam tapping from the LP turbine at 4 bar is shown in **Figure 8.7**. From **Figure 8.7(a)**, the maximum pressure at which the stripper can

operated if steam is tapped from the steam cycle at 4 bar is 2.2 bar. The net plant efficiency of the integrated system with the use of a throttle valve or a let-down turbine, for CO₂ capture only and with both CO₂ capture and CO₂ compression, is shown in **Figure 8.7(a)**. The variations of the power produced by the main steam turbine, the power produced by the let-down turbine and the power required by the CO₂ compressor with the operating pressure of the stripper are shown in **Figure 8.7(b)**. From **Figure 8.7(a)**, the net plant efficiency of the integrated system increases with the operating pressure of the stripper between 1.0 bar and 1.6 bar and then decreases gradually above 1.6 bar if a let-down turbine is used; thus, the optimum pressure at which the stripper should be operated is about 1.6 bar if a let-down turbine is used. On the other hand, and as for steam tapping from the IP-LP cross-over pipe, the net plant efficiency of the integrated system increases with an increase in the operating pressure of the stripper if a throttle valve is used; thus, the stripper should be operated at the maximum possible pressure that will minimize excessive thermal degradation of the amine. As previously stated in **Section 8.4.1** a stripper pressure ranging from 1.6 bar (~117 °C Lean MEA temperature) to 1.8 bar (~121 °C Lean MEA temperature) is recommended for the state-of-the-art 30 wt% MEA solution. The variations of the power produced by the main steam turbine, the power produced by the let-down turbine and power required by the CO₂ compressor with the operating pressure of the stripper are shown in **Figure 8.7(b)**. The trends are similar to those of **Figure 8.6(b)** and hence, the explanation of the trends in **Figure 8.6(b)** in **Section 8.4.1** is also applicable to **Figure 8.7(b)** and it will not be repeated here. As for steam tapping from the IP-LP cross-over pipe, the extra gain in the net plant efficiency of the integrated system if a let-down turbine is used as against the use of a simple throttle valve diminishes with increasing pressure of the stripper. The maximum efficiency of the integrated system with the use of a let-down turbine, which corresponds to a stripper pressure of 1.6 bar for CO₂ capture only and both CO₂ capture and CO₂ compression, is 32.3% for CO₂ capture only and 30.0% for both CO₂ capture and CO₂ compression. Similarly, the net plant efficiency of the integrated system with the use of a simple throttle valve and based on the recommended maximum pressure of 1.8 bar for the stripper is 31.7% for CO₂ capture only and 29.5% for both CO₂ capture and CO₂ compression.

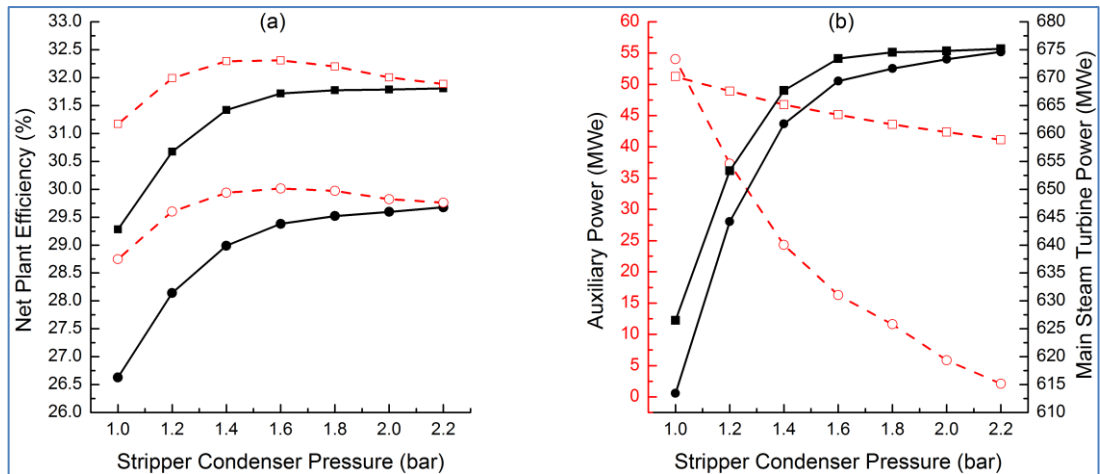


Figure 8.7. The performance of the integrated power plant-PCC plant-CCU system if a low pressure (LP) steam at 4 bar is tapped from the low pressure turbine in the steam cycle. (a) The variation of net plant efficiency with stripper pressure. Lines: solid lines, throttle valve; dashed lines, let-down turbine. Symbols: □ and ○, with CO₂ capture only; ■ and ●, with both CO₂ capture and CO₂ compression. (b) The variation of the main steam turbine power and auxiliary power (let-down turbine power and CO₂ compression load) with stripper pressure. Lines: solid line, the main steam turbine power; dashed lines, auxiliary load. Symbols: □, CO₂ compression load; ○, let-down turbine power; ■, the main steam turbine power with throttle valve; ●, the main steam turbine power with let-down turbine.

Thus, the extra gain in the net plant efficiency of the integrated system with the use of let-down turbine when compared with steam throttling coupled with a stripper pressure of 1.8 bar is 0.6% for CO₂ capture only and 0.5% for both CO₂ capture and CO₂ compression. It is clear that the extra gain in the net plant efficiency of the integrated system with the use of a let-down turbine over a simple steam throttling for steam tapping from the LP turbine at 4 bar is less attractive when compared with that of steam tapping from the IP-LP cross-over pipe in the steam cycle. In fact, from **Figure 8.7(a)**, there is little or no gain in the use of a let-down turbine over steam throttling if the stripper is operated at the maximum possible pressure of 2.2 bar. It is important to add that the net plant efficiency of the integrated system with both CO₂ capture and CO₂ compression and with steam tapping from the LP turbine at 4 bar slightly outperform steam tapping from the IP-LP cross-over pipe if a let-down turbine is used. On the other hand, the net plant efficiency of the integrated system with both CO₂ capture only and with steam tapping from the LP turbine at 4 bar is slightly outperformed by steam tapping from the IP-LP cross-over pipe if a let-down turbine is used. Furthermore, steam tapping from the LP turbine at 4 bar outperforms steam tapping from the IP-LP cross-over pipe irrespective of the operating pressure of the stripper.

8.4.3 Steam tapping from the LP Turbine at 3 bar

The overall performance of the integrated power plant-PCC plant-CCU system with steam tapping from the LP turbine at 3 bar is shown in **Figure 8.8**. From **Figure 8.8(a)**, the maximum pressure at which the stripper can operate if steam is tapped from the steam cycle at 3 bar is about 1.6 bar. The net plant efficiency of the integrated system with the use of a throttle valve or a let-down turbine, for CO₂ capture only and with both CO₂ capture and CO₂ compression, is shown in **Figure 8.8(a)**. The variations of the power produced by the main steam turbine, the power produced by the let-down turbine and power required by the CO₂ compressor with the operating pressure of the stripper are shown in **Figure 8.8(b)**. From **Figure 8.8(a)**, the net plant efficiency of the integrated system with both CO₂ capture and CO₂ compression increases with the operating pressure of the stripper between 1.0 bar and 1.6 bar; thus, the optimum pressure at which the stripper should be operated is about 1.6 bar if a let-down turbine is used. On the other hand, and as for steam tapping from the IP-LP cross-over pipe, the net plant efficiency of the integrated system increases with an increase in the operating pressure of the stripper if a throttle valve is used; thus, the stripper should be operated at the maximum possible pressure that will minimize excessive thermal degradation of the amine.

As previously stated in **Section 8.4.1** a stripper pressure ranging from 1.6 bar (~117 °C Lean MEA temperature) to 1.8 bar (~121 °C Lean MEA temperature) is recommended for the state-of-the-art 30 wt% MEA solution; thus the stripper should be operated at 1.6 bar since it is the maximum possible operating pressure of the stripper with steam tapping from the LP turbine at 3 bar. Furthermore, since the maximum net plant efficiency of the integrated system with a let-down turbine is not too different from the net plant efficiency of the integrated system with steam throttling at the maximum pressure of 1.6 bar, there is no incentive for investing in a let-down turbine and hence a simple throttle valve should be used instead. The net plant efficiency of the integrated system with the use of a simple throttle valve and a stripper pressure of 1.6 bar is 32.3% for CO₂ capture only and 30.0% for both CO₂ capture and CO₂ compression. Thus, the highest net plant efficiency of the integrated system with steam throttling is obtained if the stripper is operated at a pressure of about 1.6 bar and steam is tapped from the LP turbine at 3 bar.

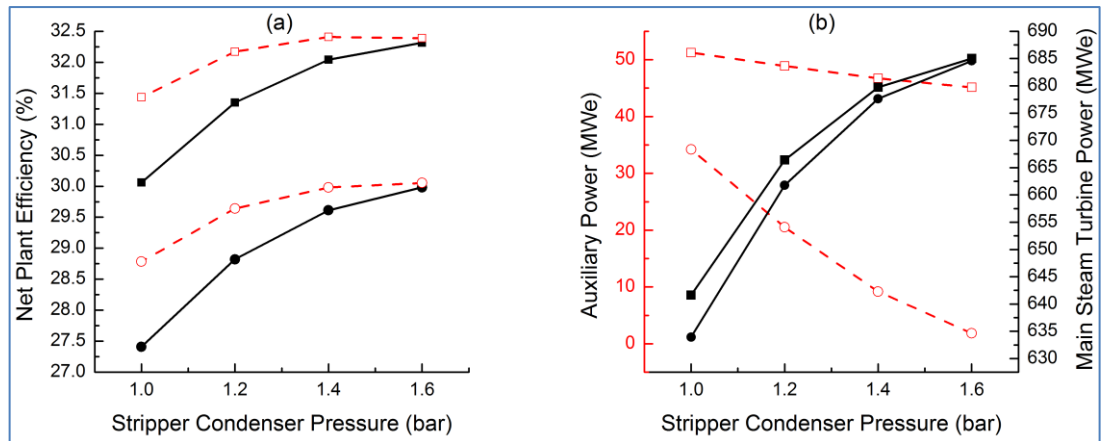


Figure 8.8. The performance of the integrated power plant-PCC plant-CCU system if a low pressure (LP) steam at 3 bar is tapped from the low pressure turbine in the steam cycle. (a) The variation of net plant efficiency with stripper pressure. Lines: solid lines, throttle valve; dashed lines, let-down turbine. Symbols: □ and ○, with CO₂ capture only; ■ and ●, with both CO₂ capture and CO₂ compression. (b) The variation of the main steam turbine power and auxiliary power (let-down turbine power and CO₂ compression load) with stripper pressure. Lines: solid line, the main steam turbine power; dashed lines, auxiliary load. Symbols: □, CO₂ compression load; ○, let-down turbine power; ■, the main steam turbine power with throttle valve; ●, the main steam turbine power with let-down turbine.

It is important to add that, if a throttle valve is used, the net plant efficiency of the integrated system with both CO₂ capture and CO₂ compression, and with a stripper pressure of 1.6 bar coupled with steam tapping from the LP turbine outperforms steam tapping from the IP-LP cross-over pipe coupled with a stripper pressure of 1.8 bar and steam tapping from the LP turbine at 4 bar coupled with a stripper pressure of 1.8 bar. Therefore, the optimal integration of the steam cycle to the PCC plant is steam tapping from the LP turbine coupled with a stripper pressure of about 1.6 bar. The optimum stripper pressure of about 1.6 bar is in line with the stripper pressure in the MEA-based Econamine FG Plus™ process, which was reported as 1.62 bar in the 2004 IEA report¹⁹³ and 1.65 bar in the FEED study report for the ROAD project.¹⁸³

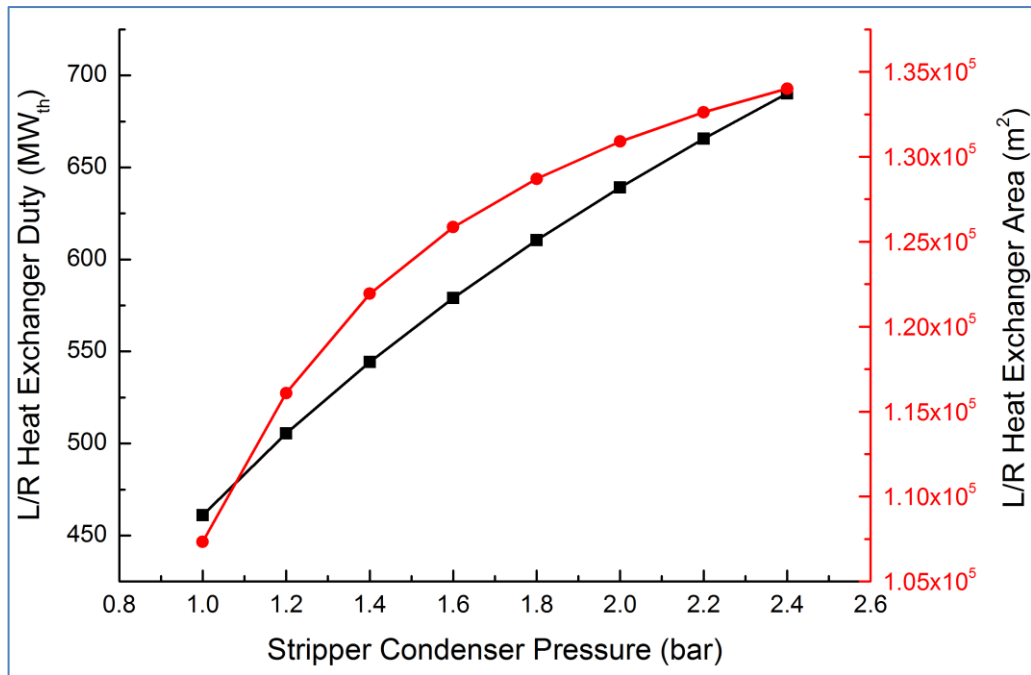


Figure 8.9. The variations of the heat duty and the heat transfer area of the lean/rich heat exchanger. Symbols: ■, heat exchanger duty; ●, heat exchanger area.

8.4.4 The Effect of Stripper Pressure on the Lean/Rich Heat Exchanger

The variations of the heat duty and the heat transfer area of the lean/rich heat exchanger with the operating pressure of the stripper are shown in **Figure 8.9**. The heat transfer area of the lean/rich heat exchanger was calculated with a temperature approach of 10 °C at the lean amine inlet end and with default parameters values for heat transfer coefficients in Aspen Plus. It is clear from **Figure 8.9** that both the heat exchanger duty and the heat transfer area increase with an increase in operating pressure of the stripper.

The increase in the heat exchanger duty, and the required heat transfer area by extension, with an increase in the operating pressure of the stripper is because of the increase in the specific or molar heat capacity of the lean MEA solution in the reboiler as the temperature of the lean MEA solution in the reboiler increases.¹²⁵ Also, the increase in the temperature of the lean MEA solution in the reboiler is related to an increase in the stripper as shown in **Figure 8.4(a)**. Therefore, the design of the lean/rich heat exchanger must take the envisaged operating range of the stripper pressure into consideration so as to avoid under-sizing of the lean/rich heat exchanger.

8.4.5 Steam Cycle Condensate Pre-heating

The pre-heating of the steam cycle condensate by the superheat in the tapped steam as an option for the elimination of the four low pressure boiler feed water (LPBFW) pre-heaters downstream of the deaerator was investigated for steam tapping from the LP turbine at 3 bar. It led to a decrease in the net plant efficiency of the integrated process by about 0.2% in absolute terms if the four LPBFW preheaters downstream of the deaerator and the associated steam bleeding from the LP turbine are eliminated. The reason for the reduction in the net plant efficiency is because more steam tapping is required to meet the reboiler duty since the reboiler duty is mainly satisfied by the latent heat of the steam condensation in the reboiler. Pre-heating the steam cycle condensate by tapped steam reduces the enthalpy of the tapped steam and, by extension, the amount of the recycled reboiler condensation used in desuperheating the tapped steam before its condensation in the reboiler is reduced as well. The consequence of the reduction in the recycled reboiler condensate is that less steam condenses in the reboiler; thus, in order to meet the required reboiler duty, more steam must be tapped from the steam cycle, which has a negative impact on the power output from the steam turbine. Therefore, the gain achieved by eliminating the four LPBFW pre-heaters if tapped steam is used to pre-heat the steam cycle condensate is countered by a loss in the net plant efficiency of the integrated system. However, it was possible to eliminate 3 of the four LPBFW pre-heaters (FWH 1, FWH 2 and FWH 3 in **Figure 8.1**) by the pre-heating of the steam cycle condensate with the tapped steam without any loss in the net plant efficiency of the plant.

The pre-heating of the steam cycle condensate by the inter-coolers in the CO₂ compressor as an option for elimination of the four low pressure boiler feed water (LPBFW) pre-heaters downstream of the deaerator was also investigated for steam tapping from the LP turbine at 3 bar, and it led to an increase in the net plant efficiency of the integrated system by about 0.4%. The steam cycle condensate, which has a temperature of about ~38 °C was divided into five streams and four of the divided streams were used to cool the compressed CO₂ to 50 °C in the first 4 inter-coolers while the last stream was used to cool the compressed CO₂ to 47 °C in the last inter-cooler; thus, further cooling of the compressed CO₂ to 30 °C is achieved by the use of cooling water. It remains unclear if the 0.4% increase in the net plant efficiency of the integrated system is more than enough to warrant the added

complexity, which will have an implication for plant control as well as reliability and availability.

8.5 Conclusions

Steam tapping from the IP-LP cross-over pipe coupled with low stripper pressure favours the use of a let-down turbine over the use of steam throttling. However, it remains unclear if the extra gain in the net plant efficiency of the integrated system with the use of a let-down turbine over a simple steam throttling is worth the investment in the let-down turbine. The optimum stripper pressure that maximizes the net plant efficiency of the integrated system if a let-down turbine is used is about 1.6 bar. If steam is tapped from the LP turbine at 4 bar, the stripper may be operated up to 1.8 bar provided there is no excessive thermal degradation of the amine. The extra gain in the net plant efficiency of the integrated system if a let-down turbine is used in conjunction with LP steam tapping at 4 bar is not attractive enough to warrant investing in a let-down turbine; thus steam tapped from the LP turbine at 4 bar should be throttled and the stripper should be operated at the maximum pressure that will limit thermal degradation of the amine. There is no benefit in the use of a let-down turbine over a throttle valve if steam is tapped from the LP turbine at 3 bar. Therefore, a throttle valve should be used if steam is tapped from the LP turbine at 3 bar and the stripper should be operated at the maximum possible pressure, which is about 1.6 bar. The optimum stripper pressure of about 1.6 bar is in line with the stripper pressure in the MEA-based Economine FG PlusTM process. The pre-heating of the steam cycle condensate by the superheat in the tapped steam as an option for the elimination of the four low pressure boiler feed water (LPBFW) pre-heaters downstream of the deareator led to a decrease in the net plant efficiency of the integrated process by about 0.16% in absolute terms. However, elimination of three of the four LPBFW pre-heaters coupled with pre-heating of the steam cycle condensate resulted in no efficiency loss. The pre-heating of the steam cycle condensate by the inter-coolers in the CO₂ compressor as an option for elimination of the four low pressure boiler feed water (LPBFW) pre-heaters downstream of the deareator was also investigated for steam tapping from the LP turbine at 3 bar, and it led to an increase in the net plant efficiency of the integrated system by about 0.4%.

Finally, having designed the PCC plant in the integrated system discussed in this chapter on the basis of a particular type of coal (Illinois No. 6 bituminous

coal), the integrated system will be simulated with the combustion of different types of coal in the power plant boiler and the impact of coal type on the overall performance of the integrated system will be quantified in **Chapter 9**.

Chapter 9

Modelling and Simulation of a Coal-Fired Power Plant Integrated to an Amine-based CO₂ Capture Plant

9.1 Introduction

The use of coal has increased substantially over the last decade and coal is expected to remain as the leading source of electricity generation, with a projected share of about 33% in 2035 according to the IEA.³ However, it has been reported that coal combustion contributed 44% of the world's CO₂ emissions in 2011,²⁰⁹ and that the deployment of CO₂ capture and storage systems is the only option that can limit CO₂ emissions arising from coal combustion.²¹⁰ Among the several technologies for CO₂ capture currently under development globally, solvent-based post-combustion CO₂ capture technology using amines is considered to be the most mature and the likely technology that will be chosen for early deployment of CCS systems.¹⁵⁸ As a consequence, the reduction of solvent regeneration energy is the focus of most of the solvent-based post-combustion CO₂ capture (PCC) research currently being performed globally. From the viewpoint of current research and development (R&D) activities worldwide, three main areas are being investigated in order to reduce the regeneration energy requirement of amine-based PCC, namely: (a) development of new solvents with better overall performance than 30 wt% monoethanolamine (MEA) aqueous solution, which is generally considered as the base-line solvent for solvent-based PCC, (b) PCC process optimization, including modifications of PCC plant configuration, and (c) optimal integration of the PCC Plant, including the associated CO₂ compression system, to the upstream power plant.¹⁴⁹

Process modelling and simulation is critical in the optimal scale-up of a PCC pilot plant to the size required for a commercial-scale coal-fired power plant. Also, the integrated modelling and simulation of a commercial-scale coal-fired power plant integrated to a commercial-scale amine-based PCC plant is equally critical as far as the optimal design and operation of the integrated power plant-PCC plant is concerned. This has led to several publications on the integration of amine-based PCC plant to coal-fired power plants based on process modelling and simulations.^{37,169-171,174,176,177,181,182,195-203} Furthermore, some of the publications also considered the CO₂

Compression Unit (CCU) as part of the integrated system in their evaluations.^{174,182,195,198,202,203} However, only a few publications^{169,171,176,177,181,182} have discussed the scale-up design of the amine-based PCC plant, but with minimal or incomplete information on the design process, and the design results reported by most of them appear to sub-optimal, or even unrealistic in some cases when compared with the design data in the non-confidential Report of the Front End Engineering Design (FEED) study undertaken by Fluor® for the “ROAD project” (Rotterdam Opslag en Afvang Demonstratieproject; Rotterdam Capture and Storage Demonstration Project),¹⁸³ as well as statements in process licensor reports.^{48,184,185} The principal reason why the design results reported by most of them appear to be sub-optimal is because the values of the lean CO₂ loading and/or the solvent circulation rate in the PCC plant were not optimized, and this has been addressed in **Chapter 8** of this thesis. It is important to note that the assertion that the values of the lean CO₂ loading and/or solvent circulation rate were not optimized in most of the previous publications is validated by experts’ responses on the lean CO₂ loading of commercial-scale amine systems currently in operation, which were collated by Rao et al.²¹¹ The scale-up of the PCC plant in the integrated power plant-PCC-CCU system discussed in this chapter is based on the design method and philosophy in the paper we have published,¹⁴⁹ and which is presented in **Chapter 7**. The details of the scale-up design of the PCC plant in the integrated power plant-PCC-CCU system discussed in this chapter can be found in **Chapter 8**, which focuses on the optimal integration of the power plant to the PCC plant.²¹²

9.2 Process Description and Modelling Framework

9.2.1 Process Description

The integrated process is comprised of a PC-fired supercritical power plant, an amine-based PCC plant for CO₂ capture and a multistage CO₂ compression unit, and it is based on the supercritical PC-fired power plant with CO₂ capture case reported by the US DOE.¹⁹² Since a detailed description of the integrated process is already presented in **Section 8.2.1, Chapter 8**, it will not be repeated here. However, the process flow diagram of the integrated system is shown in **Figure 9.1**.

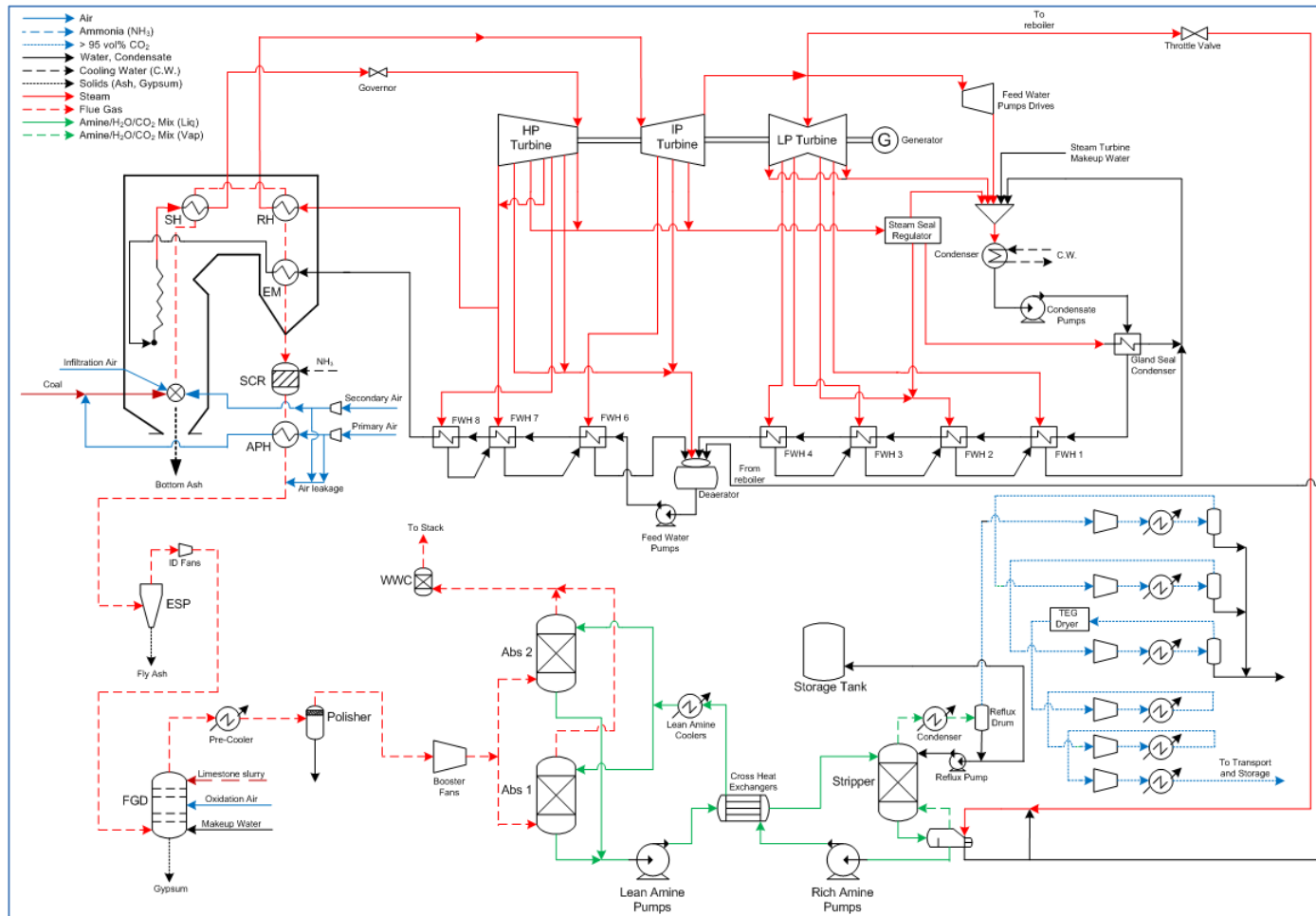


Figure 9.1. The process flow diagram (PFD) of the integrated power plant-PCC-CCU system with a PC-fired boiler and a once-through supercritical single-reheat steam cycle.

Table 9.1. The proximate analysis, the ultimate analysis and the heating value of the three different types of coal investigated.²⁰⁴

	Bituminous Coal (Illinois No. 6)		Sub-bituminous Coal (Montana Rosebud)		Lignite Coal (North Dakota)	
Proximate Analysis	As-received (wt %)	Dry (wt %)	As-received (wt %)	Dry (wt %)	As-received (wt %)	Dry (wt %)
Moisture	11.12	0.00	25.77	0.00	36.08	0.00
Volatile Matter	34.99	39.37	30.34	40.87	26.52	41.48
Ash	9.70	10.91	8.19	11.04	9.86	15.43
Fixed Carbon	44.19	49.72	35.70	48.09	27.54	43.09
Total	100.00	100.00	100.00	100.00	100.00	100.100
Ultimate Analysis	As-received (wt %)	Dry (wt %)	As-received (wt %)	Dry (wt %)	As-received (wt %)	Dry (wt %)
C	63.75	71.72	50.07	67.45	39.55	61.88
S	2.51	2.82	0.73	0.98	0.63	0.98
H ₂	4.50	5.06	3.38	4.56	2.74	4.29
H ₂ O	11.12	0.00	25.77	0.00	36.08	0.00
N ₂	1.25	1.41	0.71	0.96	0.63	0.98
O ₂	6.88	7.75	11.14	15.01	10.51	16.44
Ash	9.70	10.91	8.19	11.03	9.86	15.43
Cl	0.29	0.33	0.01	0.01	0.00	0.00
TOTAL	100.00	100.00	100.00	100.00	100.00	100.00

Heating Value	As-received	Dry	As-received	Dry	As-received	Dry
HHV (Btu/lb)	11666.00	13126.00	8564.00	11516.00	6617.00	10427.00
LHV (Btu/lb)	11252.00	12712.00	8252.00	11096.00	6364.00	10032.00
HHV (kJ/kg)	27113.00	30506.00	19920.00	26787.00	15391.00	24254.00
LHV (kJ/kg)	26151.00	29444.00	19195.00	25810.00	14804.00	23335.00

9.2.2 Modelling Framework

The power plant was modelled on the basis of $\sim 1705 \text{ MW}_{\text{th}}$ turbine thermal input and a boiler efficiency of 88%¹⁹² so as to provide meaningful comparison of the results obtained from the three different types of coal investigated in this chapter. The details of the modelling framework can be found in **Section 8.2.2**, and therefore it is not repeated here. The properties of the three different types of coal investigated are summarized in **Table 9.1**.

9.3 Results and Discussions

The results for the main streams in the PC power plant, when fired with three different types of coal, are shown in **Table 9.2**. Since the results for the three different types of coal are based on the same turbine heat input and boiler efficiency, the coal and combustion air flowrates are least for Illinois No. 6 (bituminous coal) and highest for North Dakota (lignite coal). As a consequence, the flue gas flowrate is least for Illinois No. 6 (bituminous coal) and highest for North Dakota (lignite coal). The conditions and composition of the flue gas at four different locations (SCR inlet, FGD inlet, CO₂ absorber inlet and CO₂ absorber outlet) are shown in **Table 9.3**. The optimal design data for the absorber and stripper columns in the PCC plant are shown in **Table 9.4**, while the optimum performance data for the CO₂ capture plant with a 30 wt% MEA solution, including the compression and intercooling duties needed by the CO₂ compression system, are summarized in **Table 9.5** for the three different types of coal investigated. The stripper reboiler and condenser duties, as well as the duties for the lean amine pump, the rich amine pump, the lean amine cooler and the lean/rich heat exchanger, are least for Illinois No. 6 (bituminous coal) and highest for North Dakota (lignite coal). **Table 9.6** compares the optimum energy performance of the integrated system for the three different types of coal if the PCC plant is operated with 30 wt% MEA solution. The quantifications of the impacts of MEA concentration on the overall performance of the integrated system for the three different types of coal investigate are shown in **Table 9.7**. The detailed explanation of the impacts of using different types of coal on the overall performance of the integrated system comprising the PC power plant, the PCC plant and the CCU in general and the PCC plant in particular is presented in the following sub-sections.

Table 9.2. The key performance data of the PC power plant when fired with the three different types of coal investigated.

	Bituminous Illinois No. 6	Sub-bituminous Montana Rosebud	Lignite North Dakota
Furnace/Boiler/SCR			
Coal (kg/s bar °C)	71.29 1.01 15	97.12 1.01 15	125.69 1.01 15
Primary air (kg/s bar °C)	164.68 1.01 15	284.59 1.01 15	288.15 1.01 15
Secondary Air (kg/s bar °C)	536.07 1.01 15	426.89 1.01 15	432.47 1.01 15
Air Infiltration (kg/s bar °C)	12.39 1.01 15	12.57 1.01 15	12.73 1.01 15
NH ₃ injected (kg/s bar °C)	1.56 7.24 15	1.13 7.24 15	0.79 7.24 15
Flue gas, EPS inlet (kg/s bar °C)	784.60 1.01 169	820.71 1.01 169	857.47 1.01 169
Slag (kg/s)	1.38	1.59	0.99
Primary air fans duty (MWe)	1.75	3.02	3.06
Forced draft fans duty (MWe)	2.49	1.98	2.01
Induced draft fans duty (MWe)	6.02	6.36	6.71
Supercritical Steam Turbine			
Main steam (kg/s bar °C)	633.09 242.33 593	633.09 242.33 593	633.09 242.33 593
Reheat to furnace/boiler (kg/s bar °C)	516.62 49.01 354	516.62 49.01 354	516.62 49.01 354
Reheat from furnace/boiler (kg/s bar °C)	516.62 45.22 593	516.62 45.22 593	516.62 45.22 593
Steam to stripper reboiler (kg/s bar °C)	223.80 5.07 296	236.74 5.07 296	244.94 5.07 296
Condensate return from stripper (kg/s bar °C)	223.80 3.00 130	236.74 3.00 130	244.94 3.00 130

Condensate, condenser outlet (kg/s bar °C)	247.73 0.07 38	234.79 0.07 38	226.59 0.07 38
Boiler feed water, economiser inlet (kg/s bar °C)	633.09 288.55 284	633.09 288.55 284	633.09 288.5 284
EPS/FGD			
Fly ash (kg/s)	5.53 1.01 169	6.36 1.01 169	10.05 1.01 169
Lime slurry (kg/s)	19.52 1.03 15	7.72 1.03 15	8.72 1.03 15
Oxidation Air (kg/s)	3.69 1.01 15	1.46 1.01 15	1.65 1.01 15
Makeup water (kg/s)	54.38 1.01 15	21.50 1.01 15	24.28 1.01 15
Flue gas, FGD outlet (kg/s bar °C)	819.21 1.01 58	838.02 1.01 58	850.28 1.01 58
Gypsum, moisture-free (kg/s)	9.59	3.79	4.28

Table 9.3. The conditions and composition of the flue gas from the combustion of the different types of coal investigated at various locations.

	Illinois No. 6	Montana Rosebud	North Dakota	Illinois No. 6	Montana Rosebud	North Dakota	Illinois No. 6	Montana Rosebud	North Dakota	Illinois No. 6	Montana Rosebud	North Dakota
Location	SCR Inlet			FGD Inlet			CO ₂ Absorber Inlet			CO ₂ Absorber Outlet		
T/(°C)	296.88	296.85	296.88	176.21	176.18	176.14	40.00	40.00	40.00	42.00	42.00	42.00
P/(bara)	0.99	0.99	0.99	1.06	1.06	1.06	1.20	1.20	1.20	1.01	1.01	1.01
F/(kg/s)	738.97	767.83	804.26	779.07	814.35	847.42	819.21	838.02	850.28	588.11	598.29	604.10
<u>Composition</u>												
CO ₂ (mol/mol)	0.1528	0.1568	0.1533	0.1444	0.1462	0.1435	0.1347	0.1400	0.1432	0.0158	0.0189	0.0197
H ₂ O (mol/mol)	0.0911	0.1257	0.1638	0.0918	0.1214	0.1563	0.1621	0.1620	0.1615	0.0195	0.0195	0.0195
N ₂ (mol/mol)	0.7282	0.6961	0.6662	0.7308	0.7014	0.6731	0.6750	0.6692	0.6692	0.9265	0.9226	0.9255
O ₂ (mol/mol)	0.0130	0.0097	0.0062	0.0220	0.0219	0.0182	0.2026	0.0208	0.0181	0.0278	0.0287	0.0250
Ar (mol/mol)	0.0087	0.0083	0.0079	0.0087	0.0083	0.0080	0.0080	0.0079	0.0079	0.0102	0.0101	0.0102
SO ₂ (mol/mol)	0.0022	0.0009	0.0009	0.0021	0.0008	0.0008	-	-	-	-	-	-
NO (mol/mol)	0.0037	0.0026	0.0017	-	-	-	-	-	-	-	-	-
NO ₂ (ppmv)	0.9750	0.6634	0.3859	-	-	-	-	-	-	-	-	-

Table 9.4. Optimal design data for the absorber and stripper columns in the CO₂ capture plant based on Illinois No. 6 bituminous coal

Flue Gas Flowrate (kg/s)	821.26
Optimum Lean CO ₂ loading (mol/mol)	0.18 ^a
Optimum Liquid/Gas Ratio (kg/kg)	2.74 ^a
Absorber	
Number of Absorber	2
Absorber Packing	Mellapak 250Y
Diameter (m)	16.13
Optimum Height (m)	23.04
Stripper	
Number of Stripper	1
Packing	Mellapak 250Y
Diameter (m)	14.61
Optimum Height (m)	25.62
Specific Reboiler Duty (MJ/kg CO ₂)	3.69

^aA lean CO₂ loading of 0.20 mol/mol with a liquid/gas ratio of 2.93 kg/kg is an alternative.

9.3.1 Optimum Lean CO₂ Loading and Liquid/Gas Ratio

For the three different types of coal investigated, and for 30 wt% MEA solution, the specific reboiler duty and the corresponding liquid/gas ratio needed for 90% CO₂ capture at different lean MEA CO₂ loadings are shown in **Figure 9.2(a)**. The variations of the net plant efficiencies for 90% CO₂ capture with lean CO₂ loadings is given by **Figure 9.2(b)**. From **Figure 9.2(a)** and **Figure 9.2(b)**, it is clear that the optimum lean CO₂ loading for the three different types of coal is 0.18 mol/mol and the corresponding optimum liquid/gas ratios are 2.74 kg/kg, 2.84 kg/kg and 2.89 kg/kg for Illinois No. 6 (bituminous coal), Montana Rosebud (sub-bituminous coal) and North Dakota (lignite coal), respectively.

Table 9.5. The optimum performance data for the CO₂ capture plant with a 30 wt% MEA solution, including the compression and intercooling duties of the CO₂ compression system, for the three different types of coal investigated.

	Bituminous Coal Illinois No. 6	Sub-bituminous Coal Montana Rosebud	Lignite Coal North Dakota
CO₂ Capture Plant			
Flue gas, absorber inlet (kg/s bar °C)	819.21 1.20 40.0	838.02 1.20 40.0	850.28 1.20 40.0
Flue gas, absorber outlet (kg/s bar °C)	588.11 1.01 42.0	598.29 1.01 42.0	604.10 1.01 42.0
Lean MEA solution, absorber inlet (kg/s bar °C)	2247.20 3.00 40.0	2377.70 3.00 40.0	2461.10 3.00 40.0
Lean MEA solution, stripper outlet (kg/s bar °C)	2247.20 1.62 117.10	2377.70 1.62 117.10	2461.10 1.62 117.10
Rich MEA solution, absorber outlet (kg/s bar °C)	2475.97 1.01 43.57	2617.19 1.01 43.99	2707.05 1.01 44.24
Rich MEA solution, stripper inlet (kg/s bar °C)	2475.97 3.00 107.10	2617.19 3.00 107.10	2707.05 3.00 107.10
MEA concentration, CO ₂ free basis (kg/kg)	0.30	0.30	0.30
Lean CO ₂ loading (mol/mol)	0.18	0.18	0.18
Rich CO ₂ loading (mol/mol)	0.5059	0.5064	0.5066
Lean MEA solution cooler inlet temperature (°C)	48.02	48.48	48.76
CO ₂ captured (kg/s)	152.21	161.31	167.10
Reboiler heat duty (MWth)	561.03	594.00	615.07
Specific reboiler duty (MJ/kg CO ₂)	3.686	3.682	3.681
Stripper condenser duty (MWth)	229.92	242.88	251.08
Lean MEA solution cooler duty (MWth)	65.82	73.62	78.70

Lean/Rich heat exchanger duty (MWth)	577.12	606.66	625.43
Lean MEA solution pump duty (kWe)	365.37	386.60	400.15
Rich MEA solution pump duty (kWe)	519.87	549.50	568.35
Absorber pressure drop (kPa)	2.72	2.95	3.12
Absorber fractional approach to flooding	0.71	0.73	0.75
Stripper pressure drop (kPa)	1.43	1.64	1.81
Stripper fractional approach to flooding	0.70	0.74	0.76
Stripper condenser pressure (bar)	1.62	1.62	1.62
Booster fan duty (MWe)	18.83	19.21	19.45
CO₂ Compression System			
Total compression duty (MWe)	45.697	48.051	49.456
Total intercooling duty (MWth)	78.107	81.676	84.547

Table 9.6. A comparison of the optimum energy performance of the integrated system for the three different types of coal.^b

	Bituminous Illinois No. 6	Sub-bituminous Montana Rosebud	Lignite North Dakota
Fuel heat input, HHV (MWth)	1932.94	1932.94	1932.94
Steam turbine thermal input, (MWth)	1704.75	1704.75	1704.75
Steam turbine power, without steam extraction (MWe)	811.80	811.80	811.80
Steam turbine power, with steam extraction (MWe)	662.94	654.24	649.09
Power plant auxiliary loads (MWe)	11.44	12.12	12.57
Other auxiliary loads (MWe) ^c	30.00	30.00	30.00
CO ₂ capture plant auxiliary loads (MWe)	19.72	20.15	20.42
CO ₂ Compression loads (MWe)	45.70	48.05	49.46
Power output without CO ₂ capture and compression (MWe)	767.36	767.36	767.36
Power output with CO ₂ capture only (MWe)	601.17	591.97	586.72
Power output with CO ₂ capture and compression (MWe)	555.48	543.92	536.64
Efficiency without CO ₂ capture and compression (%), HHV	39.70	39.70	39.70
Efficiency with CO ₂ capture only (%), HHV	31.10	30.60	30.30
Efficiency with CO ₂ capture and compression (%), HHV	28.73	28.12	27.74

^bOptimum implies a lean CO₂ loading of 0.18 mol/mol and liquid/gas ratios of 2.74 kg/kg, 2.84 kg/kg and 2.89 kg/kg, respectively, for Illinois No. 6, Montana Rosebud and North Dakota.

^cAssumed based on the values of auxiliary loads reported in the US DOE report.¹⁹²

Table 9.7. Overall performance of the integrated PC power plant-PCC-CCU system for the three different types of coal investigated, and for different MEA concentrations.

	Bituminous Coal (Illinois No. 6)			Sub-bituminous Coal (Montana Rosebud)			Lignite Coal (North Dakota)		
	30 wt% MEA	35 wt% MEA	40 wt% MEA	30 wt% MEA	35 wt% MEA	40 wt% MEA	30 wt% MEA	35 wt% MEA	40 wt% MEA
Optimum lean CO ₂ loading (mol/mol)	0.18	0.22	0.24	0.18	0.22	0.24	0.18	0.22	0.24
Optimum liquid/Gas Ratio (kg/kg)	2.743	2.726	2.601	2.837	2.821	2.692	2.894	2.881	2.747
Power output without CO ₂ capture and compression (MWe)	767.36	767.36	767.36	767.36	767.36	767.36	767.36	767.36	767.36
CO ₂ capture plant auxiliary loads (MWe)	19.72	19.70	19.65	20.15	20.13	20.07	20.42	20.40	20.34
Power output with CO ₂ capture only (MWe)	601.17	604.29	606.72	591.97	595.29	597.84	586.72	589.37	592.09
CO ₂ compression auxiliary loads (MWe)	45.70	45.70	45.70	48.05	48.05	48.05	49.46	49.46	49.46
Power output with CO ₂ capture and CO ₂ compression (MWe)	555.48	558.45	561.02	543.92	547.24	549.79	536.64	539.91	542.64
Efficiency without	39.70	39.70	39.70	39.70	39.70	39.70	39.70	39.70	39.70

CO ₂ capture and compression (%), HHV									
Efficiency with CO ₂ capture only (%), HHV	31.10	31.26	31.39	30.60	30.77	30.90	30.30	30.47	30.61
Efficiency with CO ₂ capture and compression (%), HHV	28.73	28.90	29.02	28.12	28.29	28.42	27.74	27.91	28.05

The 0.18 mol/mol lean CO₂ loading is in line with the lower limit of the experts' responses collated by Rao et al.²¹¹ As an alternative, a lean CO₂ loading of 0.20 mol/mol with corresponding liquid/gas ratios of 2.93 kg/kg, 3.04 kg/kg and 3.10 kg/kg for Illinois No. 6 (bituminous coal), Montana Rosebud (sub-bituminous coal) and North Dakota (lignite coal), respectively, would give about the same performance as the 0.18 mol/mol lean CO₂ loading. The combination of 0.20 mol/mol lean CO₂ loading and a liquid/gas ratio of 2.93 kg/kg for Illinois No. 6 (bituminous coal) is more or less the same as what is reported in **Table 7.4**.¹⁴⁹ Furthermore, from **Figure 9.2(a)**, the optimum specific reboiler duty is about the same for the three different types of coal. The increase in the liquid/gas ratio from the bituminous coal to the lignite coal is because of the increasing amount of CO₂ that is captured per MW_e of electricity that is generated with the different types of coal. From **Figure 9.2(b)**, it is clear that the order of performance of the three different types of coal investigated is given by: Illinois No. 6 (bituminous coal) > Montana Rosebud (sub-bituminous coal) > North Dakota (lignite coal). The optimum net plant efficiencies with only CO₂ capture are 31.10%, 30.60% and 30.30% for Illinois No. 6 (bituminous coal), Montana Rosebud (sub-bituminous coal) and North Dakota (lignite coal), respectively. Similarly, the optimum net plant efficiencies with both CO₂ capture and CO₂ compression are 28.74%, 28.12% and 27.74% for Illinois No. 6 (bituminous coal), Montana Rosebud (sub-bituminous coal) and North Dakota (lignite coal), respectively. The net efficiency of the supercritical power plant without CO₂ capture (i.e. if the steam extracted for the stripper reboiler duty is used for power generation) is 39.70%. Thus, the absolute losses in the net plant efficiency due to CO₂ capture are 8.60%, 9.10% and 9.40% for Illinois No. 6 (bituminous coal), Montana Rosebud (sub-bituminous coal) and North Dakota (lignite coal), respectively. Furthermore, the absolute losses in the net plant efficiency due to CO₂ compression are 2.36%, 2.48% and 2.56% for Illinois No. 6 (bituminous coal), Montana Rosebud (sub-bituminous coal) and North Dakota (lignite coal), respectively.

The variation of the lean and rich pumps duties with lean CO₂ loading is given by **Figure 9.3(a)**. As expected both the lean and rich pumps duties increase with lean CO₂ loading since more solvent circulation is required for 90% CO₂ capture as the lean CO₂ loading increases. For the optimum lean CO₂ loading of 0.18 mol/mol, the lean pumps duties for Montana Rosebud (sub-bituminous coal) and North Dakota (lignite coal) are higher by 5.8% and 9.5% when compared with the lean pump duty for Illinois No. 6 (bituminous coal), respectively.

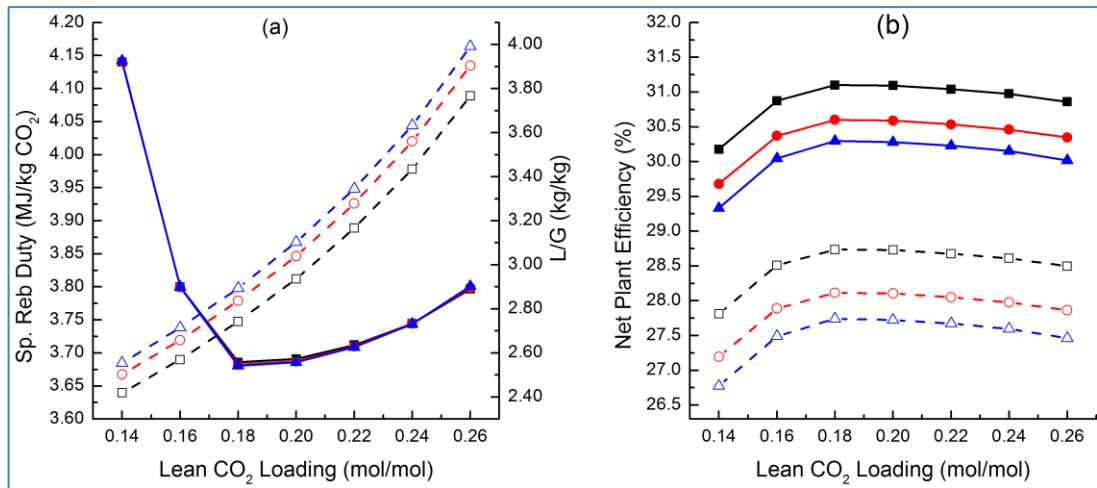


Figure 9.2. (a) The variations of the specific reboiler duty and liquid/gas with lean CO₂ loading for 90% CO₂ capture with 30 wt% MEA solution. Lines: Solid lines, specific reboiler duty; dashed lines, liquid/gas ratio. (b) The variations of the net plant efficiency with lean CO₂ loading. Lines: Solid lines, net plant efficiency with CO₂ capture only; dashed lines, net plant efficiency with CO₂ capture and compression. Symbols: ■ and □, Illinois No. 6; ● and ○, Montana Rosebud; ▲ and △, North Dakota.

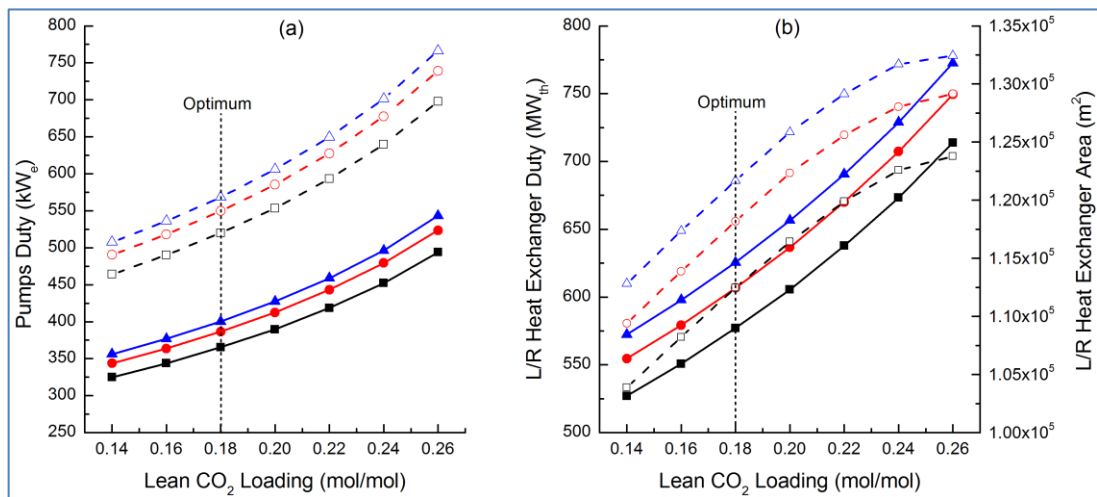


Figure 9.3. (a) The variations of the lean and rich pumps duty with lean CO₂ loading for 90% CO₂ capture with 30 wt% MEA solution. Lines: Solid lines, lean pump; dashed lines, rich pump. (b) The variations of the heat duty and the heat transfer area of the lean/rich heat exchanger. Lines: Solid lines, heat exchanger duty; dashed lines, heat exchanger area. Symbols: ■ and □, Illinois No. 6; ● and ○, Montana Rosebud; ▲ and △, North Dakota.

Similarly, the rich pumps duties for Montana Rosebud (sub-bituminous coal) and North Dakota (lignite coal) are higher by 5.7% and 9.3% when compared with the rich pump duty for Illinois No. 6 (bituminous coal), respectively. Therefore, if both pumps are designed on the basis of Illinois No. 6 (bituminous coal), both pumps would need to be over-sized by about 10% in order to allow for the use of Montana Rosebud (sub-bituminous coal) or North Dakota (lignite coal) in place of Illinois No. 6 (bituminous coal).

The variations of the heat duty and the heat transfer area of the lean/rich heat exchanger with lean CO₂ loading is given by **Figure 9.3(b)**. The heat transfer area of the lean/rich heat exchanger was calculated with a temperature approach of 10 °C at the lean amine inlet end and with default parameters values for heat transfer coefficients in Aspen Plus. It is clear from **Figure 9.3(b)** that both the heat exchanger duty and the heat transfer area increase with an increase in lean CO₂ loading because of the increase in the required solvent circulation rate with increasing lean CO₂ loading. For the optimum lean CO₂ loading of 0.18 mol/mol, the lean/rich heat exchanger duties for Montana Rosebud (sub-bituminous coal) and North Dakota (lignite coal) are higher by 5.1% and 8.4% when compared with the lean/rich heat exchanger duty for Illinois No. 6 (bituminous coal), respectively. Similarly, the heat transfer areas of the lean/rich heat exchangers for Montana Rosebud (sub-bituminous coal) and North Dakota (lignite coal) are higher by 5.2% and 8.2% when compared with the heat transfer area of the lean/rich heat exchanger for Illinois No. 6 (bituminous coal), respectively. Therefore, if the lean/rich heat exchanger is designed on the basis of Illinois No. 6 (bituminous coal), it would need to be over-sized by about 8.5% in order to allow for the use of Montana Rosebud (sub-bituminous coal) or North Dakota (lignite coal) in place of Illinois No. 6 (bituminous coal).

9.3.2 Effect of the Temperature of the Flue Gas (Absorber Inlet)

For the different types of coal investigated, and for the optimum lean CO₂ loading of 0.18 mol/mol, the effect of the inlet temperature of the flue gas on the CO₂ capture process is shown in **Figure 9.4(a)** and **Figure 9.4(b)**. The variations of the reboiler heat duty and the specific reboiler duty with the inlet temperature of the flue gas are shown in **Figure 9.4(a)**. It is clear from **Figure 9.4(a)** that the specific reboiler duty increases with an increase in the flue gas temperature even though the reboiler heat duty is more or less independent of the flue gas temperature. The increase in the specific reboiler heat duty with an increase in the inlet temperature of the flue gas is

due to the decrease in the amount of CO₂ that is captured as the temperature of the flue gas increases. **Figure 9.4(b)** shows the effect of the inlet temperature of the flue gas on the CO₂ capture efficiency. It can be seen from **Figure 9.4(b)** that the CO₂ capture efficiency decreases gradually with increasing temperature of the flue gas up to a temperature of about 45 °C, and the decrease in the CO₂ capture efficiency beyond 45 °C is more pronounced.

An increase in the inlet temperature of the flue gas from 30 °C to 45 °C leads to a loss of about 1.0% in the CO₂ capture efficiency, while an increase in the flue gas temperature from 45 °C to 60 °C leads to an additional loss of about 2.5% in the CO₂ capture efficiency. These observations clearly show the importance of cooling the flue gas before its introduction to the absorber inlet. However, from **Figure 9.4(b)**, it is clear that over-cooling of the flue gas below a temperature of about 40 °C only lead to an insignificant gain in the CO₂ capture efficiency.

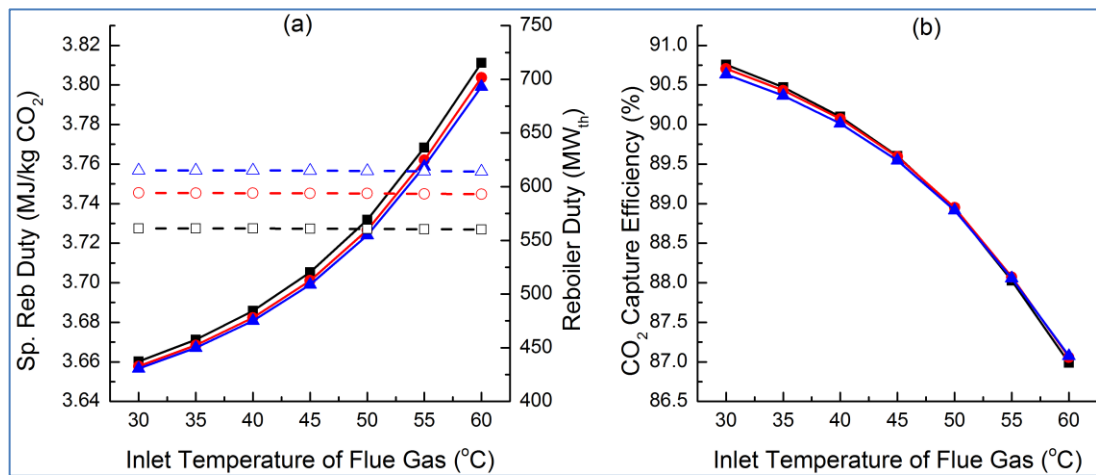


Figure 9.4. (a) The variations of the specific reboiler duty and reboiler duty with flue gas temperature at the absorber inlet, and for 0.18 mol/mol optimum CO₂ loading. Lines: Solid lines, specific reboiler duty; dashed lines, reboiler duty. (b) The variations of the CO₂ capture efficiency with flue gas temperature at the absorber inlet. Symbols: ■ and □, Illinois No. 6; ● and ○, Montana Rosebud; ▲ and △, North Dakota.

9.3.3 Effect of the Temperature of the Lean Amine Solution (Absorber Inlet)

For the different types of coal investigated, and for the optimum lean CO₂ loading of 0.18 mol/mol, the effect of the inlet temperature of the lean amine solution on the CO₂ capture process is shown in **Figure 9.5(a)** and **Figure 9.5(b)**. The variation of the specific reboiler duty with the inlet temperature of the lean amine solution is shown in **Figure 9.5(a)**. It is clear from **Figure 9.5(a)** that the specific reboiler duty is more or less independent of the lean amine solution temperature. However, it is important to note that the simulation was done with the assumption of an efficient demister at the top of the absorber such that the water vapour in the gas exiting the top of the absorber is about 2.0 vol%. **Figure 9.5(b)** shows the effect of the inlet temperature of the lean amine solution on the CO₂ capture efficiency. It can be seen from **Figure 9.5(b)** that the CO₂ capture efficiency is more or less independent of the lean amine solution temperature. The reason why the inlet temperature of the lean amine solution has very little or no effect on the CO₂ capture efficiency is because the effect of temperature on driving force for mass transfer (which is favoured by low temperature) is more or less countered by the effect of temperature on reaction kinetics (which is favoured by high temperature). Since the highest driving force for mass transfer is at the top section of the absorber, over-cooling the lean amine solution before its introduction to the absorber offers very little or no gain in the CO₂ capture efficiency as shown in **Figure 9.5(b)**.

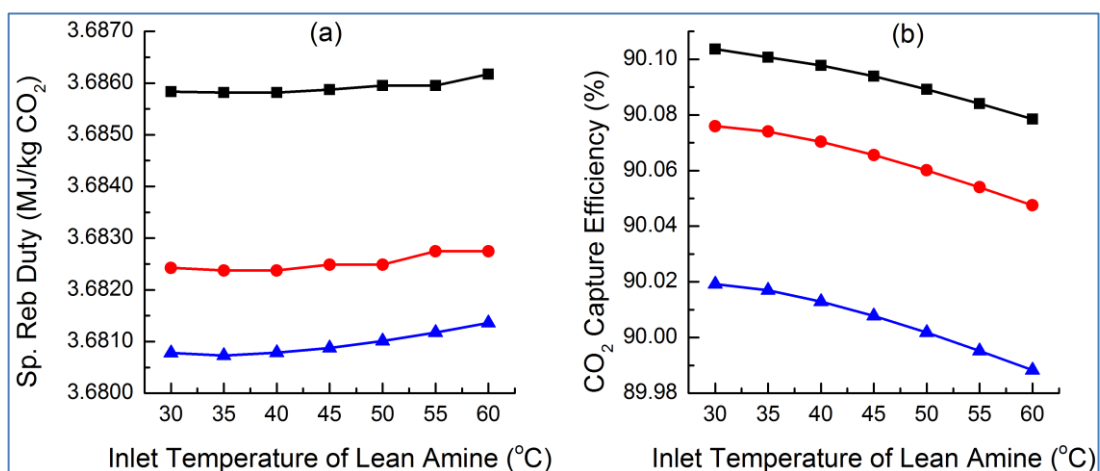


Figure 9.5. (a) The variations of the specific reboiler duty with lean amine solution temperature at the absorber inlet, and for 0.18 mol/mol optimum CO₂ loading. (b) The variations of the CO₂ capture efficiency with lean amine solution temperature at the absorber inlet. Symbols: ■, Illinois No. 6; ●, Montana Rosebud; ▲, North Dakota.

However, the temperature of the lean amine solution will have an impact on the performance of the water wash column and/or the demister at the top of the absorber because as the temperature of the lean amine solution increases, the amount of water/amine in the gas exiting the absorber increases.

9.3.4 Effect of CO₂ Capture Level

For the three different types of coal investigated, the variations of the specific reboiler duty and the net plant efficiency (with both CO₂ capture and CO₂ compression) with the percentage of CO₂ that is captured is shown in **Figure 9.6(a)**. The required liquid/gas ratios at 0.18 mol/mol lean CO₂ loading for different CO₂ capture levels are shown in **Figure 9.6(b)**. In addition, **Figure 9.6(b)** shows that the specific reboiler duty increases slightly with CO₂ capture level up to about 90% CO₂ capture but the increase becomes increasingly more pronounced with capture levels beyond 90%. However, the net plant efficiency decreases gradually with increasing CO₂ capture level for the range of CO₂ capture level shown in **Figure 9.6**.

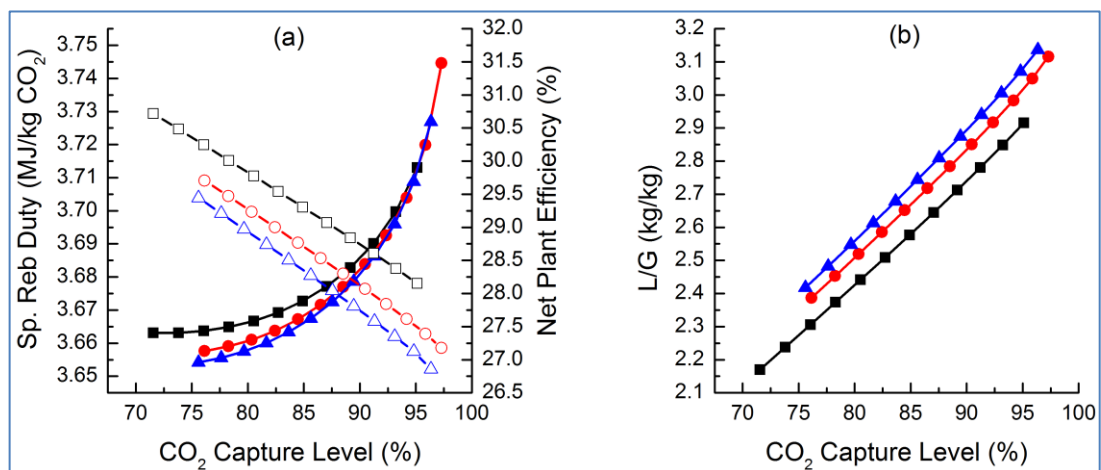


Figure 9.6. (a) The variations of the specific reboiler duty and the net plant efficiency with CO₂ capture level, and for 0.18 mol/mol optimum CO₂ loading. Lines: Solid lines, specific reboiler duty; dashed lines, net plant efficiency. (b) The variations of liquid/gas ratio at 0.18 lean CO₂ loading with CO₂ capture level. Symbols: ■ and □, Illinois No. 6; ● and ○, Montana Rosebud; ▲ and △, North Dakota.

From **Figure 9.6**, it is clear that a proportional reduction or increase of the liquid/gas ratio with CO₂ capture level, while maintaining the optimum lean CO₂ loading of 0.18 mol/mol, will result in a proportional increase or reduction in the net plant efficiency of the power plant. Therefore liquid/gas ratios per unit percent CO₂ capture level of 2.74/90, 2.84/90 and 2.89/90 can be used for Illinois No. 6 (bituminous coal), Montana Rosebud (sub-bituminous coal) and North Dakota (lignite coal), respectively, over the range of CO₂ capture level shown in **Figure 9.6** with minimal loss of performance.

A reduction of the CO₂ capture level from 90% to 75% results in an increase of 1.57 %, 1.60 % and 1.70 % in the net plant efficiency for Illinois No. 6 (bituminous coal), Montana Rosebud (sub-bituminous coal) and North Dakota (lignite coal), respectively. On the other hand, an increase in the CO₂ capture level from 90% to 95% results in a decrease of 0.58 %, 0.73 % and 0.75 % in the net plant efficiency for the 3 coals, respectively.

9.3.5 Effect of Amine Concentration

For the three different types of coal investigated, the specific reboiler duty and the corresponding liquid/gas ratio needed for 90% CO₂ capture at different lean MEA CO₂ loadings are shown in **Figure 9.7(a)** and **Figure 9.8(a)**, respectively, for 35 wt% MEA solution and 40 wt% MEA solution.

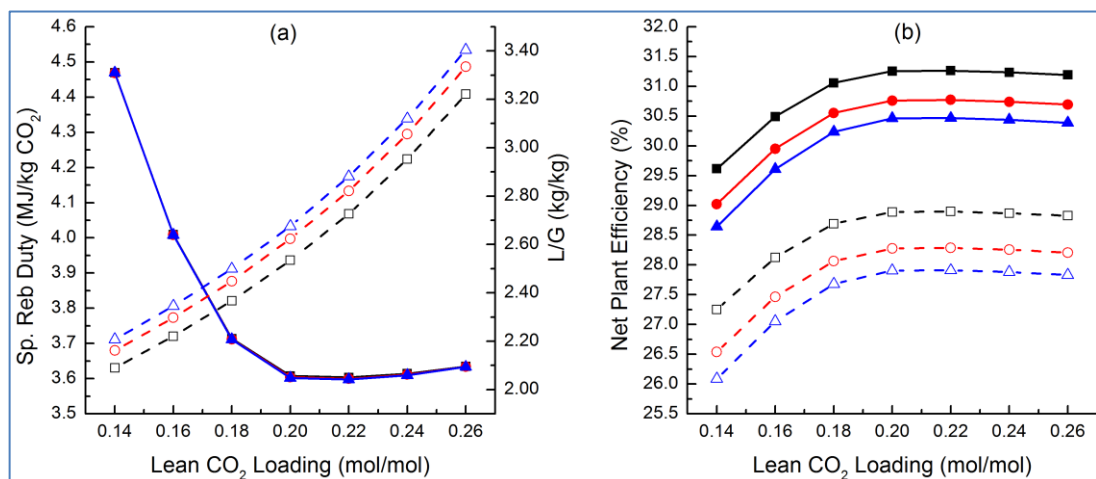


Figure 9.7. (a) The variations of the specific reboiler duty and liquid/gas with lean CO₂ loading for 90% CO₂ capture with 35 wt% MEA solution. Lines: Solid lines, specific reboiler duty; dashed lines, liquid/gas ratio. (b) The variations of the net plant efficiency with lean CO₂ loading. Lines: Solid lines, net plant efficiency with CO₂ capture only; dashed lines, net plant efficiency with CO₂ capture and compression. Symbols: ■ and □, Illinois No. 6; ● and ○, Montana Rosebud; ▲ and △, North Dakota.

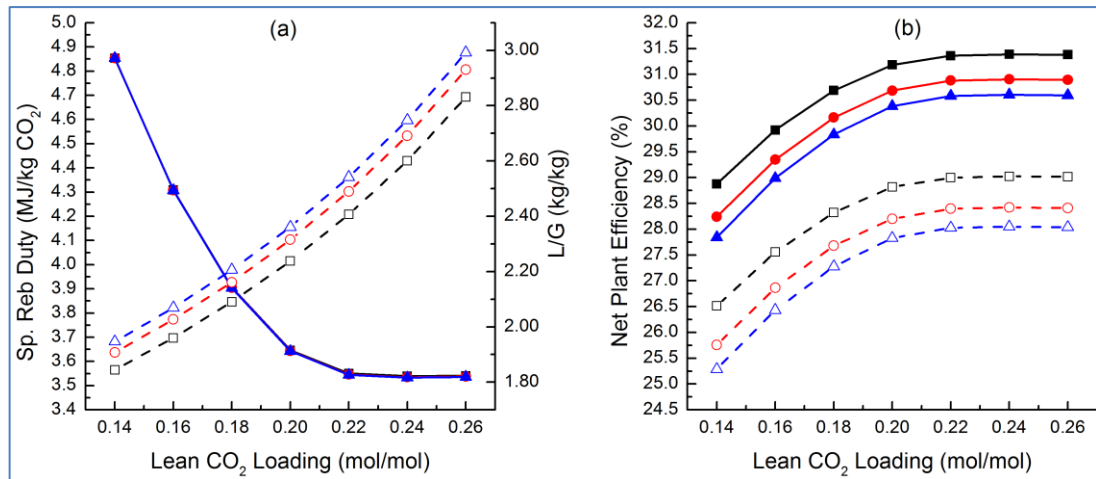


Figure 9.8. (a) The variations of the specific reboiler duty and liquid/gas with lean CO₂ loading for 90% CO₂ capture with 40 wt% MEA solution. Lines: Solid lines, specific reboiler duty; dashed lines, liquid/gas ratio. (b) The variations of the net plant efficiency with lean CO₂ loading. Lines: Solid lines, net plant efficiency with CO₂ capture only; dashed lines, net plant efficiency with CO₂ capture and compression. Symbols: ■ and □, Illinois No. 6; ● and ○, Montana Rosebud; ▲ and △, North Dakota.

The variations of the net plant efficiencies for 90% CO₂ capture with lean CO₂ loadings is given by **Figure 9.7(b)** and **Figure 9.8(b)**, respectively, for 35 wt% MEA solution and 40 wt% MEA solution. From **Figure 9.7** and **Figure 9.8**, it is clear that the optimum lean CO₂ loadings for the three different types of coal are 0.22 mol/mol and 0.24 mol/mol for 35 wt% MEA solution and 40 wt% MEA solution, respectively.

The optimum liquid/gas ratios for 35 wt% MEA solution are 2.73 kg/kg, 2.82 kg/kg and 2.88 kg/kg for Illinois No. 6 (bituminous coal), Montana Rosebud (sub-bituminous coal) and North Dakota (lignite coal), respectively. Similarly, the optimum liquid/gas ratios for 40 wt% MEA solution with the 3 coals are 2.601 kg/kg, 2.69 kg/kg and 2.75 kg/kg, respectively. Furthermore, from **Figure 9.7(a)** and **Figure 9.8(a)**, the optimum specific reboiler duty is about the same for the three different types of coal, and the optimum specific reboiler duties are 3.60 MJ/kg CO₂ and 3.54 MJ/kg CO₂ for the 35 wt% MEA solution and the 40 wt% MEA solution, respectively.

For the 35 wt% MEA solution, the optimum net plant efficiencies with only CO₂ capture are 31.26 %, 30.77 % and 30.47 % for Illinois No. 6 (bituminous coal), Montana Rosebud (sub-bituminous coal) and North Dakota (lignite coal), respectively. Similarly, for the 40 wt% MEA solution, the optimum net

plant efficiencies with only CO₂ capture are 31.39 %, 30.90% and 30.61 % for the 3 coals, respectively. Furthermore, for the 35 wt% MEA solution, the optimum net plant efficiencies with both CO₂ capture and CO₂ compression are 28.90 %, 28.29 % and 27.91 % for the 3 coals, respectively. Also, for the 40 wt% MEA solution, the optimum net plant efficiencies for the 3 coals with both CO₂ capture and CO₂ compression are 29.02 %, 28.42 % and 28.05 %, respectively. It is important to note that the CO₂ compression duty is more or less independent of the concentration of MEA that is used. Since the net efficiency of the supercritical power plant without CO₂ capture is 39.70%, it follows that the absolute losses in the net plant efficiency due to CO₂ capture are 8.44 %, 8.93 % and 9.23 % for Illinois No. 6 (bituminous coal), Montana Rosebud (sub-bituminous coal) and North Dakota (lignite coal), respectively, if 35 wt% MEA solution is used. Similarly, the absolute losses in the net plant efficiency due to CO₂ capture are 8.31 %, 8.80 % and 9.09 % for the 3 coals, respectively, if 40 wt% MEA solution is used. A switch from 30 wt% MEA solution to 35 wt% MEA solution results in an efficiency gain of 0.16 %, 0.17 % and 0.17 % for the 3 coals, respectively. Similarly, a switch from 30 wt% MEA solution to 40 wt% MEA solution results in an efficiency gain of 0.29 %, 0.30 % and 0.31 % for the 3 coals, respectively. Since the use of higher MEA concentration is associated with an increasing corrosion rate of the plant equipment, the optimum MEA concentration can only be arrived at on the basis of an economic analysis, which will depend on several factors such as the price of electricity, maintenance costs, etc.

The variations of the heat duty and the heat transfer area of the lean/rich heat exchanger with lean CO₂ loading are shown in **Figure 9.9(a)** and **Figure 9.9(b)** for 35 wt% MEA solution and 40 wt% MEA solution, respectively. As for the 30 wt% MEA solution, as shown in **Figure 9.3(b)**, both the heat exchanger duty and the heat transfer area increase with an increase in lean CO₂ loading since the required solvent circulation rate has to be increased with increasing lean CO₂ loading. A comparison of **Figure 9.9(a)** and **Figure 9.9(b)** with **Figure 9.3(b)** shows a decrease in the lean/rich heat exchanger duty with increasing concentration of the MEA solution. However, contrary to what is expected on the basis of the heat exchanger duty, the heat transfer area of the lean/rich heat exchanger increases with increasing concentration of the MEA solution. The reason for the increase in the heat transfer area with increasing concentration of the MEA solution is because the temperature approach at the rich inlet end decreases with increasing MEA concentration and, since the temperature approach at the rich outlet end is fixed at 10 °C, the log mean temperature

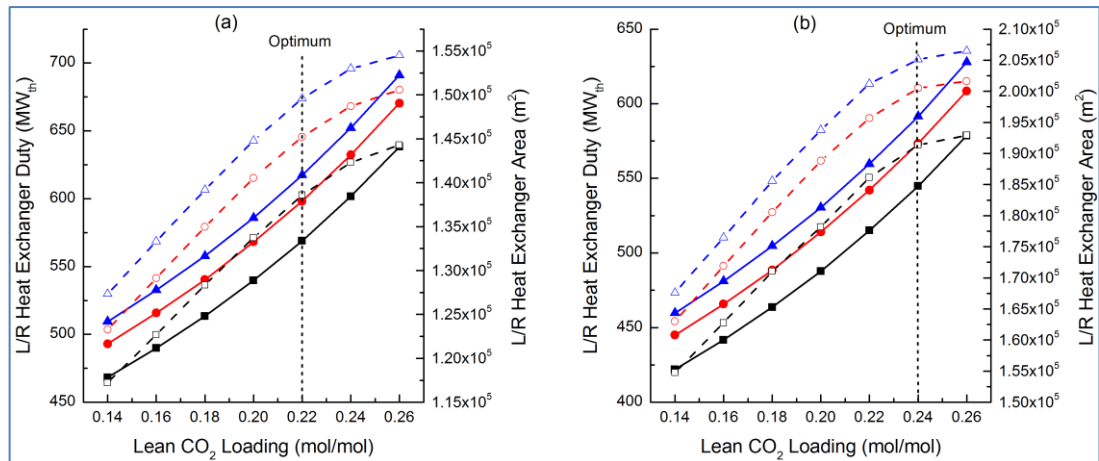


Figure 9.9. The variations of the heat duty and the heat transfer area of the lean/rich heat exchanger with lean CO₂ loading for 90% CO₂ capture. (a) 35 wt% MEA solution. (b) 40 wt% MEA solution. Lines: Solid lines, heat exchanger duty; dashed lines, heat exchanger area. Symbols: ■ and □, Illinois No. 6; ● and ○, Montana Rosebud; ▲ and △, North Dakota.

difference (LMTD) of the heat exchanger also decreases with increasing MEA concentration. The LMTDs at the optimum lean CO₂ loadings for the three different MEA concentrations (0.18 mol/mol for 30 wt% MEA solution, 0.22 mol/mol for 35 wt% MEA solution and 0.24 mol/mol for 40 wt% MEA solution) are approximately the same for the three different types of coal and the LMTDs on the basis of Illinois No. 6 (bituminous coal) are 6.85 °C, 5.80 °C and 4.29 °C for 30 wt% MEA solution, 35 wt% MEA solution and 40 wt% MEA solution respectively. Therefore, if the lean/rich heat exchanger is designed on the basis of Illinois No. 6 (bituminous coal) and 30 wt% MEA solution, it would need to be over-sized by about 23.2 % and 70.2 % if 30 wt% MEA solution is replaced with 35 wt% MEA solution and 40 wt% MEA solution, respectively.

9.4 Conclusions

A PCC plant that is designed on the basis of a particular coal can handle the flue gas from a different type of coal without operational issues if the PCC plant is designed with coal flexibility in mind. Since the fractional approach to maximum capacity varies from one coal to the other, as shown in **Table 9.5**, it is recommended that the absorber and stripper columns should be designed with a conservative fractional approach to maximum capacity of 0.7 as against the limiting value of 0.8 if the power plant is to be fired with

different types of coal. The optimum lean CO₂ loading is independent of coal type for a given MEA concentration but it varies with MEA concentration. The optimum lean CO₂ loadings for 30 wt% MEA solution, 35 wt% MEA solution and 40 wt% MEA solution are 0.18 mol/mol, 0.22 mol/mol and 0.24 mol/mol, respectively. Furthermore, the optimum liquid/gas ratio for a given MEA concentration varies with coal type, and it also varies with MEA concentration. An increase in MEA concentration led to an increase in the required heat transfer area of the lean/rich heat exchanger; thus, if an increase in amine concentration is envisaged for the PCC plant, then the lean/rich heat exchanger must be designed accordingly.

The lean amine temperature has little or no impact on the performance of the CO₂ capture process provided the efficiency of the demister and/or water wash is sufficient to prevent carry-over of water/amine mixture by the treated gas exiting the absorber. On the hand, the flue gas temperature has a minimal impact on the CO₂ capture efficiency of the PCC plant up to a temperature of about 45 °C and the impact becomes increasingly more pronounced with increasing temperature from 45 °C to 60 °C. Very little gain in performance is achieved if the flue gas is cooled below 40 °C and hence there is no need to over-cool the flue gas below 40 °C.

The net plant efficiency, with CO₂ capture only and with CO₂ capture and CO₂ compression, is highest for Illinois No. 6 (bituminous coal) and least for North Dakota (lignite coal). Also, the net plant efficiency increases slightly with an increase in MEA concentration. For 30 wt% MEA solution, the optimum net plant efficiencies with only CO₂ capture are 31.10%, 30.60% and 30.30%, respectively, for Illinois No. 6 (bituminous coal), Montana Rosebud (sub-bituminous coal) and North Dakota (lignite coal), while the optimum net plant efficiencies with both CO₂ capture and compression are 28.74%, 28.12% and 27.74% for Illinois No. 6 (bituminous coal), Montana Rosebud (sub-bituminous coal) and North Dakota (lignite coal), respectively. The net plant efficiency decreases with increasing CO₂ capture level for the different types of coal.

Finally, the same liquid/gas ratio per unit CO₂ capture efficiency can be used for 75% to 90% CO₂ capture efficiency with minimal loss of performance, which is a plus for power plant flexibility and control system design.

Chapter 10

Conclusions and Recommendations

This chapter summarizes the conclusions of the research in this thesis, as well as the recommendations for future research work that can be embarked upon by any interested researcher.

In this thesis, an integrated process comprising a 550MWe pulverized coal-fired power plant, an MEA-based PCC plant, and a CO₂ compression train, has been modelled, simulated and optimised. The modelling, simulation and optimisation of the integrated process was realized with Aspen Plus[®] V8.4. The boiler, the steam cycle and the CO₂ compression system were modelled based on a 2010 US DOE report¹⁹² as well as a 2004 IEA report,¹⁹³ while the MEA-based PCC plant was modelled as a rigorous rate-based process. The scaling of the amine plant was performed using a rate-based calculation as against the traditional equilibrium-based approach for 90% CO₂ capture; thus, the scaling of the PCC plant was optimized and unnecessary over design of the PCC columns was avoided.

The power plant was integrated to the PCC plant in three ways: (i) the boiler flue gas to the PCC absorber, (ii) the steam tapping from the IP turbine-LP turbine cross-over in the steam cycle to the PCC reboiler and (iii) the condensate return from the PCC reboiler to the steam cycle deaerator. Extensive parametric studies aimed at optimising the integration of the power plant to the PCC plant have been performed. The parametric studies included the pressure at which steam is tapped from the steam cycle, the use of a steam throttling valve, the use of a letdown turbine, the preheating of boiler feed water with tapped steam. Also, the optimal integration of the steam cycle to the CO₂ compression inter-stage coolers as an option for the elimination of some of the feed water heaters has been investigated. Furthermore, extensive simulations of the integrated process using different types of coal have been performed and the impacts of coal type on the overall performance of the process have been quantified.

Also, a semi-empirical model that can accurately estimate the heat capacity of aqueous solutions of alkanolamines, including aqueous solutions of two alkanolamines, both before and after CO₂ absorption, has been developed in this thesis.

The specific conclusions and recommendations, based on **Chapter 5** to **Chapter 9** in this thesis, are organized as follows:

10.1 Heat Capacity of Aqueous Solutions of Alkanolamines (Chapter 5)

10.1.1 Conclusions

- The semi-empirical model developed in this thesis can accurately estimate the heat capacity of aqueous solutions of alkanolamines, including aqueous solutions of two alkanolamines, both before and after CO₂ absorption.
- The model predictions provide some insights on the relative accuracy of the experimental data reported by different authors for the same system. Overall, the model predictions are in excellent agreement with most of the experimental data reported by the different authors for all the systems modelled.
- The model, along with the parameters regressed for the various systems, can serve as a valuable tool for design engineers involved in the design of amine-based gas purification plants, especially the heat exchange equipment in such plants.
- It is postulated that the model equations can be used by researchers in the regression of new sets of data generated for aqueous solutions of alkanolamines, especially the solutions loaded with CO₂.

10.1.2 Recommendations for Future Research Work

1. Since there is limited experimental data on the heat capacity of CO₂ loaded aqueous solutions of alkanolamines in the open literature, it is recommended that future research work should aim at generating reliable heat capacity data for CO₂ loaded aqueous solutions of alkanolamines over a wide range of temperature and CO₂ loading. Specifically, data are lacking for the following systems:
 - i. PZ-MEA-H₂O
 - ii. CO₂-PZ-MDEA-H₂O
 - iii. CO₂-AMP-H₂O

Furthermore, only limited data (at a temperature of 25 °C) have been reported for the following systems:

- iv. CO₂-DEA-H₂O
 - v. CO₂-MDEA-H₂O
 - vi. CO₂-MEA-MDEA-H₂O
 - vii. CO₂-DEA-MDEA-H₂O
2. It is recommended that the set of equations presented in **Chapter 5** be applied to other systems in addition to those considered in this thesis. The other systems may include CO₂ loaded solution of amino acids or amino salts, CO₂ loaded solution of aqueous ammonia, and CO₂ loaded solution of ionic liquids.
 3. The possibility of implementing the set of equations in **Chapter 5** as a user-defined function in process simulators should be investigated. This recommendation may require collaboration with developers of process simulation softwares since calculated enthalpy values do vary from one process simulator to another for the same system.

10.2 Modelling and Simulation of Pilot-scale CO₂ Capture Plant (Chapter 6)

10.2.1 Conclusions

- The UKCCSRC/PACT pilot plant and the University of Kaiserslautern pilot plant have been modelled in Aspen Plus using a rate-based calculation approach. The developed models of the pilot plants have been validated against data reported for the pilot plants and the model results are in good agreement with these data.
- The experimental liquid/gas ratios for the UKCCSRC/PACT pilot plant cases are sub-optimal, which underscores the need for some modelling work before experiments are conducted so that effort and time will be targeted at the optimal operating regime.
- The University of Kaiserslautern pilot plant model predictions are in good agreement with the reported pilot plant data. The average percent absolute deviations of the model results for the lean CO₂ loading, the rich CO₂ loading, and the specific reboiler duty, when

compared with the 47 experimental cases reported by Notz et al.¹⁴⁸ are 7.99%, 4.19%, and 7.14%, respectively.

- A different simulation approach which targets the lean CO₂ loading as against the CO₂ capture rate is adopted in the model validation of the University of Kaiserslautern pilot plant as presented in **Chapter 7**, and the validated model has been used for scale-up design of commercial scale amine-based CO₂ capture plants as presented in **Chapter 7**.

10.2.2 Recommendations for Future Research Work

1. A comprehensive baseline experiment with 30 wt% aqueous MEA solution should be conducted using the UKCCSRC/PACT pilot plant and the results of the 30 wt% MEA baseline experiment should be used as a reference when evaluating the performance of other solvents. Furthermore, the rate-based model for the UKCCSRC/PACT pilot plant in this thesis may be used for the planning of the baseline experiment and the results of the baseline experiment should be used to further validate the rate-based model developed for the UKCCSRC/PACT pilot plant in this thesis.
2. A comprehensive experiment with 50 wt% aqueous MDEA solution should be conducted using the UKCCSRC/PACT pilot plant and the MDEA results should be compared with the results of 30 wt% MEA. Furthermore, a comprehensive experiment using aqueous solution mixture of MEA and MDEA should be conducted using the UKCCSRC/PACT pilot plant. **Figure 10.1** may be used as a guide on the range of concentration to be investigated.
3. Rate-based models should be developed for the UKCCSRC/PACT pilot plant for MDEA only and for a mixture of MEA and MDEA, and the developed models should be validated with pilot plant results. The validated models will serve as valuable tools for scale-up process design of MDEA-based and MEA/MDEA-based commercial-scale CO₂ capture plants.

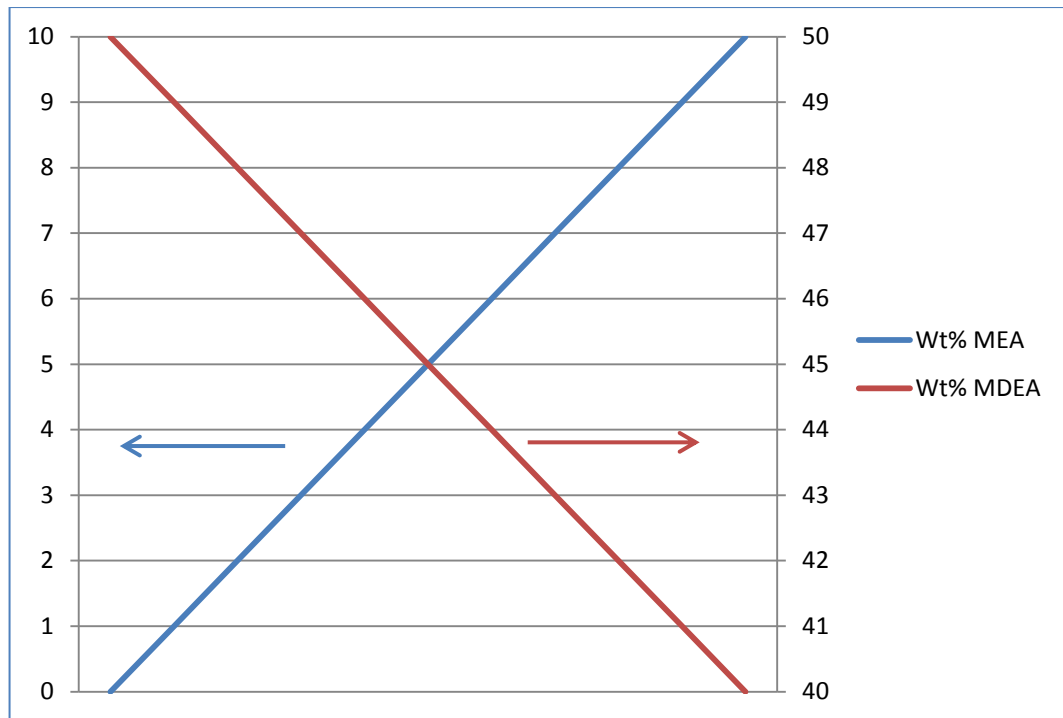


Figure 10.1. Concentration range of the mixture of MEA and MDEA recommended for investigation.

10.3 Process Design of Commercial Scale Amine-based CO₂ Capture Plant (Chapter 7)

10.3.1 Conclusions

- The design method and philosophy in this thesis is novel in the way Aspen Plus® has been employed in the design of the amine-based CO₂ capture plants considered in this thesis and, in the spirit of transparency, the details of how Aspen Plus® was used is fully explained in this thesis so that researchers and process design engineers can easily adopt the design philosophy and methodology in this thesis for their design work.
- Four commercial-scale MEA-based CO₂ plants that can service coal-fired power plants and onshore-based gas-fired power plants have been designed optimally, taking into consideration the capital and operating costs of the lean amine solution pump, the rich amine solution pump, the lean/rich cross heat exchanger, the lean amine solution cooler, the stripper condenser, the stripper reflux drum and reflux pump, and the stripper reboiler.

- A comparison of the optimal design results in this thesis with the design data from previously published works shows that any design based on values of CO₂ loadings and/or solvent circulation rates without techno-economic consideration may lead to a sub-optimal design for an amine-based CO₂ capture plant.
- The optimum lean CO₂ loading for MEA-based CO₂ capture plants that can service commercial-scale power plants, whether natural gas-fired or coal-fired, is about 0.2 mol/mol for absorber and stripper columns packed with Sulzer Mellapak 250YTM structured packing.
- The optimum liquid/gas ratio for a natural gas combined cycle (NGCC) power plant with a flue gas composition of approximately 4 mol% CO₂ is about 0.96, while the optimum liquid/gas ratio for a coal-fired power plant can range from 2.68 to 2.93 for a flue gas having a CO₂ composition that ranges from 12.38 mol% to 13.5 mol%.

10.3.2 Recommendations for Future Research Work

1. It is recommended that the design method and philosophy in this thesis be adopted as a standard for any future model-based process design of commercial-scale amine-based CO₂ capture plants, especially if Aspen Plus[®] is used as the modelling and design tool.
2. The design method and philosophy in this thesis should be used in the design of commercial-scale MDEA-based CO₂ capture plant, as well as MEA/MDEA-based commercial-scale CO₂ capture plant, and the design results should be compared with the MEA-based CO₂ capture plants considered in this thesis.
3. The design method and philosophy in this thesis should be used in the design of commercial-scale amine-based CO₂ capture plants with configurations different from the one considered in this thesis. The following configuration should be investigated.
 - i. Absorbers with intercoolers
 - ii. Lean vapour compression
 - iii. Multipressure stripper
 - iv. Split flow configurations (without heat integration)
 - v. Split flow configurations (with heat integration)

10.4 Optimal Integration of a PPC Plant with a PC Power Plant (Chapter 8)

10.4.1 Conclusions

- Steam tapping from the IP-LP cross-over pipe coupled with low stripper pressure favours the use of a let-down turbine over the use of steam throttling. However, it remains unclear if the extra gain in the net plant efficiency of the integrated system with the use of a let-down turbine over a simple steam throttling is worth the investment in the let-down turbine.
- The optimum stripper pressure that maximizes the net plant efficiency of the integrated system if a let-down turbine is used is about 1.6 bar. If steam is tapped from the LP turbine at 4 bar, the stripper may be operated up to 1.8 bar provided there is no excessive thermal degradation of the amine.
- The extra gain in the net plant efficiency of the integrated system if a let-down turbine is used in conjunction with LP steam tapping at 4 bar is not attractive enough to warrant investing in a let-down turbine; thus steam tapped from the LP turbine at 4 bar should be throttled and the stripper should be operated at the maximum pressure that will limit thermal degradation of the amine.
- There is no benefit in the use of a let-down turbine over a throttle valve if steam is tapped from the LP turbine at 3 bar. Therefore, a throttle valve should be used if steam is tapped from the LP turbine at 3 bar and the stripper should be operated at the maximum possible pressure, which is about 1.6 bar. The optimum stripper pressure of about 1.6 bar is in line with the stripper pressure in the MEA-based Econamine FG PlusTM process.
- The pre-heating of the steam cycle condensate by the superheat in the tapped steam, as an option for the elimination of the four low pressure boiler feed water (LPBFW) pre-heaters downstream of the deareator, led to a decrease in the net plant efficiency of the integrated process by about 0.16% in absolute terms. However, elimination of three of the four LPBFW pre-heaters coupled with pre-heating of the steam cycle condensate resulted in no efficiency loss.

- The pre-heating of the steam cycle condensate by the inter-coolers in the CO₂ compressor, as an option for elimination of the four low pressure boiler feed water (LPBFW) pre-heaters downstream of the deareator, led to an increase in the net plant efficiency of the integrated system by about 0.35%.

10.4.2 Recommendations for Future Research Work

1. An economic evaluation of the different integration schemes considered in this thesis should be investigated. Aspen Plus Economic Analyzer may be used for this purpose.
2. The Optimal integration of MDEA-based PCC plant, as well as MEA/MDEA-based PCC plant, with a PC power plant should be investigated and the results should be compared with the MEA-based PCC plant considered in this thesis.
3. A thermodynamic analysis of the steam cycle of the PC power plant in the integrated system should be investigated. In other words, different HP, IP and LP steam conditions, as well as the conditions of the various steam bleed for boiler feedwater preheating, should be investigated and their impact on the optimal integration of the PCC plant with the PC power plant should be quantified.

10.5 Simulation of a PC Power Plant Integrated with a PCC Plant and a CCU (Chapter 9)

10.5.1 Conclusions

- A PCC plant that is designed on the basis of a particular coal can handle the flue gas from a different type of coal without operational issues if the PCC plant is designed with coal flexibility in mind.
- The fractional approach to the maximum capacity of the absorber and stripper columns vary from one coal type to another; thus, it is recommended that the absorber and stripper columns should be designed with a conservative fractional approach to maximum capacity of 0.7 as against the limiting value of 0.8 if the power plant is to be fired with different types of coal.

- The optimum lean CO₂ loading is independent of coal type for a given MEA concentration, but it varies with MEA concentration. The optimum lean CO₂ loadings for 30 wt% MEA solution, 35 wt% MEA solution and 40 wt% MEA solution are 0.18 mol/mol, 0.22 mol/mol and 0.24 mol/mol, respectively.
- The optimum liquid/gas ratio for a given MEA concentration varies with coal type, and it also varies with MEA concentration. An increase in MEA concentration led to an increase in the required heat transfer area of the lean/rich heat exchanger; thus, if an increase in amine concentration is envisaged for the PCC plant, then the lean/rich heat exchanger must be designed accordingly.
- The lean amine temperature has little or no impact on the performance of the CO₂ capture process provided the efficiency of the demister and/or water wash is enough to prevent carry-over of water/amine mixture by the treated gas exiting the absorber.
- The flue gas temperature has a minimal impact on the CO₂ capture efficiency of the PCC plant up to a temperature of about 45 °C and the impact becomes increasingly more pronounced with increasing temperature from 45 °C to 60 °C. Very little gain in performance is achieved if the flue gas is cooled below 40 °C and hence there is no need to over-cool the flue gas below 40 °C.
- The net plant efficiency, with CO₂ capture only and with CO₂ capture and CO₂ compression, is highest for Illinois No. 6 (bituminous coal) and least for North Dakota (lignite coal). Also, the net plant efficiency increases slightly with an increase in MEA concentration.
- For 30 wt% MEA solution, the optimum net plant efficiencies with only CO₂ capture are 31.10%, 30.60% and 30.30%, respectively, for Illinois No. 6 (bituminous coal), Montana Rosebud (sub-bituminous coal) and North Dakota (lignite coal), while the optimum net plant efficiencies with both CO₂ capture and compression are 28.74%, 28.12% and 27.74% for Illinois No. 6 (bituminous coal), Montana Rosebud (sub-bituminous coal) and North Dakota (lignite coal), respectively.

- The net plant efficiency decreases with increasing CO₂ capture level for the different types of coal. The same liquid/gas ratio per unit CO₂ capture efficiency can be used for 75% to 90% CO₂ capture efficiency with minimal loss of performance, which is a plus for power plant flexibility and control system design.

10.5.2 Recommendations for Future Research Work

1. An economic evaluation of the integration system should be investigated for the different types of coal considered in this thesis. Aspen Plus Economic Analyzer may be used for this purpose.
2. A computational fluid dynamics (CFD) – process co-simulation should be used for the integrated system, if possible. The boiler/furnace of the PC power plant should be modelled using a CFD tool while the other equipment should be modelled using a process simulation tool. If this recommendation is followed, it will give valuable information on what is happening inside the boiler/furnace when there is a switch from one type of coal to another.
3. Modelling and simulation of the integrated system should be investigated if MEA is replaced with MDEA or a blend of MEA/MDEA. The results should be compared with the MEA case in this thesis. It is important to note that there may be a need for the PCC plant to be redesigned as recommended in **Section 10.3.2**.

Appendix A: Derivation of Eq. (5.2.13)

Consider 1 mole of a CO₂-free mixture with mole fractions of \tilde{x}_1 , \tilde{x}_2 and \tilde{x}_3 for the first amine (AmH), the second amine (Am) and water, respectively.

If z_1 and z_2 are the number of equivalents per mole of the first and second amines, respectively, then the mole of CO₂ in the CO₂-loaded mixture per unit mole of the CO₂-free mixture is $\alpha(z_1\tilde{x}_1 + z_2\tilde{x}_2)$. Thus, the total mole of the CO₂-loaded mixture per unit mole of the CO₂-free mixture is given by:

$$\text{Mole} = \tilde{x}_1 + \tilde{x}_2 + \tilde{x}_3 + \alpha(z_1\tilde{x}_1 + z_2\tilde{x}_2) = (1+\alpha z_1)\tilde{x}_1 + (1+\alpha z_2)\tilde{x}_2 + \tilde{x}_3$$

Also, the total mass of the CO₂-loaded mixture per unit mole of the CO₂-free mixture is given by:

$$\begin{aligned} \text{Mass} &= M_{\text{AmH}}\tilde{x}_1 + M_{\text{Am}}\tilde{x}_2 + M_{\text{H}_2\text{O}}\tilde{x}_3 + M_{\text{CO}_2}\alpha(z_1\tilde{x}_1 + z_2\tilde{x}_2) \\ &= M_{\text{AmH}}\tilde{x}_1 + M_{\text{Am}}\tilde{x}_2 + 18.015\tilde{x}_3 + 44.009\alpha(z_1\tilde{x}_1 + z_2\tilde{x}_2) \end{aligned}$$

Thus, the ratio of the mole of the mixture to the mass of the mixture is given by:

$$\frac{\text{Mole}}{\text{Mass}} = \frac{\tilde{x}_1 + \tilde{x}_2 + \tilde{x}_3 + \alpha(z_1\tilde{x}_1 + z_2\tilde{x}_2)}{M_{\text{AmH}}\tilde{x}_1 + M_{\text{Am}}\tilde{x}_2 + 18.015\tilde{x}_3 + 44.009\alpha(z_1\tilde{x}_1 + z_2\tilde{x}_2)}$$

Since the relationship between specific heat capacity and molar heat capacity is given by:

$$\frac{c_p (\text{J kg}^{-1} \text{K}^{-1})}{C_p (\text{J kmol}^{-1} \text{K}^{-1})} = \frac{\text{Mole (kmol)}}{\text{Mass (kg)}}$$

It follows therefore that:

$$\frac{c_p (\text{J kg}^{-1} \text{K}^{-1})}{C_p (\text{J mol}^{-1} \text{K}^{-1})} = \frac{[\tilde{x}_1 + \tilde{x}_2 + \tilde{x}_3 + \alpha(z_1\tilde{x}_1 + z_2\tilde{x}_2)] \times 10^3}{M_{\text{AmH}}\tilde{x}_1 + M_{\text{Am}}\tilde{x}_2 + 18.015\tilde{x}_3 + 44.009\alpha(z_1\tilde{x}_1 + z_2\tilde{x}_2)}$$

Appendix B: Standard Errors and Confidence Levels, as well as the Correlation Matrices, of the Model Parameters in Chapter 5.

Table B.1. Standard Errors and Confidence Levels of the Parameters for Pure Water and Pure Alkanolamines based on Eq.(5.2.6).

	a_0	a_1	$a_2 \times 10^4$	$a_3 \times 10^8$	
<i>Value</i>	96.3170	-0.1241	1.5981	6.9827	H ₂ O
<i>Standard Error</i>	1.7331	0.0147	0.4109	3.7703	
<i>95% LCL</i>	92.9010	-0.1531	0.7883	0.4486	
<i>95% UCL</i>	99.7330	-0.0951	2.4079	14.4139	
<i>Value</i>	78.2498	0.2932			MEA
<i>Standard Error</i>	2.0759	0.0063			
<i>95% LCL</i>	73.9195	0.2800			
<i>95% UCL</i>	82.5801	0.3064			

<i>Value</i>	59.2381	0.6454	DEA
<i>Standard Error</i>	10.5273	0.0314	
<i>95% LCL</i>	36.6593	0.2581	
<i>95% UCL</i>	81.8169	0.7127	
<i>Value</i>	90.6224	0.5991	MDEA
<i>Standard Error</i>	2.3564	0.0072	
<i>95% LCL</i>	85.8735	0.5847	
<i>95% UCL</i>	95.3713	0.6136	
<i>Value</i>	75.4034	0.5423	AMP
<i>Standard Error</i>	4.8835	0.01461	
<i>95% LCL</i>	65.5173	0.5127	
<i>95% UCL</i>	85.2895	0.5718	
<i>Value</i>	13.3859	0.5157	PZ

<i>Standard Error</i>	3.3532	0.0080
95% <i>LCL</i>	6.2387	0.4985
95% <i>UCL</i>	20.5330	0.5328

Table B.2. Standard Errors and Confidence Levels of the Parameters for the Excess Heat Capacity contribution due to Binary Interactions based on Eqs. (5.2.7) and (5.2.8).

	$A_{0,0}$	$A_{0,1}$	$A_{1,0}$	$A_{1,1}$	$A_{2,0}$	$A_{2,1}$	
<i>Value</i>	-112.4265	0.3962	199.2343	-0.5955	424.5643	-1.3143	MEA-H ₂ O
<i>Standard Error</i>	24.4684	0.0773	47.0987	0.1479	88.7757	0.2763	
95% <i>LCL</i>	-160.8343	0.2433	106.0551	-0.8882	248.9322	-1.8609	
95% <i>UCL</i>	-64.0188	0.5491	292.4135	-0.3029	600.1963	-0.7677	
<i>Value</i>	-123.5135	0.4463	73.5547	-0.2430	169.9517	-0.5052	DEA-H ₂ O
<i>Standard Error</i>	10.3286	0.0315	19.9763	0.0609	45.6843	0.1401	
95% <i>LCL</i>	-144.3574	0.3828	33.2409	-0.3660	77.7570	-0.7880	
95% <i>UCL</i>	-102.6697	0.5099	113.8684	-0.1200	262.1464	-0.2225	

<i>Value</i>	-159.5189	0.5951	72.9519	-0.3235	MDEA-H ₂ O
<i>Standard Error</i>	9.7799	0.0300	24.4397	0.0751	
<i>95% LCL</i>	-178.7548	0.5360	24.8819	-0.4711	
<i>95% UCL</i>	-140.2829	0.6541	121.0220	-0.1758	
<i>Value</i>	-89.8771	0.3741	-61.1080	0.1115	AMP-H ₂ O
<i>Standard Error</i>	8.9044	0.0273	22.2750	0.0681	
<i>95% LCL</i>	-107.4041	0.3205	-104.9530	-0.0225	
<i>95% UCL</i>	-72.3502	0.4278	-17.2630	0.2455	
<i>Value</i>	-901.8356	3.1638	-1092.1672	3.6316	PZ-H ₂ O
<i>Standard Error</i>	159.569	0.4766	211.9679	0.6308	
<i>95% LCL</i>	-1218.9626	2.2142	-1514.5225	2.3747	
<i>95% UCL</i>	-584.7086	4.1134	-669.8120	4.8885	

<i>Value</i>	-43.4098	0.0368	33.8159	-0.1303				MEA-MDEA
<i>Standard Error</i>	5.4725	0.0167	14.7068	0.0448				
95% <i>LCL</i>	-54.4701	0.0031	4.0923	-0.2208				
95% <i>UCL</i>	-32.3496	0.0705	63.5395	-0.0399				
<i>Value</i>	-100.5740	0.2348	114.2166	-0.3880				DEA-MDEA
<i>Standard Error</i>	8.6461	0.0263	22.8980	0.0697				
95% <i>LCL</i>	-117.7386	0.1826	68.7583	-0.5263				
95% <i>UCL</i>	-83.4093	0.2870	159.6750	-0.2496				
<i>Value</i>	-83.0434	0.4019	-182.1514	0.6263	-458.8218	1.4792		PZ-MDEA
<i>Standard Error</i>	3.2956	0.0100	17.0229	0.0518	18.9104	0.0576		
95% <i>LCL</i>	-89.7150	0.3816	-216.6124	0.5214	-497.1038	1.3627		
95% <i>UCL</i>	-76.3718	0.4222	-147.6904	0.7312	-420.5397	1.5958		
<i>Value</i>	62.5100	-0.1998	-33.8900	0.1015				MEA-AMP

<i>Standard Error</i>	4.6806	0.0142	12.5787	0.0383	
95% <i>LCL</i>	53.0502	-0.2285	-59.3126	0.0252	
95% <i>UCL</i>	71.9698	-0.1710	-8.4675	0.1789	
<i>Value</i>	-165.4484	0.5479	-254.0804	0.7130	PZ-AMP
<i>Standard Error</i>	50.9467	0.1551	74.8441	0.2278	
95% <i>LCL</i>	-268.4156	0.2345	-405.3459	0.2526	
95% <i>UCL</i>	-62.4813	0.8612	-102.8149	1.1733	

Table B.3. Standard Errors and Confidence Levels of the Parameters for the Excess Heat Capacity contribution due to Ternary Interactions based on Eqs. (5.2.9) and (5.2.10).

	$B_{0,0}$	$B_{0,1}$	$B_{1,0}$	$B_{1,1}$	$B_{2,0}$	$B_{2,1}$	
<i>Value</i>		-0.3430				-0.5646	MEA-MDEA-H ₂ O
<i>Standard Error</i>		0.0109				0.1037	
95% <i>LCL</i>		-0.3644				-0.7691	
95% <i>UCL</i>		-0.3216				-0.3600	

<i>Value</i>	-0.2322	0.2792	-0.9997	DEA-MDEA-H ₂ O
<i>Standard Error</i>	0.0195	0.0900	0.2489	
<i>95% LCL</i>	-0.2707	0.1016	-1.4909	
<i>95% UCL</i>	-0.1938	0.4568	-0.5086	
<i>Value</i>	1.8657	9.7302	9.0556	PZ-MDEA-H ₂ O
<i>Standard Error</i>	0.7388	2.8776	2.6925	
<i>95% LCL</i>	0.4068	4.0477	3.7387	
<i>95% UCL</i>	3.3246	15.4126	14.3725	
<i>Value</i>	-0.2786	0.1100		MEA-AMP-H ₂ O
<i>Standard Error</i>	0.0106	0.0434		
<i>95% LCL</i>	-0.2995	0.0244		
<i>95% UCL</i>	-0.2576	0.1956		

<i>Value</i>		-1.7060		-0.5940	PZ-AMP-H ₂ O
<i>Standard Error</i>		0.0580		0.2263	
<i>95% LCL</i>		-1.8206		-1.0411	
<i>95% UCL</i>		-1.5914		-0.1469	
<i>Value</i>	35422.4165	-182.6914	48133.6931	-234.5192	PZ-MEA-H ₂ O
<i>Standard Error</i>	8321.9335	23.5084	10267.0306	29.0030	
<i>95% LCL</i>	18426.761	-230.7019	27165.6194	-293.7513	
<i>95% UCL</i>	52418.072	-134.6808	69101.7667	-175.2871	

Table B.4. Standard Errors and Confidence Levels of the Parameters for the Excess Heat Capacity contribution due to CO₂ Loading Effect based on Eqs. (5.2.11) and (5.2.12).

	<i>p</i>	<i>q</i>	<i>C</i> _{0,0}	<i>C</i> _{0,1}	<i>C</i> _{0,2}	<i>C</i> _{1,0}	<i>C</i> _{1,1}	
<i>Value</i>	0.4173		1098.8042	0.7711	-233.5587	202.3859	-0.8662	CO ₂ -MEA-H ₂ O
<i>Standard Error</i>	0.0266		144.5316	0.0876	29.8812	34.1497	0.1035	
<i>95% LCL</i>	0.3648		813.2838	0.5981	-292.5887	134.9235	-1.0706	

95% UCL	0.4698	1384.3247	0.9441	-174.5287	269.8482	-0.6619	
<i>Value</i>	1.0809				-102.0025		CO ₂ -DEA-H ₂ O
<i>Standard Error</i>	0.1701				17.5042		
95% LCL	0.7363				-137.4693		
95% UCL	1.4255				-66.5357		
<i>Value</i>	2.3860	-7.67435	-15.6976				CO ₂ -MDEA-H ₂ O
<i>Standard Error</i>	0.2171	1.2204	1.9665				
95% LCL	1.9457	-10.1495	-19.6859				
95% UCL	2.8263	-5.1992	-11.7092				
<i>Value</i>	0.4668	-28.1435	0.0813		-142.9250		CO ₂ -PZ-H ₂ O
<i>Standard Error</i>	0.0564	2.8400	0.01		14.9063		
95% LCL	0.3552	-33.7689	0.0655		-172.4514		
95% UCL	0.5785	-22.5182	0.0972		-113.3985		

<i>Value</i>	1.5592	-21.3664			CO ₂ -MEA-MDEA-H ₂ O
<i>Standard Error</i>	0.3235	5.8923			
<i>95% LCL</i>	0.8947	-33.8575			
<i>95% UCL</i>	2.2237	-8.8752			
<i>Value</i>	2.5199	-22.2567			CO ₂ -DEA-MDEA-H ₂ O
<i>Standard Error</i>	0.5584	9.8134			
<i>95% LCL</i>	1.2758	-44.1224			
<i>95% UCL</i>	3.7641	-0.3910			
<i>Value</i>	0.8506	-25.7353	0.0188	70.2695	CO ₂ -PZ-MEA-H ₂ O
<i>Standard Error</i>	0.0355	2.5536	0.0064	6.8538	
<i>95% LCL</i>	0.7803	-30.7866	0.0062	56.7120	
<i>95% UCL</i>	0.9209	-20.6840	0.0314	83.8270	

Table B.5. Correlation Matrices for the Pure Component Parameters.

	a_0	a_1	a_2	a_3	
a_0	1	-0.9989	0.9956	-0.9898	H ₂ O
a_1	-0.9989	1	-0.9989	0.9953	
a_2	0.9956	-0.9989	1	-0.9988	
a_3	-0.9898	0.9953	-0.9988	1	
a_0	1	-0.9988			MEA
a_1	-0.9988	1			
a_0	1	-0.9971			DEA
a_1	-0.9971	1			
a_0	1	-0.9971			MDEA
a_1	-0.9971	1			
a_0	1	-0.9980			AMP

a_1	-0.9980	1	
a_0	1	-0.9991	PZ
a_1	-0.9991	1	

Table B.6. Correlation Matrices for the Binary Interaction Parameters.

	$A_{0,0}$	$A_{0,1}$	$A_{1,0}$	$A_{1,1}$	$A_{2,0}$	$A_{2,1}$	
$A_{0,0}$	1	-0.9975	-0.2073	0.2090	-0.6611	0.6658	MEA-H ₂ O
$A_{0,1}$	-0.9975	1	0.2089	-0.2111	0.6548	-0.6633	
$A_{1,0}$	-0.2073	0.2090	1	0.9975	0.5599	-0.5736	
$A_{1,1}$	0.2089	-0.2111	0.9975	1	-0.5669	0.5825	
$A_{2,0}$	-0.6611	0.6548	0.5599	-0.5669	1	-0.9968	
$A_{2,1}$	0.6658	-0.6633	-0.5736	0.5825	-0.9968	1	
$A_{0,0}$	1	-0.9988	-0.0765	0.0745	-0.6680	0.6655	DEA-H ₂ O

$A_{0,1}$	-0.9988	1	0.0746	-0.0727	0.6695	-0.6687
$A_{1,0}$	-0.0765	0.0746	1	-0.9988	0.1743	-0.1689
$A_{1,1}$	0.0745	-0.0727	-0.9988	1	-0.1698	0.1645
$A_{2,0}$	-0.6680	0.6695	0.1743	-0.1698	1	-0.9986
$A_{2,1}$	0.6655	-0.6687	-0.1689	0.1645	-0.9986	1

$A_{0,0}$	1	-0.9973	0.0339	-0.0334		
$A_{0,1}$	-0.9973	1	-0.0334	0.0331		
$A_{1,0}$	0.0339	-0.0334	1	-0.9973		
$A_{1,1}$	-0.0334	0.0331	-0.9973	1		

MDEA-H₂O

$A_{0,0}$	1	-0.9974	0.1464	-0.1431		
$A_{0,1}$	-0.9974	1	-0.1430	0.1401		
$A_{1,0}$	0.1464	-0.1430	1	-0.9974		
$A_{1,1}$	-0.1431	0.1401	-0.9974	1		

AMP-H₂O

$A_{0,0}$	1	-0.9981	0.9863	-0.9874			PZ-H ₂ O
$A_{0,1}$	-0.9981	1	-0.9813	0.9863			
$A_{1,0}$	0.9863	-0.9813	1	-0.9979			
$A_{1,1}$	-0.9874	0.9863	-0.9979	1			
$A_{0,0}$	1	-0.9988	5.9381E-12	-6.0682E-12			MEA-MDEA
$A_{0,1}$	-0.9988	1	-6.0844E-12	6.2149E-12			
$A_{1,0}$	5.9381E-12	-6.0844E-12	1	-0.9988			
$A_{1,1}$	-6.0682E-12	6.2149E-12	-0.9988	1			
$A_{0,0}$	1	-0.9988	-1.5192E-12	1.5583E-12			DEA-MDEA
$A_{0,1}$	-0.9988	1	.5598E-12				
$A_{1,0}$	-1.5192E-12	1.5598E-12	1	-0.9988			
$A_{1,1}$	1.5583E-12	-1.5989E-12	-0.9988	1			
$A_{0,0}$	1	-0.9988	0.9597	-0.9586	0.8980	-0.8970	PZ-MDEA

$A_{0,1}$	-0.9988	1	-0.9586	0.9597	-0.8970	0.8980	
$A_{1,0}$	0.9597	-0.9586	1	-0.9988	0.9791	-0.9780	
$A_{1,1}$	-0.9586	0.9597	-0.9988	1	-0.9780	0.9791	
$A_{2,0}$	0.8980	-0.8970	0.9791	-0.9780	1	-0.9988	
$A_{2,1}$	-0.8970	0.8980	-0.9780	0.9791	-0.9988	1	
$A_{0,0}$	1	-0.9988	-4.2191E-12	4.1897E-12			MEA-AMP
$A_{0,1}$	-0.9988	1	4.4027E-12	-4.3734E-12			
$A_{1,0}$	-4.2191E-12	4.4027E-12	1	-0.9988			
$A_{1,1}$	4.1897E-12	-4.3734E-12	-0.9988	1			
$A_{0,0}$	1	-0.9988	0.9918	-0.9907			PZ-AMP
$A_{0,1}$	-0.9988	1	-0.9907	0.9918			
$A_{1,0}$	0.9918	-0.9907	1	-0.9988			
$A_{1,1}$	-0.9907	0.9918	-0.9988	1			

Table B.7. Correlation Matrices for the Ternary Interaction Parameters.

	$B_{0,0}$	$B_{0,1}$	$B_{1,0}$	$B_{1,1}$	$B_{2,0}$	$B_{2,1}$	
$B_{0,1}$		1				-0.5756	MEA-MDEA-H ₂ O
$B_{2,1}$		-0.5756				1	
$B_{0,1}$		1		-0.2066		-0.5549	DEA-MDEA-H ₂ O
$B_{1,1}$		-0.2066		1		0.6772	
$B_{2,1}$		-0.5549		0.6772		1	
$B_{0,1}$		1		0.9951		0.9800	PZ-MDEA-H ₂ O
$B_{1,1}$		0.9951		1		0.9944	
$B_{2,1}$		0.9800		0.9944		1	
$B_{0,1}$		1		0.2760			MEA-AMP-H ₂ O
$B_{1,1}$		0.2760		1			
$B_{0,1}$		1				-0.9102	PZ-AMP-H ₂ O

$B_{2,1}$		-0.9102			1	
$B_{0,0}$	1	-0.9976	0.9992	-0.9968		PZ-MEA-H ₂ O
$B_{0,1}$	-0.9976	1	-0.9968	0.9992		
$B_{1,0}$	0.9992	-0.9968	1	-0.9976		
$B_{1,1}$	-0.9968	0.9992	-0.9976	1		

Table B.8. Correlation Matrices for the CO₂ Loading Effect Parameters.

	p	q	$C_{0,0}$	$C_{0,1}$	$C_{0,2}$	$C_{1,0}$	$C_{1,1}$	
p	1		0.1597	0.1915	-0.1652	0.1319	-0.2003	CO ₂ -MEA-H ₂ O
$C_{0,0}$	0.1597		1	0.9909	-0.9997	-0.0717	0.0537	
$C_{0,1}$	0.1915		0.9909	1	-0.9937	0.0533	-0.0722	
$C_{0,2}$	-0.1652		-0.9997	-0.9937	1	0.0506	-0.0326	
$C_{1,0}$	0.1319		-0.0717	0.0533	0.0506	1	-0.9929	

$C_{1,1}$	-0.2003		0.0537	-0.0722	-0.0326	-0.9929	1	
p	1					-0.9509		CO ₂ -DEA-H ₂ O
$C_{1,0}$	-0.9509					1		
p	1	-0.7343	-0.5684					CO ₂ -MDEA-H ₂ O
q	-0.7343	1	-0.0854					
$C_{0,0}$	-0.5684	-0.0854	1					
p	1		-0.6994	0.7187		-0.6802		CO ₂ -PZ-H ₂ O
$C_{0,0}$	-0.6994		1	-0.9843		0.3515		
$C_{0,1}$	0.7187		-0.9843	1		-0.4889		
$C_{1,0}$	-0.6802		0.3515	-0.4889		1		
p	1		-0.9641					CO ₂ -MEA-MDEA-H ₂ O
$C_{0,0}$	-0.9641		1					

p	1	-0.9811			CO ₂ -DEA-MDEA-H ₂ O
$C_{0,0}$	-0.9811	1			
p	1	-0.3869	0.1125	0.3994	CO ₂ -PZ-MEA-H ₂ O
$C_{0,0}$	-0.3869	1	-0.9136	-0.4137	
$C_{0,1}$	0.1125	-0.9136	1	0.0449	
$C_{1,0}$	0.3994	-0.4137	0.0449	1	

Appendix C: Derivation of Eq. (7.5.1)

The CO₂ recovered from the flue gas is given by:

$$F_{\text{CO}_2, \text{recovered}} = \frac{F_{\text{FG}} x_{\text{CO}_2} \Psi_{\text{CO}_2}}{100} \quad (\text{C.1})$$

where F_{FG} is the mass flowrate of the flue gas, x_{CO_2} is the mass fraction of CO₂ in the flue gas, and Ψ_{CO_2} is the percentage of the CO₂ in the flue gas that is recovered.

The CO₂ absorbed by the amine solution is given by:

$$F_{\text{CO}_2, \text{absorbed}} = z (\alpha_{\text{Rich}} - \alpha_{\text{Lean}}) \frac{F_{\text{Amine}}}{M_{\text{Amine}}} M_{\text{CO}_2} \quad (\text{C.2})$$

where z is the number of equivalents per mole of the amine; α_{Rich} and α_{Lean} are, respectively, the rich CO₂ loading and the lean CO₂ loading; F_{Amine} is the mass flowrate of the amine in the circulated amine solution; M_{Amine} is the molar mass of the amine; M_{CO_2} is the molar mass of CO₂, which is 44.009 kg/kmol.

Since the CO₂ recovered from the flue gas is theoretically equal to the CO₂ absorbed by the amine solution, it follows that:

$$z (\alpha_{\text{Rich}} - \alpha_{\text{Lean}}) \frac{F_{\text{Amine}}}{M_{\text{Amine}}} M_{\text{CO}_2} = \frac{F_{\text{FG}} x_{\text{CO}_2} \Psi_{\text{CO}_2}}{100} \quad (\text{C.3})$$

Hence,

$$F_{\text{Amine}} = \frac{F_{\text{FG}} x_{\text{CO}_2} \Psi_{\text{CO}_2}}{100z (\alpha_{\text{Rich}} - \alpha_{\text{Lean}})} \frac{M_{\text{Amine}}}{M_{\text{CO}_2}} \quad (\text{C.4})$$

If ω_{Amine} is the mass fraction of the amine in the unloaded amine solution, then the mass flowrate of water in the circulated amine solution is given by:

$$F_{\text{H}_2\text{O}} = \left(\frac{1 - \omega_{\text{Amine}}}{\omega_{\text{Amine}}} \right) F_{\text{Amine}} \quad (\text{C.5})$$

Thus, the mass flowrate of the unloaded amine solution is given by:

$$F_{\text{Unloaded}} = F_{\text{H}_2\text{O}} + F_{\text{Amine}} = \left(1 + \frac{1 - \omega_{\text{Amine}}}{\omega_{\text{Amine}}} \right) F_{\text{Amine}} \quad (\text{C.6})$$

The mass flowrate of CO₂ in the CO₂-loaded amine solution is given by:

$$F_{\text{CO}_2} = z\alpha \frac{M_{\text{CO}_2}}{M_{\text{Amine}}} F_{\text{Amine}} \quad (\text{C.7})$$

Therefore, the mass flowrate of the CO₂-loaded amine solution is given by:

$$\begin{aligned} F_{\text{CO}_2\text{-loaded}} &= F_{\text{H}_2\text{O}} + F_{\text{Amine}} + F_{\text{CO}_2} \\ &= \left(1 + \frac{1 - \omega_{\text{Amine}}}{\omega_{\text{Amine}}} + z\alpha \frac{M_{\text{CO}_2}}{M_{\text{Amine}}} \right) F_{\text{Amine}} \end{aligned} \quad (\text{C.8})$$

where α is the CO₂ loading of the CO₂-loaded amine solution

From Eqs. (C.4) and (C.8), it follows that:

$$F_{\text{CO}_2\text{-loaded}} = \frac{F_{\text{FG}} x_{\text{CO}_2} \Psi_{\text{CO}_2}}{100z (\alpha_{\text{Rich}} - \alpha_{\text{Lean}})} \left(\frac{M_{\text{Amine}}}{M_{\text{CO}_2}} \left\{ 1 + \frac{1 - \omega_{\text{Amine}}}{\omega_{\text{Amine}}} \right\} + z\alpha \right) \quad (\text{C.9})$$

Thus, the mass flowrates of the lean amine solution and the rich amine solution are:

$$F_{\text{Lean}} = \frac{F_{\text{FG}} x_{\text{CO}_2} \Psi_{\text{CO}_2}}{100z (\alpha_{\text{Rich}} - \alpha_{\text{Lean}})} \left(\frac{M_{\text{Amine}}}{M_{\text{CO}_2}} \left\{ 1 + \frac{1 - \omega_{\text{Amine}}}{\omega_{\text{Amine}}} \right\} + z\alpha_{\text{Lean}} \right) \quad (\text{C.10a})$$

$$F_{\text{Rich}} = \frac{F_{\text{FG}} x_{\text{CO}_2} \Psi_{\text{CO}_2}}{100z (\alpha_{\text{Rich}} - \alpha_{\text{Lean}})} \left(\frac{M_{\text{Amine}}}{M_{\text{CO}_2}} \left\{ 1 + \frac{1 - \omega_{\text{Amine}}}{\omega_{\text{Amine}}} \right\} + z\alpha_{\text{Rich}} \right) \quad (\text{C.10b})$$

Since M_{CO_2} is 44.009 kg/kmol, Eqs (C.10a) and (C.10b) can be written as follows:

$$F_{\text{Lean}} = \frac{F_{\text{FG}} x_{\text{CO}_2} \Psi_{\text{CO}_2}}{100z (\alpha_{\text{Rich}} - \alpha_{\text{Lean}})} \left(\frac{M_{\text{Amine}}}{44.009} \left\{ 1 + \frac{1 - \omega_{\text{Amine}}}{\omega_{\text{Amine}}} \right\} + z\alpha_{\text{Lean}} \right) \quad (\text{C.11a})$$

$$F_{\text{Rich}} = \frac{F_{\text{FG}} x_{\text{CO}_2} \Psi_{\text{CO}_2}}{100z (\alpha_{\text{Rich}} - \alpha_{\text{Lean}})} \left(\frac{M_{\text{Amine}}}{44.009} \left\{ 1 + \frac{1 - \omega_{\text{Amine}}}{\omega_{\text{Amine}}} \right\} + z\alpha_{\text{Rich}} \right) \quad (\text{C.11b})$$

Eq. (7.5.1) in **Chapter 7** is given by Eq. (C.11a).

Appendix D: Optimum design data for the MEA-based CO₂ capture plants designed in Chapter 7.

Table D.1. Summary of the optimum design data for an MEA-based CO₂ capture plants needed by four different power plants.

	Gas-fired (NGCC)	Gas-fired (NGCC)	Coal-fired (Subcritical)	Coal-fired (Ultra-supercritical)
Gross Power plant size (MWe)	400	450	673	827
Flue Gas Flowrate (kg/s)	622.2	725	892.57	932.42
Optimum Liquid Flowrate (kg/s)	597.31	694.55	2610.77	2499.81
Optimum Liquid/Gas Ratio (kg/kg)	0.96	0.96	2.93	2.68
Optimum lean CO ₂ loading (mol/mol)	0.2	0.2	0.2	0.2
Optimum rich CO ₂ loading (mol/mol)	0.483	0.483	0.506	0.505
CO ₂ Captured at 90% rate (kg/s)	35.07	40.86	165.58	160.60
Absorber				
Number of Absorber	2	2	2	2
Absorber Packing	Mellapak 250Y	Mellapak 250Y	Mellapak 250Y	Mellapak 250Y

Absorber Diameter (m)	11.93	12.88	16.67	16.92
Optimum Absorber Height (m)	19.06	19.99	23.04	23.74
Average HETP for the Absorber (m)	0.455	0.455	0.413	0.390
Absorber pressure drop (mm-H ₂ O/m)	19.19	19.12	13.48	13.82
Stripper				
Number of Stripper	1	1	1	1
Stripper Packing ^a	Mellapak 250Y	Mellapak 250Y	Mellapak 250Y	Mellapak 250Y
Stripper Diameter (m)	6.76	7.74	14.25	13.89
Optimum Stripper Height (m)	28.15	28.15	25.62	25.36
Average HETP for the Stripper (m)	0.257	0.257	0.253	0.253
Stripper pressure drop (mm-H ₂ O/m)	7.33	5.31	7.13	7.35
Reboiler Temperature (°C)	117.05	117.05	117.06	117.06
Specific Reboiler Duty (MJ/kg CO ₂)	3.96	3.96	3.69	3.72
Specific Condenser Duty (MJ/kg CO ₂)	1.63	1.63	1.49	1.47
Cross Heat Exchanger				
Duty (MW)	160.21	186.36	665.52	642.20
Rich amine inlet temperature (°C)	37.83	37.83	42.76	41.51

Lean amine outlet temperature (°C)	44.34	44.31	48.04	47.48
Lean Amine Cooler				
Duty (MW)	9.39	10.84	75.96	67.74
Lean Amine Pump				
Duty (kW)	96.91	112.46	422.84	404.84
Rich Amine Pump				
Duty (kW)	139.34	161.70	599.15	570.17
Capital and Operating Costs				
CAPEX (Million £) ^b	75.45	87.20	266.38	252.48
OPEX (Million £/yr) ^c	47.97	56.09	202.34	194.32
Total Cost per gross electricity (£/MWh) ^d	16.21	16.81	39.60	30.90
Total Cost per CO ₂ captured (£/ton CO ₂)	51.35	51.44	44.71	44.19

^aA change to Mellapak 250XTM packing will give diameter sizes of 10.57 m, 11.40 m, 14.49 m, and 14.93 m for the 400 MWe NGCC case, the 450 MWe NGCC case, the subcritical PC case, and the ultra-supercritical PC case, respectively.

^bOvernight capital cost (CAPEX) is for the basic flowsheet shown in **Figure 7.1** (excluding the FG fan) and with 316L stainless steel metallurgy. It is important to state that the cost of an actual plant will be higher due to HAZOP requirements.

^cAnnual operating cost (OPEX) is based on the assumed cost of steam, cooling water, and electricity.

^dTotal cost is based on OPEX and annualized CAPEX at 10% interest rate for 20 years. MWh is gross value.

List of References

(1) Global CCS Institute. The Global Status of CCS: 2011. Global CCS Institute: Canberra, Australia.

<http://decarboni.se/sites/default/files/publications/22562/global-status-ccs-2011.pdf>

(2) IEA. CO₂ Emissions from Fuel Combustion 2013. OECD/IEA: Paris, France.

http://www.oecd-ilibrary.org/energy/co2-emissions-from-fuel-combustion-2013_co2_fuel-2013-en

(3) IEA. World Energy Outlook 2013. OECD/IEA: Paris, France.

<http://www.worldenergyoutlook.org/publications/weo-2013/>

(4) IEA. CO₂ Emissions from Fuel Combustion Highlights. OECD/IEA: Paris, France, 2011.

<http://www.iea.org/media/statistics/co2highlights.pdf>

(5) IEA. World Energy Outlook 2010. OECD/IEA: Paris, France.

<http://www.iea.org/publications/freepublications/publication/weo2010.pdf>

(6) IEA. World Energy Outlook 2011. OECD/IEA: Paris, France.

http://www.iea.org/publications/freepublications/publication/weo2011_web.pdf

(7) IEA. Energy Technology Perspectives 2010. OECD/IEA: Paris, France.

<http://www.iea.org/publications/freepublications/publication/etp2010.pdf>

(8) IPCC. IPCC Fourth Assessment Report - Climate Change. IPCC: Geneva, 2007.

http://www.ipcc.ch/pdf/assessment-report/ar4/syr/ar4_syr_full_report.pdf

(9) UNFCCC "Report of the Conference of the Parties on its sixteenth session, held in Cancun from 29 November to 10 December 2010," United Nations, 2010.

<http://unfccc.int/resource/docs/2010/cop16/eng/07a01.pdf>

(10) IPCC. *IPCC Special Report on Carbon Dioxide Capture and Storage*; Cambridge University Press: New York, 2005.

https://www.ipcc.ch/pdf/special-reports/srccs/srccs_wholereport.pdf

(11) IEA. *Technology Roadmap: Carbon capture and storage*. OECD/IEA: Paris, France, 2009.

<http://www.iea.org/publications/freepublications/publication/CCSRoadmap2009.pdf>

(12) IEA. *Energy Technology Perspectives 2008*. OECD/IEA: Paris, France.

<http://www.iea.org/publications/freepublications/publication/etp2008.pdf>

(13) IEA. *CO₂ Capture and Storage: A key abatement option*. OECD/IEA: Paris, France, 2008.

http://www.iea.org/publications/freepublications/publication/CCS_2008.pdf

(14) Pires, J. C. M.; Martins, F. G.; Alvim-Ferraz, M. C. M.; Simões, M. Recent developments on carbon capture and storage: An overview. *Chem. Eng. Res. Des.* **2011**, *89*, 1446-1460.

(15) Versteeg, P.; Rubin, E. S. Technical and economic assessment of ammonia-based post-combustion CO₂ capture. *Energy Procedia* **2011**, *4*, 1957-1964.

(16) Wang, M.; Lawal, A.; Stephenson, P.; Sidders, J.; Ramshaw, C. Post-combustion CO₂ capture with chemical absorption: A state-of-the-art review. *Chem. Eng. Res. Des.* **2011**, *89*, 1609-1624.

(17) Kohl, A.; Nielsen, R. *Gas Purification*, Fifth Edition; Gulf Professional Publishing: Houston, 1997.

(18) Astarita, G.; Savage, D. W.; Bisio, A. *Gas Treating with Chemical Solvents*; John Wiley: New York, 1983.

(19) Rao, A. B.; Rubin, E. S. A Technical, Economic, and Environmental Assessment of Amine-Based CO₂ Capture Technology for Power Plant Greenhouse Gas Control. *Environmental Science & Technology* **2002**, *36*, 4467-4475.

(20) APGTF "Cleaner fossil power generation in the 21st century - Maintaining a leading role: A technology strategy for fossil fuel carbon abatement technologies," UK Advanced power generation technology forum (APGTF), 2011.

(21) Global CCS Institute. The Global Status of CCS: 2010. Global CCS Institute: Canberra, Australia.

(22) MacDowell, N.; Florin, N.; Buchard, A.; Hallett, J.; Galindo, A.; Jackson, G.; Adjiman, C. S.; Williams, C. K.; Shah, N.; Fennell, P. An overview of CO₂ capture technologies. *Energy & Environmental Science* **2010**, *3*, 1645-1669.

(23) Le Moullec, Y.; Kanniche, M. Screening of flowsheet modifications for an efficient monoethanolamine (MEA) based post-combustion CO₂ capture. *Int. J. Greenhouse Gas Control* **2011**, *5*, 727-740.

(24) Le Moullec, Y.; Kanniche, M. Optimization of MEA based post combustion CO₂ capture process: Flowsheeting and energetic integration. *Energy Procedia* **2011**, *4*, 1303-1309.

(25) Oyekan, B. A.; Rochelle, G. T. Energy Performance of Stripper Configurations for CO₂ Capture by Aqueous Amines. *Ind. Eng. Chem. Res.* **2006**, *45*, 2457-2464.

(26) Oyekan, B. A.; Rochelle, G. T. Alternative stripper configurations for CO₂ capture by aqueous amines. *AIChE J.* **2007**, *53*, 3144-3154.

(27) Kvamsdal, H. M.; Jakobsen, J. P.; Hoff, K. A. Dynamic modeling and simulation of a CO₂ absorber column for post-combustion CO₂ capture. *Chem. Eng. Process.* **2009**, *48*, 135-144.

(28) Mangalapally, H. P.; Hasse, H. Pilot plant experiments for post combustion carbon dioxide capture by reactive absorption with novel solvents. *Energy Procedia* **2011**, *4*, 1-8.

(29) Mangalapally, H. P.; Hasse, H. Pilot plant study of post-combustion carbon dioxide capture by reactive absorption: Methodology, comparison of different structured packings, and comprehensive results for monoethanolamine. *Chem. Eng. Res. Des.* **2011**, *89*, 1216-1228.

(30) Mangalapally, H. P.; Notz, R.; Hoch, S.; Asprion, N.; Sieder, G.; Garcia, H.; Hasse, H. Pilot plant experimental studies of post combustion CO₂ capture by reactive absorption with MEA and new solvents. *Energy Procedia* **2009**, *1*, 963-970.

(31) Kvamsdal, H. M.; Haugen, G.; Svendsen, H. F.; Tobiesen, A.; Mangalapally, H.; Hartono, A.; Mejdell, T. Modelling and simulation of the Esbjerg pilot plant using the Cesar 1 solvent. *Energy Procedia* **2011**, *4*, 1644-1651.

(32) Moser, P.; Schmidt, S.; Sieder, G.; Garcia, H.; Stoffregen, T.; Stamatov, V. The post-combustion capture pilot plant Niederaussem—Results of the first half of the testing programme. *Energy Procedia* **2011**, *4*, 1310-1316.

(33) Moser, P.; Schmidt, S.; Sieder, G.; Garcia, H.; Stoffregen, T. Performance of MEA in a long-term test at the post-combustion capture pilot plant in Niederaussem. *Int. J. Greenhouse Gas Control* **2011**, *5*, 620-627.

(34) Moser, P.; Schmidt, S.; Sieder, G.; Garcia, H.; Ciattaglia, I.; Klein, H. Enabling post combustion capture optimization—The pilot plant project at Niederaussem. *Energy Procedia* **2009**, *1*, 807-814.

(35) Yeh, J. T.; Pennline, H. W.; Resnik, K. P. Study of CO₂ Absorption and Desorption in a Packed Column. *Energy & Fuels* **2001**, *15*, 274-278.

(36) Freguia, S.; Rochelle, G. T. Modeling of CO₂ capture by aqueous monoethanolamine. *AIChE J.* **2003**, *49*, 1676-1686.

(37) Aroonwilas, A.; Veawab, A. Integration of CO₂ capture unit using single- and blended-amines into supercritical coal-fired power plants: Implications for emission and energy management. *Int. J. Greenhouse Gas Control* **2007**, *1*, 143-150.

(38) Aroonwilas, A.; Veawab, A. Characterization and Comparison of the CO₂ Absorption Performance into Single and Blended Alkanolamines in a Packed Column. *Ind. Eng. Chem. Res.* **2004**, *43*, 2228-2237.

(39) Qader, A.; Hooper, B.; Innocenzi, T.; Stevens, G.; Kentish, S.; Scholes, C.; Mumford, K.; Smith, K.; Webley, P. A.; Zhang, J. Novel post-combustion capture technologies on a lignite fired power plant - results of the CO₂CRC/H3 capture project. *Energy Procedia* **2011**, *4*, 1668-1675.

(40) Tangen, G.; Mølnvik, M. J.; Røkke, N. A. BIGCO₂ R&D Platform Breakthrough CCS technologies enabling large-scale CO₂ chains. *Energy Procedia* **2011**, *4*, 6077-6084.

(41) *Perry's Chemical Engineers' Handbook*: 8th ed.; Green, D. W.; Perry, R. H., Eds.; McGraw Hill: New York, 2007.

(42) Danckwerts, P. V. *Gas-Liquid Reactions*; McGraw-Hill Inc.: London, 1970.

(43) Levenspiel, O. *Chemical Reaction Engineering*, 3rd; John Wiley & Sons, Inc.: New York, 1999.

(44) Morrison, R. T.; Boyd, R. N. *Organic Chemistry*, 6th; Prentice Hall: New Jersey, 1992.

(45) Maddox, R. N. *Gas Conditioning and Processing*, 3rd; Campbell Petroleum Series: Oklahoma, 1982; Vol. 4.

(46) Bottoms, R. R. Organic Bases for Gas Purification. *Ind. Eng. Chem.* **1931**, 23, 501-504.

(47) Bottoms, R. R. Process for Separating Acidic Gases. U. S. patent 1783901, 1930.

(48) Reddy, S.; Scherffius, J. R.; Yonkoski, J.; Radgen, P.; Rode, H. Initial Results from Fluor's CO₂ Capture Demonstration Plant Using Econamine FG PlusSM Technology at E.ON Kraftwerke's Wilhelmshaven Power Plant. *Energy Procedia* **2013**, 37, 6216-6225.

(49) Endo, T.; Kajiya, Y.; Nagayasu, H.; Iijima, M.; Ohishi, T.; Tanaka, H.; Mitchell, R. Current status of MHI CO₂ capture plant technology, large scale demonstration project and road map to commercialization for coal fired flue gas application. *Energy Procedia* **2011**, 4, 1513-1519.

(50) Shaw, D. Cansolv CO₂ capture: The value of integration. *Energy Procedia* **2009**, 1, 237-246.

(51) Oexmann, J.; Kather, A. Minimising the regeneration heat duty of post-combustion CO₂ capture by wet chemical absorption: The misguided focus on low heat of absorption solvents. *Int. J. Greenhouse Gas Control* **2010**, 4, 36-43.

(52) Sander, M. T.; Mariz, C. L. The Fluor Daniel® econamine FG process: Past experience and present day focus. *Energy Convers. Manage.* **1992**, 33, 341-348.

(53) Kittel, J.; Idem, R.; Gelowitz, D.; Tontiwachwuthikul, P.; Parrain, G.; Bonneau, A. Corrosion in MEA units for CO₂ capture: Pilot plant studies. *Energy Procedia* **2009**, 1, 791-797.

(54) Lepaumier, H.; Picq, D.; Carrette, P.-L. New Amines for CO₂ Capture. I. Mechanisms of Amine Degradation in the Presence of CO₂. *Ind. Eng. Chem. Res.* **2009**, 48, 9061-9067.

(55) Lepaumier, H.; Picq, D.; Carrette, P.-L. New Amines for CO₂ Capture. II. Oxidative Degradation Mechanisms. *Ind. Eng. Chem. Res.* **2009**, *48*, 9068-9075.

(56) Meldon, J. H. Amine screening for flue gas CO₂ capture at coal-fired power plants: Should the heat of desorption be high, low or in between? *Current Opinion in Chemical Engineering* **2011**, *1*, 55-63.

(57) Frazier, H. D.; Kohl, A. L. Selective Absorption of Hydrogen Sulfide from Gas Streams. *Industrial & Engineering Chemistry* **1950**, *42*, 2288-2292.

(58) Ramachandran, N.; Aboudheir, A.; Idem, R.; Tontiwachwuthikul, P. Kinetics of the Absorption of CO₂ into Mixed Aqueous Loaded Solutions of Monoethanolamine and Methyldiethanolamine. *Ind. Eng. Chem. Res.* **2006**, *45*, 2608-2616.

(59) Liao, C. H.; Li, M. H. Kinetics of absorption of carbon dioxide into aqueous solutions of monoethanolamine+N-methyldiethanolamine. *Chem. Eng. Sci.* **2002**, *57*, 4569-4582.

(60) Zhang, X.; Zhang, C. F.; Liu, Y. Kinetics of absorption of CO₂ into aqueous solution of MDEA blended with DEA. *Ind. Eng. Chem. Res.* **2002**, *41*, 1135-1141.

(61) Rinker, E. B.; Ashour, S. S.; Sandall, O. C. Absorption of Carbon Dioxide into Aqueous Blends of Diethanolamine and Methyldiethanolamine. *Ind. Eng. Chem. Res.* **2000**, *39*, 4346-4356.

(62) Sartori, G.; Savage, D. W. Sterically hindered amines for carbon dioxide removal from gases. *Industrial & Engineering Chemistry Fundamentals* **1983**, *22*, 239-249.

(63) Goldstein, A. M. Commercialization of a new gas treating agent. In *Petroenergy '83 Conference*: Houston, TX, 1983.

(64) Goldstein, A. M.; Beisner, W. D.; Edelman, A. M.; Ruziska, P. A. Hindered amines yield improved gas treating. *Oil Gas J.* **1984**, *82*, 70-76.

(65) Polasek, J. C.; Iglesias-Silva, G. A.; Bullin, J. A. Using Mixed Amine Solutions for Gas Sweetening. In *Proceedings of the 71st GPA Annual Convention*; Gas Processors Association: Tulsa, OK, 1992; pp 58-63.

(66) Bullin, J. A.; Polasek, J. C.; Donnelly, S. T. The Use of MDEA and Mixtures of Amines for Bulk CO₂ Removal. In *Proceedings of the 69th*

GPA Convention; Gas Processors Association: Tulsa, OK, 1990; pp 135-139.

(67) Chakravarty, T.; Phukan, U. K.; Weiland, R. H. Reaction of Acid Gases with Mixtures of Amines. *Chem. Eng. Prog.* **1985**, *81*, 32-36.

(68) Glasscock, D. A.; Critchfield, J. E.; Rochelle, G. T. CO₂ absorption/desorption in mixtures of methyldiethanolamine with monoethanolamine or diethanolamine. *Chem. Eng. Sci.* **1991**, *46*, 2829-2845.

(69) Vaidya, P. D.; Kenig, E. Y. CO₂-Alkanolamine Reaction Kinetics: A Review of Recent Studies. *Chemical Engineering & Technology* **2007**, *30*, 1467-1474.

(70) Liu, Y.; Zhang, L.; Watanasiri, S. Representing Vapor-Liquid Equilibrium for an Aqueous MEA-CO₂ System Using the Electrolyte Nonrandom-Two-Liquid Model. *Ind. Eng. Chem. Res.* **1999**, *38*, 2080-2090.

(71) Austgen, D. M.; Rochelle, G. T.; Chen, C. C. Model of vapor-liquid equilibria for aqueous acid gas-alkanolamine systems. 2. Representation of hydrogen sulfide and carbon dioxide solubility in aqueous MDEA and carbon dioxide solubility in aqueous mixtures of MDEA with MEA or DEA. *Ind. Eng. Chem. Res.* **1991**, *30*, 543-555.

(72) Austgen, D. M.; Rochelle, G. T.; Peng, X.; Chen, C. C. Model of Vapor Liquid Equilibria for Aqueous Acid Gas Alkanolamine Systems Using the Electrolyte NRTL Equation. *Ind. Eng. Chem. Res.* **1989**, *28*, 1060-1073.

(73) Versteeg, G. F.; Van Dijck, L. A. J.; Van Swaaij, W. P. M. On the kinetics between CO₂ and alkanolamines both in aqueous and non-aqueous solutions. An overview. *Chem. Eng. Commun.* **1996**, *144*, 113-158.

(74) Aboudheir, A.; Tontiwachwuthikul, P.; Chakma, A.; Idem, R. Kinetics of the reactive absorption of carbon dioxide in high CO₂-loaded, concentrated aqueous monoethanolamine solutions. *Chem. Eng. Sci.* **2003**, *58*, 5195-5210.

(75) Blauwhoff, P. M. M.; Versteeg, G. F.; Vanswaaij, W. P. M. A Study on the Reaction between CO₂ and Alkanolamines in Aqueous-Solutions. *Chem. Eng. Sci.* **1984**, *38*, 1411-1429.

(76) Danckwerts, P. V. The reaction of CO₂ with ethanolamines. *Chem. Eng. Sci.* **1979**, *34*, 443-446.

(77) Mahajani, V. V.; Joshi, J. B. Kinetics of reactions between carbon dioxide and alkanolamines. *Gas Separation & Purification* **1988**, *2*, 50-64.

(78) Sharma, M. M. Kinetics of reactions of carbonyl sulphide and carbon dioxide with amines and catalysis by Bronsted bases of the hydrolysis of COS. *Transactions of the Faraday Society* **1965**, *61*, 681-688.

(79) Donaldson, T. L.; Nguyen, Y. N. Carbon Dioxide Reaction Kinetics and Transport in Aqueous Amine Membranes. *Industrial & Engineering Chemistry Fundamentals* **1980**, *19*, 260-266.

(80) Caplow, M. Kinetics of Carbamate Formation and Breakdown. *J. Am. Chem. Soc.* **1968**, *90*, 6795-6803.

(81) Crooks, J. E.; Donnellan, J. P. Kinetics and mechanism of the reaction between carbon dioxide and amines in aqueous solution. *Journal of the Chemical Society, Perkin Transactions 2* **1989**.

(82) da Silva, E. F.; Svendsen, H. F. Ab Initio Study of the Reaction of Carbamate Formation from CO₂ and Alkanolamines. *Ind. Eng. Chem. Res.* **2004**, *43*, 3413-3418.

(83) Jorgensen, E.; Faurholt, C. Reactions between carbon dioxide and amino alcohols II. Triethanolamine. *Acta Chem. Scand.* **1954**, *8*, 1141-1144.

(84) Benitez-Garcia, J.; Ruiz-Ibanez, G.; Al-Ghawas, H. A.; Sandall, O. C. On the effect of basicity on the kinetics of CO₂ absorption in tertiary amines. *Chem. Eng. Sci.* **1991**, *46*, 2927-2931.

(85) Vaidya, P. D.; Kenig, E. Y. Termolecular Kinetic Model for CO₂-Alkanolamine Reactions: An Overview. *Chemical Engineering & Technology* **2010**, *33*, 1577-1581.

(86) Li, Y. G.; Mather, A. E. Correlation and Prediction of the Solubility of Carbon Dioxide in a Mixed Alkanolamine Solution. *Ind. Eng. Chem. Res.* **1994**, *33*, 2006-2015.

(87) Aspen Technology. *Aspen Physical Property System, V7.3*; Aspen Technology, Inc.: Burlington, MA, 2011.

(88) Hilliard, M. D. A Predictive Thermodynamic Model for an Aqueous Blend of Potassium Carbonate, Piperazine, and Monoethanolamine for Carbon Dioxide Capture from Flue Gas. PhD Thesis, The University of Texas at Austin, 2008.

(89) Edwards, T. J.; Maurer, G.; Newman, J.; Prausnitz, J. M. Vapor-liquid equilibria in multicomponent aqueous solutions of volatile weak electrolytes. *AIChE J.* **1978**, *24*, 966-976.

(90) Gibbs, J. W. *The Scientific papers of J. Williard Gibbs, Vol 1, Thermodynamics*; Dover Publications: New York, 1961.

(91) Smith, J. M.; Van Ness, H. C.; Abbott, M. M. *Introduction to Chemical Engineering Thermodynamics*, 7th; McGraw Hill: New York, 2005.

(92) Denbigh, K. G. *The Principles of Chemical Equilibrium*, 4th; Cambridge University Press: Cambridge, UK, 1981.

(93) Lewis, G. N.; Randall, M. *Thermodynamics (Revised by K. S. Pitzer and L. Brewer)*; McGraw-Hill Book Co.: New York, 1961.

(94) Kontogeorgis, G. M.; Folas, G. K. *Thermodynamic Models for Industrial Applications: From Classical and Advanced Mixing Rules to Association Theories*; John Wiley & Sons Ltd: Chichester, United Kingdom, 2010.

(95) Austgen, D. M. A model of vapor-liquid equilibria for acid gas-alkanolamine-water systems. PhD Thesis, The University of Texas at Austin, 1989.

(96) Edwards, T. J.; Newman, J.; Prausnitz, J. M. Thermodynamics of aqueous solutions containing volatile weak electrolytes. *AIChE J.* **1975**, *21*, 248-259.

(97) Yan, Y.; Chen, C. C. Thermodynamic modeling of CO₂ solubility in aqueous solutions of NaCl and Na₂SO₄. *The Journal of Supercritical Fluids* **2010**, *55*, 623-634.

(98) Zhang, Y.; Chen, C.-C. Thermodynamic Modeling for CO₂ Absorption in Aqueous MDEA Solution with Electrolyte NRTL Model. *Ind. Eng. Chem. Res.* **2011**, *50*, 163-175.

(99) Brelvi, S. W.; O'Connell, J. P. Corresponding states correlations for liquid compressibility and partial molal volumes of gases at infinite dilution in liquids. *AIChE J.* **1972**, *18*, 1239-1243.

(100) Rackett, H. G. Equation of state for saturated liquids. *Journal of Chemical & Engineering Data* **1970**, *15*, 514-517.

(101) Zhang, Y.; Que, H.; Chen, C.-C. Thermodynamic modeling for CO₂ absorption in aqueous MEA solution with electrolyte NRTL model. *Fluid Phase Equilib.* **2011**, *311*, 67-75.

(102) Poling, B. E.; Prausnitz, J. M.; O'Connell, J. P. *The Properties of Gases and Liquids*, 5th; McGraw-Hill: New York, 2001.

(103) Abbott, M. M. Cubic Equations of State: An Interpretive Review. In *Equations of State in Engineering and Research*; American Chemical Society, 1979; Vol. 182; pp 47-70.

(104) Redlich, O.; Kwong, J. N. S. On the Thermodynamics of Solutins. *Chem. Rev.* **1949**, *44*, 233-244.

(105) Giorgio, S. Equilibrium constants from a modified Redlich-Kwong equation of state. *Chem. Eng. Sci.* **1972**, *27*, 1197-1203.

(106) Peng, D.-Y.; Robinson, D. B. A New Two-Constant Equation of State. *Industrial & Engineering Chemistry Fundamentals* **1976**, *15*, 59-64.

(107) Renon, H.; Prausnitz, J. M. Local compositions in thermodynamic excess functions for liquid mixtures. *AIChE J.* **1968**, *14*, 135-144.

(108) Abrams, D. S.; Prausnitz, J. M. Statistical thermodynamics of liquid mixtures: A new expression for the excess Gibbs energy of partly or completely miscible systems. *AIChE J.* **1975**, *21*, 116-128.

(109) Debye, P.; Hückel, E. Zur Theorie der Elektrolyte. I. Gefrierpunktserniedrigung und verwandte Erscheinungen. *Physikalische Zeitschrift* **1923**, *24*, 185-206.

(110) Guggenheim, E. A. The specific thermodynamic properties of aqueous solutions of strong electrolytes. *Philosophical Magazine Series 7* **1935**, *19*, 588-643.

(111) Pitzer, K. S. Thermodynamics of electrolytes. I. Theoretical basis and general equations. *The Journal of Physical Chemistry* **1973**, *77*, 268-277.

(112) Pitzer, K. S. Electrolytes. From dilute solutions to fused salts. *J. Am. Chem. Soc.* **1980**, *102*, 2902-2906.

(113) Chen, C.-C.; Britt, H. I.; Boston, J. F.; Evans, L. B. Local composition model for excess Gibbs energy of electrolyte systems. Part I:

Single solvent, single completely dissociated electrolyte systems. *AIChE J.* **1982**, 28, 588-596.

(114) Sander, B.; Fredenslund, A.; Rasmussen, P. Calculation of vapour-liquid equilibria in mixed solvent/salt systems using an extended UNIQUAC equation. *Chem. Eng. Sci.* **1986**, 41, 1171-1183.

(115) Kaewsichan, L.; Al-Bofersen, O.; Yesavage, V. F.; Selim, M. S. Predictions of the solubility of acid gases in monoethanolamine (MEA) and methyldiethanolamine (MDEA) solutions using the electrolyte-UNIQUAC model. *Fluid Phase Equilib.* **2001**, 183, 159-171.

(116) Faramarzi, L.; Kontogeorgis, G. M.; Thomsen, K.; Stenby, E. H. Extended UNIQUAC model for thermodynamic modeling of CO₂ absorption in aqueous alkanolamine solutions. *Fluid Phase Equilib.* **2009**, 282, 121-132.

(117) Aronu, U. E.; Gondal, S.; Hessen, E. T.; Haug-Warberg, T.; Hartono, A.; Hoff, K. A.; Svendsen, H. F. Solubility of CO₂ in 15, 30, 45 and 60 mass% MEA from 40 to 120 °C and model representation using the extended UNIQUAC framework. *Chem. Eng. Sci.* **2011**, 66, 6393-6406.

(118) Chen, C. C.; Evans, L. B. A Local Composition Model for the Excess Gibbs Energy of Aqueous-Electrolyte Systems. *AIChE J.* **1986**, 32, 444-454.

(119) Mock, B.; Evans, L. B.; Chen, C.-C. Thermodynamic representation of phase equilibria of mixed-solvent electrolyte systems. *AIChE J.* **1986**, 32, 1655-1664.

(120) Chen, C. C.; Song, Y. Generalized electrolyte-NRTL model for mixed-solvent electrolyte systems. *AIChE J.* **2004**, 50, 1928-1941.

(121) Bollas, G. M.; Chen, C. C.; Barton, P. I. Refined electrolyte-NRTL model: Activity coefficient expressions for application to multi-electrolyte systems. *AIChE J.* **2008**, 54, 1608-1624.

(122) Rashin, A. A.; Honig, B. Reevaluation of the Born model of ion hydration. *The Journal of Physical Chemistry* **1985**, 89, 5588-5593.

(123) Robinson, R. A.; Stokes, R. H. *Electrolyte Solutions*, Second Revised; Butterworths: London, 1970.

(124) Watson, K. M. Thermodynamics of liquid state: Generalized prediction of properties. *Ind. Eng. Chem.* **1943**, 35, 398-406.

(125) Agbonghae, E. O.; Hughes, K. J.; Ingham, D. B.; Ma, L.; Pourkashanian, M. A Semi-Empirical Model for Estimating the Heat Capacity of Aqueous Solutions of Alkanolamines for CO₂ Capture. *Ind. Eng. Chem. Res.* **2014**, *53*, 8291–8301.

(126) Blanchon le Bouhelec, E.; Mougín, P.; Barreau, A.; Solimando, R. Rigorous Modeling of the Acid Gas Heat of Absorption in Alkanolamine Solutions. *Energy & Fuels* **2007**, *21*, 2044-2055.

(127) Mathias, P. M.; O'Connell, J. P. The Gibbs–Helmholtz Equation and the Thermodynamic Consistency of Chemical Absorption Data. *Ind. Eng. Chem. Res.* **2012**, *51*, 5090-5097.

(128) Kim, I.; Svendsen, H. F. Heat of Absorption of Carbon Dioxide (CO₂) in Monoethanolamine (MEA) and 2-(Aminoethyl)ethanolamine (AEEA) Solutions. *Ind. Eng. Chem. Res.* **2007**, *46*, 5803-5809.

(129) Kim, I.; Hoff, K. A.; Hessen, E. T.; Haug-Warberg, T.; Svendsen, H. F. Enthalpy of absorption of CO₂ with alkanolamine solutions predicted from reaction equilibrium constants. *Chem. Eng. Sci.* **2009**, *64*, 2027-2038.

(130) Gabrielsen, J.; Michelsen, M. L.; Stenby, E. H.; Kontogeorgis, G. M. A Model for Estimating CO₂ Solubility in Aqueous Alkanolamines. *Ind. Eng. Chem. Res.* **2005**, *44*, 3348-3354.

(131) Steele, W. V.; Chirico, R. D.; Knipmeyer, S. E.; Nguyen, A.; Smith, N. K. Thermodynamic Properties and Ideal-Gas Enthalpies of Formation for Dicyclohexyl Sulfide, Diethylenetriamine, Di-n-octyl Sulfide, Dimethyl Carbonate, Piperazine, Hexachloroprop-1-ene, Tetrakis(dimethylamino)ethylene, N,N'-Bis-(2-hydroxyethyl)ethylenediamine, and 1,2,4-Triazolo[1,5-a]pyrimidine. *J. Chem. Eng. Data* **1997**, *42*, 1037-1052.

(132) Maham, Y.; G. Hepler, L.; E. Mather, A.; W. Hakin, A.; A. Marriott, R. Molar heat capacities of alkanolamines from 299.1 to 397.8 K Group additivity and molecular connectivity analyses. *J. Chem. Soc., Faraday Trans.* **1997**, *93*, 1747-1750.

(133) Chiu, L. F.; Liu, H. F.; Li, M. H. Heat Capacity of Alkanolamines by Differential Scanning Calorimetry. *J. Chem. Eng. Data* **1999**, *44*, 631-636.

(134) Chen, Y. J.; Shih, T. W.; Li, M. H. Heat Capacity of Aqueous Mixtures of Monoethanolamine with N-Methyldiethanolamine. *J. Chem. Eng. Data* **2001**, *46*, 51-55.

(135) Chen, Y. J.; Li, M. H. Heat Capacity of Aqueous Mixtures of Monoethanolamine with 2-Amino-2-methyl-1-propanol. *J. Chem. Eng. Data* **2001**, *46*, 102-106.

(136) Zhang, K.; Hawrylak, B.; Palepu, R.; Tremaine, P. R. Thermodynamics of aqueous amines: excess molar heat capacities, volumes, and expansibilities of {water+ methyldiethanolamine (MDEA)} and {water + 2-amino-2-methyl-1-propanol (AMP)}. *J. Chem. Thermodyn.* **2002**, *34*, 679-710.

(137) Mundhwa, M.; Henni, A. Molar Heat Capacity of Various Aqueous Alkanolamine Solutions from 303.15 K to 353.15 K. *J. Chem. Eng. Data* **2007**, *52*, 491-498.

(138) Hayden, T. A.; Smith, T. G. A.; Mather, A. E. Heat capacity of aqueous methyldiethanolamine solutions. *J. Chem. Eng. Data* **1983**, *28*, 196-197.

(139) Pagé, M.; Huot, J.-Y.; Jolicoeur, C. A comprehensive thermodynamic investigation of water–ethanolamine mixtures at 10, 25, and 40 °C. *Can. J. Chem.* **1993**, *71*, 1064-1072.

(140) Weiland, R. H.; Dingman, J. C.; Cronin, D. B. Heat Capacity of Aqueous Monoethanolamine, Diethanolamine, N-Methyldiethanolamine, and N-Methyldiethanolamine-Based Blends with Carbon Dioxide. *J. Chem. Eng. Data* **1997**, *42*, 1004-1006.

(141) Chiu, L. F.; Li, M. H. Heat Capacity of Alkanolamine Aqueous Solutions. *J. Chem. Eng. Data* **1999**, *44*, 1396-1401.

(142) Chen, Y. R.; Caparanga, A. R.; Soriano, A. N.; Li, M. H. Liquid heat capacity of the solvent system (piperazine + n-methyldiethanolamine + water). *J. Chem. Thermodyn.* **2010**, *42*, 54-59.

(143) Shih, T. W.; Soriano, A. N.; Li, M. H. Heat capacities of aqueous solutions containing diethanolamine and N-methyldiethanolamine. *J. Chem. Thermodyn.* **2009**, *41*, 1259-1263.

(144) Chen, Y. R.; Caparanga, A. R.; Soriano, A. N.; Li, M. H. Liquid heat capacity of the solvent system (piperazine + 2-amino-2-methyl-1-propanol + water). *J. Chem. Thermodyn.* **2010**, *42*, 518-523.

(145) Wagner, W.; Kretzschmar, H.-J. *International Steam Tables: Properties of Water and Steam Based on the Industrial Formulation IAPWS-IF97*, 2nd; Springer: Verlag Berlin Heidelberg, 2008.

(146) Lemmon, E. W.; McLinden, M. O.; Friend, D. G. Thermophysical Properties of Fluid Systems. In *NIST Chemistry WebBook, NIST Standard Reference Database Number 69*; Linstrom, P. J., Mallard, W. G., Eds.; National Institute of Standards and Technology: Gaithersburg MD, 20899, <http://webbook.nist.gov>, (retrieved January 30, 2013).

(147) Agbonghae, E. O.; Best, T.; Finney, K. N.; Font Palma, C.; Hughes, K. J.; Pourkashanian, M. Experimental and Process Modelling Study of Integration of a Micro-turbine with an Amine Plant. *Energy Procedia* **2014**, *63*, 1064-1073.

(148) Notz, R.; Mangalapally, H. P.; Hasse, H. Post combustion CO₂ capture by reactive absorption: Pilot plant description and results of systematic studies with MEA. *Int. J. Greenhouse Gas Control* **2012**, *6*, 84-112.

(149) Agbonghae, E. O.; Hughes, K. J.; Ingham, D. B.; Ma, L.; Pourkashanian, M. Optimal Process Design of Commercial-scale Amine-based CO₂ Capture Plants. *Ind. Eng. Chem. Res.* **2014**, *53*, 14815-14829.

(150) Zhang, Y.; Chen, C.-C. Modeling CO₂ Absorption and Desorption by Aqueous Monoethanolamine Solution with Aspen Rate-based Model. *Energy Procedia* **2013**, *37*, 1584-1596.

(151) Zhang, Y.; Chen, H.; Chen, C.-C.; Plaza, J. M.; Dugas, R.; Rochelle, G. T. Rate-Based Process Modeling Study of CO₂ Capture with Aqueous Monoethanolamine Solution. *Ind. Eng. Chem. Res.* **2009**, *48*, 9233-9246.

(152) Hanley, B.; Chen, C.-C. New mass-transfer correlations for packed towers. *AIChE J.* **2012**, *58*, 132-152.

(153) Bravo, J. L.; Rocha, J. A.; Fair, J. R. Mass Transfer in Gauze Packings. *Hydrocarbon Processing* **1985**, 91-95.

(154) Stichlmair, J.; Bravo, J. L.; Fair, J. R. General model for prediction of pressure drop and capacity of countercurrent gas/liquid packed columns. *Gas Sep. Purif.* **1989**, *3*, 19-28.

(155) Bravo, J. L.; Rocha, J. A.; Fair, J. R. A comprehensive model for the performance of columns containing structured packings. *Inst. Chem. Eng. Symp. Ser.* **1992**, *129*, A439-657.

(156) Taylor, R.; Krishna, R. *Multicomponent Mass Transfer*, John Wiley & Sons, Inc.: New York, 1993.

(157) Kvamsdal, H. M.; Rochelle, G. T. Effects of the Temperature Bulge in CO₂ Absorption from Flue Gas by Aqueous Monoethanolamine. *Ind. Eng. Chem. Res.* **2008**, *47*, 867-875.

(158) Rochelle, G. T. Amine Scrubbing for CO₂ Capture. *Science* **2009**, *325*, 1652-1654.

(159) Dugas, R. E. Pilot Plant Study of Carbon Dioxide Capture by Aqueous Monoethanolamine. MSc Thesis, The University of Texas at Austin, 2006.

(160) Carey, J.; Damen, K.; Fitzgerald, F. D.; Gardiner, R. A. CCPilot100+ Operating Experience and Test Results. *Energy Procedia* **2013**, *37*, 6170-6178.

(161) Knudsen, J. N.; Jensen, J. N.; Vilhelmsen, P.-J.; Biede, O. Experience with CO₂ capture from coal flue gas in pilot-scale: Testing of different amine solvents. *Energy Procedia* **2009**, *1*, 783-790.

(162) Cottrell, A. J.; McGregor, J. M.; Jansen, J.; Artanto, Y.; Dave, N.; Morgan, S.; Pearson, P.; Attalla, M. I.; Wardhaugh, L.; Yu, H. Post-combustion capture R&D and pilot plant operation in Australia. *Energy Procedia* **2009**, *1*, 1003-1010.

(163) Idem, R.; Wilson, M.; Tontiwachwuthikul, P.; Chakma, A.; Veawab, A.; Aroonwilas, A.; Gelowitz, D. Pilot Plant Studies of the CO₂ Capture Performance of Aqueous MEA and Mixed MEA/MDEA Solvents at the University of Regina CO₂ Capture Technology Development Plant and the Boundary Dam CO₂ Capture Demonstration Plant. *Ind. Eng. Chem. Res.* **2006**, *45*, 2414-2420.

(164) Tobiesen, F. A.; Svendsen, H. F.; Juliussen, O. Experimental validation of a rigorous absorber model for CO₂ postcombustion capture. *AIChE J.* **2007**, *53*, 846-865.

(165) Lawal, A.; Wang, M.; Stephenson, P.; Yeung, H. Dynamic modelling of CO₂ absorption for post combustion capture in coal-fired power plants. *Fuel* **2009**, *88*, 2455-2462.

(166) Tobiesen, F. A.; Juliussen, O.; Svendsen, H. F. Experimental validation of a rigorous desorber model for post-combustion capture. *Chem. Eng. Sci.* **2008**, *63*, 2641-2656.

(167) Lawal, A.; Wang, M.; Stephenson, P.; Koumpouras, G.; Yeung, H. Dynamic modelling and analysis of post-combustion CO₂ chemical absorption process for coal-fired power plants. *Fuel* **2010**, *89*, 2791-2801.

(168) Huepen, B.; Kenig, E. Y. Rigorous Modeling and Simulation of an Absorption-Stripping Loop for the Removal of Acid Gases. *Ind. Eng. Chem. Res.* **2010**, *49*, 772-779.

(169) Abu-Zahra, M. R. M.; Schneiders, L. H. J.; Niederer, J. P. M.; Feron, P. H. M.; Versteeg, G. F. CO₂ capture from power plants: Part I. A parametric study of the technical performance based on monoethanolamine. *Int. J. Greenhouse Gas Control* **2007**, *1*, 37-46.

(170) Abu-Zahra, M. R. M.; Niederer, J. P. M.; Feron, P. H. M.; Versteeg, G. F. CO₂ capture from power plants: Part II. A parametric study of the economical performance based on mono-ethanolamine. *Int. J. Greenhouse Gas Control* **2007**, *1*, 135-142.

(171) Cifre, P. G.; Brechtel, K.; Hoch, S.; García, H.; Asprion, N.; Hasse, H.; Scheffknecht, G. Integration of a chemical process model in a power plant modelling tool for the simulation of an amine based CO₂ scrubber. *Fuel* **2009**, *88*, 2481-2488.

(172) Hetland, J.; Kvamsdal, H. M.; Haugen, G.; Major, F.; Kårstad, V.; Tjellander, G. Integrating a full carbon capture scheme onto a 450 MWe NGCC electric power generation hub for offshore operations: Presenting the Sevan GTW concept. *Applied Energy* **2009**, *86*, 2298-2307.

(173) Kvamsdal, H. M.; Hetland, J.; Haugen, G.; Svendsen, H. F.; Major, F.; Kårstad, V.; Tjellander, G. Maintaining a neutral water balance in a 450MWe NGCC-CCS power system with post-combustion carbon dioxide capture aimed at offshore operation. *Int. J. Greenhouse Gas Control* **2010**, *4*, 613-622.

(174) Sanpasertparnich, T.; Idem, R.; Bolea, I.; deMontigny, D.; Tontiwachwuthikul, P. Integration of post-combustion capture and storage into a pulverized coal-fired power plant. *Int. J. Greenhouse Gas Control* **2010**, *4*, 499-510.

(175) CAESAR "European best practice guidelines for assessment of CO₂ capture technologies, D 4.9," CAESAR Consortium, February 2011.

(176) Khalilpour, R.; Abbas, A. HEN optimization for efficient retrofitting of coal-fired power plants with post-combustion carbon capture. *Int. J. Greenhouse Gas Control* **2011**, *5*, 189-199.

(177) Lawal, A.; Wang, M.; Stephenson, P.; Obi, O. Demonstrating full-scale post-combustion CO₂ capture for coal-fired power plants through dynamic modelling and simulation. *Fuel* **2012**, *101*, 115-128.

(178) Sipöcz, N.; Tobiesen, F. A. Natural gas combined cycle power plants with CO₂ capture – Opportunities to reduce cost. *Int. J. Greenhouse Gas Control* **2012**, *7*, 98-106.

(179) Biliyok, C.; Yeung, H. Evaluation of natural gas combined cycle power plant for post-combustion CO₂ capture integration. *Int. J. Greenhouse Gas Control* **2013**, *19*, 396-405.

(180) IEAGHG "Post-Combustion CO₂ Capture Scale-up Study," IEA Greenhouse Gas R&D Programme, February 2013.

(181) Mac Dowell, N.; Shah, N. Dynamic modelling and analysis of a coal-fired power plant integrated with a novel split-flow configuration post-combustion CO₂ capture process. *Int. J. Greenhouse Gas Control* **2014**, *27*, 103-119.

(182) Hanak, D. P.; Biliyok, C.; Yeung, H.; Białecki, R. Heat integration and exergy analysis for a supercritical high-ash coal-fired power plant integrated with a post-combustion carbon capture process. *Fuel* **2014**, *134*, 126-139.

(183) Huizeling, E.; van den Weijde, G. "Non-confidential FEED study report: Special report for the Global Carbon Capture and Storage Institute," 2011.

(184) Reddy, S.; Johnson, D.; Gilmartin, J. Fluor's Econamine FG PlusSM Technology For CO₂ Capture at Coal-fired Power Plants. In *Power Plant Air Pollutant Control "Mega" Symposium*: Baltimore, August 25-28, 2008.

(185) Reddy, S.; Scherffius, J.; Freguia, S.; Roberts, C. Fluor's Econamine FG PlusSM Technology: An Enhanced Amine-Based CO₂ Capture Process. In *Second National Conference on Carbon Sequestration*: NETL/DOE Alexandria VA, May 5-8, 2003.

(186) Strigle, R. F. *Packed Tower Design and Applications: Random and Structured Packings*, 2nd; Gulf Publishing Company: Houston, Texas, 1994.

(187) Kister, Z. H. *Distillation Design*; McGraw-Hill, Inc.: New York, 1992.

(188) Khalilpour, R.; Abbas, A. Optimal synthesis and design of solvent-based PCC process using a rate-based model. *Sep. Purif. Technol.* **2014**, *132*, 149-167.

(189) Wang, G. Q.; Yuan, X. G.; Yu, K. T. Review of Mass-Transfer Correlations for Packed Columns. *Ind. Eng. Chem. Res.* **2005**, *44*, 8715-8729.

(190) Gualito, J. J.; Cerino, F. J.; Cardenas, J. C.; Rocha, J. A. Design Method for Distillation Columns Filled with Metallic, Ceramic, or Plastic Structured Packings. *Ind. Eng. Chem. Res.* **1997**, *36*, 1747-1757.

(191) Aspen Technology. *Aspen Icarus Reference Guide: Icarus Evaluation Engine (IEE) V8.0*; Aspen Technology, Inc.: Burlington, MA, 2012.

(192) US DOE "Cost and Performance Baseline for Fossil Energy Plants. Volume 1: Bituminous Coal and Natural Gas to Electricity," US Department of Energy, Revision 2, November 2010.

(193) IEAGHG "Improvement in Power Generation with Post-Combustion Capture of CO₂," IEA Greenhouse Gas R&D Programme, November 2004.

(194) Rubin, E. S.; Short, C.; Booras, G.; Davison, J.; Ekstrom, C.; Matuszewski, M.; McCoy, S. A proposed methodology for CO₂ capture and storage cost estimates. *Int. J. Greenhouse Gas Control* **2013**, *17*, 488-503.

(195) Gibbins, J. R.; Crane, R. I. Scope for reductions in the cost of CO₂ capture using flue gas scrubbing with amine solvents. *Proceedings of the Institution of Mechanical Engineers, Part A: Journal of Power and Energy* **2004**, *218*, 231-239.

(196) Rao, A. B.; Rubin, E. S. Identifying Cost-Effective CO₂ Control Levels for Amine-Based CO₂ Capture Systems. *Ind. Eng. Chem. Res.* **2006**, *45*, 2421-2429.

(197) Romeo, L. M.; Bolea, I.; Escosa, J. M. Integration of power plant and amine scrubbing to reduce CO₂ capture costs. *Appl. Therm. Eng.* **2008**, *28*, 1039-1046.

(198) Pfaff, I.; Oexmann, J.; Kather, A. Optimised integration of post-combustion CO₂ capture process in greenfield power plants. *Energy* **2010**, *35*, 4030-4041.

(199) Strube, R.; Manfrida, G. CO₂ capture in coal-fired power plants—Impact on plant performance. *Int. J. Greenhouse Gas Control* **2011**, *5*, 710-726.

(200) Lucquiaud, M.; Gibbins, J. On the integration of CO₂ capture with coal-fired power plants: A methodology to assess and optimise solvent-based post-combustion capture systems. *Chem. Eng. Res. Des.* **2011**, *89*, 1553-1571.

(201) Lucquiaud, M.; Gibbins, J. Effective retrofitting of post-combustion CO₂ capture to coal-fired power plants and insensitivity of CO₂ abatement costs to base plant efficiency. *Int. J. Greenhouse Gas Control* **2011**, *5*, 427-438.

(202) Duan, L.; Zhao, M.; Yang, Y. Integration and optimization study on the coal-fired power plant with CO₂ capture using MEA. *Energy* **2012**, *45*, 107-116.

(203) Hasan, M. M. F.; Baliban, R. C.; Elia, J. A.; Floudas, C. A. Modeling, Simulation, and Optimization of Postcombustion CO₂ Capture for Variable Feed Concentration and Flow Rate. 1. Chemical Absorption and Membrane Processes. *Ind. Eng. Chem. Res.* **2012**, *51*, 15642-15664.

(204) DOE/NETL. Quality Guidelines for Energy Systems Studies: Detailed Coal Specifications. US Department of Energy, January 2012.

(205) Singer, J. G. Steam Fundamentals. In *Standard Handbook of Powerplant Engineering*
Elliott, T. C., Ed.; McGraw-Hill Professional, 1997.

(206) Black & Veatch. *Power Plant Engineering*; Springer: New York, 1996.

(207) DOE/NETL "Quality Guidelines for Energy Systems Studies: Process Modeling Design Parameters," US Department of Energy, May 2014.

(208) DOE/NETL "Quality Guidelines for Energy Systems Studies: Process Modeling Design Parameters," US Department of Energy, January 2012.

(209) IEA. Key World Energy Statistics. OECD/IEA: Paris, France, 2013.

(210) IEA. Technology Roadmap: Carbon capture and storage. OECD/IEA: Paris, France, 2013.

(211) Rao, A. B.; Rubin, E. S.; Keith, D. W.; Granger Morgan, M. Evaluation of potential cost reductions from improved amine-based CO₂ capture systems. *Energy Policy* **2006**, *34*, 3765-3772.

(212) Agbonghae, E. O.; Font Palma, C.; Hughes, K. J.; Ingham, D. B.; Ma, L.; Pourkashanian, M. Optimal Integration of a Coal-fired Power Plant to a CO₂ Capture Plant Based on Parametric Studies. *Fuel* **2014**, Submitted for Publication.